

# Graph Neural Network Flavour Tagging and Boosted Higgs Measurements at the LHC

Samuel John Van Stroud  
University College London

Submitted to University College London in fulfilment  
of the requirements for the award of the  
degree of **Doctor of Philosophy**

December 15, 2022

## **Declaration**

I, Samuel John Van Stroud confirm that the work presented in this thesis is my own. Where information has been derived from other sources, I confirm that this has been indicated in the thesis.

Samuel Van Stroud

---

# Abstract

This thesis presents investigations into the challenges of, potential improvements to, and the application of  $b$ -jet identification at the ATLAS experiment at the Large Hadron Collider (LHC). A focus is placed on the high transverse momentum regime, which is a critical region in which to study the Standard Model, but within which successful  $b$ -jet identification becomes difficult.

As  $b$ -jet identification relies on the successful reconstruction of charged particle trajectories (tracks), the tracking performance is investigated and potential improvements are assessed. Track reconstruction becomes increasingly difficult at high transverse momentum due to the increased multiplicity and collimation of tracks, and also due to the presence of displaced tracks that may occur as the result of the decay of a long-flying  $b$ -hadron. The investigations revealed that the track quality selections applied during track reconstruction are suboptimal for tracks inside high transverse momentum  $b$ -jets, motivating future studies into the optimisation of these cuts.

To improve  $b$ -tagging performance two novel techniques are employed: the classification of the origin of tracks and the application of graph neural networks. An algorithm has been developed to classify the origin of tracks, which allows a more optimal collection of tracks to be selected for use in other algorithms. A graph neural network (GNN) jet flavour tagger has also been developed. This tagger requires only tracks and jet variables as inputs, making a break from previous algorithms, which relied on the outputs of several other algorithms. This model is trained to simultaneously predict the jet

flavour, track origins, and track-pair compatibility (i.e. vertexing), and demonstrates markedly improvements in  $b$ -tagging performance, both at low and high transverse momenta. The closely related task of c-jet identification also benefits from these methods.

Analysis of high transverse momentum  $H \rightarrow b\bar{b}$  decays, where the Higgs boson is produced in association with a vector boson, was also performed using  $139\text{ fb}^{-1}$  of 13 TeV proton-proton collision data from Run 2 of the LHC. The analysis is described, with a focus on the detailed modelling studies performed by the author. The analysis measured provided first measurements in this channel of the Higgs boson production in two high transverse momentum regions. The impact of applying the improved GNN-based  $b$ -tagging algorithms to the analysis is also studied.

# **Impact Statement**

impact statement 500 words [link to ucl info](#)

## Acknowledgements

Here is an example of how to declare commands for use in a single file that will not be needed elsewhere. Additionally, it serves to illustrate the chapter referencing system.

J. Shlomi for GNN.

Brian Moser and Francesco Di Bello provided useful guidance and insights into the studies in Chapter 7.

This thesis was made in L<sup>A</sup>T<sub>E</sub>X 2 <sub>$\varepsilon$</sub>  using the “heptesis” class [1].

# Contents

<b>1</b>	<b>Introduction</b>	<b>11</b>
<b>2</b>	<b>Theoretical Framework</b>	<b>13</b>
2.1	The Standard Model . . . . .	13
2.1.1	Quantum Electrodynamics . . . . .	14
2.1.2	Quantum Chromodynamics . . . . .	16
2.1.3	The Electroweak Sector . . . . .	17
2.2	The Higgs Mechanism . . . . .	18
2.2.1	Electroweak Symmetry Breaking . . . . .	19
2.2.2	Fermionic Yukawa Coupling . . . . .	22
2.2.3	Higgs Sector Phenomenology . . . . .	24
<b>3</b>	<b>The Large Hadron Collider and the ATLAS Detector</b>	<b>27</b>
3.1	The Large Hadron Collider . . . . .	28
3.2	Coordinate System & Collider Definitions . . . . .	29
3.2.1	ATLAS Coordinate System . . . . .	30
3.2.2	Track Parameterisation . . . . .	31
3.2.3	Hadron Collider Definitions . . . . .	31
3.3	The ATLAS Detector . . . . .	35
3.3.1	Inner Detector . . . . .	36
3.3.2	Calorimeters . . . . .	39
3.3.3	Muon Spectrometer . . . . .	41
3.3.4	The Trigger . . . . .	42
3.4	Reconstructed Physics Objects . . . . .	43
3.4.1	Tracks . . . . .	43
3.4.2	Vertices . . . . .	46
3.4.3	Jets . . . . .	47
3.4.4	Leptons . . . . .	49

3.4.5	Missing Transverse Momentum . . . . .	51
<b>4</b>	<b>Tracking and <math>b</math>-tagging</b>	<b>52</b>
4.1	$b$ -hadron Reconstruction . . . . .	53
4.1.1	Decay Topology . . . . .	53
4.1.2	Challenges Facing $b$ -hadron Reconstruction . . . . .	55
4.2	Investigations into High $p_T$ $b$ -hadron Tracking . . . . .	58
4.2.1	Shared Hits . . . . .	59
4.2.2	Global $\chi^2$ Fitter Outlier Removal . . . . .	60
4.3	Conclusion . . . . .	63
<b>5</b>	<b>Track Classification MVA</b>	<b>65</b>
5.1	Machine Learning Background . . . . .	65
5.1.1	Neural Networks . . . . .	66
5.1.2	Training with Gradient Descent . . . . .	68
5.2	Track Truth Origin Labelling . . . . .	69
5.3	Fake Track Identification Tool . . . . .	70
5.3.1	Datasets . . . . .	72
5.3.2	Model Inputs . . . . .	73
5.3.3	Model Hyperparameters . . . . .	73
5.3.4	Results . . . . .	76
5.4	$b$ -hadron Track Identification . . . . .	77
5.5	Combined Approach . . . . .	77
5.6	Conclusion . . . . .	79
<b>6</b>	<b>Graph Neural Network Flavour Tagger</b>	<b>81</b>
6.1	Motivation . . . . .	82
6.2	Graph Neural Network Theory . . . . .	85
6.3	Experiemental Setup . . . . .	86
6.3.1	Datasets . . . . .	86
6.4	Model Architecture . . . . .	87
6.4.1	Model Inputs . . . . .	87
6.4.2	Auxiliary Training Objectives . . . . .	88
6.4.3	Architecture . . . . .	90
6.4.4	Training . . . . .	94

6.5	Results . . . . .	95
6.5.1	<i>b</i> -tagging Performance . . . . .	96
6.5.2	<i>c</i> -tagging Performance . . . . .	101
6.5.3	Jet Display Diagrams . . . . .	102
6.5.4	Ablations . . . . .	104
6.5.5	Inclusion of Low-Level Vertexing Algorithms . . . . .	106
6.5.6	Vertexing Performance . . . . .	109
6.5.7	Track Classification Performance . . . . .	112
6.5.8	Looser Track Selection . . . . .	115
6.6	Conclusion . . . . .	115
<b>7</b>	<b>Boosted VHbb Analysis</b>	<b>120</b>
7.1	Analysis Overview . . . . .	121
7.1.1	Data & Simulated Samples . . . . .	122
7.1.2	Object Reconstruction . . . . .	123
7.1.3	Selection Criteria . . . . .	125
7.1.4	Control Regions . . . . .	127
7.1.5	Background Composition . . . . .	127
7.2	Systematic Uncertainties & Background Modelling . . . . .	129
7.2.1	Sources of Systematic Uncertainties . . . . .	130
7.2.2	Implementation of Variations . . . . .	132
7.2.3	Vector Boson + Jets Modelling . . . . .	133
7.2.4	Diboson Modelling . . . . .	140
7.3	Statistical Treatment . . . . .	142
7.3.1	Likelihood Function . . . . .	143
7.3.2	Background Normalisations . . . . .	145
7.3.3	Asimov Dataset & Expected Results . . . . .	146
7.4	Results . . . . .	146
7.4.1	Post-fit Distributions . . . . .	147
7.4.2	Observed Signal Strength & Significance . . . . .	147
7.4.3	Impact of Systematics . . . . .	151
7.5	Improved <i>b</i> -tagging using GNNs . . . . .	154
7.6	Conclusion . . . . .	154
<b>8</b>	<b>Conclusion</b>	<b>156</b>

---

**Contents** **10**

**Bibliography** 157

**List of figures** 171

**List of tables** 182

# <sup>2</sup> Chapter 1

## <sup>3</sup> Introduction

- <sup>4</sup> This thesis describes various efforts in improving the understanding of the Higgs boson and its coupling to heavy flavour quarks, primarily through the improvement of the algorithms used to reconstruct and analyse jets.
- <sup>7</sup> Chapter 2 describes the theoretical foundations of the work presented in the rest of the thesis.
- <sup>9</sup> Chapter 3 describes the ATLAS detector at the CERN accelerator complex. Details of reconstructed physics objects are also provided.
- <sup>11</sup> Chapter 4 provides an overview of tracking and  $b$ -tagging at ATLAS, and studies into the challenges of high transverse momentum  $b$ -tagging.
- <sup>13</sup> Chapter 5 describes a tool to predict the origins of tracks. The tool is used to improve  $b$ -tagging performance by the identification and removal of fake tracks before their input to the  $b$ -tagging algorithms.
- <sup>16</sup> Chapter 6 introduces a novel monolithic approach to  $b$ -tagging using graph neural networks and auxiliary training objectives.
- <sup>18</sup> Chapter 7 describes the measurement of the associated production of a Higgs boson decaying into a pair of  $b$ -quarks at high transverse momentum.
- <sup>20</sup> Chapter 8 contains some concluding remarks.

- 21 The author's contribution to the work presented in this thesis is as follows.
- 22 **Tracking:** The author was been an active member of the Cluster and Tracking  
23 in Dense Environments group for the duration of their qualification task on the  
24 understanding of tracking performance at high transverse momentum. The author  
25 played a key role in software r22 validation studies for the tracking group, including  
26 the validation of the quasi-stable particle interaction simulation and the radiation  
27 damage Monte-Carlo simulation. The author helped design and improve several  
28 tracking software frameworks, and contributed to heavy flavour tracking efficiency  
29 studies in dense environments.
- 30 ***b*-tagging:** The author has been an active member of the Flavour Tagging group  
31 since September 2014. The author played a key role in investigating the performance  
32 of the low level taggers at high transverse momentum and led studies into the  
33 labelling and classification of track origins. Based on work by J. Shlomi, the author  
34 helped develop a new flavour tagging algorithm which offers a large performance  
35 improvement with respect to the current state of the art. The author also played a key  
36 role in software r22 validation studies for the Flavour Tagging group, including the  
37 validation of the quasi-stable particle interaction simulation. The author maintains  
38 and contributes to various software frameworks used in the Flavour Tagging group,  
39 and contributes to group documentation.
- 40 **Higgs:** The author was an active member of the Boosted VHbb analysis group The  
41 author performed various studies deriving systematic uncertainties for the  $V+jets$   
42 and diboson backgrounds. The author also produced and maintained samples, ran fit  
43 studies and cross checks, and gave the diboson unblinding approval talk to the Higgs  
44 group. The author also contributed to the developement of the analysis software.

<sup>45</sup> **Chapter 2**

<sup>46</sup> **Theoretical Framework**

<sup>47</sup> The Standard Model (SM) of particle physics is the theory describing all known  
<sup>48</sup> elementary particles and their interactions via three of the four fundamental forces.  
<sup>49</sup> Developed by merging the successful theories of quantum mechanics and relativity  
<sup>50</sup> in the second half of the 20th century, the SM's position today at the centre of our  
<sup>51</sup> understanding of the nature of the Universe is firmly established by an unparalleled  
<sup>52</sup> level of agreement between the predictions from the model and experimental results  
<sup>53</sup> [2, 3].

<sup>54</sup> The SM has predicted the discovery of the top and bottom quarks [4–6], the  $W$   
<sup>55</sup> and  $Z$  bosons [7], and the tau neutrino [8]. The last missing piece of the SM to be  
<sup>56</sup> discovered was the Higgs boson, first theorised in the 1960s [9–11], and eventually  
<sup>57</sup> observed at the LHC in 2012 [12, 13]. After its discovery, much ongoing work has  
<sup>58</sup> been carried out performing detailed measurements of its mass and interactions with  
<sup>59</sup> other particles.

<sup>60</sup> In this chapter, an overview of the SM is given in Section 2.1, and a more detailed  
<sup>61</sup> discussion of the Higgs sector and Higgs phenomenology is provided in Section 2.2.

<sup>62</sup> **2.1 The Standard Model**

<sup>63</sup> The SM is formulated in the language of Quantum Field Theory (QFT). In this  
<sup>64</sup> framework, particles are localised excitations of corresponding quantum fields, which  
<sup>65</sup> are operator-valued distributions across spacetime.

Central to QFT is the Lagrangian density which describes the kinematics and dynamics of a field. Observations of conserved quantities are linked, via Noether's theorem, to symmetries which are expressed by the Lagrangian. Alongside Global Poincaré symmetry, the SM Lagrangian observes a local non-Abelian  $SU(3)_C \otimes SU(2)_L \otimes U(1)_Y$  gauge symmetry. Gauge symmetries leave observable properties of the system unchanged when the corresponding gauge transformations are applied to the fields. The full Lagrangian of the SM can be broken up into distinct terms corresponding to the different sectors, as in Eq. (2.1). An overview of each sector is given in the following chapters.

$$\mathcal{L}_{\text{SM}} = \mathcal{L}_{\text{EW}} + \mathcal{L}_{\text{QCD}} + \mathcal{L}_{\text{Higgs}} + \mathcal{L}_{\text{Yukawa}} \quad (2.1)$$

The SM provides a mathematical description of how three of the four fundamental forces interact with the matter content of the Universe. The SM contains 12 spin-1/2 fermions, listed in Table 2.1, and five bosons listed in Table 2.2.

<b>Generation</b>	Leptons			Quarks		
	<b>Flavour</b>	<b>Mass [MeV]</b>	<b>Charge [e]</b>	<b>Flavour</b>	<b>Mass [MeV]</b>	<b>Charge [e]</b>
First	$e$	0.511	-1	$u$	2.16	$2/3$
	$\nu_e$	$< 1.1 \times 10^{-6}$	0	$d$	4.67	$-1/3$
Second	$\mu$	105.7	-1	$c$	$1.27 \times 10^3$	$2/3$
	$\nu_\mu$	$< 0.19$	0	$s$	93.4	$-1/3$
Third	$\tau$	1776.9	-1	$t$	$173 \times 10^3$	$2/3$
	$\nu_\tau$	$< 18.2$	0	$b$	$4.18 \times 10^3$	$-1/3$

**Table 2.1:** The fermions of the SM [14]. Three generations of particles are present. Also present (unlisted) are the antiparticles, which are identical to the particles up to a reversed charge sign.

77

### 2.1.1 Quantum Electrodynamics

Quantum electrodynamics (QED) is the relativistic quantum theory which describes the interaction between the photon and charged matter. Consider a Dirac spinor field  $\psi = \psi(x)$  and its adjoint  $\bar{\psi} = \psi^\dagger \gamma^0$ , where  $\psi^\dagger$  denotes the Hermitian conjugate of  $\psi$ . The field  $\psi$  describes fermionic spin-1/2 particle, for example an electron. The

Name	Symbol	Mass [GeV]	Charge [ $e$ ]	Spin
Photon	$\gamma$	$< 1 \times 10^{-27}$	$< 1 \times 10^{-46}$	1
Charged Weak boson	$W^\pm$	$80.377 \pm 0.012$	$\pm 1$	1
Neutral Weak boson	$Z$	$91.1876 \pm 0.0021$	0	1
Gluon	$g$	0	0	1
Higgs	$H$	$125.25 \pm 0.17$	0	0

**Table 2.2:** The bosons of the SM [14]. The photon, weak bosons and gluons are gauge bosons arising from gauge symmetries, and carry the four fundamental forces of the SM. The recently discovered Higgs boson is the only fundamental scalar particle in the SM.

<sup>83</sup> Dirac Lagrangian density is

$$\mathcal{L}_{\text{Dirac}} = \bar{\psi}(i\cancel{\partial} - m)\psi, \quad (2.2)$$

<sup>84</sup> where  $\cancel{\partial} = \gamma^\mu \partial_\mu$  denotes the contraction with the Dirac gamma matrices  $\gamma^\mu$  (summation over up-down pairs of indices is assumed). Application of the Euler-Lagrange equation on Eq. (2.2) yields the Dirac equation

$$(i\cancel{\partial} - m)\psi = 0. \quad (2.3)$$

<sup>87</sup> Suppose some fundamental symmetry that requires invariance under a local  $U(1)$   
<sup>88</sup> gauge transformation

$$\psi \rightarrow \psi' = \psi e^{-iq\alpha(x)}, \quad (2.4)$$

<sup>89</sup> where  $\alpha$  varies over every spacetime point  $x$ . Under this transformation, the Dirac  
<sup>90</sup> equation transforms as

$$(i\cancel{\partial} - m)\psi e^{-iq\alpha(x)} + q\cancel{\partial}\alpha(x)\psi e^{-iq\alpha(x)} = 0. \quad (2.5)$$

<sup>91</sup> For the Dirac equation to remain invariant under the transformation in Eq. (2.4),  
<sup>92</sup> a new field  $A_\mu$  which transforms as  $A_\mu \rightarrow A'_\mu = A_\mu + \partial_\mu \alpha(x)$  must be added. The  
<sup>93</sup> transformed interaction term

$$-q\cancel{A}\psi \rightarrow -q\cancel{A}\psi e^{-iq\alpha(x)} - q\cancel{\partial}\alpha(x)\psi e^{-iq\alpha(x)} \quad (2.6)$$

will then cancel the asymmetric term in Eq. (2.5) as required. The  $U(1)$  invariant Lagrangain can therefore be constructed by adding an interaction between  $\psi$  and  $A_\mu$  to Eq. (2.2). For completeness, the kinetic term for the new field  $A_\mu$  is also added in terms of  $F_{\mu\nu} = \partial_\mu A_\nu - \partial_\nu A_\mu$ , which is trivially invariant under the transformation in Eq. (2.4). The interaction term is typically absorbed into the covariant derivative  $D_\mu = \partial_\mu + iqA_\mu$ , thus named as it transforms in the same way as the field  $\psi$ . Collecting these modifications to Eq. (2.2) yields the QED Lagrangain

$$\mathcal{L}_{\text{QED}} = -\frac{1}{4}F_{\mu\nu}F^{\mu\nu} + \bar{\psi}(iD^\mu - m)\psi. \quad (2.7)$$

The quadratic term  $A_\mu A^\mu$  is not invariant and therefore the field  $A_\mu$  must be massless. Requiring invariance under local  $U(1)$  gauge transformations necessitated the addition of a new field  $A_\mu$ , interpreted as the photon field, which interacts with charged matter. In the SM, the QED Lagrangian is absorbed into the electroweak sector, discussed in Section 2.1.3.

### 2.1.2 Quantum Chromodynamics

Quantum Chromodynamics (QCD) is the study of quarks, gluons and their interactions. Quarks and gluons carry colour charge, which comes in three kinds, called red, green and blue. While the  $U(1)$  symmetry group in Section 2.1.1 was Abelian, the QCD Lagrangian is specified by requiring invariance under transformations from the non-Abelian  $SU(3)$  group, making it a Yang-Mills theory [15] which requires the addition of self-interacting gauge fields. The infinitesimal  $SU(3)$  group generators are given by  $T_a = \lambda_a/2$ , where  $\lambda_a$  are the eight Gell-Mann matrices. These span the space of infinitesimal group transformations and do not commute with each other, instead satisfying the commutation relation

$$[T_a, T_b] = if_{abc}T_c, \quad (2.8)$$

where  $f_{abc}$  are the group's structure constants. Consider the six quark fields  $q_k = q_k(x)$ . Each flavour of quark  $q_k$  transforms in the fundamental triplet representation, in which each component of the triplet corresponds to the colour quantum number for red, green and blue colour charged respectively.  $G_{\mu\nu}^a$  are the eight gluon field

120 strength tensors, one for each generator  $T_a$ , defined as

$$G_{\mu\nu}^a = \partial_\mu A_\nu - \partial_\nu A_\mu - g_s f^{abc} A_\mu^b A_\nu^c, \quad (2.9)$$

121 where  $A_\mu^a$  are the gluon fields and  $g_s$  is the strong coupling constant. The covariant  
122 derivative is written as

$$D_\mu = \partial_\mu + i g_s T_a A_\mu^a. \quad (2.10)$$

123 The full QCD Lagrangian is then given by

$$\mathcal{L}_{\text{QCD}} = -\frac{1}{4} G_{\mu\nu}^a G_a^{\mu\nu} + q_k (i \not{D} - m_k) q_k. \quad (2.11)$$

124 Cubic and quartic terms of the gauge fields  $A_\mu^a$  appear in the Lagrangian, leading to  
125 the gluon's self interaction.

126 The QCD coupling constant  $g_s$  varies, or “runs”, with energy. At lower energy  
127 scales (and corresponding larger distance scales) the interaction is strong. This  
128 leads to quark confinement, whereby an attempt to isolate individual colour-charged  
129 quarks requires so much energy that additional quark-antiquark are produced. At  
130 higher energy scales (and corresponding smaller distance scales), asymptotic freedom  
131 occurs as the interactions become weaker, allowing perturbative calculations to be  
132 performed. Hadrons are bound states of quarks. They are invariant under  $SU(3)$   
133 gauge transformations (i.e. are colour-charge neutral, or *colourless*).

### 134 2.1.3 The Electroweak Sector

135 The weak and electromagnetic forces are unified in the Glashow-Weinberg-Salam  
136 (GWS) model of electroweak interaction [16–18]. The Lagrangian is specified by  
137 requiring invariance under the symmetry group  $SU(2)_L \otimes U(1)_Y$ , as motivated by a  
138 large amount of experimental data. Here,  $SU(2)_L$  is referred to as weak isospin and  
139  $U(1)_Y$  as weak hypercharge.

- 140 The generators of  $SU(2)_L$  are  $T_a = \sigma_a/2$ , where  $\sigma_a$  are the three Pauli spin matrices  
141 which satisfy the commutation relation

$$[T_a, T_b] = i\varepsilon_{abc}T_c. \quad (2.12)$$

- 142 The generator of  $U(1)_Y$  is  $Y = 1/2$ . Each generator corresponds to a gauge field,  
143 which, after symmetry breaking (discussed in Section 2.2), give rise to the massive  
144 vector bosons,  $W^\pm$  and  $Z$ , and the massless photon. The massive vector bosons  
145 are the carriers of the weak force. Due to the mass of the force carriers, the weak  
146 force has a short range and so it appears weak even though its intrinsic strength is  
147 comparable to that of QED.

- 148 The charge operator  $Q$  can be written as a combination of the third  $SU(2)_L$  generator  
149 and the  $U(1)_Y$  generator as in

$$Q = T_3 + Y. \quad (2.13)$$

- 150 The weak force violates parity conservation [19–21], i.e. invariance under parity  
151 transformations (mirror reflections). Only left handed fermions participate in the  
152 weak interaction. Since there is no other force through which neutrinos interact with  
153 other particles, there are no right handed neutrinos in the standard model.

## 154 2.2 The Higgs Mechanism

- 155 The Brout-Englert-Higgs mechanism (henceforth just “Higgs mechanism”) is the  
156 mechanism through which the fundamental particles of the SM acquire mass [9–11].  
157 Experimentally it was known that the weak force had a weak effective strength,  
158 which was suggestive of a massive mediating gauge particle. However, directly  
159 adding mass to the weak gauge bosons violates the non-Abelian symmetry of the  
160 SM. Instead, the gauge bosons can gain mass through the interaction with a scalar  
161 Higgs field which results from the spontaneous breakdown of symmetry as discussed  
162 in Section 2.2.1. Similarly, the Higgs mechanism gives mass to the fermions, as  
163 discussed in Section 2.2.2. Section 2.2.3 described some basic phenomenology of the  
164 Higgs particle relevant to hadron colliders.

### <sup>165</sup> 2.2.1 Electroweak Symmetry Breaking

<sup>166</sup> Spontaneous symmetry breaking (SSB) is a key part of the Higgs mechanism. It  
<sup>167</sup> is the transition of a physical system from a state of manifest symmetry to a state  
<sup>168</sup> of hidden, or *broken*, symmetry. In particular, this applies to physical systems  
<sup>169</sup> where the Lagrangian observes some symmetry, but the lowest energy vacuum states  
<sup>170</sup> do not exhibit that same symmetry. In other words, the symmetry is broken for  
<sup>171</sup> perturbations around the vacuum state.

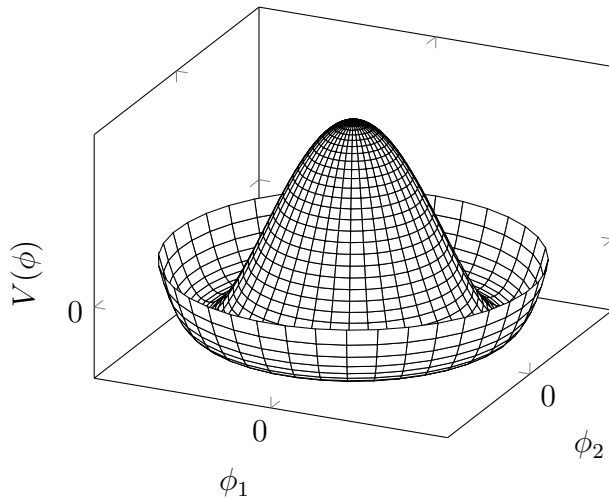


**Figure 2.1:** The Higgs potential  $V(\phi)$  of the complex scalar field singlet  $\phi = \phi_1 + i\phi_2$ , with a choice of  $\mu^2 < 0$  leading to a continuous degeneracy in the true vacuum states. A false vacuum is present at the origin. The SM Higgs mechanism relies on a complex scalar doublet with a corresponding 5-dimensional potential.

<sup>172</sup> Consider gauge fields from the local  $SU(2)_L \otimes U(1)_Y$  symmetry group discussed in  
<sup>173</sup> Section 2.1.3 coupled to a complex scalar field  $\phi = \phi(x)$ . The scalar field  $\phi$  transforms  
<sup>174</sup> as a weak isospin doublet. Omitting the kinetic term of the gauge fields, and writing  
<sup>175</sup>  $\phi^2 \equiv \phi^\dagger \phi$ , the Lagrangian is

$$\mathcal{L}_{\text{Higgs}} = (D_\mu \phi)^\dagger (D^\mu \phi) - [\mu^2 \phi^2 + \lambda \phi^4], \quad (2.14)$$

<sup>176</sup> where the covariant derivative is given by

$$D_\mu = \partial_\mu + igA_\mu^a T^a + ig' B_\mu, \quad (2.15)$$

and  $T^a$  are the generators of  $SU(2)$ . The potential term  $V(\phi)$  is made up of a quadratic and quartic term in the scalar field  $\phi$ , which each contain an arbitrary parameter, respectively  $\lambda$  and  $\mu$ . The quartic term gives the field self-interaction, and cannot be negative as this would lead to a potential that was unbounded from below. The quadratic term can be positive or negative. In the case where the quadratic term is positive, it is interpreted as a mass term for the scalar field. By choosing  $\mu^2 < 0$  the field becomes unphysical due to its negative mass. In order to obtain a physical interpretation of the Lagrangian in Eq. (2.14) for the case where  $\mu^2 < 0$ , the field  $\phi$  is expanded around the vacuum state. The vacuum expectation value (VEV) is the expected value of the field  $\phi$  which minimises the potential  $V(\phi)$  (equivalently the expected value of the field operator  $\phi$  when the system is in a vacuum state,  $|\langle \phi \rangle_0|^2 \equiv |\langle 0 | \phi | 0 \rangle|^2 \equiv \phi_0^2$ ). Minimising the potential gives a VEV of

$$\phi_0^2 = -\mu^2/\lambda = v^2. \quad (2.16)$$

Due to the shape of the potential in Fig. 2.1, there is a degeneracy in the direction that the complex doublet  $\phi$  points. As all the different vacuum states minimise the potential and therefore yield identical physics, one can arbitrarily choose the state to lie along the second component of the doublet. Application of Eq. (2.13) shows this choice is manifestly invariant under the charge operator. This allows the identification of the unbroken subgroup  $U(1)_Q$ , under which the ground state is invariant. The generator of  $U(1)_Q$  is the charge operator  $Q$ .

Adding the particle content back to the theory by expanding the field around the vacuum state, and making a transformation to the unitary gauge to remove unphysical Nambu-Goldstone modes (which arise in the context of global symmetries [22, 23]), yields

$$\phi = \frac{1}{\sqrt{2}} \begin{bmatrix} 0 \\ v + H \end{bmatrix}, \quad (2.17)$$

where  $H$  is a real scalar field, the *true vacuum* Higgs field. Substituting this into Eq. (2.14) and identifying physical fields from the quadratic terms of linear combinations of unphysical fields, one can write the physical fields  $W_\mu^\pm$ ,  $Z_\mu$  and  $A_\mu$

203 in terms of the original fields  $A_\mu^a$  and  $B_\mu$ . This gives

$$W_\mu^\pm = \frac{1}{\sqrt{2}}(A_\mu^1 \mp iA_\mu^2) \quad \begin{bmatrix} A_\mu \\ Z_\mu \end{bmatrix} = \begin{bmatrix} \cos \theta_W & \sin \theta_W \\ -\sin \theta_W & \cos \theta_W \end{bmatrix} \begin{bmatrix} B_\mu \\ A_\mu^3 \end{bmatrix}. \quad (2.18)$$

204 where  $\theta_W$  is the weak mixing angle defined by

$$\cos \theta_W = \frac{g}{\sqrt{g^2 + g'^2}}. \quad (2.19)$$

205 The corresponding masses of the now massive vector bosons can be read off as

$$m_W = \frac{1}{2}gv \quad m_Z = \frac{m_W}{\cos \theta_W}, \quad (2.20)$$

206 while the photon remains massless. The Higgs mass is  $m_H = v\sqrt{\lambda} = \mu$ .

207 This is the Higgs mechanism. It maintains the renormalisability and unitarity of  
208 the SM whilst allowing the weak vector bosons to acquire mass. In summary, an  
209 unphysical complex scalar field  $\phi$  with a nonzero VEV leads to spontaneous symmetry  
210 breaking. Due to the non-Abelian symmetry breaking, would-be massless Nambu-  
211 Goldstone modes, which arise after expansion around the true vacuum state, are  
212 exactly cancelled out by making a local gauge transformation to the unitary gauge,  
213 and instead are absorbed by the vector bosons, allowing them to acquire mass.

214 This sector of the SM contains four fundamental parameters that must be determined  
215 from experiment. These can be specified by the Lagrangian parameters  $g$ ,  $g'$ ,  $v$   
216 and  $\lambda$  or the physically measurable parameters  $m_Z$ ,  $\sin \theta_W$ ,  $m_H$  and  $e$ . In the  
217 local neighbourhood around the true vacuum, the macroscopic symmetry of the  
218 system is not realised, and therefore the physical particles do not obey the original  
219 symmetry. However, information about the symmetry is retained through some  
220 additional constraints on the parameters of the theory. Prior to symmetry breaking,  
221 the potential contained two terms and two constants. After symmetry breaking  
222 there are three terms but still only two constants that relate these terms. This is the  
223 vestige of the original symmetry.

224 Spontaneous symmetry breaking has modified the original symmetry group of the SM  
225  $SU(2)_L \times U(1)_Y \rightarrow SU(3)_C \otimes U(1)_Q$ . Three broken generators from the symmetry  
226 group  $SU(2)_L \times U(1)_Y$  have been absorbed into the definition of the physical weak

227 vector bosons, giving them mass. The same methodology can be used to generate  
228 the fermion masses, as shown in the next section.

### 229 2.2.2 Fermionic Yukawa Coupling

230 Adding the masses of the fermions by hand breaks the gauge invariance of the  
231 theory. Instead, we can use a Yukawa coupling between the fermion fields and the  
232 Higgs field in order to generate mass terms after spontaneous electroweak symmetry  
233 breakdown [17]. In this way, the fermion masses are determined by both the respective  
234 couplings to the Higgs field and the VEV of the Higgs field itself, which sets the  
235 basic mass scale of the theory.

236 The Higgs field  $\phi$  transforms as an  $SU(2)$  doublet with  $Y = 1/2$ , as does the left-  
237 handed fermion field  $\psi_L$ . The right-handed fermion field  $\psi_R$  transforms as an  $SU(2)$   
238 singlet.

### 239 Lepton Masses

240 The renormalisable and gauge invariant coupling between a fermionic field  $\psi$  and a  
241 scalar Higgs field  $\phi$  can be written as

$$\mathcal{L}_{\text{Yukawa}} = -g_f(\bar{\psi}_L \phi \psi_R + \bar{\psi}_R \phi^\dagger \psi_L). \quad (2.21)$$

242 where  $\psi_L = (\nu_L, e_L)$  and  $\psi_R = e_R$  for the first generation leptons. After spontaneous  
243 symmetry breaking (see Section 2.2.1), the scalar Higgs field in unitary gauge  
244 Eq. (2.17) consists of a VEV and the true vacuum Higgs field  $H$ . Substituting this  
245 in to Eq. (2.21) yields

$$\mathcal{L}_{\text{Yukawa}} = -\frac{v g_e}{\sqrt{2}} \bar{e} e - \frac{g_e}{\sqrt{2}} \bar{e} H e, \quad (2.22)$$

246 using  $\bar{e} e = (\bar{e}_L + \bar{e}_R)(e_L + e_R) = \bar{e}_L e_R + \bar{e}_R e_L$ . The VEV component of  $\phi$  provides  
247 the first term in Eq. (2.22) which is quadratic in the electron field, and can therefore  
248 be identified as the electron mass term. An interaction term between the electron  
249 field  $e$  and the true vacuum Higgs field  $H$  is also present. Mass is generated for the  
250 other lepton generations in the same way.

251 **Quark Masses**

252 The down-type quarks acquire their mass analogous to the leptons, with  $\psi_L = (u_L, d_L)$   
253 and  $\psi_R = d_R$  for the first quark generation. Mass is generated for the up-type quarks  
254 using the conjugate field to  $\phi$  which transforms under  $SU(2)$  as a doublet with  
255  $Y = -1/2$ . The conjugate field  $\tilde{\phi}$  is constructed as

$$\tilde{\phi} = i\sigma_2 \phi^\dagger = \begin{bmatrix} 0 & 1 \\ -1 & 0 \end{bmatrix} \begin{bmatrix} \phi_1^\dagger \\ \phi_2^\dagger \end{bmatrix} = \frac{1}{\sqrt{2}} \begin{bmatrix} v + H \\ 0 \end{bmatrix}, \quad (2.23)$$

256 and transforms in the same way as  $\phi$ . This field can be used to write an additional  
257 Yukawa coupling which provides mass for the up-type quarks in a similar way as  
258 before.

$$\mathcal{L}_{\text{Yukawa}}^{\text{up}} = -g_q (\bar{\psi}_L \tilde{\phi} \psi_R + \bar{\psi}_R \tilde{\phi}^\dagger \psi_L) \quad (2.24)$$

259 Considering the first generation of up-type quarks with  $\psi_L = (u_L, d_L)$  and  $\psi_R = u_R$ ,  
260 substitution into Eq. (2.24) yields

$$\mathcal{L}_{\text{Yukawa}}^{\text{up}} = -\frac{vg_u}{\sqrt{2}} \bar{u}u - \frac{g_u}{\sqrt{2}} \bar{u}Hu. \quad (2.25)$$

261 The Yukawa terms mix quarks of different generations of lepton and quark. Physical  
262 particles are detected in their mass eigenstates  $q$ , which diagonalise the mass matrix,  
263 but interact via the weak interaction according to their weak eigenstates  $\tilde{q}$ , which  
264 are superpositions of the mass eigenstates. This feature of the weak sector leads to  
265 mixing between different generations of quarks and leptons. Quark mixing can be  
266 expressed using the Cabibbo-Kobayashi-Maskawa (CKM) matrix, which specifies the  
267 strength of flavour-changing weak currents. The entries in the matrix are enumerated  
268 as

$$\begin{bmatrix} \tilde{d} \\ \tilde{s} \\ \tilde{b} \end{bmatrix} = \begin{bmatrix} V_{ud} & V_{us} & V_{ub} \\ V_{cd} & V_{cs} & V_{cb} \\ V_{td} & V_{ts} & V_{tb} \end{bmatrix} \begin{bmatrix} d \\ s \\ b \end{bmatrix}, \quad (2.26)$$

269 where the size of the elements  $|V_{pq}|^2$  measures the probability of a transition between  
270 states  $p$  and  $q$ .

### **2.2.3 Higgs Sector Phenomenology**

As previous discussed in this section, the Higgs field plays a key role in the SM, giving mass to fundamental particles. The strength of the coupling between the Higgs field and another particle is proportional to that particle's mass. This fact dictates which production mechanisms and decay modes are dominant at the LHC. The cross sections for different production mechanisms at a centre of mass energy  $\sqrt{s} = 13 \text{ TeV}$  are shown as a function of the Higgs mass  $m_H$  in Fig. 2.3. Higgs boson production occurs mainly through four modes, shown in Fig. 2.2. The dominant production mode is gluon-gluon fusion ( $pp \rightarrow H$ ), which is predominantly mediated by a virtual top quark loop. Vector boson fusion ( $pp \rightarrow qqH$ ) is the second most dominant production mechanism, in which a pair of  $W$  or  $Z$  bosons fuse to produce a Higgs after being radiated by two quarks, which also occur in the final state. Next most common is the associated production of a Higgs boson and a vector boson ( $pp \rightarrow VH$ ), in which a pair of quarks fuse to produce a single  $W$  or  $Z$  boson which radiates a Higgs. The final of the four leading production modes is top quark fusion, in which two gluons each radiate a quark-antiquark pair, and a quark from each pair fuses to produce a Higgs boson.

Although gluon-gluon fusion is the dominant production mode, for hadronic decays of the Higgs boson the associated production with a vector boson has the advantage of leading to a more conspicuous final state due to the likelihood of the vector bosons decaying leptons. Leptons provide a clean signals to detect and trigger on.

Since the Higgs boson couples proportional to mass as already mentioned, decays to heavier particles are favoured. The branching ratios of different Higgs boson decay modes are shown as a function of  $m_H$  in Fig. 2.4. Approximately 58% of the time the Higgs boson decays to a pair of  $b$ -quarks, the dominant decay mode. The next heaviest fermions are the tau lepton and the  $c$ -quark, decays to pairs of these particles happen approximately an order of magnitude less often. Decays to pairs of vector bosons are via a virtual off shell Higgs boson only. While the  $H \rightarrow \gamma\gamma$  and  $H \rightarrow ZZ$  branching ratios are small compared with fermionic decay modes (around 0.2% for  $H \rightarrow \gamma\gamma$ ), these decay channels were instrumental in the initial discovery of the Higgs due to the low level of background processes which mimic the final state.

This thesis presents a measurement of the Higgs bosons production rate using events with a Higgs boson produced in association with vector boson and decaying to a pair

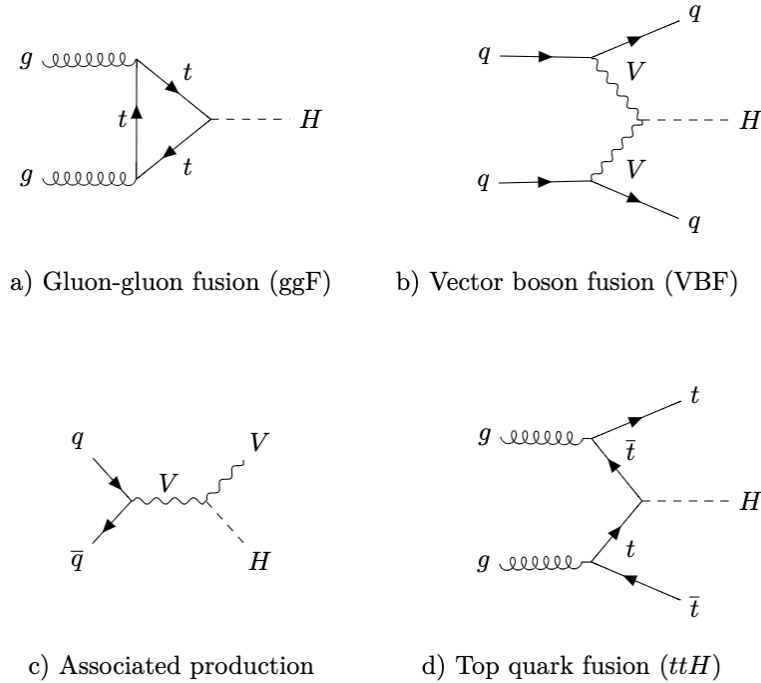


**Figure 2.2:** Diagrams for the four main Higgs boson production modes at the LHC for a Higgs mass  $m_H = 125$  GeV at a centre of mass energy  $\sqrt{s} = 13$  TeV.

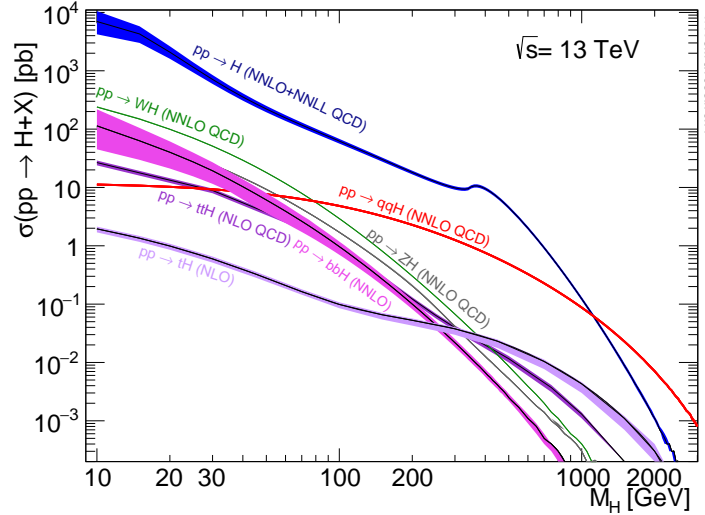


**Figure 2.3:** Higgs boson production cross sections as a function of Higgs mass ( $m_H$ ) at  $\sqrt{s} = 13$  TeV [24]. Uncertainties are shown in the shaded bands. At  $m_H = 125$  GeV, Higgs boson production is dominated by gluon-gluon fussion, vector boson fusion, associated production with vector bosons, and top quark fusion.

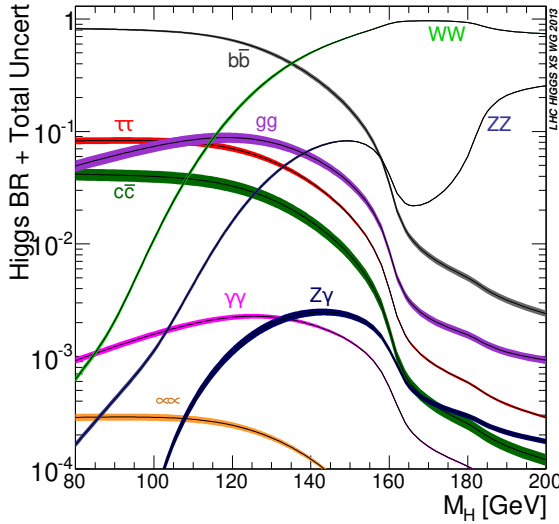


**Figure 2.4:** Higgs boson branching ratios as a function of Higgs mass ( $m_H$ ) at  $\sqrt{s} = 13 \text{ TeV}$  [24]. Uncertainties are shown in the shaded bands. At  $m_H = 125 \text{ GeV}$ , the Higgs predominantly decays to a pair of  $b$ -quarks, around 58% of the time. The leading subdominant decay mode is to a pair of  $W$  bosons.

of  $b$ -quarks, i.e.  $pp \rightarrow VH(bb)$ . The  $H \rightarrow b\bar{b}$  decay mode directly probes the Higgs coupling to the second generation fermions, and more specifically to the bottom quark. This coupling was first observed in 2018 [25, 26]. Ongoing work measuring the coupling strengths, in particular in the high energy regime, is the focus of the analysis presented in this thesis in Chapter 7.

309 Chapter 3

310 The Large Hadron Collider and the  
311 ATLAS Detector

312 Since the completion of its construction in 2008, the Large Hadron Collider (LHC) [27]  
313 at CERN has extended the frontiers of particle physics through its unprecedented  
314 energy and luminosity. The LHC accelerates protons around a 27 km ring until they  
315 are travelling just  $3 \text{ m s}^{-1}$  slower than the speed of light, at which point they  
316 are made to collide. The protons travel round the ring 11,000 times per second in  
317 two concentric beams, which are guided by superconducting magnets cooled using  
318 liquid helium to  $-271.3^\circ\text{C}$  ( $1.9\text{ K}$ ). The beams travel in opposite directions around  
319 the ring and are crossed at four locations so that collisions between protons can  
320 take place. Around these collision points four specialised detectors, ALICE [28],  
321 CMS [29], LHCb [30] and ATLAS [31], are located to capture information about the  
322 products of the collisions.

323 In this chapter, a brief overview of the LHC and the accelerator complex at CERN  
324 is given in Section 3.1. The coordinate system used at the ATLAS detector and  
325 other common definitions are introduced in Section 3.2. Next, an overview of the  
326 different detector systems is provided in Section 3.3, and finally descriptions of  
327 various commonly used reconstructed objects is given in Section 3.4.

### <sup>328</sup> 3.1 The Large Hadron Collider

<sup>329</sup> The LHC is operated in multi-year *runs* during which beams of protons are circulated  
<sup>330</sup> and collided. Between runs there are periods of shutdown while the accelerator and  
<sup>331</sup> detector machinery is maintained and upgraded. Run 1 began in 2010 when the LHC  
<sup>332</sup> collided proton bunches, each containing more than  $10^{11}$  particles, 20 million times  
<sup>333</sup> per second, providing 7 TeV proton-proton collisions at instantaneous luminosities  
<sup>334</sup> of up to  $2.1 \times 10^{32} \text{ cm}^{-2} \text{ s}^{-1}$ . The centre-of-mass energy was increased to 8 TeV  
<sup>335</sup> towards the end of Run 1 in 2012. Run 2, which spanned in 2015–2018, further  
<sup>336</sup> increased the the proton-proton collision energy to 13 TeV. During Run 2 the bunch  
<sup>337</sup> spacing was reduced, leading to a collisison rate of 40 MHz. Over the course of  
<sup>338</sup> Run 2 a total usable integrated luminosity of  $139 \text{ fb}^{-1}$  was recorded. 2022 marked the  
<sup>339</sup> beginning of Run 3 which, with a higher center of mass energy and peak luminosity,  
<sup>340</sup> is expected to culminate in the approximate tripling of the dataset size. A summary  
<sup>341</sup> of key information about each run is listed in Table 3.1.

Period	Year	$\sqrt{s}$ [TeV]	$\langle\mu\rangle$	Bunch spacing [ns]	Luminosity [ $\text{cm}^{-2} \text{ s}^{-1}$ ]
Run 1	2010–2012	7–8	18	50	$8 \times 10^{33}$
Run 2	2015–2018	13	34	25	$1\text{--}2 \times 10^{34}$
Run 3	2022–2025	13.6	50	25	$2 \times 10^{34}$

**Table 3.1:** Overview of the different LHC runs [32,33]. The average number of interactions per bunch-crossing is denoted as  $\langle\mu\rangle$  (see Section 3.2.3), and is here averaged over the entire run. Numbers for Run 3 are preliminary and are only provided to give an indication of expected performance.

<sup>342</sup> An overview of the accelerator complex at CERN is shown in Fig. 3.1. The LHC is  
<sup>343</sup> at the final stage of a chain of accelerators which incrementally step-up the energy  
<sup>344</sup> of incoming protons. The first accelerator is Linac4, a linear accelerator which  
<sup>345</sup> accelerates negative hydrogen ions to an energy of 160 MeV. Upon leaving Linac4,  
<sup>346</sup> the ions are stripped of both electrons and the resulting protons are fed into the  
<sup>347</sup> Proton Synchrotron Booster (PSB), which increases the energy of the protons to  
<sup>348</sup> 2 GeV. The protons leaving the PSB are passed to the Proton Synchrotron (PS),  
<sup>349</sup> which increases the energy to 26 GeV, and then from the PS to the Super Proton  
<sup>350</sup> Synchrotron (SPS) which further increases the energy to 450 GeV. Finally, the proton

<sup>351</sup> beams are injected in the LHC where they are accelerated to their final energy of  
<sup>352</sup> 6.5 TeV (for Run 2).

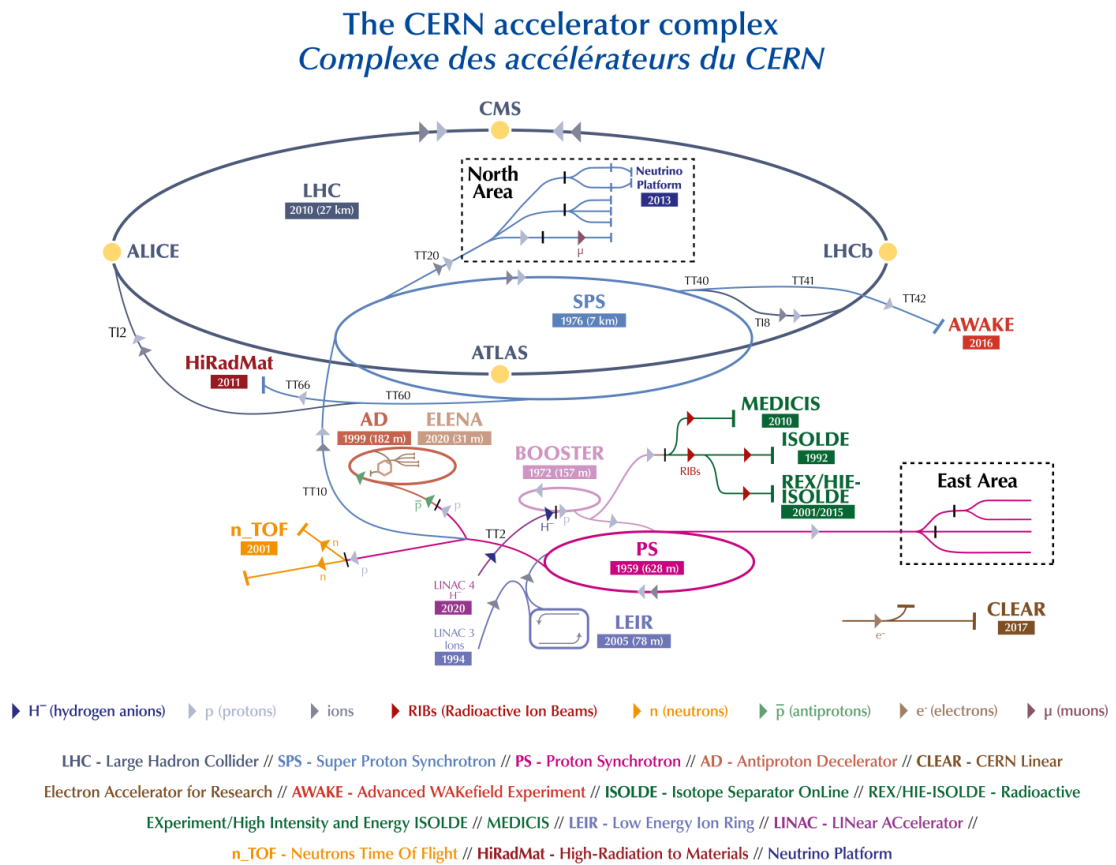


**Figure 3.1:** An overview of the CERN accelerator complex [34]. The LHC is fed by a series of accelerators starting with Linac4. Next are the Proton Synchrotron Booster, the Proton Synchrotron, and finally the Super Proton Synchrotron which injects protons into the LHC.

## <sup>353</sup> 3.2 Coordinate System & Collider Definitions

354 In Section 3.2.1, the coordinate system used at ATLAS is introduced. The parameter-  
355 isation used for the specifying the trajectory of charged particle tracks is described in  
356 Section 3.2.2, and definitions for some frequently occurring concepts and quantities  
357 is provided in Section 3.2.3.

### 358 3.2.1 ATLAS Coordinate System

359 The origin of the coordinate system used by ATLAS is the nominal interaction point  
 360 in the centre of the detector. As shown in Fig. 3.2, the  $z$ -axis points along the  
 361 direction the beam pipe, while the  $x$ -axis points from the interaction point to the  
 362 centre of the LHC ring, and the  $y$ -axis points upwards. The transverse plane lies  
 363 in  $x$ - $y$  while the longitudinal plane lies along the  $z$ -axis. A cylindrical coordinate  
 364 system with coordinates  $(r, \phi)$  is used in the transverse plane, where  $r$  is the radius  
 365 from the origin and  $\phi$  is the azimuthal angle around the  $z$ -axis.

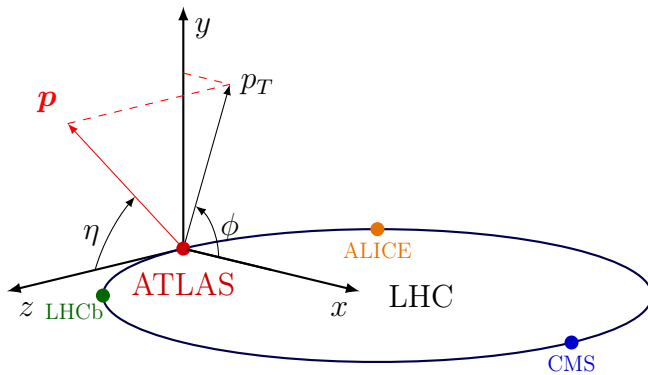


**Figure 3.2:** The coordinate system used at the ATLAS detector, showing the locations of the four main experiments located at various points around the LHC. The 3-vector momentum  $\mathbf{p} = (p_x, p_y, p_z)$  is shown by the red arrow. Reproduced from Ref. [35].

366 The polar angle  $\theta$  is commonly specified in terms of the pseudorapidity  $\eta$ , defined as

$$\eta = -\ln \left[ \tan \left( \frac{\theta}{2} \right) \right]. \quad (3.1)$$

367 The pseudorapidity is a convenient quantity to work with as differences in  $\eta$  are  
 368 invariant under Lorentz boosts. In addition, particle production is constant as a  
 369 function of  $\eta$ .

370 The transverse momentum  $p_T$  of an object is the sum in quadrature of the momenta  
 371 in the transverse plane

$$p_T = \sqrt{p_x^2 + p_y^2}. \quad (3.2)$$

<sup>372</sup> Angular distance between two objects is measured in units of  $\Delta R$  and is defined as  
<sup>373</sup> the sum in quadrature of the  $\eta$  and  $\phi$  displacements

$$\Delta R = \sqrt{(\Delta\eta)^2 + (\Delta\phi)^2}. \quad (3.3)$$

### <sup>374</sup> 3.2.2 Track Parameterisation

<sup>375</sup> The trajectories of charged particle tracks are parameterised as a helix which is  
<sup>376</sup> fully specified using five parameters:  $(d_0, z_0, \phi, \theta, q/p)$ . Transverse and longitudinal  
<sup>377</sup> impact parameters (IP)  $d_0$  and  $z_0$  specify the closest approach of the trajectory of  
<sup>378</sup> a particle to the origin. The transverse IP  $d_0$  and longitudinal IP  $z_0$  are measured  
<sup>379</sup> with respect to the hard scatter primary vertex (see Section 3.4.2).  $\phi$  and  $\theta$  are  
<sup>380</sup> the azimuthal and polar angles respectively, and  $q/p$  is the measured charge on the  
<sup>381</sup> track<sup>1</sup> divided by the scalar 3-momentum. Fig. 3.3 shows each of these parameters  
<sup>382</sup> diagrammatically.

<sup>383</sup> Impact parameter significances are defined as the IP divided by its corresponding  
<sup>384</sup> uncertainty,  $s(d_0) = d_0/\sigma(d_0)$  and  $s(z_0) = z_0/\sigma(z_0)$ . When used in flavour tagging  
<sup>385</sup> (see Chapter 4), track IP significances are lifetime signed according to the track's  
<sup>386</sup> direction with respect to the jet axis and the primary vertex [37]. The sign IP  
<sup>387</sup> significances is positive if the track crosses the jet axis in front of the primary vertex  
<sup>388</sup> and negative if the crossing is behind the primary vertex.

### <sup>389</sup> 3.2.3 Hadron Collider Definitions

#### <sup>390</sup> Cross Section

<sup>391</sup> The cross section  $\sigma$  is closely related to the probability of an interaction between  
<sup>392</sup> two colliding particles, and is analogous to an effective cross-sectional area of the  
<sup>393</sup> particles. The cross section of a process depends on the transition matrix element,  
<sup>394</sup> obtained using the Feynman rules of the theory which are derived using QFT, and a  
<sup>395</sup> phase space integral. At hadron colliders such as the LHC, the proton-proton cross

---

<sup>1</sup>Reconstructed charged particles are assumed to have a charge of  $\pm 1$ .

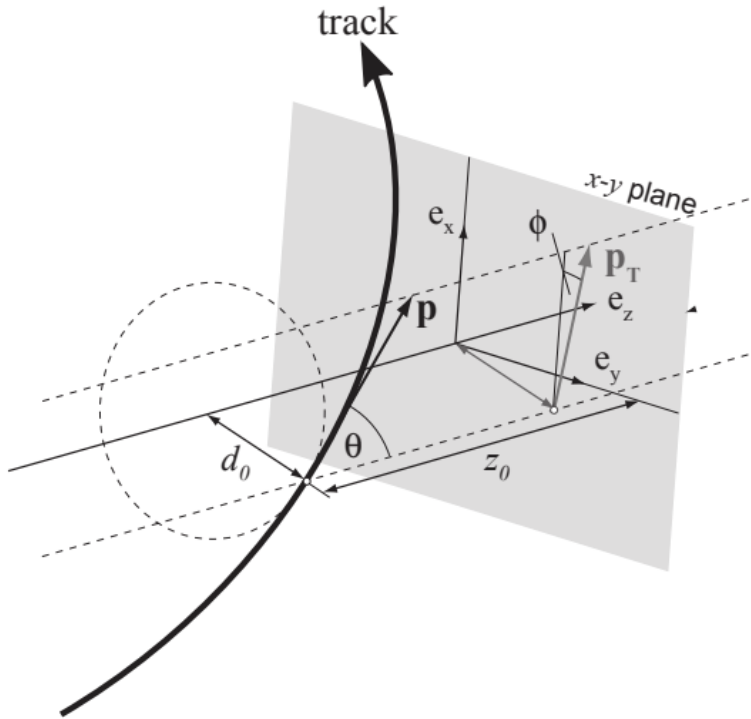


**Figure 3.3:** The track parameterisation used at the ATLAS detector. Five coordinates ( $d_0, z_0, \phi, \theta, q/p$ ) are specified, defined at the track's point of closest approach to the nominal interaction point at the origin of the coordinate system. The figure shows the three-momentum  $\mathbf{p}$  and the transverse momentum  $p_T$  (defined in Eq. (3.2)). The basis vectors  $e_x, e_y$  and  $e_z$  are also shown. Reproduced from Ref. [36].

<sup>396</sup> section can be factorised as

$$\sigma(pp \rightarrow X) \approx \text{PDFs} \cdot \text{partonic cross section.} \quad (3.4)$$

<sup>397</sup> The partonic cross section can be calculated at sufficiently high energies such as  
<sup>398</sup> those found at the LHC, while the parton distribution functions (PDFs) have to be  
<sup>399</sup> extracted from experimental results.

## <sup>400</sup> Luminosity

<sup>401</sup> The total number of proton-proton collisions  $N$  is related to the total  $pp$  cross  $\sigma$   
<sup>402</sup> section by the integrated luminosity  $L$ , as in

$$N = \sigma L = \sigma \int \mathcal{L} dt. \quad (3.5)$$

<sup>403</sup> The instantaneous luminosity  $\mathcal{L}$  relates the cross section to the number of collisions  
<sup>404</sup> per unit time. For two colliding bunched proton beams, it is defined as

$$\mathcal{L} = \frac{1}{\sigma} \frac{dN}{dt} = \frac{fn_1 n_2}{4\pi\sigma_x\sigma_y}, \quad (3.6)$$

<sup>405</sup> where  $n_1$  and  $n_2$  are the number of protons in the colliding bunches,  $f$  is the bunch  
<sup>406</sup> crossing frequency, and  $\sigma_x$  and  $\sigma_y$  are the rms width of the beam in the horizontal  
<sup>407</sup> and vertical directions.

<sup>408</sup> The total luminosity recorded over the course of Run 2 is shown in Fig. 3.4. In  
<sup>409</sup> total,  $139 \text{ fb}^{-1}$  of usable physics data was collected over the three-year run. The  
<sup>410</sup> uncertainty on the total integrated luminosity is 1.7% [38].

## <sup>411</sup> Pile-up

<sup>412</sup> At the centre of the ATLAS detector, bunches of more than  $10^{11}$  protons meet at a  
<sup>413</sup> small crossing angle. Each bunch-crossing is called an *event*. There is generally at  
<sup>414</sup> most one hard proton-proton scatter per event. Additional interactions are typically  
<sup>415</sup> relatively soft and are known as *pile-up*. Pile-up from interactions within the same  
<sup>416</sup> bunch-crossing is known as *in-time* pile-up while residual signatures from previous  
<sup>417</sup> bunch-crossings is known as *out-of-time* pile-up. The number of pile-up interactions

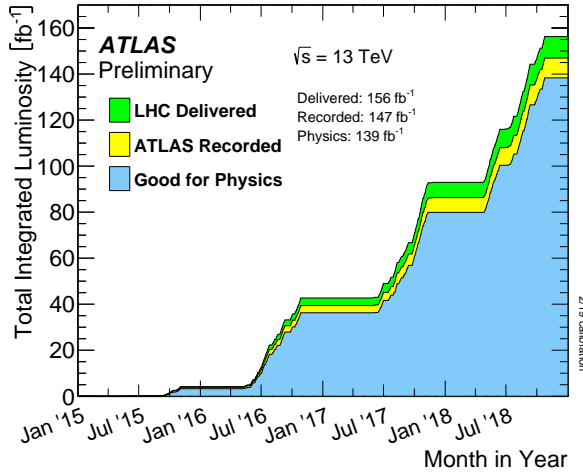


**Figure 3.4:** Delivered, recorded, and usable integrated luminosity as a function of time over the course of Run 2 [33]. A total of  $139 \text{ fb}^{-1}$  of collision data is labelled as good for physics, meaning all sub-detector systems were operating nominally.

is denoted  $\mu$ , which is often given as a time-averaged value  $\langle \mu \rangle$ . Histograms showing the number of pile-up interactions over the course of Run 2 are shown in Fig. 3.5.

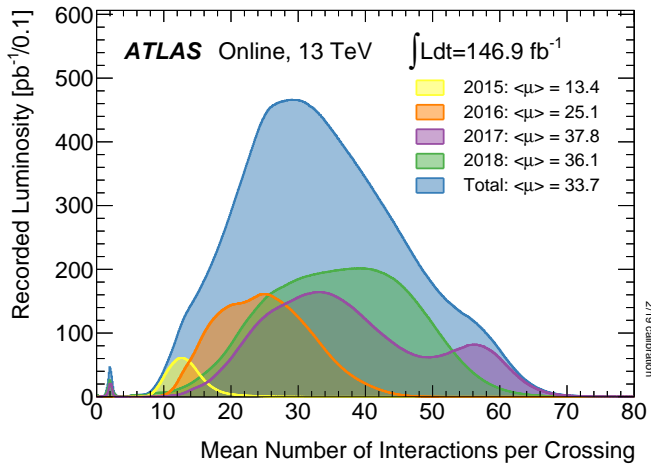


**Figure 3.5:** Average pile-up profiles measured by ATLAS during Run 2 [33]. Higher levels of pile-up are planned for Run 3.

### 420 3.3 The ATLAS Detector

421 The ATLAS<sup>2</sup> detector is made up of several specialised sub-detectors which are  
422 arranged concentrically around the nominal interaction point at the centre of the  
423 detector. The detector is designed to cover nearly the entire solid angle around the  
424 collision point. In this section a condensed overview of each sub-detector is given, in  
425 order of increasing radial distance from the point of collision. The inner tracking  
426 detector is described in Section 3.3.1, the electromagnetic and hadronic calorimeters  
427 in Section 3.3.2, the muon spectrometer in Section 3.3.3, and finally the trigger is  
428 described in Section 3.3.4. More complete information on the detector can be found  
429 in Ref. [31], while an overview of physics performance is given in [39].

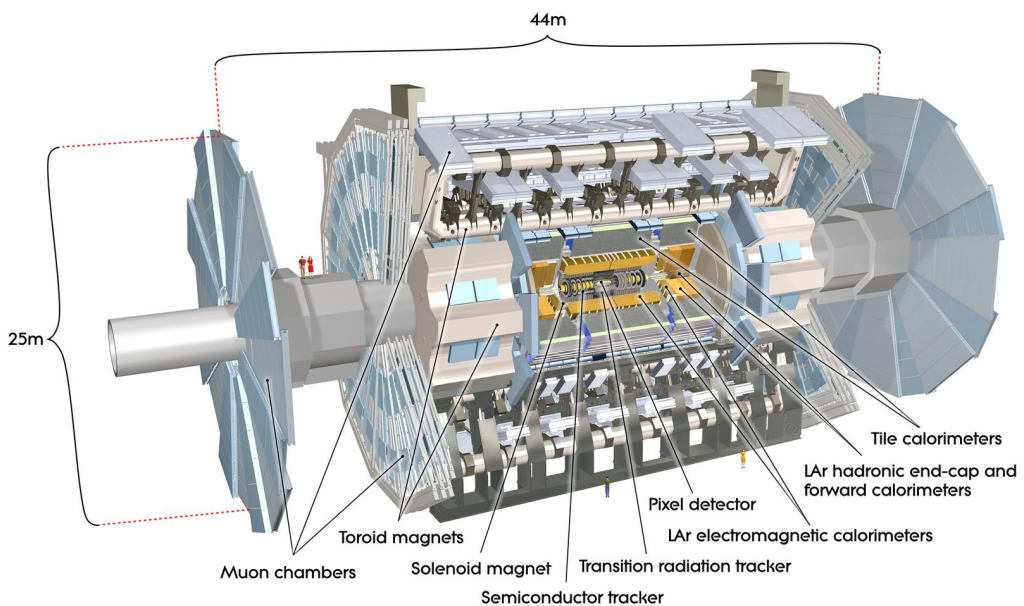


**Figure 3.6:** A 3D model of the entire ATLAS detector [40]. The detector is 46 m long and 25 m in diameter. Cutouts to the centre of the detector reveal the different subdetectors which are arranged in concentric layers around the nominal interaction point.

<sup>2</sup>A Toroidal LHC ApparatuS.

### 430 3.3.1 Inner Detector

431 The inner-detector system (ID) provides high-resolution charged particle trajectory  
432 tracking in the range  $|\eta| < 2.5$ . The ID is immersed in a 2 T axial magnetic field,  
433 produced by a superconducting solenoidal magnet, which enables the measurement  
434 of particle momentum and charge. After Run 3, the ID will be replaced by the  
435 ITk [41, 42].

436 The inner detector is made up of several sub-systems, shown in Figs. 3.7 and 3.8. The  
437 high-granularity silicon pixel detector covers the vertex region and typically provides  
438 four spacepoint measurements per track. It is followed by the silicon microstrip  
439 tracker (SCT), which usually provides a further four spacepoint measurements per  
440 track. These silicon detectors are complemented by the Transition Radiation Tracker  
441 (TRT), which enables radially extended track reconstruction up to  $|\eta| = 2.0$ .

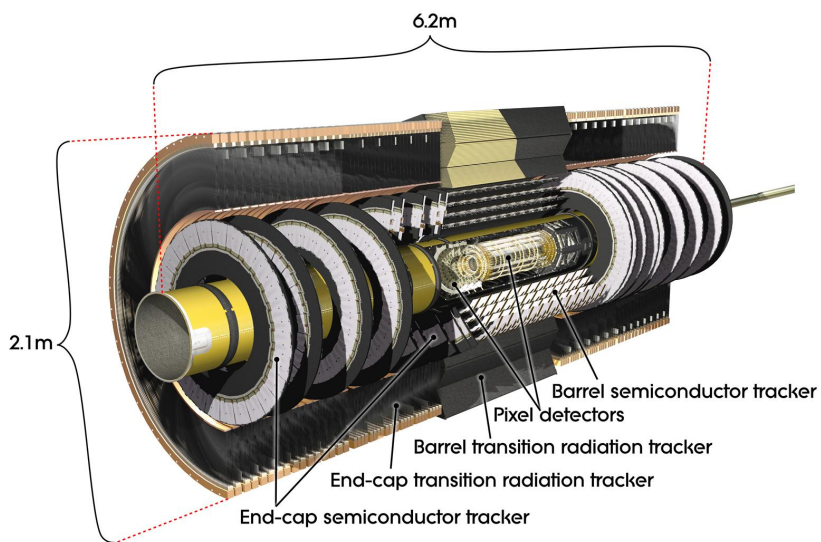


**Figure 3.7:** A 3D model of the ATLAS ID, made up of the pixel and SCT subdetectors, showing the barrel layers and end-cap disks [43].

442 The target inverse momentum resolution for the combined ID measurement is  
443 parameterised as a function of the track transverse momentum and polar angle [39].  
444 The parameterisation is given by

$$\sigma(1/p_T) = 0.36 \oplus \frac{13}{p_T \sin \theta} \text{TeV}^{-1}, \quad (3.7)$$

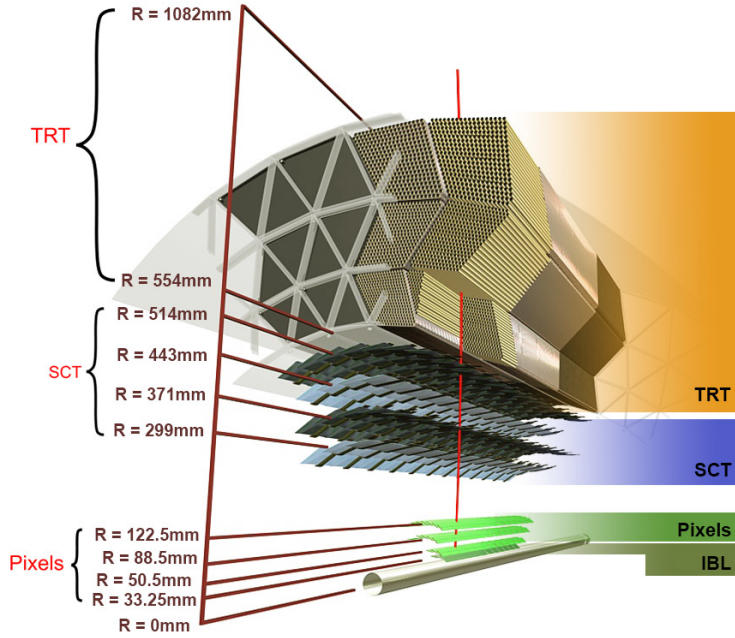


**Figure 3.8:** A cross-sectional view of the ATLAS ID, with the radii of the different barrel layers shown [36].

445 where  $\oplus$  denotes a sum in quadrature. For high- $p_T$  tracks (e.g.  $p_T \approx 100$  GeV) in  
 446 the central region,  $\sigma(1/p_T) \approx 0.4$  TeV $^{-1}$  corresponding to a relative error of 4%. The  
 447 momentum resolution generally good enough to correctly identify the sign of the  
 448 charge on particles up to the highest energies expected at the LHC. The transverse  
 449 impact parameter resolution  $\sigma(d_0)$  is parameterised similarly as

$$\sigma(d_0) = 11 \oplus \frac{115}{p_T \sin \theta} \mu\text{m}. \quad (3.8)$$

#### 450 Pixel Detector

451 The silicon pixel detector is comprised of four cylindrical barrels at increasing radii  
 452 from the beamline, and four disks on each side. The innermost barrel layer is  
 453 the insertable B-layer (IBL), which was installed before Run 2 [44, 45] and lies  
 454 approximately just 33 mm from the beam axis. The second-to-innermost layer is  
 455 often referred to as the B-layer. The specification of the pixel detector determines the  
 456 impact parameter resolution and the ability to reconstruct primary and secondary

vertices. The detector is required to have a high granularity (i.e. resolution) to maintain the low occupancy required to resolve nearby particles. Individual pixels are 50  $\mu\text{m}$  in the transverse direction  $R\phi$  and 400  $\mu\text{m}$  in the longitudinal  $z$  direction (250  $\mu\text{m}$  for the IBL). Cluster positions have a resolution of approximately 10  $\mu\text{m}$  in  $R\phi$  and 100  $\mu\text{m}$  in  $z$ .

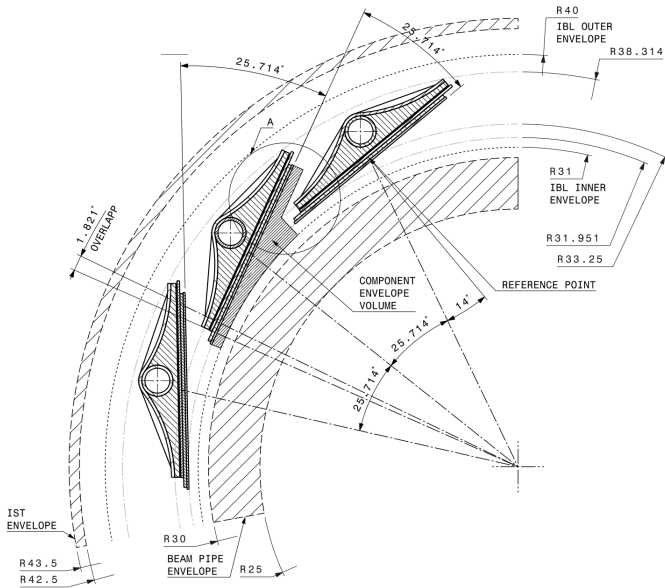


**Figure 3.9:** A schematic cross-sectional view of the ATLAS IBL [44].

## 462 Semi-Conductor Tracker (SCT)

463 The SCT is made up of four concentric barrel layers in the central region, and nine  
 464 disks in each end-cap. Each layer is itself made of a pair of silicon microstrip layers,  
 465 with a small stereo angle (20 mrad) between the two layers enabling the  $z$ -coordinate  
 466 to be measured from a pair of strip measurements. The SCT typically provides four  
 467 precision spacepoint measurements (eight strip measurements) per track in the barrel  
 468 region. These have intrinsic uncertainties of 17  $\mu\text{m}$  in the transverse direction  $R\phi$ , and  
 469 580  $\mu\text{m}$  in the longitudinal direction  $z$  [46]. The measurements provide a contribution  
 470 to the measurement of charged particle momentum and impact parameter, along  
 471 with vertex position. Charge-particle tracks can be distinguished if separated by  
 472 more than  $\sim 200 \mu\text{m}$ .

#### **473 Transition Radiation Tracker (TRT)**

474 The TRT is a straw-tube tracker which complements the higher-resolution silicon-  
475 based tracks by offering a larger number of hits per track (typically around 30) and  
476 a long lever arm, which aids the accurate measurement of particle momentum. It is  
477 made up of approximately 300 000 drift tubes with a diameter of 4 mm which are filled  
478 with an argon/xenon gas mixture. The walls of each tube are electrically charged,  
479 and a thin conducting wire runs along the center. When a charged particle traverses  
480 a tube, it ionises the gas and the resulting liberated electrons drift along the electric  
481 field to the wire, where an associated charge is registered. In the barrel the straws  
482 run parallel to the  $z$ -axis and therefore the TRT only provides tracking information  
483 in  $R\phi$ . Straws are arranged radially in the end-caps. The resulting two-dimensional  
484 spacepoints have a resolution of approximately 120  $\mu\text{m}$ . The spaces between the  
485 straws are filled with a polymer which encourages the emission of transition radiation,  
486 aiding electron identification.

#### **487 3.3.2 Calorimeters**

488 The calorimeter system measures the energy of incident particles over the range  
489  $|\eta| < 4.9$ . There are two main sub-systems: the electromagnetic calorimeter (ECal),  
490 which focuses on the measurement of electrons and photons, and the hadronic  
491 calorimeter (HCal), which measures the energy of hadrons. Upon entering the  
492 calorimeter, incident particles will interact with the detector material to produce a  
493 shower of secondary particles with reduced energies. The charge deposited in this  
494 process is measured to reconstruct the energy of the initial incident particle. The  
495 two calorimeter sub-systems must provide strong containment of showering particles  
496 to prevent punch-through of EM and non-muon particles to the HCal and muon  
497 system respectively.

#### **498 Liquid Argon (LAr) Electromagnetic Calorimeter**

499 The more granular lead/liquid-argon ECal covers the region  $|\eta| < 3.2$  and is split  
500 into barrel (covering  $|\eta| < 1.475$ ) and end-cap (covering  $1.375 < |\eta| < 3.2$ ) regions.  
501 EM calorimetry works by encouraging electrons and photons to interact with electri-

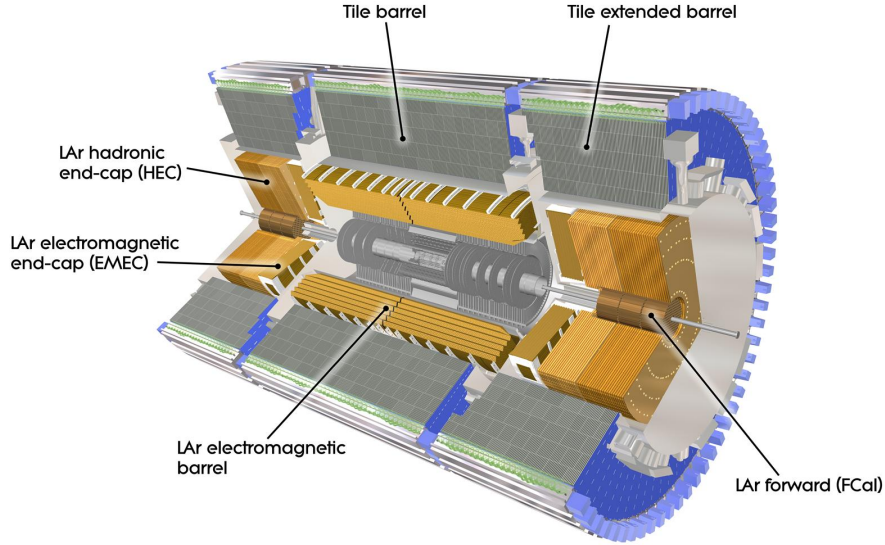


**Figure 3.10:** The ATLAS calorimeters [47]. The ECal uses LAr-based detectors, while the HCal uses mainly scintillating tile detectors. In the forward region the HCal also includes the LAr hadronic endcaps.

502 cally charged particles in detector material via bremsstrahlung ( $e \rightarrow e\gamma$ ) and pair  
 503 production ( $\gamma \rightarrow e^+e^-$ ). The EM calorimeter uses lead absorber plates to initiate  
 504 EM showers, resulting in secondary particles which ionise the surrounding liquid  
 505 argon. The charge is collected on copper electrodes and read out. The accordion  
 506 geometry of the ECal allows for a full coverage in  $\phi$  without any azimuthal cracks.

507 The energy resolution of the LAr calorimeter is made up of a sampling and a constant  
 508 term, which are summed in quadrature to produce the overall energy resolution. The  
 509 sampling term contributes approximately  $10\%/\sqrt{E}$ , while the constant term adds an  
 510 additional 0.7%. Photons with moderate transverse energy  $E_T \approx 50 \text{ GeV}$  have an  
 511 overall energy resolution of at most 1.6% over most of the pseudorapidity range. At  
 512 lower  $E_T \approx 10 \text{ GeV}$ , the resolution is degraded to approximately 5%. The resolution  
 513 measurements are obtained from test beam data [39].

#### 514 **Hadronic Tile Calorimeter**

515 In the central barrel region with  $|\eta| < 1.7$ , the HCal uses a tile calorimeter with  
 516 steel as an absorbing material, and scintillating tiles as the active material. Two

517 copper/liquid-argon calorimeter end-caps are also used. Incident hadrons interact  
518 via the strong and electromagnetic forces with the absorber material, mainly loosing  
519 energy due to multiple inelastic nuclear collisions. The active material captures the  
520 resulting electrons and photons to measure the energy of the incident hadron.

521 The jet energy resolution of the HCal is parameterised as a function of the jet  
522 transverse energy

$$\sigma(E_T)/E_T = 50\% \sqrt{E_T} \oplus 3\%, \quad (3.9)$$

523 corresponding to a jet energy resolution of 10% at a jet  $p_T$  of approximately 100 GeV  
524 [48].

### 525 3.3.3 Muon Spectrometer

526 Due to their higher mass, muons easily pass unimpeded through the ID and calorime-  
527 ters and therefore require specialised detectors for their measurement. The Muon  
528 Spectrometer (MS) is made up of dedicated tracking and triggering hardware. The  
529 precision tracking system uses three layers of monitored drift tubes with a barrel  
530 region covering  $|\eta| < 1.2$  and end-caps covering  $1 < |\eta| < 2.7$ . The inner layers of  
531 the end-caps use cathode strip chambers to better cope with the high occupancy  
532 in the forward region. Precision tracking resolution is approximately 50  $\mu\text{m}$ . The  
533 trigger system is comprised of resistive plate chambers in the barrel region covering  
534  $|\eta| < 1.0$  and thin gap chambers in the end-cap regions covering  $1 < |\eta| < 2.4$ . A set  
535 of three superconducting air-core toroidal magnets, each made up of eight coils, is  
536 used in each of the barrel and end-caps to deflect the muons as they pass through  
537 the MS, allowing their momentum and charge to be measured from the direction  
538 and magnitude of curvature. The toroidal magnets generate a field which is largely  
539 orthogonal to the muon trajectories which allows for maximum deflection. The  
540 transverse momentum resolution has been measured to be approximately 1.7% in the  
541 central region for low- $p_T$  muons, increasing to 4% for high- $p_T$  muons in the forward  
542 regions [49].

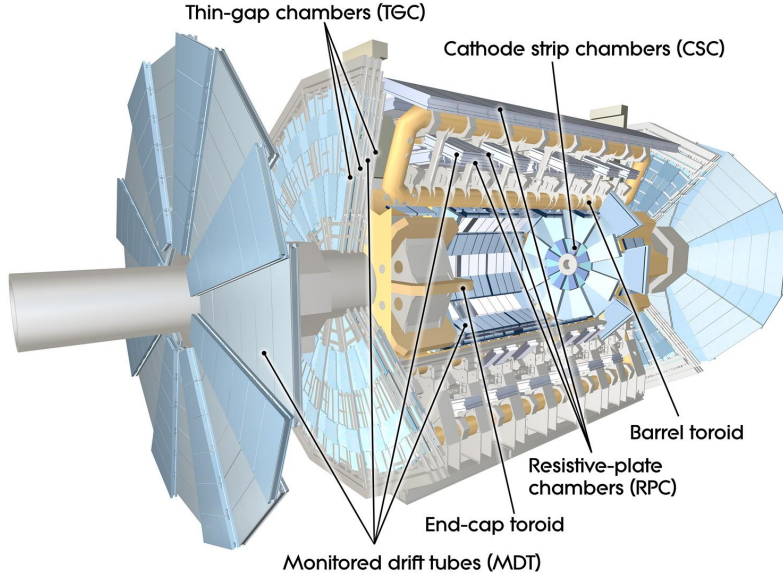


**Figure 3.11:** The ATLAS muon spectrometer [50].

### 543 3.3.4 The Trigger

544 The 25 ns bunch spacing used over the course of Run 2 corresponds to a bunch-  
 545 crossing or event rate of 40 MHz (see Table 3.1). If the full information for the  
 546 detector was written out for each event, this would correspond to the generation  
 547 of 60 TB of data each second. This is more than can be feasibly read out from  
 548 the hardware, processed and stored, requiring the use of a trigger system which  
 549 quickly makes a decision about whether or not an event is potentially interesting  
 550 and should be kept for further analysis. The trigger system is comprised of two  
 551 levels which search for signs of electrons, muons, taus, photons, and jets, as well as  
 552 events with large total or missing transverse energy. The hardware-based Level-1  
 553 (L1) trigger uses coarse information from the calorimeters and MS to accept events at  
 554 an average rate of 100 kHz approximately 2.5  $\mu$ s after the event. After the L1 trigger,  
 555 the software-based High Level Trigger (HLT) makes use of 40 000 CPU cores to make  
 556 a final selection on surviving events in approximately a few hundred milliseconds.  
 557 The final event read-out rate is approximately 1.2 kHz, corresponding to  $1.2 \text{ GB s}^{-1}$   
 558 of permanent data storage. More information is provided in [51].

## 559 3.4 Reconstructed Physics Objects

560 Event reconstruction is the process of analysing the output from the detector to  
561 determine the type and properties of particles present in an event. The reconstructed  
562 event provides information about the underlying physics process that led to these  
563 observable final state particles. Events passing the trigger selection (described in  
564 Section 3.3.4) undergo offline reconstruction, which makes use of the full information  
565 from the detector. Reconstruction and analysis of events relies on the extensive  
566 ATLAS software stack, see Ref. [52] for more information.

567 Several different reconstructed objects are used for physics analyses. Objects relevant  
568 to this thesis are described below.

### 569 3.4.1 Tracks

570 The reconstructed trajectories of charged particles are referred to as *tracks*. Track are  
571 reconstructed from the energy depositions (called *hits*) left by the particles as they  
572 traverse the the inner detector. Tracks are widely used for a variety of downstream  
573 applications, including vertexing and jet tagging, so their accurate reconstruction  
574 is a critical task. A comprehensive introduction to ATLAS tracking is available  
575 in Ref. [53], while specific optimisations for dense environments are detailed in  
576 Refs. [54, 55]. An overview of track reconstruction is given below.

### 577 Space-point Formation (Clustering)

578 When a charged particle traverses a silicon layer, charge can be collected in more  
579 than one pixel or strip. This is due to the incident angle of the particles with respect  
580 to the sensor, and also the drift of electrons between sensors caused by the magnetic  
581 field. Clusters (also called *hits* or *space-points*) are formed by clustering neighbouring  
582 pixels or strips and estimating locations of space-points using the shape and energy  
583 distribution of the clusters.

**584 Track Finding**

585 Space-points are used to build track seeds. These are groups of three hits which  
586 are geometrically compatible with being part of a track segment. A combinatorial  
587 Kalman filter (KF) is used to build track candidates by extending track seeds. The  
588 filter can create multiple track candidates per seed, with bifurcations along the track  
589 occurring when more than one compatible space-point exists on a given layer. In  
590 this way, the KF creates an excess of *track candidates*, which are only required to  
591 satisfy basic quality requirements. Track candidates are allowed to reuse or *share*  
592 hits freely (a single hit may be used by multiple track candidates). Typically, the  
593 presence of shared hits is a predictor of a bad track due to the high granularity of  
594 the ATLAS tracking detectors. At this stage, there can also be a large number of  
595 incorrect hits assigned to otherwise good tracks, and additionally large number of  
596 *fake* tracks, which are comprised of a majority of wrong hits and do not correspond  
597 to the trajectory of any one physical particle (fake tracks are defined as those where  
598 the majority of associated hits do not originate from one single truth particle, see  
599 Eq. (5.5)). The low quality of tracks at this stage necessitates an ambiguity solving  
600 step, in which candidates are cleaned, and the highest quality track are selected.

**601 Ambiguity Solving**

602 Ambiguity solving was introduced as part of the ATLAS New Tracking effort [53],  
603 which was intended to improve track reconstruction performance in dense envi-  
604 ronments. In the ambiguity solver, track candidates are processed individually in  
605 descending order of a track score. The track score quantifies the likelihood of the  
606 track corresponding to the trajectory of a real particle. Scoring uses a number of  
607 variables, including the number and positions of hits (preferring hits in more precise  
608 regions of the detector), the transverse momentum of the track and the track fit  
609 quality. The track fit quality describes the quality of the track as the  $\chi^2$  divided  
610 by the number degrees of freedom on the track. A preference for high transverse  
611 momentum tracks promotes the successful reconstruction of the more physically  
612 interesting energetic particles, and suppresses the large number of wrong hits assigned  
613 to low momentum tracks. The ambiguity solver also penalises tracks with missing  
614 hits on the innermost detector layers.

615 During the processing of a given highest-scoring track candidate, the track is cleaned  
616 (whereby problematic hits are removed), and, if the resulting track satisfies the quality  
617 selection criteria, a high precision fit of the track parameters using the surviving hits  
618 is performed. The high precision fit makes full use of all available information, and  
619 uses an updated position and uncertainty estimate for each cluster obtained from  
620 a Neural Network (NN) [56]. If the track has reached this stage without rejection  
621 by passing various quality regiments, it is re-scored and returned to the list of track  
622 candidates. If the same track is then processed again without requiring modification,  
623 it is added to the final track collection. Track candidates that fall below a certain  
624 quality cut are rejected. This selection does allow for the possibility of a track having  
625 small number of shared hits.

list shared  
hit cut?

## 626 Neural Network Cluster Splitting

627 As part of track cleaning, shared hits are classified by a NN to determine if they are  
628 compatible with the characteristic features of a merged cluster [54, 56]. A merged  
629 cluster is one made up of a combination of energy deposits from more than one  
630 particle, which have become merged due to the closeness of the associated particles  
631 and the limited resolution of the detector. While in general this event is rare, it  
632 is common for clusters to become merged in dense environments, as discussed in  
633 Section 4.1. If the cluster is predicted to be merged it is labelled as being freely  
634 shareable, or *split*. Hits not compatible with the merged hypothesis can still be  
635 shared by a limited number of tracks, but come with a penalty for the track which  
636 may hinder its acceptance into the final track collection.

## 637 Pseudotracking

638 Pseudotracking uses Monte Carlo truth information to group together all the hits  
639 left by each truth particle. Each collection of hits which, as a unit, satisfies basic  
640 quality requirements is directly used in a full resolution track fit. If the track fit is  
641 successful, a “pseudotrack” track is created and stored. If the track fit fails, or the  
642 collection of hits does not pass the basic quality requirements (for example because  
643 of a lack of hits) then the particle is said to be un-reconstructable. In this way,  
644 pseudotracking performance represents the ideal reconstruction performance given the

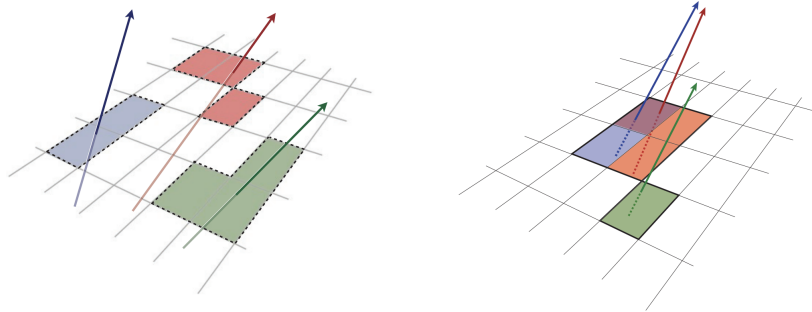


**Figure 3.12:** Particles (left) which have enough separation will leave charge depositions which are resolved into separate clusters. Sufficiently close particles (right) can lead to merged clusters. Their combined energy deposits are reconstructed as a single merged cluster [55].

645 ATLAS detector, with perfect hit-to-track association and and track reconstruction  
 646 efficiency. The approach was introduced in Ref. [57] as a way to obtain a fast  
 647 approximation of tracking reconstruction for simulated data, however the technique  
 648 has become a useful tool for studying tracking performance in general [54].

### 649 3.4.2 Vertices

650 Groups of reconstructed tracks can be examined to determine whether the particles  
 651 originated from a common spatial point of origin. This occurs when proton-proton  
 652 collisions take place (primary vertices), when a particle decays or radiates, and also  
 653 as a result of interaction with the detector material (secondary vertices). Vertex  
 654 reconstruction is made up of two stages. First, vertex finding takes place, which  
 655 is the process of grouping tracks into compatible vertices. Second, vertex fitting  
 656 combines information from compatible tracks to reconstruct the physical properties  
 657 of the vertex, such as mass and position.

#### 658 Primary Vertices

659 Each proton-proton interaction happens at a *primary vertex* (PV). Primary vertices  
 660 are iteratively reconstructed with tracks using the iterative vertex finder (IVF) [58].  
 661 In Run 3, the IVF will be replaced with an adaptive multi-vertex finder (AMVF) [59].

662 The *hard scatter vertex* of an event is chosen as the primary vertex whose associated  
663 tracks have the largest sum of transverse momentum squared,  $\Sigma(p_T^2)$ .

664 **Secondary Vertices**

665 Secondary vertices (SV) occur when a particle radiates or decays at a sufficient  
666 distance from the primary vertex to be resolved from the primary vertex (see  
667 Section 4.1.1). Two widely used secondary vertexing tools are used within ATLAS:  
668 SV1 and JetFitter [60]. Each attempts to reconstruct secondary vertices inside a jet  
669 using the tracks associated to that jet (see Section 3.4.3 for more information about  
670 track association). SV1 by design attempts to reconstruct only a single inclusive  
671 vertex per jet. This inclusive vertex groups all  $b$ -hadron decay products, including  
672 tracks from the  $b$ -hadron decay itself and tracks from  $b \rightarrow c$  decays. The second tool,  
673 JetFitter attempts to resolve each displaced vertex inside the jet, such that secondary  
674 vertices from  $b$ -hadron decays are reconstructed separately to tertiary vertices from  
675  $b \rightarrow c$  decay chains.

676 **3.4.3 Jets**

677 Jets are an aggregate reconstructed object corresponding to a collection of collimated  
678 stable particles which results from a decay chain of an quark or gluon progenitor. Jets  
679 are built by clustering constituent objects (e.g. tracks or calorimeter clusters) using  
680 a jet finding algorithm, for example the anti- $k_t$  algorithm [61], which is implemented  
681 in FASTJET [62].

682 **EMTopo Jets**

683 EMTopo jets are reconstructed from noise-suppressed topological clusters (topoclus-  
684 ters) of calorimeter energy depositions. The clustering uses the energy significance  
685 of each cell, defined as

$$S_{\text{cell}} = \frac{E_{\text{cell}}}{\sigma_{\text{noise, cell}}}, \quad (3.10)$$

686 where  $E_{\text{cell}}$  is the energy measured in a given calorimeter cell, and  $\sigma_{\text{noise}, \text{cell}}$  is the  
 687 expected level of noise on the cell (e.g. from pile-up interactions). Topoclusters are  
 688 formed from a seed cell with a large  $S_{\text{cell}}$ , and expanded by iteratively adding neigh-  
 689 bouring cells with a sufficiently large energy significance. Collections of topoclusters  
 690 are then clustered into a jet using the anti- $k_t$  algorithm with a radius parameter of  
 691 0.4 (small- $R$  jets) or 1.0 (large- $R$  jets). More information is available in Ref. [63].

## 692 Particle Flow Jets

693 Particle-flow (PFlow) jets are reconstructed from particle-flow objects [64] using  
 694 the anti- $k_t$  algorithm with a radius parameter of 0.4. Particle-flow objects integrate  
 695 information from both the ID and the calorimeters, improving the energy resolution  
 696 at high transverse momenta and reducing pile-up contamination. The PFlow jet  
 697 energy scale is calibrated according to Ref. [65].

698 Tracks are associated to jets using a  $\Delta R$  association cone, the width of which  
 699 decreases as a function of jet  $p_T$ , with a maximum cone size of  $\Delta R \approx 0.45$  for jets  
 700 with  $p_T = 20 \text{ GeV}$  and minimum cone size of  $\Delta R \approx 0.25$  for jets with  $p_T > 200 \text{ GeV}$ .  
 701 If a track is within the association cones of more than one jet, it is assigned to the  
 702 jet which has a smaller  $\Delta R(\text{track}, \text{jet})$ .

703 Jet flavour labels are assigned according to the presence of a truth hadron within  
 704  $\Delta R(\text{hadron}, \text{jet}) < 0.3$  of the jet axis. If a  $b$ -hadron is found the jet is labelled a  $b$ -jet.  
 705 In the absence of a  $b$ -hadron, if a  $c$ -hadron is found the jet is called a  $c$ -jet. If no  $b$ -  
 706 or  $c$ -hadrons are found, but a  $\tau$  is found in the jet, it is labelled as a  $\tau$ -jet, else it is  
 707 labelled as a light-jet.

708 PFlow jets are used to train the algorithms discussed in Chapter 5 and Chapter 6.

## 709 Large- $R$ Jets

710 Large- $R$  jets have a radius parameter  $R = 1.0$  and are built by clustering topological  
 711 calorimeter clusters using the anti- $k_t$  algorithm [66]. The large radius parameter  
 712 is especially useful for containing the decay products of a boosted Higgs boson, as  
 713 discussed in Chapter 7. Due to their large size, large- $R$  jets benefit from a grooming  
 714 procedure called trimming which remove soft contaminants inside the jet [67, 68].

715 Trimming aims to remove jet constituents from pile-up and the underlying event,  
716 which helps to improve the jet mass resolution and its robustness to varying levels  
717 of pile-up. The jet mass is computed using a combination of information from the  
718 calorimeters and ID, and a calibration to data is applied [69].

719 **Track-jets**

720 Track-jets are built by clustering tracks using the anti- $k_t$  clustering algorithm and  
721 are used in the analysis described in Chapter 7. The radius parameter is allowed  
722 to vary with transverse momentum such that a broader cone (up to  $R = 0.4$ ) is  
723 used for low- $p_T$  track-jets and a narrower cone (down to  $R = 0.02$ ) for high- $p_T$   
724 track-jets [70, 71]. The narrower cone is better suited to clustering highly collimated  
725 jet constituents at high- $p_T$ . Truth flavour labels for track-jets are derived using the  
726 same  $\Delta R(\text{hadron}, \text{jet}) < 0.3$  matching scheme as used for PFlow jets.

727 **3.4.4 Leptons**

728 Electrons and muons leave characteristic signatures that are picked up in the ECal  
729 and MS respectively. The reconstruction of both types of stable lepton is briefly  
730 outlined below.

731 **Electrons**

732 Electrons candidates are reconstructed by matching PV-compatible<sup>3</sup> inner detector  
733 tracks to topological calorimeter clusters. The track-cluster matching criteria takes  
734 into account the significant energy loss of the electron due to bremsstrahlung. If a  
735 match is found, a refit of the track is performed using the Gaussian Sum Filter (GSF)  
736 [72], which better handles trajectory reconstruction in the presence of bremsstrahlung.  
737 Various identification criteria are then applied to the candidates using a likelihood-  
738 based (LH) method to improve purity. These include requirements on the track  
739 quality and cluster matching, the shape of electromagnetic shower in the ECal,  
740 leakage into the HCal, and the amount of transition radiation detected in the TRT.

---

<sup>3</sup>The ID track associated with the electron is required to satisfy  $d_0/s(d_0) < 5$  and  $z_0 \sin \theta < 0.5$  mm.

- 741 Isolation criteria with respect to other nearby ID tracks and calorimeter clusters may also be applied. A full description can be obtained from Ref. [73].

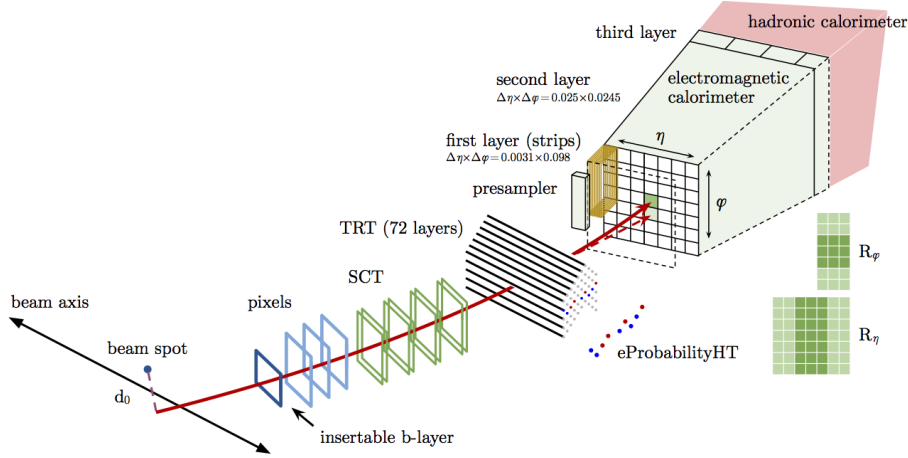


**Figure 3.13:** A sketch of electron reconstruction using the ATLAS detector [73]. Electron reconstruction makes use of the entire ID and the calorimeters. In particular, discriminating information comes from the TRT and ECal.

742

### 743 Muons

744 Muon reconstruction makes use of the dedicated MS (see Section 3.3.3), the tracks 745 from the ID, and the presence of characteristic signatures in the calorimeters. Muon 746 tracks (i.e. a track reconstructed in the MS) are reconstructed by connecting straight-747 line track segments, which are identified via a Hough transform, and combined into 748 an approximately parabolic trajectory. Finally, a global  $\chi^2$  fit is performed, taking 749 into account possible interactions between the muon and the detector material. A 750 reconstructed muon is called *combined* if it completes successful matching to an 751 ID track. Combined muons undergo a further fit with the combined ID and MS 752 hits, with the energy loss due to the traversal of the calorimeters being taken into 753 account.

754 After reconstruction, candidate muons further undergo an identification processes 755 which helps to efficiently identify prompt muons whilst rejecting background sig-756 nals (e.g. non-prompt muons from pion and kaon decays, the punch-through of a 757 hadron from the calorimeter, or the semi-leptonic decay of a heavy flavour hadron). 758 Combined muon identification takes into account discrepancies in the  $p_T$  and charge

759 measurements in the MS and ID, and the  $\chi^2$  of the combined track fit. Selections  
760 on the number of hits in the ID and MS are also applied. At the medium identifi-  
761 cation working point, approximately 96% of muons with  $20 \text{ GeV} < p_T < 100 \text{ GeV}$   
762 are successfully identified. On top of the identification requirements, a number of  
763 isolation requirements can also be applied to further suppress background signals. In  
764 the region  $|\eta| < 2.2$ , the momentum resolution of reconstructed muons is 1.7%.

765 More information on muon reconstruction, identification and isolation can be found  
766 in Ref. [74].

### 767 3.4.5 Missing Transverse Momentum

768 An imbalance in the final state transverse momentum can occur as a result of  
769 incomplete measurement of the final state particles. In particular, neutrinos are  
770 not measured by the detector and contribute to the missing transverse momentum  
771  $\mathbf{E}_T^{\text{miss}}$ . Incomplete detector acceptance and inaccuracies in the reconstruction of the  
772 final state can also contribute to the missing transverse momentum of an event. In  
773 order to calculate the missing transverse momentum, the negative vector sum of  
774 the momentum of all photons, leptons and small- $R$  jets with  $p_T > 20 \text{ GeV}$  is taken.  
775 The momenta of tracks associated to the primary vertex are also taken into account.  
776 The magnitude of  $\mathbf{E}_T^{\text{miss}}$  is written  $E_T^{\text{miss}}$ . More information about missing transverse  
777 momentum reconstruction is provided in [75].

778

# Chapter 4

779

## Tracking and $b$ -tagging

780 Many ATLAS analyses rely on  $b$ -tagging, which is the identification of jets instantiated  
781 by  $b$ -hadrons ( $b$ -jets), as opposed to those instantiated by quarks ( $c$ - and light-  
782 flavour hadrons). These  $b$ -jet identification algorithms (also called *taggers*) work  
783 by identifying the unique signatures of  $b$ -jets, which are outlined in Section 4.1.  
784 The various  $b$ -tagging algorithms ultimately take as their input information about  
785 the reconstructed jet and its associated tracks. Successful  $b$ -tagging relies therefore  
786 on the efficient and accurate reconstruction of tracks, and especially those tracks  
787 corresponding to the products of  $b$ -hadron decays.

788 Historically a two tiered approach to  $b$ -tagging has been taken, in which so called  
789 *low-level* taggers take as inputs information about the jet and associated tracks, and  
790 attempt to reconstruct or identify some aspect of a  $b$ -jet, such as displaced tracks  
791 or secondary vertices. The outputs of several low-level taggers are then fed into a  
792 *high-level* tagger, which uses a multivariate approach to discriminate between jet  
793 flavours.

794 As the different  $b$ -tagging algorithms ultimately rely on tracks, accurate and efficient  
795 track reconstruction is essential. This chapter summarises the challenges facing  
796 tracking and  $b$ -tagging at high transverse momentum with an investigation into track  
797 reconstruction performance in Section 4.1. Some preliminary investigations into  
798 improving tracking in this regime are investigated in Section 4.2.

## <sup>799</sup> 4.1 *b*-hadron Reconstruction

<sup>800</sup> This section outlines the typical detector signature of a *b*-hadron in Section 4.1.1  
<sup>801</sup> and discusses some associated reconstruction difficulties in Section 4.1.2.

### <sup>802</sup> 4.1.1 Decay Topology

<sup>803</sup> *b*-hadrons are quasi-stable bound states of a bottom quark and one or more lighter  
<sup>804</sup> quarks. Collectively, these are the *B*-mesons (e.g.  $B^+ = u\bar{b}$ ,  $B^0 = d\bar{b}$ ) and baryons  
<sup>805</sup> (e.g.  $\Lambda_b^0 = udb$ ). After a *b*-quark is produced as the result of a proton-proton collision,  
<sup>806</sup> they quickly hadronise. The hadronisation process is hard – around 70-80% of  
<sup>807</sup> the *b*-quark’s momentum is passed to the *b*-hadron, with the rest being radiated  
<sup>808</sup> as prompt hadronisation or fragmentation particles. See Ref. [76] for a more in  
<sup>809</sup> depth discussion on hadronisation and the closely related process of fragmentation.  
<sup>810</sup> Henceforth the combined hadronisation and fragmentation products will be referred  
<sup>811</sup> to collectively as fragmentation.

<sup>812</sup> *b*-hadrons are interesting objects of study due to their relatively long proper lifetimes  
<sup>813</sup>  $\tau \approx 1.5$  ps [77]. This lifetime corresponds to a proper decay length  $c\tau \approx 450$   $\mu\text{m}$ . In  
<sup>814</sup> the rest frame of the detector, the typical *b*-hadron travels a distance

$$d = \gamma\beta c\tau \approx \gamma c\tau \quad (4.1)$$

<sup>815</sup> before decaying, where in the high energy limit  $\gamma = E_b/m_b$  and  $\beta = v/c = 1$ .

<sup>816</sup> For a 50 GeV *b*-hadron, this gives  $d \approx 4.5$  mm, which is displaced enough to be  
<sup>817</sup> resolved from the primary vertex. Meanwhile for a 1 TeV *b*-hadron,  $d \approx 90$  mm –  
<sup>818</sup> well beyond the radius of the first pixel layer (the IBL) which is situated at a radius  
<sup>819</sup> of approximately 33 mm from the center of the detector (the distance varies due  
<sup>820</sup> to the interleaved structure) Fig. 4.1 shows how the mean decay radius varies as a  
<sup>821</sup> function of *b*-hadron  $p_T$ . This significant displacement is characteristic of *b*-jets and  
<sup>822</sup> makes it possible to reconstruct secondary vertices at the *b*-hadron decay point.

<sup>823</sup> *b*-hadrons decay weakly to on average four or five collimated stable particles [78].  
<sup>824</sup> These particles, along with any other fragmentation particles, are reconstructed in  
<sup>825</sup> the detector as a jet. A *b*-jet has several characteristic features which differentiate

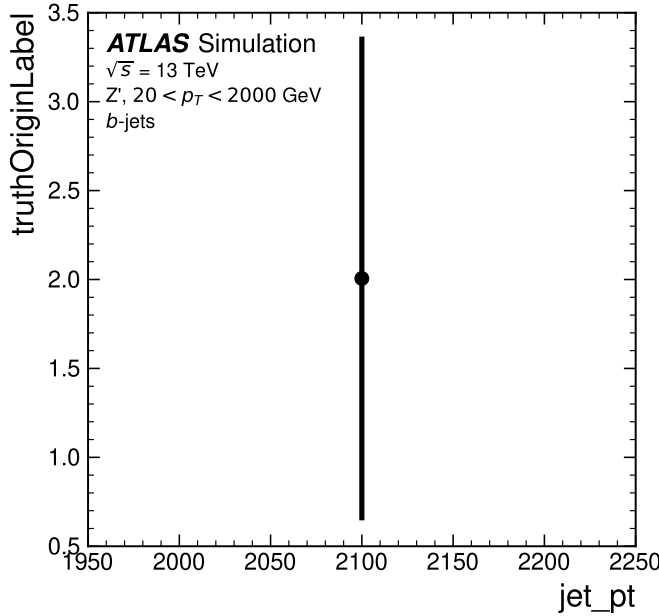


**Figure 4.1:** The truth *b*-hadron decay radius  $L_{xy}$  as a function of truth transverse momentum  $p_T$  for reconstructed *b*-jets in  $Z'$  events. Error bars show the standard deviation. The pixel layers are shown in dashed horizontal lines.

it from light-jets. These features stem from the significant displacement of the *b*-hadron that can occur due to its lifetime. The primary feature is the presence of a high mass secondary vertex that is significantly displaced from the primary vertex. Reconstruction of these vertices from tracks with common points of spatial origin is a common approach used in the identification of *b*-jets.

Additional signatures of *b*-hadrons are as follows. Associated tracks and SVs can have a large transverse impact parameter  $d_0$  as a result of the *b*-hadron displacement (as shown in Fig. 4.2). Since it is common for the *b*-hadron to decay to a *c*-hadron with non-negligible lifetime, tertiary vertices can be found within *b*-jets resulting from  $b \rightarrow c$  decay chains. The *b*-hadron also decays semileptonically in approximately 23% of cases [14]. The presence of a reconstructed electron or muon inside a jet can also be a key indicator that the jet was instantiated by a *b*-hadron.

These signatures are primarily identified using tracks associated to jets, or using reconstructed electrons or muons, which also rely on tracks as discussed in Section 3.4.4. As such, efficient and accurate track reconstruction is essential for high performance flavour tagging.

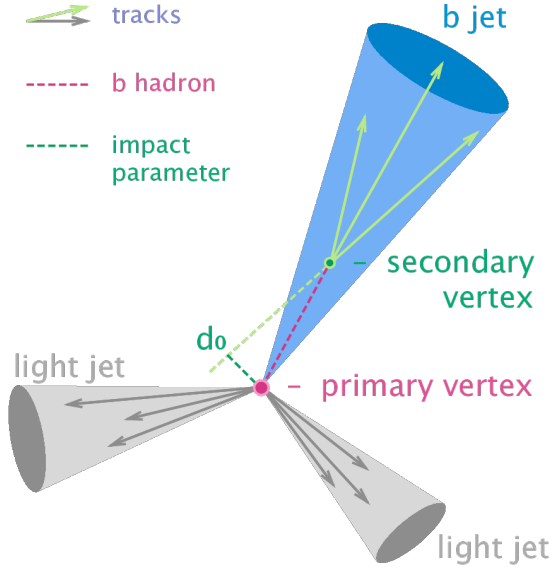


**Figure 4.2:** Diagram of a typical  $b$ -jet (blue) which has been produced in an event alongside two light jets (grey) [79]. The  $b$ -hadron has travelled a significant distance (pink dashed line) from the primary interaction point (pink dot) before its decay. The large transverse impact parameter  $d_0$  is a characteristic property of the trajectories of  $b$ -hadron decay products.

#### 842 4.1.2 Challenges Facing $b$ -hadron Reconstruction

843 As discussed, a necessary requirement for successful  $b$ -tagging is the efficient and  
 844 accurate reconstruction of the charged particle trajectories in the jet. For high  $p_T$  jets  
 845 ( $p_T > 200$  GeV) this task becomes difficult due to a combination of effects. As the  
 846  $b$ -hadron energy increases, the multiplicity of the fragmentation products inside the  
 847 jet increases, while the multiplicity of the products of the weak decay is unaffected.  
 848 The “signal” tracks (those from the weak decay of the  $b$ -hadron) therefore become  
 849 outnumbered. Both fragmentation and  $b$ -hadron weak decay products also become  
 850 increasingly collimated as their inherited transverse momentum increases. At high  
 851 energies, the increased decay length of  $b$ -hadrons (and  $c$ -hadrons) means that decay  
 852 products have less of an opportunity to diverge before reaching the first tracking  
 853 layers of the detector (shown in Fig. 4.3). If the weak decay of the  $b$ -hadron takes  
 854 place close enough to a detector layer, or if the particles are otherwise sufficiently  
 855 collimated, charge deposits left by nearby particles may not be resolved individually,  
 856 instead being reconstructed as merged clusters.

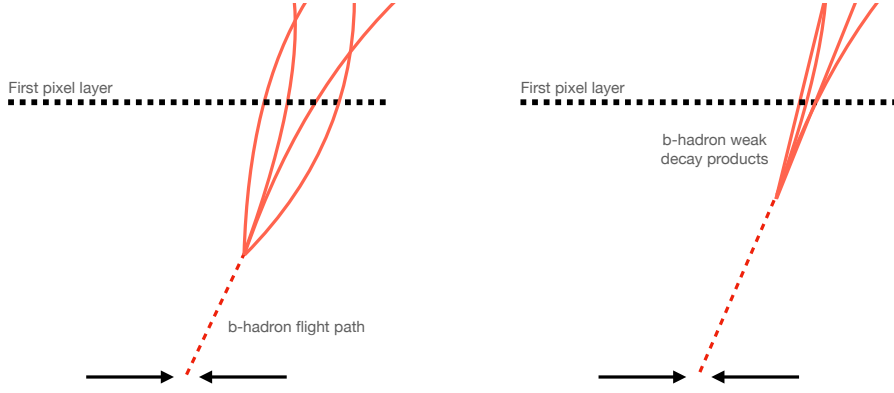


**Figure 4.3:** At lower  $p_T$  (left) the decay length of the  $b$ -hadron is reduced, and the resulting decay tracks are less collimated. At higher  $p_T$  (right) the  $b$ -hadron decay length increases and the resulting decay tracks are more collimated and have less distance over which to diverge before reaching detector elements. As a result, the ID may be unable to resolve charged depositions from different particles, resulting merged clusters.

As discussed in Section 3.4.1, merged clusters are generally rare, and so shared hits generally predict bad tracks and are correspondingly penalised during track reconstruction. However, in the core of high  $p_T$   $b$ -jets the density of particles is high enough that the probability of cluster merging increases dramatically. Successful reconstruction of such tracks requires the presence of shared hits to be effectively dealt with but in the standard reconstruction the presence of these can end up impairing the successful reconstruction of the track. Furthermore, decays may also take place inside the tracking detectors themselves, which at best leads to missing measurements on the most sensitive detector layers, and at worst can lead to wrong inner layer hits being added to displaced tracks, since the reconstruction process penalises tracks without inner layer hits.

The above effects create two related, but distinct problems for  $b$ -tagging. The first part is a drop in track reconstruction efficiency. The presence of shared and missing hits reduces a track's score in the ambiguity solver meaning that higher ranking, but potentially worse, track candidates are processed first and take ownership of the hits. This can make it difficult for otherwise reasonable  $b$ -hadron decay tracks to meet the ambiguity solver's stringent track quality requirements, leading to their rejection at this stage and an overall decrease in the  $b$ -hadron decay track reconstruction efficiency as shown in Fig. 4.4.

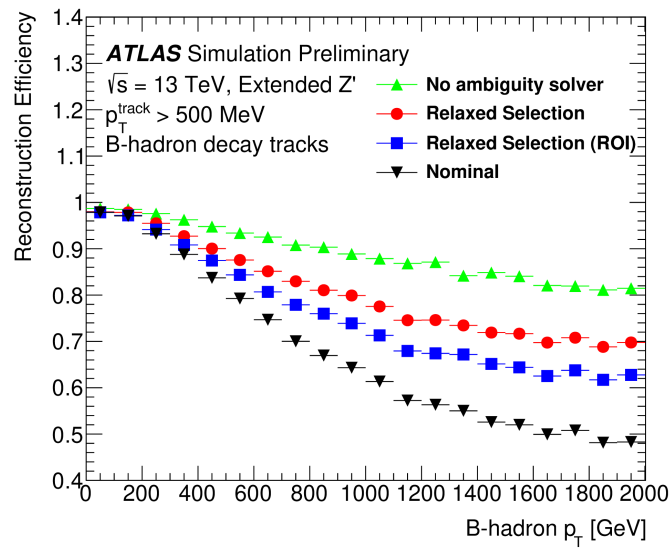


**Figure 4.4:** *b*-hadron decay track reconstruction efficiency as a function of truth *b*-hadron  $p_T$  [80]. Nominal track reconstruction is shown in black, while the track reconstruction efficiency for track candidates (i.e. the pre-ambiguity solver efficiency) is shown in green. For high- $p_T$  *b*-hadrons, the ambiguity solver is overly aggressive in its removal of *b*-hadron decay tracks. Suggestions for the improvement of the track reconstruction efficiency in this regime by the loosening of cuts in the ambiguity solver are shown in blue and red.

876 The second part of the problem is that, due to the high multiplicity of clusters available  
 877 for assignment in the vicinity of the typical high energy  $b$ -hadron decay track, and  
 878 also given the strong positive bias of the ambiguity solver towards those tracks  
 879 with pixel measurements in each layer (especially the innermost IBL measurement),  
 880 many  $b$ -hadron decay tracks are assigned incorrect inner layer hits. This is only a  
 881 problem for those decay products which were produced within the pixel detector  
 882 as a result of a significantly displaced  $b$ -hadron decay, and so do not have a correct  
 883 hit available for assignment. Fig. 4.5 shows the number of hits as a function of the  
 884 reconstructed track  $p_T$  for fragmentation tracks and tracks from the weak decay of  
 885 the  $b$ -hadron. The baseline tracks represent the standard reconstruction setup, while  
 886 the pseudotracks represent the ideal tracking setup as outlined in Section 3.4.1. The  
 887 incorrect hits may skew the parameters of the track, which can in turn mislead the  
 888 downstream  $b$ -tagging algorithms. In particular,  $b$ -tagging algorithms rely heavily on  
 889 the transverse impact parameter significance  $s(d_0)$  of the track. The quality of this  
 890 measurement is expected to be adversely affected by wrong inner-layer hits on the  
 891 track. Furthermore, multiple tracks sharing an incorrect hit can lead to the creation  
 892 of spurious secondary vertices, which can cause further problems for the downstream  
 893  $b$ -tagging algorithms.

894 The combination of the effects described makes reconstructing tracks in the core  
 895 of high  $p_T$   $b$ -jets particularly challenging. The reduced reconstruction efficiency of  
 896  $b$ -hadron decay tracks and incorrectly assigned hits is thought to be the primary  
 897 cause of the observed drop in  $b$ -tagging efficiency at high energies, however further  
 898 study is required to determine which effect may dominate.

## 899 4.2 Investigations into High $p_T$ $b$ -hadron Tracking

900 In Section 4.2.1 pseudotracks, a key tool for studying the ideal tracking performance  
 901 of the ATLAS detector, are used to study the shared hit requirements on tracks in  
 902 the dense cores of high- $p_T$   $b$ -jets. Section 4.2.2 details a study which investigated  
 903 modifying the global track fitter to improve reconstruction performance in this  
 904 regime.

include plot  
from sebs  
study show-  
ing they  
are approx  
similar im-  
pacts? or  
just mention  
result? Can  
do put need  
to remove  
ATLAS la-  
bels. Alter-  
natively you  
can put an  
internal refer-  
ence to his  
work and  
state what  
the outcome  
is

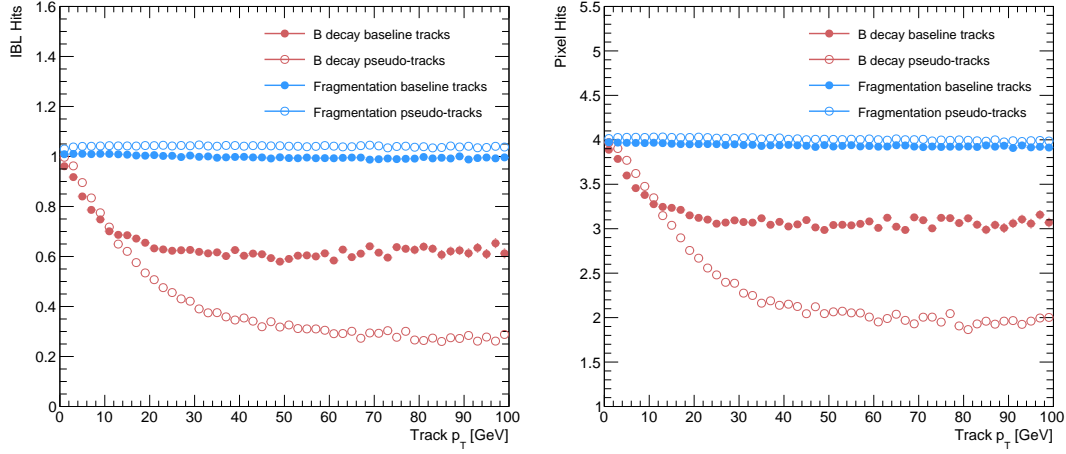


**Figure 4.5:** Hit multiplicities on the IBL (left) and the pixel layers (right) as a function of the  $p_T$  of the reconstructed track. Tracks from the weak decay of the  $b$ -hadron are shown in red, while fragmentation tracks (which are prompt) are in blue. Baseline tracks are those produced in the standard reconstruction described in Section 3.4.1, while pseudotrack represent the ideal performance of the ATLAS detector and are described in Section 3.4.1. Hit multiplicities on the pseudotracks decrease at high  $p_T$  due to the flight of the  $b$ -hadron before its decay. The baseline tracks have more hits than the pseudotracks, indicating that they are being incorrectly assigned additional hits on the inner layers of the detector.

### 905 4.2.1 Shared Hits

906 The ambiguity solver is not run for pseudotracks. However, if the standard track  
 907 collection is produced alongside the pseudotracks, then cluster splitting neural  
 908 networks will be run for the standard tracks, and the resulting classification of  
 909 clusters will be propagated to hits on pseudotracks. This quirk allows one to study  
 910 the inefficiencies of the cluster splitting process, and relatedly to determine whether  
 911 shared hit cuts in the ambiguity solver are too loose or too tight. The fraction of hits  
 912 that are shared for the IBL and the B-layer is shown in Fig. 4.6. The shared hits on  
 913 pseudotracks represent correctly assigned hits from merged clusters that were not  
 914 able to be classified as split by the cluster splitting neural networks. As such, these  
 915 represent the number of shared hits the ambiguity solver should aim to allow given  
 916 the current performance of the cluster splitting algorithm. For shared hits on the IBL  
 917 for particles produced before the IBL, the baseline selection appears to be successful  
 918 in disallowing excessive numbers of shared hits. However, the ambiguity solver fails to  
 919 limit shared hits for those particles produced after the IBL, reflecting the previously  
 920 discussed problem of displaced tracks picking up incorrect hits. Meanwhile, it is clear

921 that for the B-layer, the ambiguity solver is being overly aggressive in its rejection of  
 922 shared hits.

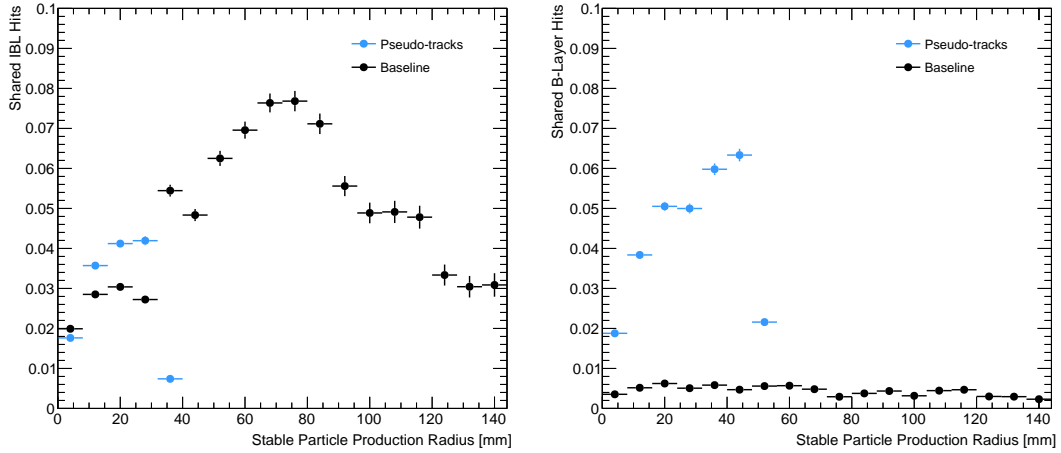


**Figure 4.6:** The fraction of hits which are shared on  $b$ -hadron decay tracks on the IBL (left), and the B-layer (right), as a function of the production radius of the  $b$ -hadron decay product. Pseudotracks represent the ideal performance given the ATLAS detector, see Section 3.4.1.

### 923 4.2.2 Global $\chi^2$ Fitter Outlier Removal

924 This section documents ongoing progress into improvement of hit-to-track assignment  
 925 by using the Global  $\chi^2$  Fitter (GX2F) to identify and prevent incorrect hits from  
 926 being assigned to tracks during the track fit. This is in contrast to a previously  
 927 investigated approach [81] which attempted to identify and remove wrong hits after  
 928 the reconstruction of the track. As part of the track fit, an outlier removal procedure  
 929 is run, in which suspicious hits are identified and removed.

930 The GX2F code, as a relatively low-level component of track reconstruction, has  
 931 not undergone significant modification for several years, and was originally only  
 932 optimised in the context of prompt, isolated tracks. During this time, a new tracking  
 933 sub-detector, the IBL, was installed. The motivation for looking at the GX2F is that  
 934 these changes may require re-optimisation of the GX2F code, and in particular the  
 935 outlier removal procedures. Further motivation for this approach comes from the low  
 936 rate of labelled outliers in baseline tracking. For example, while approximately 15%  
 937 of  $b$ -hadron decay tracks have a wrong IBL hit (a value which only increases with

938 the  $p_T$  of the *b*-hadron), less than 1% of this tracks have had their IBL hit labelled  
 939 and removed as an outlier.

940 **Implementation**

941 The outlier removal procedure for the pixel detector is described in this section.  
 942 The hits on the track are looped over in order of increasing radial distance to the  
 943 beam pipe. For each hit, errors  $\sigma(m_i)$  on the measurement of the transverse and  
 944 longitudinal coordinates are calculated. These errors are dependent on the sub-  
 945 detector which recorded the measurement (some sub-detectors are more precise than  
 946 others). Additionally, a residual displacement  $r_i = m_i - x_i$  between the predicted  
 947 position of the track  $x_i$  (inclusive of the current measurement), and the position of  
 948 the hit itself,  $m_i$ , is calculated. The pull  $p_i$  on the track state due to the current  
 949 measurement is calculated according to

$$p_i = \frac{m_i - x_i}{\sqrt{\sigma(m_i)^2 - \sigma(x_i)^2}} \quad (4.2)$$

950 This pull is computed for the transverse and longitudinal coordinates of the mea-  
 951 surement, and the maximum of the two is selected and checked to see if it exceeds  
 952 a certain selection threshold. If it does, the hit will be removed if the track also  
 953 exceeds a threshold on the total  $\chi^2/n$ . The results of varying the outlier selection  
 954 and  $\chi^2/n$  thresholds are described below.

955 **Cut Optimisation**

956 A systematic variation of the outlier selection and  $\chi^2/n$  thresholds has been carried  
 957 out. Both thresholds were reduced in fixed step sizes of 0.25 for the outlier selection  
 958 threshold and 1 for the  $\chi^2/n$  threshold. The results for the best performing selections  
 959 are discussed below. The value of the outlier selection threshold was reduced from 4  
 960 down to 1.75, a change which affects all silicon layers (the TRT has separate outlier  
 961 removal logic). Furthermore, a specific cut for the IBL was introduced, and is set  
 962 to 1.25. The second threshold on the track  $\chi^2/n$  was also reduced from 7 to 4.  
 963 Finally, instead of taking the maximum of the pulls in the longitudinal and transverse

964 directions, a quadrature sum is taken of these two values and used. This variation is  
 965 labelled “Mod GX2F” in plots.

966 The results are shown in Fig. 4.7 and demonstrate a reduction in wrong hit assignment  
 967 whist also improving slightly the rate at which good hits are assigned to tracks. For a  
 968 1 TeV track, the rate to assignment good hits to the track increases by approximately  
 969 10%, while the rate to assign incorrect hits decreases by approximately 16%. The  
 970 improvements are also observed when looking inclusively in all tracks, which avoids  
 971 the need for a specific *b*-jet region-of-interest selection.

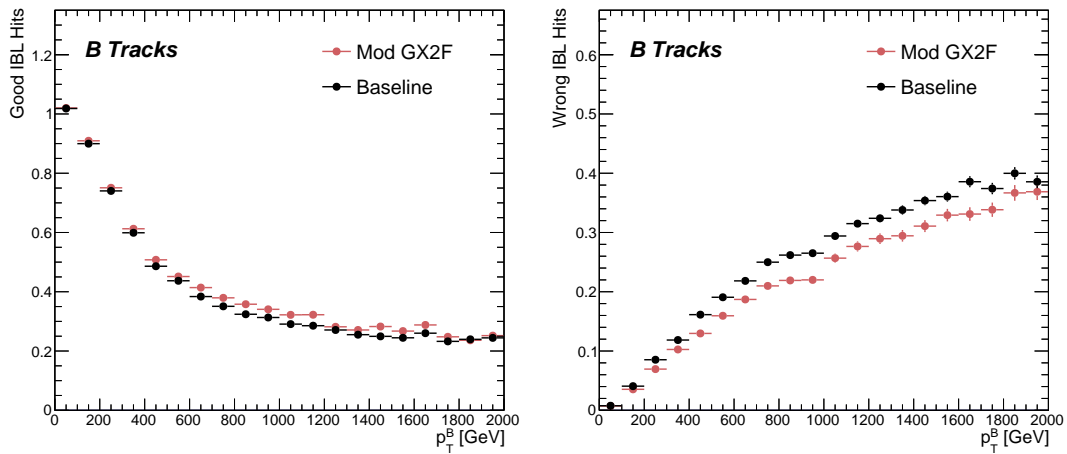


**Figure 4.7:** The rate to assign good (left) and wrong (right) IBL hits as a function of *b*-hadron  $p_T$  for tracks using baseline tracking (black) and the modified version of the outlier removal procedure (red). For each track, the corresponding  $p_T$  bin is filled with the number of good or wrong hits and this value is averaged to show the overall rate.

972 An improvement, though modest, of all track parameter resolutions and pulls is  
 973 observed. The improvement for the transverse impact parameter pull is shown in  
 974 Fig. 4.8. The results demonstrate an improvement in hit assignment, unchanged  
 975 reconstruction efficiency, and modest improvement in track parameter resolutions  
 976 and pulls. In addition, the truth match probability of track is unchanged, suggesting  
 977 that there is no increase in fake track rates. The changes are expected to have a  
 978 negligible impact on computational resources.

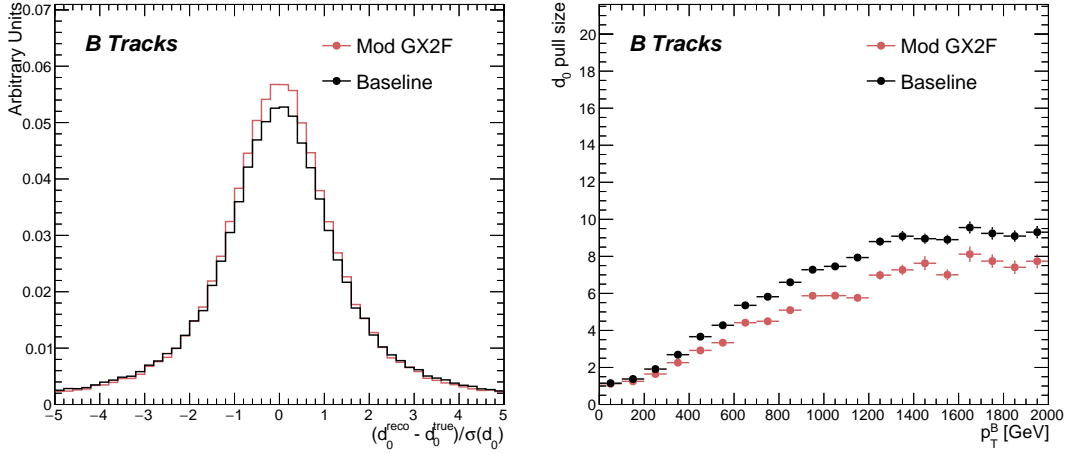


**Figure 4.8:** (left)  $b$ -hadron decay track  $d_0$  pulls ( $d_0/s(d_0)$ ) for baseline and modified GX2F tracks. (right) The absolute value of the  $d_0$  pull as a function of  $b$ -hadron transverse momentum.

### 4.3 Conclusion

In this section, the difficulties facing efficient and accurate track reconstruction, and hence performant  $b$ -tagging, have been outlined. The ambiguity solver, which attempts to clean or reject tracks which have an excessive number of shared hits, is shown to be overly aggressive in the removal of  $b$ -hadron decay product track candidates. The ambiguity solving process relies on a complicated pre-defined selection which has not been optimised for high transverse momentum  $b$ -hadron track reconstruction. These conclusions have motivated further ongoing studies into the improvement of the track reconstruction in dense environments and the high- $p_T$  regime, such as those in Ref. [80].

An optimisation of the outlier removal process in the global  $\chi^2$  fitter was carried out. Though the results show some improvement over the baseline tracking scenario, these results need to be expanded upon by looking at the impact on the downstream  $b$ -tagging algorithms before putting them into production. As there are some known data-MC discrepancies, fine tuned optimisation such as the work presented here presents an opportunity to over-optimize the tracking algorithms on MC. The studies were carried out in Release 21 of the ATLAS software, and need to be reproduced using the newer Release 22 to confirm the results against other changes in the baseline tracking configuration. Thanks to the all-in-one flavour tagging approach described

998 in Chapter 6, it will also be easier in future to verify that the improvements to the  
999 track reconstruction have a positive impact on the flavour tagging performance.

1000 **Chapter 5**

1001 **Track Classification MVA**

1002 The chapter details work on implementing a multivariate algorithm (MVA) to predict  
1003 the truth origin of reconstructed tracks. An introduction to formalisms of machine  
1004 learning is given in Section 5.1. In Section 5.2, the truth origin label is defined,  
1005 and in Section 5.3 these labels are used to train a machine learning model that can  
1006 effectively discriminate between good and fake tracks. Several studies motivated this  
1007 work by demonstrating that at high  $p_T$ ,  $b$ -tagging performance was degraded by the  
1008 presence of large numbers of poorly reconstructed or fake tracks. If an algorithm  
1009 could be trained to detect fake tracks, these could be removed before their input to  
1010 the  $b$ -tagging algorithms with the aim of improving performance.

1011 **5.1 Machine Learning Background**

1012 Over the past few decades, machine learning (ML) techniques have become increasing-  
1013 ly popular in high energy physics experiments due the increased volumes of  
1014 high-dimensional data and improvements in the techniques used (in particular deep  
1015 learning). Machine learning is the process by which a computer program uses data  
1016 to learn suitable parameters for a predictive model. This is opposed to explicitly  
1017 providing instructions on how to perform a task. A subfield known as *supervised*  
1018 *learning* is used in this work, and consists of exposing a model to a large number of  
1019 labelled examples in order to extract relationships between the input data and their  
1020 labels. These relationships are often complex, and explicitly programmed rules can  
1021 fail to fully capture the relationships between inputs and outputs.

In the simplest case, a set of  $m$  labelled training examples  $S = \{(x_1, y_1), \dots, (x_m, y_m)\}$  is collected. Each element  $(x_i, y_i)$  consists of a input vector  $x_i \in \mathbb{R}^{\text{input}}$ , and the corresponding label  $y_i$ . In classification problems, these labels are integer *class labels*  $y_i \in \{0, \dots, N - 1\}$ , where  $N$  is the number of classes, which specify which of a pre-determined set of categorical classes the training example belongs to. The rest of the discussion in this chapter is limited to binary classification problems ( $N = 2$ ). The two classes are often referred to as signal ( $y_i = 1$ ) and background ( $y_i = 0$ ), which need to be separated. Collecting sufficient and suitable data is one of the primary challenges of machine learning, as such data is not always readily available. Fortunately, sophisticated tools to simulate particle collisions have already been developed by the scientific community [82, 83]. These tools play a key role in generating a suitably large amount of labelled data which is used to train algorithms. More detail on the input datasets is given in Section 5.3.1.

After obtaining suitable training data, the next step is to define a model. Given an input domain  $\mathbb{R}^{\text{input}}$  and an output domain  $(0, 1)$ , the model  $f_\theta : \mathbb{R}^{\text{input}} \rightarrow (0, 1)$  is a parameterised functional mapping from input space to output space. Given an input example  $x_i$  and a set of parameters  $\theta$ , the model outputs a prediction  $\hat{y}_i \in (0, 1)$  for the true label  $y_i$ , as in

$$f_\theta(x_i) = \hat{y}_i. \quad (5.1)$$

The output  $\hat{y}_i$  is in the interval  $(0, 1)$  so as to be interpreted as the probability that the input example  $x_i$  belongs to the signal class. The parameters  $\theta$  of the model are randomly initialised, and the model is designed to be expressive enough to correctly map the inputs  $x_i$  to the outputs  $y_i$  given a reasonable optimisation of the parameters. To perform this optimisation, the model is then trained, which amounts to showing the model a series of labelled training examples and modifying the parameters of the model based on its ability to correctly predict the labels.

### 5.1.1 Neural Networks

Neural networks (NNs) are a common choice for the machine learning model  $f$  since they have the ability to approximate any function [84] and are easy to train via backpropagation [85].

1051 **Artificial Neurons**

1052 The basic functional component of a NN is the *artificial neuron* or node, which is  
1053 loosely inspired by a mathematical model of a biological neuron [86, 87]. A diagram  
1054 of an artificial neuron is shown in Fig. 5.1 Each neuron is defined by its parameters  
1055 or *weights*  $\theta$  and a choice of activation function. Each neuron takes a fixed number  
1056 of inputs and computes the dot product of the input and weight vectors  $x^T \theta$  and  
1057 additionally adds a constant bias term  $\theta_0$ . This term plays the role of a trainable  
1058 constant value that is independent of the inputs.

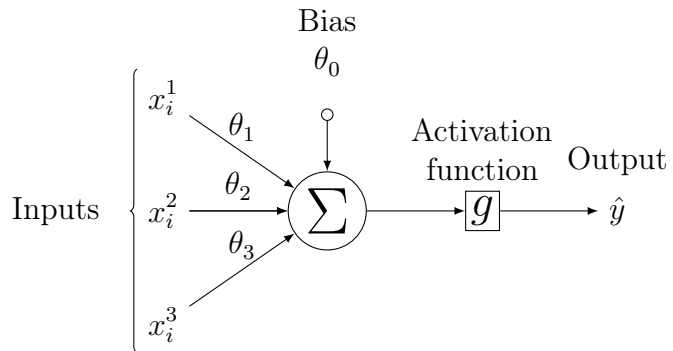


**Figure 5.1:** A diagram displaying the logical flow of a single neuron with three inputs  $x_i^j$ . Each input is multiplied by a weight  $\theta_j$ , and the resulting values are summed. A bias term  $\theta_0$  is added, and the result  $z$  is passed to an activation function. Each neuron can be thought of as a logistic regression model.

1059 The output of the dot product and bias term  $z$  is fed into an activation function  
1060  $g$ . The activation function has several uses, most notably acting as a source of  
1061 non-linearity and bounding the output of the neuron. Some common activation  
1062 functions (sigmod, tanh, ReLU and SiLU) are shown in Fig. 5.2. The choice of  
1063 activation function can have implications for the performance and convergence of  
1064 the network, since the gradient of  $g$  is used to compute the weight updates during  
1065 training. This is also why input data is typically normalised to have zero mean and  
1066 unity variance [88].

1067 **Networks**

1068 Several neurons are linked together in layers to form a neural network. The inputs  
1069 are propagated layer-by-layer through the network until reaching the final output

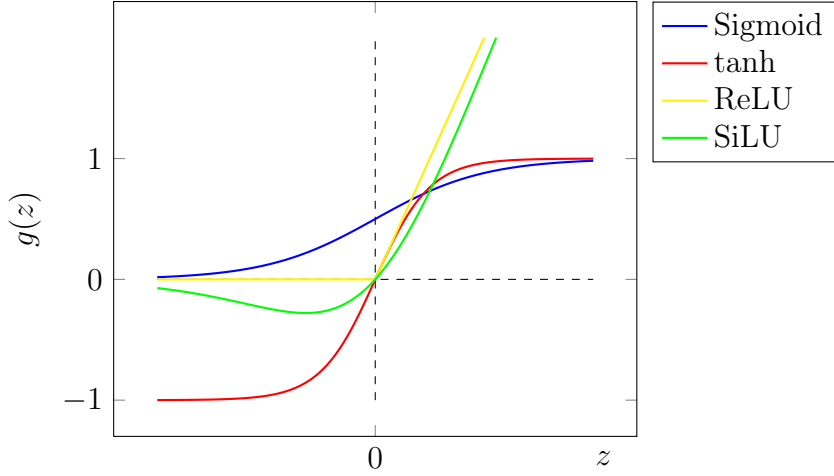


**Figure 5.2:** The output of several common choices for the activation function  $g(z)$  of an artificial neuron. The input  $z$  is the output of the dot product between the activation and the weights, plus a bias term.

layer. The number of layers and neurons per layer are important hyperparameters (those parameters which are not optimised as part of the training process) which influence the performance of the model. In the case of binary classification, the final output layer consists of a single neuron with a sigmoid activation

$$g(z) = \frac{1}{1 + e^{-z}}, \quad (5.2)$$

where  $z$  is the output from the dot product of the inputs and the weights, plus the bias term. This value is bounded between zero and one allowing the final output to be interpreted as the probability that the input sample belongs to the signal class. NNs have the crucial property of being differentiable functions, which facilitates training process described in the next section.

### 5.1.2 Training with Gradient Descent

A training algorithm is used to optimise the weights of a NN after exposure to the training data. The training algorithm works by minimising a loss function  $L$ , which quantifies the error in the model's predictions. NNs are commonly trained using backpropagation in combination with a variant of the stochastic gradient descent algorithm to iteratively update the model parameters. In binary classification

1085 problems, the binary cross entropy given in Eq. (5.3) loss if often used.

$$L(x_i, \theta) = y_i \ln[f_\theta(x_i)] + (1 - y_i) \ln[1 - f_\theta(x_i)] \quad (5.3)$$

1086 Since the model  $f$  is differentiable, the error for each parameter  $\theta_i$  can be computed by  
 1087 taking the partial derivative of  $L$  with respect to the parameter. Updated parameters  
 1088  $\theta'_i$  are calculated by updating the original parameter in the direction which reduces  
 1089 the loss.

$$\theta'_i = \theta_i - \alpha \frac{\partial L}{\partial \theta_i} \quad (5.4)$$

1090 The hyperparameter  $\alpha$  is known as the *learning rate* and dictates the size of the  
 1091 step taken in the direction of the slope. The errors for each parameter are efficiently  
 1092 calculated using the backpropagation algorithm [85]. The process of updating weights  
 1093 is repeated until the weights converge, which means the network is trained. In practice,  
 1094 small batches of the input data are shown to the network at a time. For each batch  
 1095 the average loss is calculated and the network's weights are updated. There are many  
 1096 extensions and variations of the gradient descent algorithm. This work uses the Adam  
 1097 optimiser which adds momentum to the weight updates (dampening oscillations)  
 1098 and an adaptive per-parameter learning rate [89].

## 1099 5.2 Track Truth Origin Labelling

1100 Crucial to supervised learning techniques are the ground truth class labels which the  
 1101 machine learning model is trained to predict. A set of track truth labels which a  
 1102 high degree of granularity have been implemented in the ATLAS software stack, and  
 1103 are listed in Table 5.1. The labelling scheme has been designed to be useful beyond  
 1104 the classification of good and fake tracks. The origins are determined by analysing  
 1105 the simulated record to determine the physical process that led to the creation of  
 1106 the truth (i.e. simulated) particle which is associated with each reconstructed track.  
 1107 Tracks are associated with truth particles by selecting the particle with the highest  
 1108 *truth-matching probability* (TMP), defined in Eq. (5.5). This is a weighted sum of  
 1109 the number of hits on a reconstructed track which are from the same truth particle,  
 1110 versus the total number of hits on the track. The weights are subdetector-dependent  
 1111 and are designed to account for the varying importance of the different subdetectors

1112 (based upon their precision) in the reconstruction of a track.

$$\text{TMP} = \frac{10N_{\text{Pix}}^{\text{good}} + 5N_{\text{SCT}}^{\text{good}} + N_{\text{TRT}}^{\text{good}}}{10N_{\text{Pix}}^{\text{all}} + 5N_{\text{SCT}}^{\text{all}} + N_{\text{TRT}}^{\text{all}}} \quad (5.5)$$

1113 For the fake track classification tool, the track truth origins in Table 5.1 are used  
1114 to construct a binary label by assigning all fake tracks to the background category,  
1115 and all other tracks as signal. The fake track classifier is then trained to distinguish  
1116 between these two categories of tracks. Fake tracks are defined using the TMP,  
1117 with a  $\text{TMP} < 0.75$ <sup>1</sup> giving a track the label of fake. Fake tracks are made up of  
1118 combinatorial fakes, which are tracks which do not correspond to the trajectory of  
1119 any truth particle, and poorly reconstructed tracks, which may somewhat resemble  
1120 the trajectory of a truth particle due to the presence of some wrong hits on the track,  
1121 will not accurately reproduce a true trajectory.

Truth Origin	Description
Pileup	From a $pp$ collision other than the primary interaction
Fake	Created from the hits of multiple particles
Primary	Does not originate from any secondary decay
fromB	From the decay of a $b$ -hadron
fromBC	From a $c$ -hadron decay which itself is from the decay of a $b$ -hadron
fromC	From the decay of a $c$ -hadron which is not from the decay of a $b$ -hadron
OtherSecondary	From other secondary interactions and decays

**Table 5.1:** Truth origins which are used to categorise the physics process that led to the production of a track. Tracks are matched to charged particles using the truth-matching probability [55]. A truth-matching probability of less than 0.5 indicates that reconstructed track parameters are likely to be mismeasured and may not correspond to the trajectory of a single charged particle. The “OtherSecondary” origin includes tracks from photon conversions,  $K_S^0$  and  $\Lambda^0$  decays, and hadronic interactions.

### 1122 5.3 Fake Track Identification Tool

1123 The rate of fake tracks increases at high transverse momentum as shown in Fig. 5.3 due  
1124 to the difficulties in track reconstruction outlined in Section 4.1.2. The performance

<sup>1</sup>An alternative definition of a fake track as one with  $\text{TMP} < 0.5$  is also in use within ATLAS. Both values were investigated, but 0.75 was used for this study.

of  $b$ -tagging algorithms is reduced as a direct result of the presence of these tracks as shown for SV1 (see Section 3.4.2) in Fig. 5.4, where the light-efficiency decreases by up to 35% at a  $b$ -efficiency of 35%.

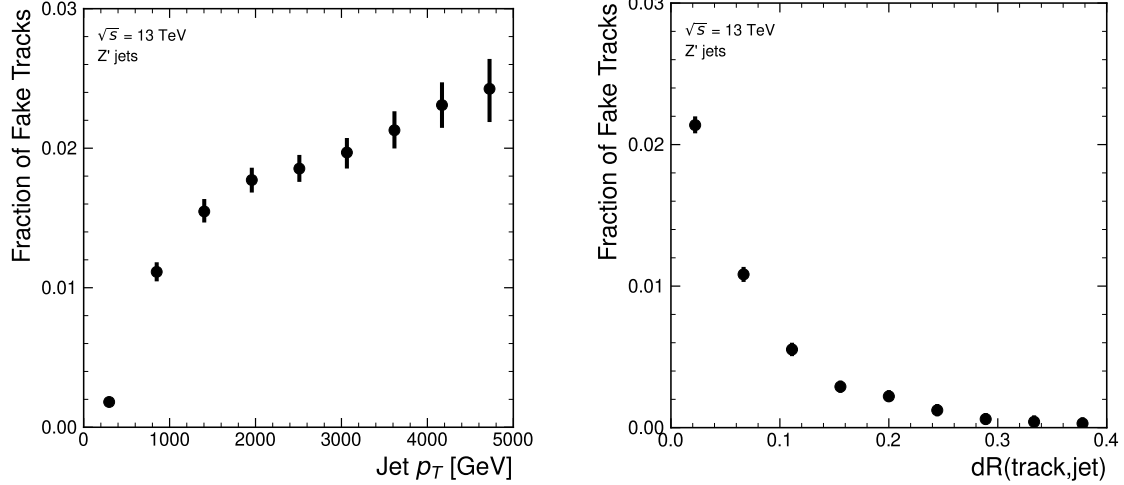


**Figure 5.3:** Rate of fake tracks as a function of jet transverse momentum (left) and  $\Delta R(\text{track}, \text{jet})$  (right). The rate of fake tracks increases significantly as a function of  $p_T$ , and also increases as the distance to the jet axis decreases.

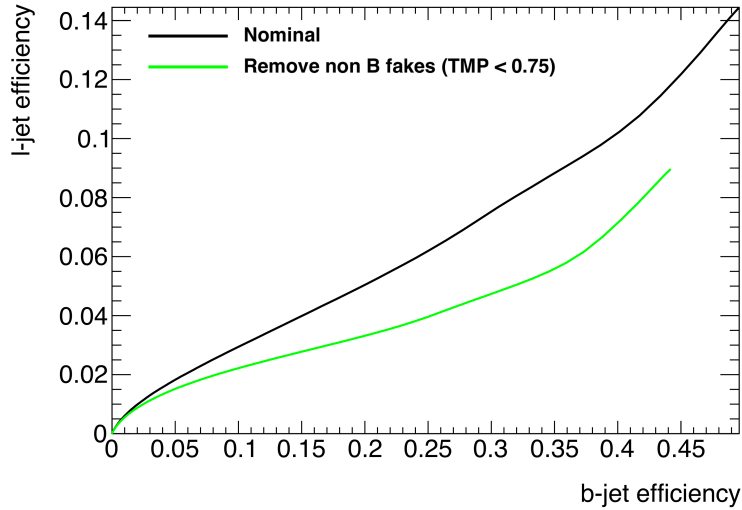


**Figure 5.4:** The light-jet efficiency of the low level tagger SV1 for jets in the  $Z'$  sample with  $250 < p_T < 5000$  GeV, as a function of  $b$ -jet efficiency. The nominal tracking setup (black) is shown alongside the case where fake tracks which are not from the decay of a  $b$ -hadron are removed. The light-jet efficiency is decreased, demonstrating that the presence of fake tracks is detrimental to the algorithm performance.

1128 To identify and remove fake tracks, a NN classification tool was trained with all  
1129 non-fake tracks as the signal class and fake tracks as the background class. Inputs to  
1130 the model are described in Section 5.3.2, while fake track removal performance is  
1131 given in Section 5.3.4.

1132 **5.3.1 Datasets**

1133 To train and evaluate the model, simulated SM  $t\bar{t}$  and BSM  $Z'$  events initiated by  
1134 proton-proton collisions at a center of mass energy  $\sqrt{s} = 13$  TeV are used. The  $Z'$   
1135 sample is constructed in such a manner that it has a relatively flat jet  $p_T$  spectrum  
1136 up to 5 TeV and decays democratically to equal numbers of  $b$ -,  $c$ - and light-jets.  
1137 The generation of the simulated event samples includes the effect of multiple  $pp$   
1138 interactions per bunch crossing with an average pileup of  $\langle \mu \rangle = 40$ , which includes  
1139 the effect on the detector response due to interactions from bunch crossings before  
1140 or after the one containing the hard interaction.

1141 The  $t\bar{t}$  events are generated using the POWHEGBox [90–93] v2 generator at next-  
1142 to-leading order with the NNPDF3.0NLO [94] set of parton distribution functions  
1143 (PDFs). The  $h_{\text{damp}}$  parameter<sup>2</sup> is set to 1.5 times the mass of the top-quark ( $m_{\text{top}}$ ) [95],  
1144 with  $m_{\text{top}} = 172.5$  GeV. The events are interfaced to PYTHIA 8.230 [96] to model the  
1145 parton shower, hadronisation, and underlying event, with parameters set according  
1146 to the A14 tune [97] and using the NNPDF2.3LO set of PDFs [98].  $Z'$  events are  
1147 generated with PYTHIA 8.2.12 with the same tune and PDF set. The decays of  $b$ -  
1148 and  $c$ -hadrons are performed by EVTGEN v1.6.0 [99]. Particles are passed through  
1149 the ATLAS detector simulation [100] based on GEANT4 [101].

1150 Jets are required to have a pseudorapidity  $|\eta| < 2.5$  and  $p_T > 20$  GeV. Additionally, a  
1151 standard selection using the Jet Vertex Tagger (JVT) algorithm at the tight working  
1152 point is applied to jets with  $p_T < 60$  GeV and  $|\eta| < 2.4$  in order to suppress pile-up  
1153 contamination [102].

---

<sup>2</sup>The  $h_{\text{damp}}$  parameter is a resummation damping factor and one of the parameters that controls the matching of POWHEG matrix elements to the parton shower and thus effectively regulates the high- $p_T$  radiation against which the  $t\bar{t}$  system recoils.

### 5.3.2 Model Inputs

The fake track MVA is given two jet variables and 20 tracking related variables for each track fed into the network. The jet transverse momentum and signed pseudorapidity constitute the jet-level inputs, with the track-level inputs listed in Table 5.2. The track parameters and hit pattern are key indicators of whether or not a track is fake. The FracRank variable is the ordered index of the tracks that pass the ambiguity solver’s selection divided by the total number of successfully reconstructed tracks in the event. The ambiguity solver processes track candidates iteratively in order of an internal score (see Section 3.4.1), and the order in which tracks are accepted is preserved. Since tracks with shared hits have lower scores, tracks which do not require the removal of shared hits are likely to be processed and accepted earlier on, whereas tracks with shared hits will be processed later and potentially have their shared hits removed. Hence the FracRank variable gives an indication of the of how easy it was for the track to be reconstructed.

Track selection follows the loose selection described in Ref. [103] and outlined in Table 5.3, which was found to improve the performance compared to previous tighter selections, whilst ensuring good resolution of tracks and a low fake rate [55]. Inputs are scaled to have a central value of zero and a variance of unity before training and evaluation.

### 5.3.3 Model Hyperparameters

Due to the imbalance between the two classes (with fake tracks being relatively uncommon), a weight was added to the loss function for the background class to account for this. The NN was made up of two hidden layers with 220 nodes per layer. The ReLU activation function was used in conjunction with the Adam optimiser with a learning rate of  $1e-3$ . Optimisation of the networks architecture was carried out to ensure optimal performance with a relatively small number of learnable parameters – 54 thousand. The model was trained using 40 million tracks with a futher 1 million tracks each used for validation and testing. A full list of the model hyperparameters is given in Table 5.4.

Jet Input	Description
$p_T$	Jet transverse momentum
$\eta$	Signed jet pseudorapidity
Track Input	Description
$p_T$	Track transverse momentum
$\Delta R$	Angular distance between the track and jet
$d_0$	Closest distance from the track to the PV in the longitudinal plane
$z_0$	Closest distance from the track to the PV in the transverse plane
nIBLHits	Number of IBL hits
nPixHits	Number of pixel hits
nSCTHits	Number of SCT hits
nTRTHits	Number of TRT hits
nBLHits	Number of B-layer hits
nIBLShared	Number of shared IBL hits
nIBLSplit	Number of split IBL hits
nPixShared	Number of shared pixel hits
nPixSplit	Number of split pixel hits
nSCTShared	Number of shared SCT hits
$r_{\text{first}}$	Radius of first hit
nDOF	Number of degrees of freedom on the track
FracRank	Ambiguity solver ordering variable

**Table 5.2:** Input features to the fake track classification NN. Basic jet kinematics, along with information about the reconstructed track parameters and constituent hits are used. Shared hits, are hits used on multiple tracks which have not been classified as split by the cluster-splitting neural networks [55], while split hits are hits used by multiple tracks which have been identified as merged, and therefore split.

Parameter	Selection
$p_T$	> 500 MeV
$ d_0 $	< 3.5 mm
$ z_0 \sin \theta $	< 5 mm
Silicon hits	$\geq 8$
Shared silicon hits	< 2
Silicon holes	< 3
Pixel holes	< 2

**Table 5.3:** Quality selections applied to tracks, where  $d_0$  is the transverse IP of the track,  $z_0$  is the longitudinal IP with respect to the PV and  $\theta$  is the track polar angle (see Section 3.2.2 for the IP definitions). Shared hits are hits used on multiple tracks which have not been classified as split by the cluster-splitting neural networks [55]. A hole is a missing hit, where one is expected, on a layer between two other hits on a track.

Hyperparameter	Value
Batch size	2048
Activation	ReLU
Optimiser	Adam
Initial learning rate	$1e-3$
Training epochs	20
Training tracks	40m
Validation tracks	4m
Testing tracks	4m

**Table 5.4:** Hyperparameter for the track classification model

### 5.3.4 Results

In order to evaluate the fake track classification tool, a orthogonal test sample of 1 million tracks in jets in the combined  $t\bar{t}$  and  $Z'$  samples is used. The continuous scalar output from the NN model is interpreted as the probability that a given track is a signal track (i.e. not fake). Fig. 5.5 shows the performance of the fake track classification MVA. The signal and background classes are well separated in the output of the tool. Also shown is a receiver operating characteristic (ROC) curve, which plots the rate of true positives against the rate of false positives over a scan of cut points on the NN output ranging from zero to one. The area under the curve (AUC) gives a summary of the aggregate classification power of the model. The fake track classification tool achieves an AUC of 0.935 for all tracks, which is indicative of a well-performing model. Considering only tracks from  $b$ -hadron decays, this value drops slightly to 0.928.

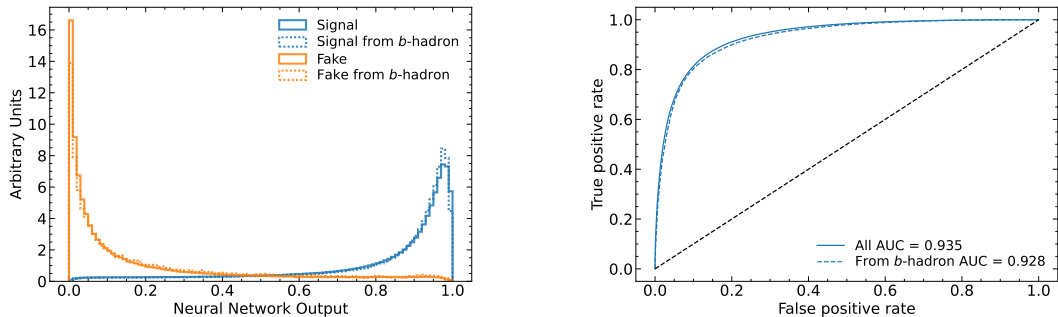


**Figure 5.5:** (left) Normalised histogram of the model output separated for signal and fake tracks, and further separated by those tracks which are from the decay of a  $b$ -hadron. (right) The ROC curve for all tracks (solid line) and tracks from the decay of a  $b$ -hadron (dashed line). The model is able to successfully discriminate between signal and fake tracks, and shows a very similar performance when looking specifically at tracks from the decay of a  $b$ -hadron.

Signal and fake track efficiencies at two different NN output cut points are shown in Table 5.5. The results demonstrate that the tool is effective in retaining 98.8% of signal tracks, while correctly identifying (and therefore enabling the removal of) 45.6% of fake tracks. Table 5.5 also shows that a significant amount of tracks which are labelled as both fake and from the decay of a  $b$ -hadron are also removed. This can happen because fake tracks with  $TMP < 0.75$  are still matched to a truth particle, which can be the decay product of a  $b$ -hadron.

MVA Output Cut	Signal Track Efficiency		Fake Track Efficiency	
	All	From $b$	All	From $b$
0.06	98.8%	98.9%	45.6%	39.8%
0.12	97.3%	97.5%	59.4%	53.6%

**Table 5.5:** Good and fake track selection efficiencies for the combined  $t\bar{t}$  and  $Z'$  samples. Two working points are defined, cutting on the NN output at 0.06 and 0.12. The continuous output of the model allows for the tuning of good and fake track identification efficiencies.

## 5.4 $b$ -hadron Track Identification

After initial tests and investigation, it was found that fake tracks which were the result of  $b$ -hadron decays actually aided  $b$ -tagging performance. The application of a single tool which removed all fake tracks was therefore not optimal. A second tool was therefore trained in the same manner as the first, this one was designed to distinguish between those tracks which were from the decay of a  $b$ -hadron (FromB and FromBC in Table 5.1) and those which were not (all other truth origins). The  $b$ -hadron decay track MVA was trained using the same setup as described above, with the same tracks, input variables, and training procedure. The performance of the model to separate  $b$ -hadron decay tracks from other tracks is shown in Fig. 5.6. Using a selection WP of 0.1, the model can retain 98.5% of  $b$ -hadron tracks and reject 46.2% of tracks not from the decay of a  $b$ -hadron. In Section 5.5, this model is used in conjunction with the fake track identification MVA described in Section 5.3.4 to identify and remove fake tracks which are not from the decay of a  $b$ -hadron.

## 5.5 Combined Approach

A 2-dimensional cut was then used to only reject those tracks that had a high probability of being fake, and also a low probability of being a  $b$ -hadron decay track. The light-jet efficiency of SV1 is successfully reduced when using the combined tools to remove fake tracks that are not from a  $b$ -hadron decay, as shown in Fig. 5.7. At a  $b$ -efficiency of 70%, the light-jet mistag rate for jets with  $250 < p_T < 400$  GeV is

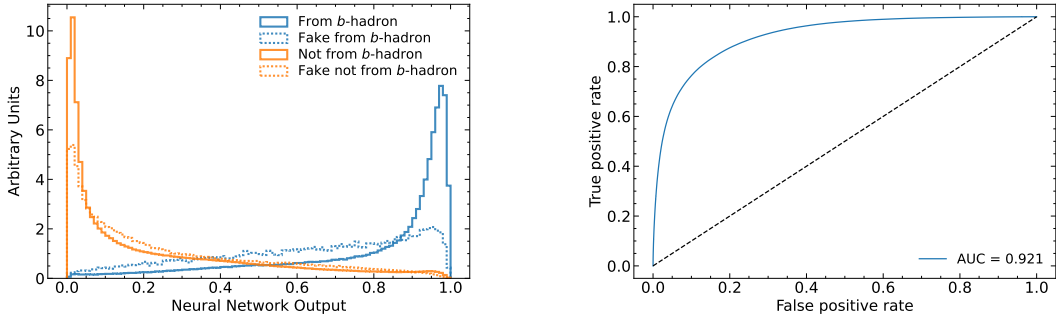


**Figure 5.6:** (left) Normalised histogram of the model output separated for tracks from the decay of a  $b$ -hadron and tracks from other sources. The two groups are further separated into those tracks which are fake. (right) The ROC curve for all tracks (solid line).

WP	Fake Cut	MVA	$b$ -hadron Decay MVA Cut	Retained Tracks	$b$ -hadron	Fake & Non $b$ -hadron Tracks Rejected
A	0.5		0.4	98.6%		50.7%
B	0.6		0.5	97.5%		62.0%

**Table 5.6:** Cut values for the fake and  $b$ -hadron decay track MVAs for the two defined working points. Working point “B” cuts more aggressively on the MVA outputs than WP “A”, removing more fake tracks but resulting in an increased loss of signal tracks (which here are all  $b$ -hadron decay tracks).

reduced from 0.054 to 0.044, a relative improvement of approximately 20%. For jets with  $400 < p_T < 1000$  GeV the mistage rate drops from 0.1 to 0.08 for a similar relative improvement of 20%. The performance of the fake track removal approach was also tested for the other low level vertexing algorithm: JetFitter. A similar level of improvement in the light-jet mistag rate was observed of up to a 20% reduction for both low- and high- $p_T$  jets in the  $Z'$  sample. Together, these results demonstrate that by identifying and removing fake tracks which are not the result of the weak decay of a  $b$ -hadron, the performance of the low level tagging algorithms can be improved.

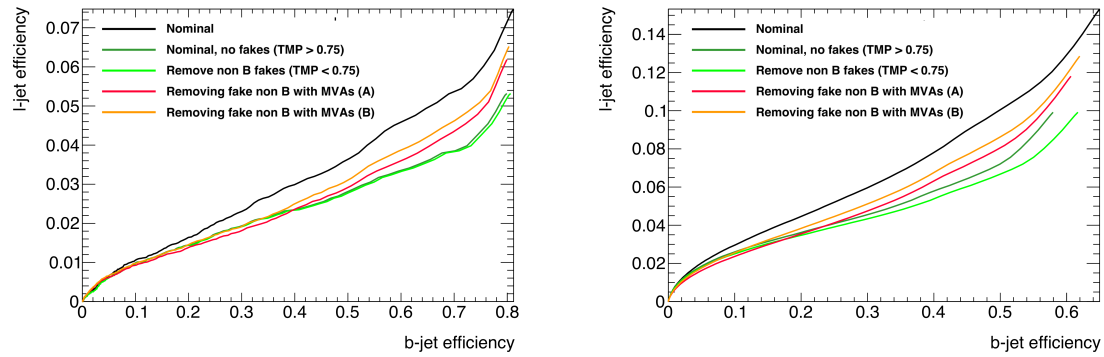


**Figure 5.7:** The effect of applying the fake track identification algorithm together with the  $b$ -hadron decay track identification on the jet tagging performance of SV1 for jets in the  $Z'$  sample with  $250 \text{ GeV} < p_T < 400 \text{ GeV}$  (left) and  $400 \text{ GeV} < p_T < 1 \text{ TeV}$  (right). The nominal SV1 light-jet rejection (black) is compared to two working points of fake track removal, labelled “A” (red) and “B” (orange), which represent two different 2D working points of the track classification tools. Removal of fake tracks based on truth information is shown by the green curves.

## 5.6 Conclusion

Fake tracks, which are prevalent in the core of high  $p_T$  jets, have an adverse impact on  $b$ -tagging performance. A ML tool to identify fake tracks has been developed, which can be used to limit the number of fake tracks being input to the  $b$ -tagging algorithms. Since it was found that  $b$ -hadron decay tracks can also be poorly reconstructed and thus marked as fake, it was deemed necessary also to train a second algorithm to detect  $b$ -hadron decay tracks so that the removal of these tracks could be avoided. Removing fake and non- $b$  decay tracks in this way was found to improve the light-jet

1240 mistagging rate of SV1 and JetFitter by up to 20% at high transverse momentum.  
1241 The improvement achieved using the classification tools was in general comparable with  
1242 the improvement achieved when using the truth information to remove the fake  
1243 tracks not from the decay of a  $b$ -hadron.

1244 **Future Work**

1245 While removing tracks prior to their input to the low level tagging algorithms is  
1246 shown here to be beneficial, a more performant alternative might be to keep these  
1247 tracks but label them as being fake (for example using the output of the classification  
1248 tool), and allow the tagging algorithms to take this into consideration, potentially  
1249 making use of this information. This is not straightforward with manually optimised  
1250 taggers such as SV1 and JetFitter, but is possible with more advanced taggers as  
1251 described in Chapter 6.

1252 Tools which identify the origin of a given track have other potential uses. One  
1253 application is to isolate a relatively pure sample of fake tracks which can be used  
1254 to estimate the fake track rate in data, which would be useful for estimating the  
1255 uncertainty on fake track modelling. Another application would be to use the  
1256  $b$ -hadron track identification tool to improve the track-to-jet association. Both  
1257 applications are currently under investigation.

1258 The approach here works on a track-by-track basis, but a more sophisticated approach  
1259 would consider the correlations between the tracks inside a jet, as shown in Chapter 6.

1260 Also left for future work is to simultaneously train a single tool which discriminates  
1261 between all the truth origins listed in Table 5.1. Such a tool would be useful as a  
1262 general purpose multiclass classifier.

<sub>1263</sub> **Chapter 6**

<sub>1264</sub> **Graph Neural Network Flavour  
Tagger**

<sub>1266</sub> Some of the work in this chapter has previously been published in Ref. [104]. The  
<sub>1267</sub> author of this thesis was on the editorial team and was the primary author. As such,  
<sub>1268</sub> figures and tables from the published note are reproduced here.

<sub>1269</sub> As discussed in Chapter 4, flavour tagging is the identification of jets originating from  
<sub>1270</sub>  $b$ - and  $c$ -quarks. Flavour tagging is a critical component of the physics programme of  
<sub>1271</sub> the ATLAS experiment. It is crucial importance for the study of the Standard Model  
<sub>1272</sub> (SM) Higgs boson and the top quark, which decay preferentially to  $b$ -quarks [105, 106],  
<sub>1273</sub> and additionally for several Beyond Standard Model (BSM) resonances that readily  
<sub>1274</sub> decay to heavy flavour quarks [107].

<sub>1275</sub> Existing flavour tagging algorithms, such as DL1r [108, 109], use as inputs the outputs  
<sub>1276</sub> from a number of low-level algorithms. The low-level algorithms each reconstruct  
<sub>1277</sub> various features of jets using the tracks which have been associated to the jet. The  
<sub>1278</sub> outputs from the low-level algorithms are then combined in a machine learning model.  
<sub>1279</sub> This chapter introduces GN1, a novel ML-based flavour tagging algorithm based on  
<sub>1280</sub> graph neural networks (GNNs).

<sub>1281</sub> As opposed to the previous two-tiered approach described in Chapter 4, which requires  
<sub>1282</sub> the use of both low- and high-level algorithms, GN1 takes as inputs information from  
<sub>1283</sub> an unordered variable number of tracks to predict the jet flavour without requiring  
<sub>1284</sub> outputs from the intermediate low-level algorithms. In addition to predicting the  
<sub>1285</sub> flavour of the jet, the model predicts which physical processes produced the various

1286 jet tracks, and groups the tracks in the jet into vertices. These auxiliary training  
1287 objectives provide valuable additional information about the contents of the jet and  
1288 enhance the performance of the primary flavour prediction task.

1289 GN1 outperforms the existing ATLAS flavour tagging algorithms as shown in Sec-  
1290 tions 6.5.1 and 6.5.2. For a  $b$ -jet efficiency of 70%, the light ( $c$ )-jet rejection is  
1291 improved by a factor of  $\sim 1.8$  ( $\sim 2.1$ ) for jets coming from  $t\bar{t}$  decays with transverse  
1292 momentum  $20 < p_T < 250$  GeV. For jets coming from  $Z'$  decays with transverse  
1293 momentum  $250 < p_T < 5000$  GeV, the light ( $c$ )-jet rejection improves by a factor  $\sim 6$   
1294 ( $\sim 2.8$ ) for a comparative 30%  $b$ -jet efficiency.

1295 In Section 6.1, an overview of the approach used for GN1 is provided. An introduction  
1296 to the theory of GNNs is provided in Section 6.2. Details of the experimental setup  
1297 are provided in Section 6.3, while the architecture of GN1 is specified in Section 6.4.3.  
1298 In Section 6.4.4, the training procedure is described, and in Section 6.5 the results  
1299 are shown.

## 1300 6.1 Motivation

1301 GN1 is a monolithic approach to flavour tagging as illustrated in Fig. 6.1. The use  
1302 of GNNs offers a natural way to classify jets with variable numbers of unordered  
1303 associated tracks (see Section 6.2), while allowing for the inclusion of auxiliary  
1304 training objectives [110, 111].

1305 The current ATLAS flavour tagger, DL1r [108], is a deep neural network which takes  
1306 the outputs of a number of independently optimised “low-level” algorithms [60] as  
1307 its inputs. Each of these low-level algorithms reconstructs a distinct feature of the  
1308 experimental signature of heavy flavour jets using the tracks associated to the jet,  
1309 and outputs some variables which are discriminating in the jet flavour.

1310 The low-level algorithms are a combination of manually optimised reconstruction  
1311 algorithms, for example the SV1 and JetFitter algorithms that reconstruct displaced  
1312 decay vertices, and trained taggers such as RNNIP and DIPS that use the IP and  
1313 hit information from a variable number of tracks to identify the flavour of the  
1314 jet [60, 103, 112, 113]. In contrast GN1 consists of only a single neural network, which  
1315 takes the tracks as inputs along with some kinematic information about the jet. As a

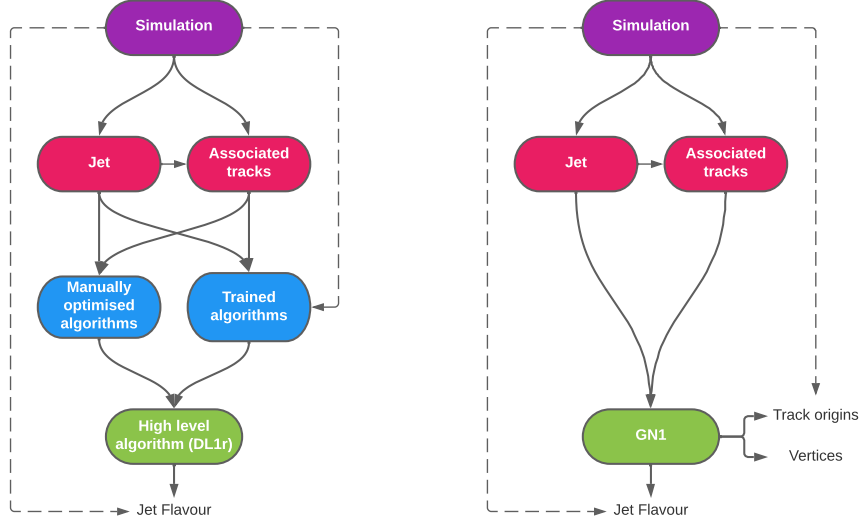


**Figure 6.1:** Comparison of the existing flavour tagging scheme (left) and GN1 (right). The existing approach utilises low-level algorithms (shown in blue), the outputs of which are fed into a high-level algorithm (DL1r). Instead of being used to guide the design of the manually optimised algorithms, additional truth information from the simulation is now being used as auxiliary training targets for GN1. The solid lines represent reconstructed information, whereas the dashed lines represent truth information.

result, it does not depend on the outputs of any other flavour tagging algorithm. A simple training of the model fully optimises its parameters, representing a significant simplification with respect to the optimisation procedure for DL1r. This is particularly important when optimising the tagger for new regions of phase space (e.g.  $c$ -tagging or high- $p_T$   $b$ -tagging), or when the detector or charged particle reconstruction algorithms are updated.

GN1 is trained to learn about the internal structure of the jet through the use of two auxiliary training objectives: the prediction of the underlying physics process from which each track originated, and the grouping of tracks originating from a common spatial position (i.e. a common vertex). These auxiliary objectives are meant to guide the neural network towards a more complete understanding of the underlying physics inside the jet, thereby removing the need for the low-level algorithms, which previously contained information about the underlying physics in their design. The training targets for the primary and auxiliary objectives are extracted from truth information, i.e. information that is only available in simulation, as opposed to reconstructed quantities available in both collision data and simulation.

In this chapter, the following advantages of the GN1 approach will be demonstrated:

1. GN1 boasts improved performance with respect to the current ATLAS flavour tagging algorithms, with significantly larger background rejection rates for a given signal efficiency. Alternatively the rejection rates can be kept fixed for a substantial increase in signal efficiency, in particular at high- $p_T$ .
2. The same network architecture can be easily optimised for a wider variety of use cases (e.g.  $c$ -jet tagging and high- $p_T$  jet tagging) since there are no low-level algorithms to retune.
3. There are fewer algorithms to maintain.
4. Alongside the network's prediction of the jet flavour, the auxiliary vertex and track origin predictions provide more information on why a jet was (mis)tagged or not. This information can also have uses in other applications, for instance to explicitly reconstruct displaced decay vertices or to remove fake tracks.<sup>1</sup>

---

<sup>1</sup>A fake track is defined as a track with a truth-matching probability less than 0.5, where the truth-matching probability is defined in Ref. [55].

## 6.2 Graph Neural Network Theory

Graph neural networks are a more sophisticated neural network model (see Section 5.1.1) that are designed to operate on graph structured data. A brief introduction to GNNs is provided this section following the formalism in Ref. [114].

A graph  $\mathcal{G}$  consists of a set of  $N^n$  nodes  $\mathcal{N} = \{h_i\}_{i=1:N^n}$  (also called *vertices*), a set of  $N^e$  edges  $\mathcal{E} = \{e_i\}_{i=1:N^e}$ , and a global representation  $u$ . Each node represents a individual object, and edges are directed connections between two nodes, called the *sender* and *receiver* nodes. The connectivity of the graph therefore encodes information about the relationships between objects that exist in the graph.

A single graph network layer consists of three separate update functions, one for each of the nodes, edges, and global graph representation, and three aggregation functions. The update functions are typically each implemented as a dense feedforward neural network (as described in Section 5.1.1). The edges  $e_i$  are updated by a edge network  $\phi^e$  as in

$$e'_i = \phi^e(e_i, h_s, h_r, u), \quad (6.1)$$

where  $h_s$  and  $h_r$  are the sender and receiver nodes respectively. The nodes are updated with a node network  $\phi^h$  as in

$$h'_i = \phi^h(\bar{e}'_i, h_i, u), \quad (6.2)$$

where  $\bar{e}'_i = \rho^{e \rightarrow h}(E'_i)$ , and  $E'_i$  is the set of sender nodes for receiver node  $h_i$ .  $\rho^{e \rightarrow h}$  is referred to as the edge aggregation function. The global representation is updated using the global network  $\phi^u$  as in

$$u' = \phi^u(\bar{e}', \bar{h}', u), \quad (6.3)$$

where  $\bar{e}'$  is the aggregation  $\rho^{e \rightarrow u}$  over all updated edges  $e'_i$  and  $\bar{h}'$  is the aggregation  $\rho^{e \rightarrow u}$  over all updated nodes  $h'_i$ .

The graph network layer performs a graph convolution, in an analogous way to a convolutional neural network operating on a grid of pixels. The above description is general, and not all concrete implementations of GNNs need implement every aspect.

1369 For example, the global graph representation need not be present, and it is also  
 1370 possible that no dedicated edge features are present. In such cases the corresponding  
 1371 update and aggregation functions are not needed. Fig. 6.2 shows two possible graph  
 1372 network update layers.

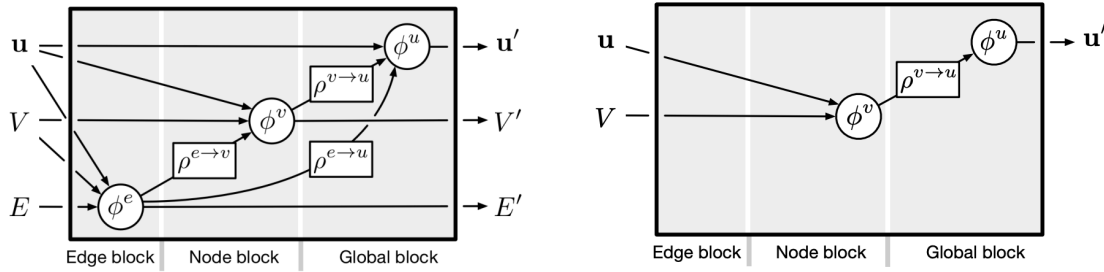


**Figure 6.2:** The flow of information through a graph neural network layer for (left) a full implementation of the layer and (right) a deep sets model [115]. Reproduced from Ref. [114].

1373 The layer used in the GN1 model is specified in more detail in Section 6.4.3.

## 1374 6.3 Experimental Setup

### 1375 6.3.1 Datasets

1376 Datasets used to train the GN1 tagger are the same as described in Section 5.3.1.

1377 The training dataset contains 30 million jets, 60% of which are  $t\bar{t}$  jets and 40% of  
 1378 which are  $Z'$  jets. Although DL1r uses 70%  $t\bar{t}$  jets and 30%  $Z'$  jets, the composition  
 1379 of the training samples was found to have a negligible impact on the final performance  
 1380 of GN1

1381 In order to evaluate the performance of the model, a statistically independent set of  
 1382 500k testing jets from both the  $t\bar{t}$  and  $Z'$  were used. Before being fed into the model,  
 1383 the track- and jet-level inputs were normalised to have a mean of zero and a variance  
 1384 of unity.

1385 Jet flavour labels are assigned according to the presence of a truth hadron within  
 1386  $\Delta R(\text{hadron}, \text{jet}) < 0.3$  of the jet axis. If a  $b$ -hadron is found the jet is labelled a  
 1387  $b$ -jet. In the absence of a  $b$ -hadron, if a  $c$ -hadron is found the jet is called a  $c$ -jet.

1388 If no  $b$ - or  $c$ -hadrons are found, but a  $\tau$  is found in the jet, it is labelled as a  $\tau$ -jet,  
1389 else it is labelled as a light-jet. Truth labelled  $b$ -,  $c$ - and light-jets are kinematically  
1390 re-sampled in  $p_T$  and  $\eta$  to ensure identical distributions in these variables.

## 1391 6.4 Model Architecture

### 1392 6.4.1 Model Inputs

1393 As inputs, GN1 is fed two kinematic jet variables and an unordered set of up to 40  
1394 tracks which have been associated to the jet. Each track consists of 21 variables. The  
1395 kinematic jet variables are the jet transverse momentum and signed pseudorapidity.  
1396 The input variables which are provided for each track are listed in Table 6.1. The  
1397 track parameters and associated uncertainties, along with detailed hit information,  
1398 are used as these variables carry critical information about the jet flavour. If more  
1399 than 40 tracks are associated to a given jet, only the first 40 tracks with the largest  
1400 transverse IP significance<sup>2</sup>  $s(d_0)$  are fed into the model as inputs.

1401 In cores of high- $p_T$  jets, tracks density is high due to the increased multiplicity and  
1402 collimation fo tracks (see Chapter 4). As a result, the separation between tracks can  
1403 be of the same order as the active sensor dimensions, resulting in merged clusters  
1404 and tracks which share hits [55]. Due to the relatively long lifetimes of  $b$ -hadrons  
1405 and  $c$ -hadrons, which can traverse several layers of the ID before decaying and have  
1406 highly collimated decay products, the presence of shared or missing hits is a critical  
1407 signature of heavy flavour jets.

1408 Dependence of the model on the absolute value of the azimuthal jet angle  $\phi$  is  
1409 explicitly removed by providing only the azimuthal angle of tracks relative to the jet  
1410 axis. The track pseudorapidity is also provided relative to the jet axis. The sign of  
1411 the jet pseudorapidity is included, but could be removed in the future to also build  
1412 in the forward-backwards symmetry present at ATLAS.

1413 Since heavy flavour hadrons can decay semileptonically, the presence of a recon-  
1414 structed lepton in the jet carries discriminating information about the jet flavour. To

---

<sup>2</sup>Impact parameter significances are defined as the IP divided by its corresponding uncertainty,  $s(d_0) = d_0/\sigma(d_0)$  and  $s(z_0) = z_0/\sigma(z_0)$ . Track IP significances are lifetime signed according to the track's direction with respect to the jet axis and the primary vertex [37].

1415 exploit this, a variant of GN1 called GN1Lep is trained in addition to the baseline  
1416 model. The GN1Lep variant is identical to the baseline model, up to the inclusion  
1417 an additional track-level input, leptonID, which indicates if the track was used in  
1418 the reconstruction of an electron, a muon or neither. The variable is signed by  
1419 the charge of the reconstructed lepton. The leptons used in the definition of the  
1420 leptonID variable are required to satisfy basic quality requirements. The muons are  
1421 required to be combined [116], and the electrons are required to pass the *VeryLoose*  
1422 likelihood-based identification working point [117].

1423 The selections applied to the tracks is the same as that used for the fake track  
1424 classification MVA described in Chapter 5. The full set of track selections is listed  
1425 in Table 5.3. This selection was found to improve the flavour tagging performance  
1426 compared to previous tighter selections, whilst ensuring good resolution of tracks  
1427 and a low fake rate [55]. However, Section 6.5.8 demonstrates that further relaxation  
1428 of the track selection requirements may be warranted.

#### 1429 6.4.2 Auxiliary Training Objectives

1430 In addition to the jet flavour classification, two auxiliary training objectives are  
1431 defined. The first auxiliary objective is the prediction of the origin of each track  
1432 within the jet, while the second is the prediction of track-pair vertex compatibility.  
1433 Each auxiliary training objective comes with a training target which, similar to  
1434 the jet flavour label, is a truth labels derived from the simulation. The presence  
1435 of the auxiliary training objectives improves the jet classification performance as  
1436 demonstrated in Section 6.5.4.

1437 For the track origin prediction objective, each track is labelled with one of the  
1438 exclusive categories defined in Table 5.1 after analysing the particle interaction that  
1439 led to its formation. Since the presence of different track origins is strongly related to  
1440 the flavour of the jet, training GN1 to recognise the origin of the tracks provides an  
1441 additional handle on the classification of the jet flavour. This task may also aid the  
1442 jet flavour prediction by acting as a form of supervised attention [118] - in detecting  
1443 tracks from heavy flavour decays the model may learn to pay more attention to these  
1444 tracks.

Jet Input	Description
$p_T$	Jet transverse momentum
$\eta$	Signed jet pseudorapidity
Track Input	Description
$q/p$	Track charge divided by momentum (measure of curvature)
$d\eta$	Pseudorapidity of the track, relative to the jet $\eta$
$d\phi$	Azimuthal angle of the track, relative to the jet $\phi$
$d_0$	Closest distance from the track to the PV in the longitudinal plane
$z_0 \sin \theta$	Closest distance from the track to the PV in the transverse plane
$\sigma(q/p)$	Uncertainty on $q/p$
$\sigma(\theta)$	Uncertainty on track polar angle $\theta$
$\sigma(\phi)$	Uncertainty on track azimuthal angle $\phi$
$s(d_0)$	Lifetime signed transverse IP significance
$s(z_0)$	Lifetime signed longitudinal IP significance
nPixHits	Number of pixel hits
nSCTHits	Number of SCT hits
nIBLHits	Number of IBL hits
nBLHits	Number of B-layer hits
nIBLShared	Number of shared IBL hits
nIBLSplit	Number of split IBL hits
nPixShared	Number of shared pixel hits
nPixSplit	Number of split pixel hits
nSCTShared	Number of shared SCT hits
nPixHoles	Number of pixel holes
nSCTHoles	Number of SCT holes
leptonID	Indicates if track was used to reconstruct an electron or muon

**Table 6.1:** Input features to the GN1 model. Basic jet kinematics, along with information about the reconstructed track parameters and constituent hits are used. Shared hits, are hits used on multiple tracks which have not been classified as split by the cluster-splitting neural networks [55], while split hits are hits used on multiple tracks which have been identified as merged. A hole is a missing hit, where one is expected, on a layer between two other hits on a track. The track leptonID is an additional input to the GN1Lep model.

1445 The vertexing auxiliary objective makes use of the fact that displaced decays of  $b$ -  
 1446 and  $c$ -hadrons lead to secondary and tertiary vertices inside the jet, as described  
 1447 in Section 4.1.1. The presence of displaced secondary vertices is not a completely  
 1448 clean signal of a heavy flavour jet, as displaced secondary vertices can also occur in  
 1449 light-jets as a result of material interactions and long-lived particle decays (e.g.  $K_S^0$   
 1450 and  $\Lambda^0$ ). For the auxiliary object, GN1 predicts a binary label for each pair of tracks  
 1451 in the jet. The label has a value of 1 if the truth particles associated with the two  
 1452 tracks in the pair originated from the same spatial point, and 0 otherwise. To derive  
 1453 the corresponding truth labels for training, truth production vertices within 0.1 mm  
 1454 are merged, as these are assumed to be unresolvable given the granularity of the ID.  
 1455 Track-pairs where one or both of the tracks in the pair have an origin label of either  
 1456 Pileup or Fake are given a label of 0. Using the pairwise predictions from the model,  
 1457 groups of tracks that have common compatibility can be formed, resulting in the  
 1458 finding of vertices. Two existing low-level tagging algorithms, SV1 and JetFitter, are  
 1459 currently used to find and reconstruct vertices inside jets and are used as inputs to  
 1460 the existing jet flavour tagger DL1r. The addition of this auxiliary training objective  
 1461 removes the need for inputs from a dedicated secondary vertexing algorithm.

1462 Both of the auxiliary training objectives described here can be considered as “stepping  
 1463 stones” on the way to classifying the flavour of the jet. By requiring the model to  
 1464 predict the truth origin of each track and the vertex compatibility of each track-pair,  
 1465 the model is guided to learn representations of the jet which are connected to the  
 1466 underlying physics and therefore relevant for classifying the jet flavour.

### 1467 6.4.3 Architecture

1468 As discussed in the previous sections, GN1 is a graph neural network which makes  
 1469 use of auxiliary training objectives in order to determine the jet flavour. A coarse  
 1470 optimisation of the network architecture hyperparameters (for example number of  
 1471 layers and number of neurons per layer) has been carried out in order to maximise  
 1472 the flavour tagging performance, but it is likely that further dedicated optimisation  
 1473 studies could lead to further performance improvements.

1474 The model architecture builds on a previous implementation of a GNN-based jet  
 1475 tagger [111]. The previous approach was comprised of two separate graph neural  
 1476 networks with the auxiliary tasks being performed at an intermediate stage after the

1477 first and before the second. This two stage approach was found to be unnecessary and  
1478 as such GN1 simplifies the architecture into a single graph neural network with the  
1479 auxiliary tasks being performed at the end, alongside the primary jet classification  
1480 task. GN1 makes use of a more sophisticated graph neural network layer [119],  
1481 which is described in more detail below. The changes significantly improved tagging  
1482 performance and also led to a significant reduction in training time.

1483 As inputs, the model takes information about the jet and a number of associated  
1484 tracks, as detailed in Section 6.4.1. The jet variables are concatenated with the  
1485 variables for each track as shown in Fig. 6.3. The combined jet-track input vectors  
1486 are then fed into a per-track initialisation network with three hidden layers, each  
1487 containing 64 neurons, and an output layer with a size of 64, as shown in Fig. 6.4. The  
1488 track initialisation network is similar to a deep sets model [115], but does not include  
1489 a reduction operation (mean or summation) over the output track representations.  
1490 The initialisation network allows for initial per-track input processing without the  
1491 associated parameter count cost of the graph convolutional layers described below.

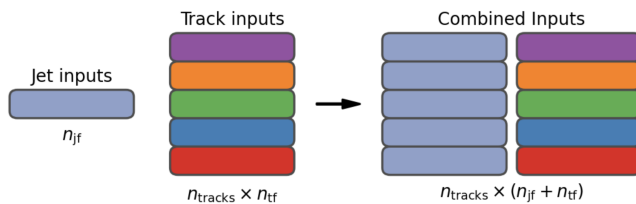


**Figure 6.3:** The inputs to GN1 are the two jet features ( $n_{\text{jf}} = 2$ ), and an array of  $n_{\text{tracks}}$ , where each track is described by 21 track features ( $n_{\text{tf}} = 21$ ). The jet features are copied for each of the tracks, and the combined jet-track vectors of length 23 form the inputs of GN1.

1492 The outputs of the track initialisation network are used to populate the nodes of a  
1493 fully connected graph, such that each node in the graph neighbours every other node.  
1494 Each node  $h_i$  in the graph corresponds to a single track in the jet, and is characterised  
1495 by a feature vector, also called a representation. The per-track output representations  
1496 from the initialisation networks are used as the initial feature vectors of each node in  
1497 the graph. In each layer of the graph network, output node representations  $h'_i$  are  
1498 computed by aggregating the features of  $h_i$  and neighbouring nodes  $\mathcal{N}_i$  as described  
1499 in Ref. [119]. First, the feature vectors of receiver and sender nodes are fed into two  
1500 fully connected linear layers  $\mathbf{W}_r$  and  $\mathbf{W}_s$ , to produce an updated representation for

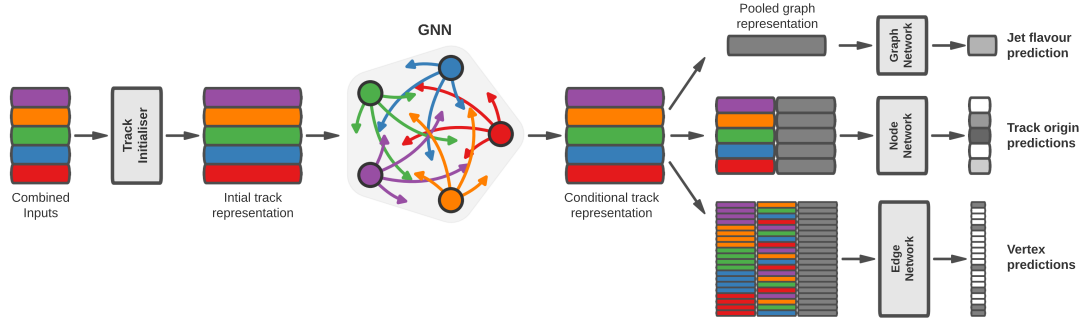


**Figure 6.4:** The network architecture of GN1. Inputs are fed into a per-track initialisation network, which outputs an initial latent representation of each track. These representations are then used to populate the node features of a fully connected graph network. After the graph network, the resulting node representations are used to predict the jet flavour, the track origins, and the track-pair vertex compatibility.

1501 each sender and receiver node  $\mathbf{W}_r h_i$  and  $\mathbf{W}_s h_j$ . These updated feature vectors are  
 1502 used to compute edge scores  $e(h_i, h_j)$  for each node pair, as in

$$e(h_i, h_j) = \mathbf{a} \cdot \theta [\mathbf{W}_r h_i + \mathbf{W}_s h_j], \quad (6.4)$$

1503 where,  $\theta$  is a non-linear activation function, and  $\mathbf{a}$  is a learned vector. These edge  
 1504 scores are then used to calculate attention weights  $a_{ij}$  for each pair of nodes using  
 1505 the softmax function over the edge scores

$$a_{ij} = \text{softmax}_j [e(h_i, h_j)]. \quad (6.5)$$

1506 Finally, the updated representations for the receiver nodes  $h'_i$  are computed by taking  
 1507 the weighted sum over each updated node representation  $\mathbf{W}_r h_i$ , with weights  $a_{ij}$

$$h'_i = \sigma \left[ \sum_{j \in \mathcal{N}_i} a_{ij} \cdot \mathbf{W}_r h_j \right]. \quad (6.6)$$

1508 The set of operations described above constitute a single graph network layer. Three  
 1509 such layers are stacked to construct the graph network, representing a balance  
 1510 between achieving good performance and avoiding overtraining due to inflation of  
 1511 the parameter count of the model. The final output from the graph neural network is  
 1512 a set of per-node (i.e. per-track) feature vectors that are conditional representations  
 1513 of each track given the other tracks in the jet. In order to perform the jet flavour  
 1514 prediction, a flattened global representation of the jet is needed. To produce this, the  
 1515 output track representations are combined using a weighted sum, where the weights  
 1516 are learned during training and therefore act as a form of single-headed attention  
 1517 over the different tracks. The flattened outputs from the sum are then fed into a  
 1518 fully connected feedforward neural network with four layers and three outputs, one  
 1519 for each jet flavour. Two other separate fully connected feedforward neural networks  
 1520 are then used to independently perform the auxiliary classification objectives of GN1.  
 1521 Both of the auxiliary classification tasks also take in the global representation of the  
 1522 jet as inputs. A summary of the different classification networks used for the various  
 1523 training objectives is shown in Table 6.2.

**Table 6.2:** A summary of GN1’s different classification networks used for the different training objectives. The hidden layers column contains a list specifying the number of neurons in each layer.

Network	Hidden layers	Output size
Node classification network	128, 64, 32	7
Edge classification network	128, 64, 32	1
Graph classification network	128, 64, 32, 16	3

1524 A node classification network predicts the track truth origin as defined in Table 5.1.  
 1525 This network takes as inputs the features from a single output node from the graph  
 1526 network and the global representation of the jet. The node network has three hidden  
 1527 layers containing 128, 64 and 32 neurons respectively, and an output size of seven,  
 1528 corresponding to the seven different truth origins defined in Table 5.1.  
 1529 An edge classification network is used to predict whether the tracks in the track-  
 1530 pair belong to a common vertex. This network takes as inputs the concatenated  
 1531 representations from each pair of tracks and the global jet representation. Similar  
 1532 to the node network, the edge network has three hidden layers containing 128,

1533 64 and 32 neurons respectively, and a single output, which is used to perform  
1534 binary classification of the track-pair compatibility. The output predictions for the  
1535 two auxiliary networks are used for the auxiliary training objectives discussed in  
1536 Section 6.4.2.

1537 Finally, the graph classification network is used to predict the jet flavour. This  
1538 network takes only the global jet representation as input. The graph classification  
1539 network is comprised of four fully connected hidden layers with 128, 64, 32 and 16  
1540 neurons respectively, and has three outputs corresponding to the  $b$ -,  $c$ - and light-jet  
1541 classes.

#### 1542 6.4.4 Training

1543 The full GN1 training procedure minimises the total loss function  $L_{\text{total}}$ , defined  
1544 in Eq. (6.7). This loss is composed of three terms:  $L_{\text{jet}}$ , the categorical cross  
1545 entropy loss over the different jet flavours;  $L_{\text{vertex}}$ , the binary track-pair compatibility  
1546 cross entropy loss; and  $L_{\text{track}}$ , the categorical cross entropy loss for the track origin  
1547 prediction.  $L_{\text{vertex}}$  is computed by averaging over all intra-jet track-pairs in the batch,  
1548 and  $L_{\text{track}}$  is computed by averaging over all tracks in the batch.

$$L_{\text{total}} = L_{\text{jet}} + \alpha L_{\text{vertex}} + \beta L_{\text{track}} \quad (6.7)$$

1549 The different losses converge to different values during training, reflecting differences  
1550 in the relative difficulty of the various training objectives. The values of  $L_{\text{vertex}}$  and  
1551  $L_{\text{track}}$  are weighted by  $\alpha = 1.5$  and  $\beta = 0.5$  respectively to ensure they converge to  
1552 similar values, giving them an equal weighting towards  $L_{\text{total}}$ . The values of  $\alpha$  and  $\beta$   
1553 are chosen to ensure that  $L_{\text{jet}}$  converges to a larger value than either  $L_{\text{vertex}}$  and  $L_{\text{track}}$ ,  
1554 which reflects the primary importance of the jet classification objective. It was found  
1555 that in practice the overall performance of the model was not sensitive to modest  
1556 changes in the loss weights  $\alpha$  and  $\beta$ . Pre-training using  $L_{\text{total}}$  (i.e. on all tasks) and  
1557 fine tuning on only the jet classification task also did not improve performance versus  
1558 the described standard setup, indicating that the auxiliary tasks are not in direct  
1559 competition with the jet classification task. As there was a large variation in the

1560 relative abundance of tracks of the different origins, the contribution of each origin to  
1561  $L_{\text{track}}$  was weighted by the inverse of the frequency of their occurrence. In vertexing  
1562 loss  $L_{\text{vertex}}$ , the class weight for track-pairs where both tracks are from either a  $b$ - or  
1563  $c$ -hadron was increased by a factor of two as compared with other track-pairs, to  
1564 encourage the network to focus on correctly classifying heavy flavour vertices.

1565 GN1 can be trained with either the node or edge networks (and their corresponding  
1566 auxiliary tasks), or both, removed, as discussed in Section 6.5.4. In such cases,  
1567 the corresponding losses  $L_{\text{vertex}}$  and  $L_{\text{track}}$  are also removed from the calculation  
1568 of the overall loss  $L_{\text{total}}$ . The performance of the resulting models provides a  
1569 useful indication of the benefit of including the auxiliary tasks to the primary jet  
1570 classification objective.

1571 GN1 is trained for 100 epochs on 4 NVIDIA V100 GPUs. Each epoch takes approxi-  
1572 mately 25 mins to complete over the training sample of 30 million jets described in  
1573 Section 6.3.1. The Adam optimiser [120] with an initial learning rate of 1e−3, and a  
1574 batch size of 4000 jets (spread across the 4 GPUs) was used. Typically the validation  
1575 loss, calculated on 500k jets, became stable after around 60 epochs. The epoch that  
1576 minimized the validation loss was used for evaluation. GN1 has been integrated into  
1577 the ATLAS software [52] using ONNX [121]. The test sample jet flavour predictions  
1578 scores are computed using the ATLAS software stack as a verification of this process.

## 1579 6.5 Results

1580 The GN1 tagger is evaluated both as a  $b$ -tagging and  $c$ -tagging algorithm in Sec-  
1581 tion 6.5.1 and Section 6.5.2 respectively. Evaluation is performed separately on  
1582 both jets in the  $t\bar{t}$  sample with  $20 < p_{\text{T}} < 250 \text{ GeV}$  and jets in the  $Z'$  sample with  
1583  $250 < p_{\text{T}} < 5000 \text{ GeV}$ . The performance of the model is compared to the DL1r  
1584 tagger [108, 109], which has been retrained on 75 million jets from the same samples  
1585 as GN1. The input RNNIP tagger [113] to DL1r has not been retrained. As discussed,  
1586 each tagger predicts the probability that a jet belongs to the  $b$ -,  $c$ - and light-classes.  
1587 To use the model for  $b$ -tagging, these probabilities are combined into a single score  
1588  $D_b$ , which is defined as

$$D_b = \log \frac{p_b}{(1 - f_c)p_l + f_c p_c}, \quad (6.8)$$

1589 where  $f_c$  is a free parameter that determines the relative weight of  $p_c$  to  $p_l$  in the  
 1590 score  $D_b$ , controlling the trade-off between  $c$ - and light-jet rejection performance.  
 1591 The choice of  $f_c$  is arbitrary, with the different optimised values reflecting the relative  
 1592  $c$ - versus light-jet rejection performance of the various taggers. This parameter is  
 1593 set to a value of  $f_c = 0.018$  for the DL1r model, obtained through an optimisation  
 1594 procedure designed to maximise the  $c$ - and light-jet rejection of DL1r described in  
 1595 Ref. [108]. Based on a similar optimisation procedure, a value of  $f_c = 0.05$  is used  
 1596 for the GN1 models. A fixed-cut working point (WP) defines the corresponding  
 1597 selection applied to the tagging discriminant  $D_b$  in order to achieve a given efficiency  
 1598 on the inclusive  $t\bar{t}$  sample.

1599 The technical implementation of GN1 in the ATLAS software stack requires any jet  
 1600 with zero or one associated tracks to be classified as a light-jet. The impact of this  
 1601 on the tagging performance of GN1 was found to be negligible, with 0.12% of  $b$ -jets  
 1602 in the  $t\bar{t}$  sample and 0.02% of  $b$ -jets in the  $Z'$  sample affected. Of those, 89% of the  
 1603  $b$ -jets in the  $t\bar{t}$  sample and 98% of the  $b$ -jets in the  $Z'$  sample are also classified as  
 1604 light-jets by DL1r at the 70%  $t\bar{t}$  WP.

1605 A comparison of the  $b$ -tagging discriminant  $D_b$  between DL1r and GN1 is shown in  
 1606 Fig. 6.5. The shapes of the  $D_b$  distributions are generally similar for  $b$ -,  $c$ - and light-  
 1607 jets between both models, however, GN1 shifts the  $b$ -jet distribution to higher values  
 1608 of  $D_b$  in the regions with the greatest discrimination. The GN1  $c$ -jet distribution is  
 1609 also shifted to lower values of  $D_b$  when compared with DL1r, enhancing the separation  
 1610 and indicating that GN1 is improving  $c$ -jet rejection when compared with DL1r.

### 1611 6.5.1 $b$ -tagging Performance

1612 The performance of  $b$ -tagging algorithms is quantified by their ability to reject  $c$ -  
 1613 and light-jets for a given  $b$ -jet selection efficiency, or working point (WP). In order  
 1614 to compare the  $b$ -tagging performance of the different taggers for the  $b$ -jet tagging  
 1615 efficiencies in the range typically used by analyses, the corresponding  $c$ - and light-jet

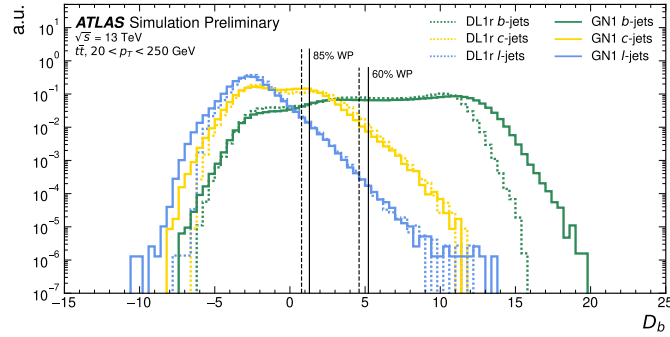


**Figure 6.5:** Comparison between the DL1r and GN1  $b$ -tagging discriminant  $D_b$  for jets in the  $t\bar{t}$  sample. The 85% WP and the 60% WP are marked by the solid (dashed) lines for GN1 (DL1r), representing respectively the loosest and tightest WPs used by analyses. A value of  $f_c = 0.018$  is used in the calculation of  $D_b$  for DL1r and  $f_c = 0.05$  is used for GN1. The distributions of the different jet flavours have been normalised to unity area.

rejection rates are displayed in Figs. 6.6 and 6.7 for jets in the  $t\bar{t}$  and  $Z'$  samples respectively. Four standard WPs are defined with  $b$ -jet tagging efficiencies of 60%, 70%, 77% and 85% respectively. These WPs are commonly used by physics analyses depending on their specific signal and background requirements. The WPs are defined based on jets in the  $t\bar{t}$  sample only. Due to the much higher jet  $p_T$  range in the  $Z'$  sample, and the increased difficulty in tagging jets at high- $p_T$  (see Chapter 4), the  $b$ -jet tagging efficiencies for jets in the  $Z'$  sample are lower than the corresponding WPs calculated in the  $t\bar{t}$  sample. For instance the WP cut value compute to provide a 70%  $b$ -jet tagging efficiency on the  $t\bar{t}$  sample results in a  $b$ -jet tagging efficiency of just  $\sim 30\%$  on the  $Z'$  sample. In order to account for this, the range of  $b$ -jet tagging efficiencies displayed for plots showing the performance for jets in the  $Z'$  sample (for example Fig. 6.7) is chosen to span the lower efficiencies achieved in the  $Z'$  sample at high- $p_T$ .

For jets in the  $t\bar{t}$  sample with  $20 < p_T < 250$  GeV, GN1 demonstrates considerably better  $c$ - and light-jet rejection when compared with DL1r across the full range of  $b$ -jet tagging efficiencies studied. The relative improvement is strongly dependent on the  $b$ -jet tagging efficiency under study. The largest improvements are found at lower  $b$ -jet tagging efficiencies. At a  $b$ -jet tagging efficiency of 70%, the  $c$ -rejection improves by a factor of  $\sim 2.1$  while the light-jet rejection improves by a factor of  $\sim 1.8$  with respect to DL1r. For high- $p_T$  jets in the  $Z'$  sample with  $250 < p_T < 5000$  GeV, GN1 also brings a significant performance improvement with respect to DL1r across the

range of  $b$ -jet tagging efficiencies studied. Again, the largest relative improvement in performance comes at the lower  $b$ -jet tagging efficiencies. At a  $b$ -jet efficiency of 30%, GN1 improves the  $c$ -rejection with respect to DL1r by a factor of  $\sim 2.8$  and the light-jet rejection by a factor of  $\sim 6$ . The performance comparison at lower  $b$ -jet tagging efficiencies is made more difficult due to the increased statistical uncertainties which result from the high rejection of background. It is estimated that for a  $b$ -jet tagging efficiency of 70% in the  $t\bar{t}$  sample,  $\sim 5\%$  ( $\sim 30\%$ ) of the relative improvement in the  $c$ -jet (light-jet) rejection comes from loosening the track selection and for a  $b$ -jet tagging efficiency of 30% in the  $Z'$  the corresponding number is  $\sim 10\%$  for both  $c$ -jets and light-jets. Given that GN1 exploits the low-level detector information in a more complete and sophisticated way than DL1r, further studies are needed to confirm that the performance gain observed in these simulated samples is also observed in experimental data.

The GN1Lep variant of GN1 demonstrates further improved performance with respect to the baseline model. This demonstrates the additional jet flavour discrimination power provided by the leptonID track input. For jets in the  $t\bar{t}$  sample, the relative  $c$ -rejection improvement with respect to DL1r at the 70%  $b$ -jet WP increases from a factor of  $\sim 2.1$  for GN1 to a factor of  $\sim 2.8$  for GN1Lep. The improvement in light-jet rejection also increases from a factor of  $\sim 1.8$  to  $\sim 2.5$  at the same WP. For jets in the  $Z'$  sample, the relative  $c$ -rejection (light-jet rejection) improvement with respect to DL1r increases from a factor of  $\sim 2.8$  to  $\sim 3$  ( $\sim 6$  to  $\sim 7.5$ ) at a  $b$ -jet tagging efficiency of 30%. As shown in Fig. 6.8, the greatest improvement of GN1Lep over GN1 is seen at lower transverse momenta.

In general, the performance of all the taggers is strongly dependent on the jet  $p_T$ . This is due to the increased multiplicity and collimation of tracks, and the displaced decays that result from within the heavy flavour jets. These factors are described in more detail in Chapter 4. Together, they contribute to a reduced reconstruction efficiency for heavy flavour tracks, and a general degradation in quality of tracks inside the core of a jet, which in turn reduces the jet tagging performance.

In order to study how the tagging performance changes as a function of the jet  $p_T$ , the  $b$ -jet tagging efficiency as a function of  $p_T$  for a fixed light-jet rejection of 100 in each bin is shown in Fig. 6.8. For jets in the  $t\bar{t}$  sample, at a fixed light-jet rejection of 100, GN1 improves the  $b$ -jet tagging efficiency by approximately 4% across all the jet  $p_T$  bins. Meanwhile, GN1Lep again demonstrates improved performance with

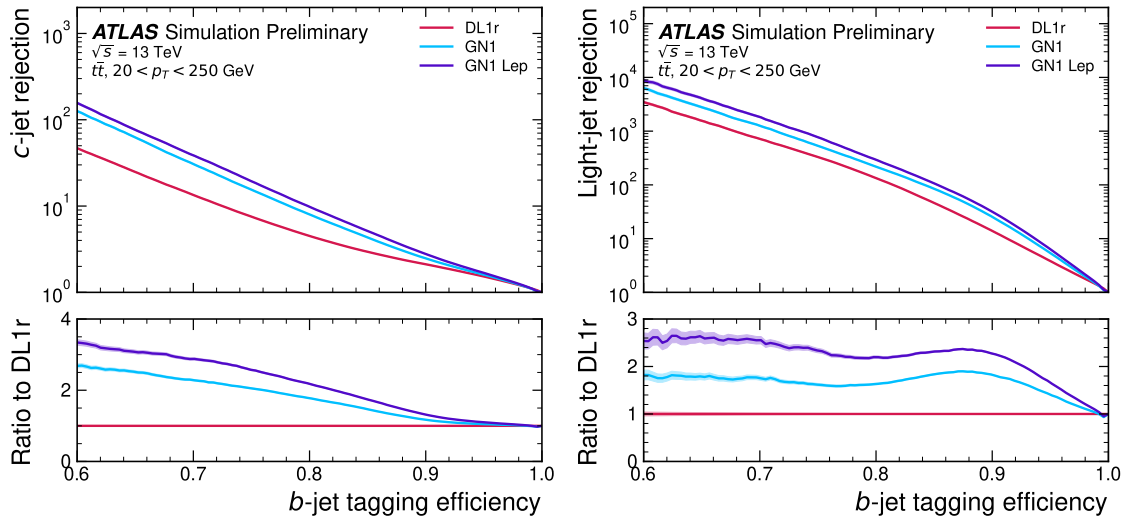


**Figure 6.6:** The  $c$ -jet (left) and light-jet (right) rejections as a function of the  $b$ -jet tagging efficiency for jets in the  $t\bar{t}$  sample with  $20 < p_T < 250 \text{ GeV}$ . The ratio with respect to the performance of the DL1r algorithm is shown in the bottom panels. A value of  $f_c = 0.018$  is used in the calculation of  $D_b$  for DL1r and  $f_c = 0.05$  is used for GN1 and GN1Lep. Binomial error bands are denoted by the shaded regions. At  $b$ -jet tagging efficiencies less than  $\sim 75\%$ , the light-jet rejection becomes so large that the effect of the low number of jets is visible. The lower  $x$ -axis range is chosen to display the  $b$ -jet tagging efficiencies usually probed in these regions of phase space.

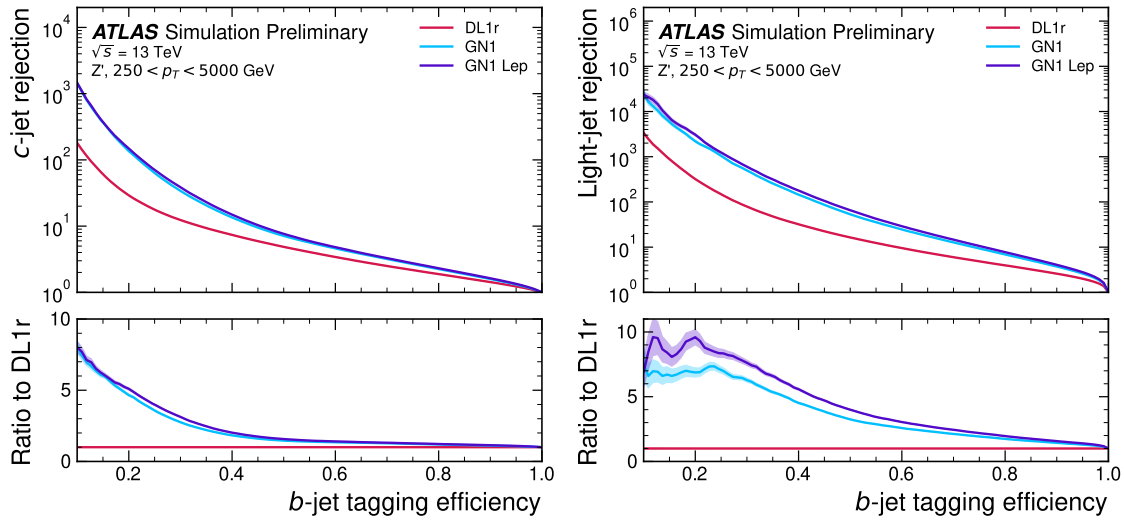


**Figure 6.7:** The  $c$ -jet (left) and light-jet (right) rejections as a function of the  $b$ -jet tagging efficiency for jets in the  $Z'$  sample with  $250 < p_T < 5000 \text{ GeV}$ . The ratio with respect to the performance of the DL1r algorithm is shown in the bottom panels. A value of  $f_c = 0.018$  is used in the calculation of  $D_b$  for DL1r and  $f_c = 0.05$  is used for GN1 and GN1Lep. Binomial error bands are denoted by the shaded regions. At  $b$ -jet tagging efficiencies less than  $\sim 20\%$ , the light-jet rejection becomes so large that the effect of the low number of jets is visible. The lower  $x$ -axis range is chosen to display the  $b$ -jet tagging efficiencies usually probed in these regions of phase space.

respect to GN1, in particular at lower  $p_T$ . The relative increase in the  $b$ -jet tagging efficiency increases from 4% to 8% with respect to DL1r. For jets in the  $Z'$  sample, GN1 again outperforms DL1r across the entire jet  $p_T$  range studied. The largest relative improvement in performance is found at the highest transverse momenta of jet  $p_T > 2$  TeV, and corresponds to an approximate factor of 2 improvement in efficiency with respect to DL1r.

The performance of the model was also evaluated as a function of the average number of pileup interactions in the event. No significant dependence of the tagging performance was observed.

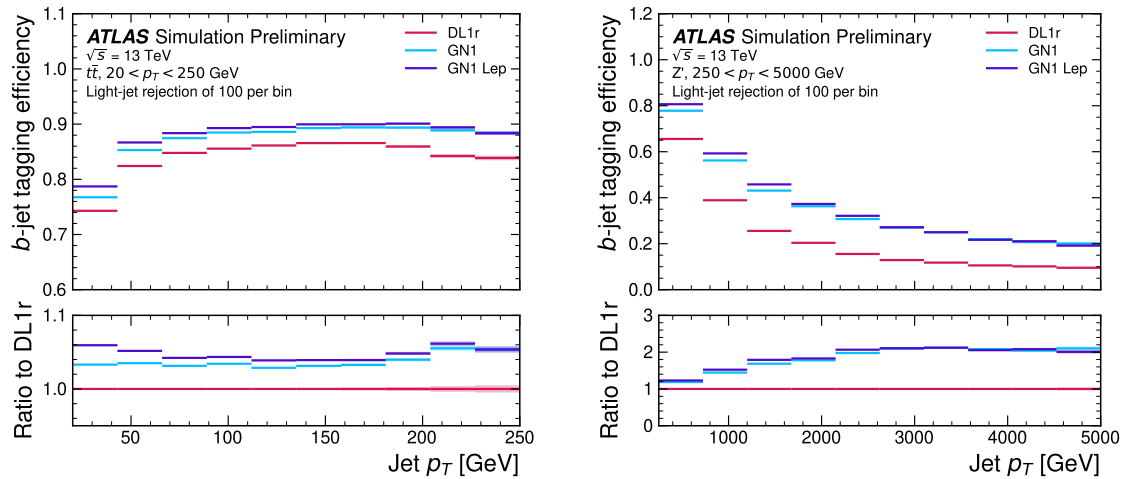


**Figure 6.8:** The  $b$ -jet tagging efficiency for jets in the  $t\bar{t}$  sample (left) and jets in the  $Z'$  sample (right) as a function of jet  $p_T$  with a fixed light-jet rejection of 100 in each bin. A value of  $f_c = 0.018$  is used in the calculation of  $D_b$  for DL1r and  $f_c = 0.05$  is used for GN1 and GN1Lep. GN1 demonstrates improved performance with respect to DL1r accross the  $p_T$  range shown. Binomial error bands are denoted by the shaded regions.

### 6.5.2 $c$ -tagging Performance

As discussed previously, GN1 does not rely on any inputs from manually optimised low-level tagging algorithms. Since these algorithms were originally designed and tuned with the aim of  $b$ -tagging, and not  $c$ -tagging, the low level tagging algorithms may perform suboptimally for  $c$ -tagging purposes. The tagging of  $c$ -jets therefore presents a compelling use case for GN1. As each of the the models is trained with three output classes, using it as a  $c$ -tagging algorithm is trivially analogous to the

1687 approach used for  $b$ -tagging. The model output probabilities are combined into a  
1688 single score  $D_c$ , which is defined similarly to Eq. (6.8) as

$$D_c = \log \frac{p_c}{(1 - f_b)p_l + f_b p_b}. \quad (6.9)$$

1689 A value of  $f_b = 0.2$  is used for all models, based on the same optimisation procedure  
1690 that was used for the  $b$ -tagging use case. Similar to Section 6.5.1, the different  
1691 taggers are compared to one another by scanning through a range of  $c$ -jet tagging  
1692 efficiencies and plotting the corresponding  $b$ - and light-jet rejection rates. As in  
1693 Section 6.5.1, the WPs are defined using jets in the  $t\bar{t}$  sample. Standard  $c$ -jet tagging  
1694 efficiency WPs used by physics analyses are significantly lower than the  $b$ -tagging  
1695 WPs in order to maintain reasonable  $b$ - and light-jet rejection rates. This is reflected  
1696 in the range of  $c$ -jet tagging efficiencies used in  $c$ -tagging plots such as Figs. 6.9  
1697 and 6.10. Fig. 6.9 displays the  $c$ -tagging performance of the models on the jets in  
1698 the  $t\bar{t}$  sample. GN1 is shown to perform significantly better than DL1r. Similar to  
1699 the  $b$ -tagging case, the  $b$ - and light-jet rejection improve most at lower  $c$ -jet tagging  
1700 efficiencies, with both background rejections increasing by a factor of 2 with respect  
1701 to DL1r at a  $c$ -jet tagging efficiency of 25%. GN1Lep again outperforms GN1, though  
1702 the improvements with respect to the baseline model are more modest, with the  
1703  $b$ -rejection (light-jet rejection) relative improvement increasing from a factor of 2 to  
1704 2.1 (2 to 2.3) at the 25%  $c$ -jet WP. Fig. 6.10 shows the  $c$ -tagging performance on the  
1705 jets in the  $Z'$  sample with  $250 < p_T < 5000$  GeV. Both GN1 and GN1Lep perform  
1706 similarly, improving the  $b$ -rejection by 60% and the light-jet rejection by a factor of  
1707 2 at the 25%  $c$ -jet WP.

### 1708 6.5.3 Jet Display Diagrams

1709 The auxiliary training objectives of GN1 allow for improved model interpretability,  
1710 which is especially important for a monolithic approach as the low level taggers,  
1711 which provide useful physical insight, are no longer present. Figs. 6.11 and 6.12  
1712 show a comparison of the true origin and vertexing information compared with  
1713 the predicted values from GN1, SV1 and JetFitter. Such comparisons can be used

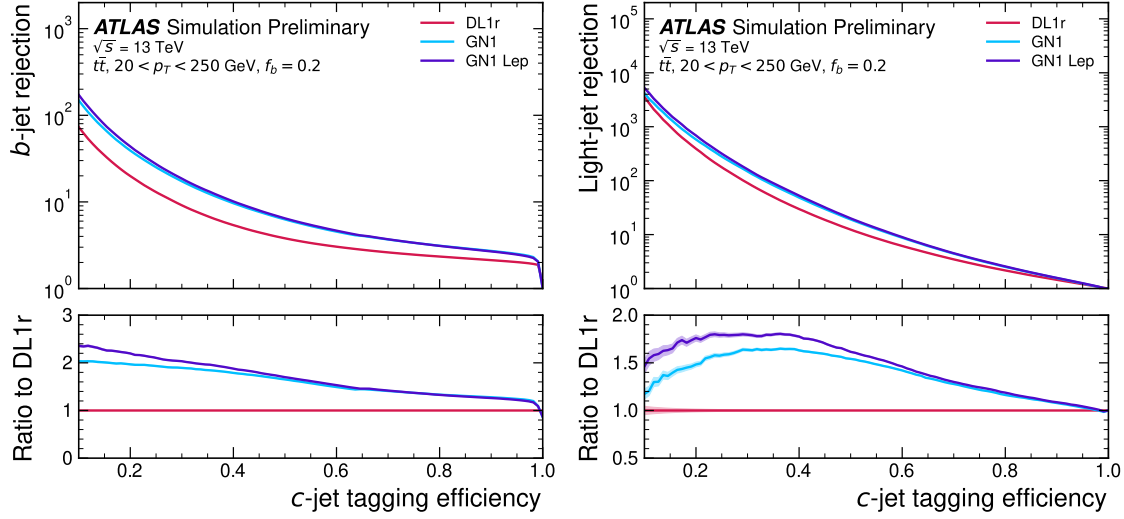


**Figure 6.9:** The  $b$ -jet (left) and light-jet (right) rejections as a function of the  $c$ -jet tagging efficiency for  $t\bar{t}$  jets with  $20 < p_T < 250 \text{ GeV}$ . The ratio to the performance of the DL1r algorithm is shown in the bottom panels. Binomial error bands are denoted by the shaded regions. At  $c$ -jet tagging efficiencies than  $\sim 25\%$ , the light-jet rejection becomes so large that the effect of the low number of jets is visible. The lower  $x$ -axis range is chosen to display the  $c$ -jet tagging efficiencies usually probed in these regions of phase space.

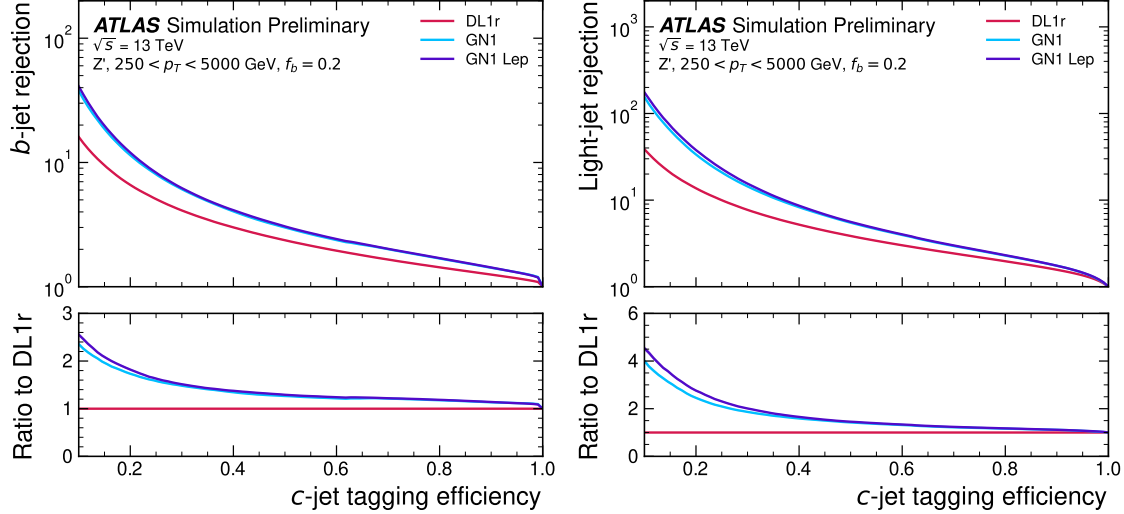


**Figure 6.10:** The  $b$ -jet (left) and light-jet (right) rejections as a function of the  $c$ -jet tagging efficiency for  $Z'$  jets with  $250 < p_T < 5000 \text{ GeV}$ . The ratio to the performance of the DL1r algorithm is shown in the bottom panels. Binomial error bands are denoted by the shaded regions. The lower  $x$ -axis range is chosen to display the  $c$ -jet tagging efficiencies usually probed in these regions of phase space.

1714 to provide an indication that GN1 recovers the intended representation of the jet  
1715 structure, and may also help to identify limitations of the model.

1716 The diagrams show the truth (left) and predicted (right) structure of a  $b$ -jet. The  
1717 shaded black boxes show the groupings of tracks into different vertices. In Fig. 6.11,  
1718 GN1 correctly groups the three primary tracks as having come from the primary  
1719 vertex. The  $b$ -hadron and  $b \rightarrow c$ -hadron decay vertices are also correctly predicted,  
1720 and the origin of the tracks in each is correct. There is a single OtherSecondary track  
1721 which GN1 incorrectly predicts as having come pileup. Meanwhile SV1 (by design)  
1722 merges the two heavy flavour decay vertices, but incorrectly includes a track from  
1723 the primary vertex. JetFitter reconstructs two vertices, one which is a combination  
1724 of two tracks from the different truth vertices and two other single track vertices in  
1725 each of the heavy flavour vertices. GN1 also predicts the flavour of the jet with a  
1726 high degree of certainty.

1727 Similarly, Fig. 6.11 shows that, at least in some cases, GN1 is able to accurately  
1728 predict the origin and vertex information of tracks inside a jet. The pileup tracks  
1729 and primary vertex tracks are correctly identified, and the heavy flavour decay tracks  
1730 are also correctly identified with the exception of one of the  $b$ -hadron decay tracks.  
1731 Again, SV1 is overly aggressive by merging the two heavy flavour decay vertices  
1732 along with a track from pileup, while JetFitter shows signs of being underconstrained  
1733 by reconstructing two single track vertices, one with a pileup track and one with a  
1734 track from a  $b \rightarrow c$ -hadron decay.

#### 1735 6.5.4 Ablations

1736 Ablation studies (the removal of certain components of a given model in order to  
1737 study the impact of that component) are carried are carried out to determine the  
1738 importance of the auxiliary training objectives of GN1 to the overall performance.  
1739 The “GN1 No Aux” variant retains the primary jet classification objective, but  
1740 removes both track classification and vertexing auxiliary objectives (see Section 6.4.2)  
1741 and correspondingly only minimises the jet classification loss. The “GN1 TC” variant  
1742 includes track classification objective but not the vertexing objective. Finally, the  
1743 “GN1 Vert” includes the vertexing objective, but not the track classification objective.

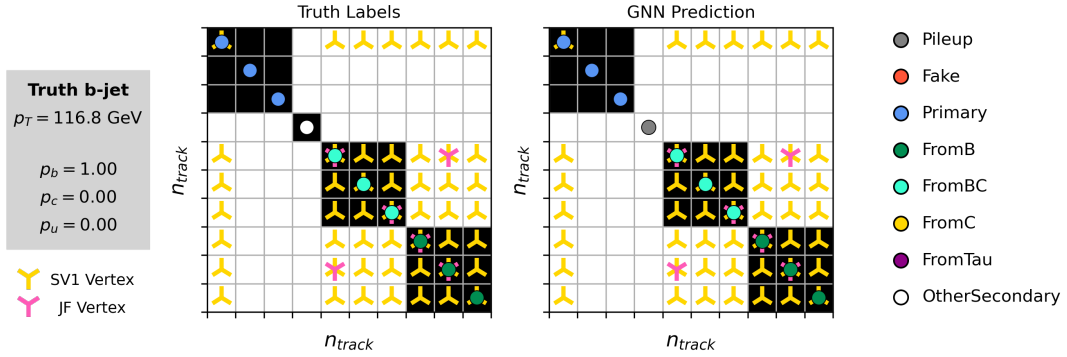


**Figure 6.11:** A schematic showing the truth track origin and vertex information (left) compared with the predictions from GN1 (right). Vertices reconstructed by SV1 and JetFitter are also marked. Class probabilities  $p_b$ ,  $p_c$  and  $p_u$  are rounded to three significant figures. GN1 improves over SV1 and JetFitter by successfully determining the origins and vertex compatibility of all the tracks in the jet with the exception of the truth OtherSecondary track, which is misidentified as pileup.

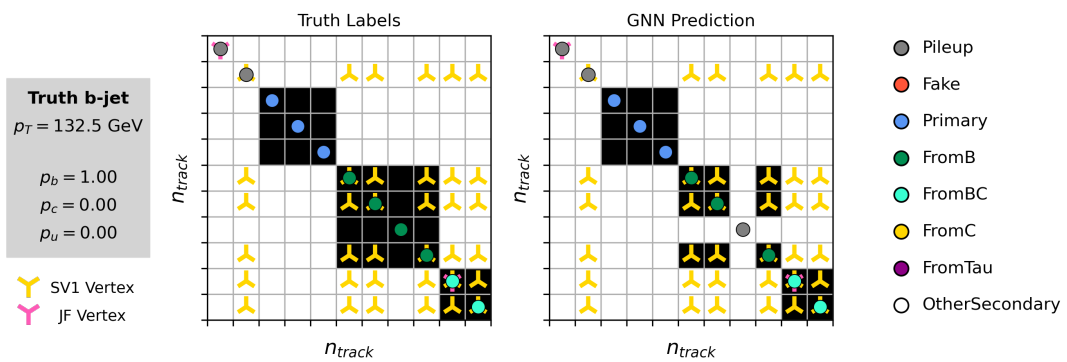


**Figure 6.12:** A schematic showing the truth track origin and vertex information (left) compared with the predictions from GN1 (right). Vertices reconstructed by SV1 and JetFitter are also marked. Class probabilities  $p_b$ ,  $p_c$  and  $p_u$  are rounded to three significant figures.

1744 For jets in both the  $t\bar{t}$  and  $Z'$  samples, a general trend is observed that the models  
1745 trained without one or both of the auxiliary objectives results in significantly reduced  
1746  $c$ - and light-jet rejection when compared with the baseline GN1 model. This result  
1747 is shown clearly in Figs. 6.13 and 6.14. For jets in the  $t\bar{t}$  sample, the performance  
1748 of GN1 No Aux is similar to DL1r, while GN1 TC and GN1 Vert perform similarly  
1749 to each other with improvements in the  $c$ -rejection of 80% and improvements in  
1750 the light-jet rejection of 75% at a  $b$ -jet tagging efficiency of 60%. For jets in the  $Z'$   
1751 sample meanwhile, the GN1 No Aux model already shows a clear improvement in  $c$ -  
1752 and light-jet rejection when compared with DL1r at lower  $b$ -jet tagging efficiencies.  
1753 Similar to jets in the  $t\bar{t}$  sample, GN1 TC and GN1 Vert perform similarly, and bring  
1754 large gains in background rejection when compared with GN1 No Aux, but the  
1755 combination of both auxiliary objectives yields the best performance.

1756 It is notable that the GN1 No Aux model matches or exceeds the performance of  
1757 DL1r without the need for inputs from the low-level algorithms. This indicates that  
1758 the performance improvements enabled by the improved neural network architecture  
1759 used in GN1 appear to be able to compensate for the removal of the low-level  
1760 algorithm inputs. The GN1 TC and GN1 Vert variants each similarly outperform  
1761 DL1r, demonstrating that both contribute to the overall high performance of the  
1762 baseline model. The overall best performing model is the full version of GN1 trained  
1763 with both auxiliary objective, demonstrating that the both auxiliary objectives are  
1764 complementary.

### 1765 6.5.5 Inclusion of Low-Level Vertexing Algorithms

1766 As already mentioned, GN1 does not include any inputs from the low-level tagging  
1767 algorithms, including the vertexing algorithms SV1 and JetFitter [60]. Since these  
1768 algorithms are known to play a key role in contributing to the performance of DL1r, it  
1769 was necessary to study whether their inclusion in GN1 resulted in further performance  
1770 improvements. In a dedicated training of GN1 the SV1 and JetFitter tagger outputs  
1771 were added to the GN1 jet classification network as an input, similar to how they  
1772 are used in DL1r. These outputs include information on the reconstructed vertices,  
1773 including the number of vertices, and the mass, displacement, and other properties of  
1774 the highest ranking reconstructed vertex. In addition, the index of the reconstructed  
1775 SV1 or JetFitter vertices were included as two track-level inputs to GN1. These

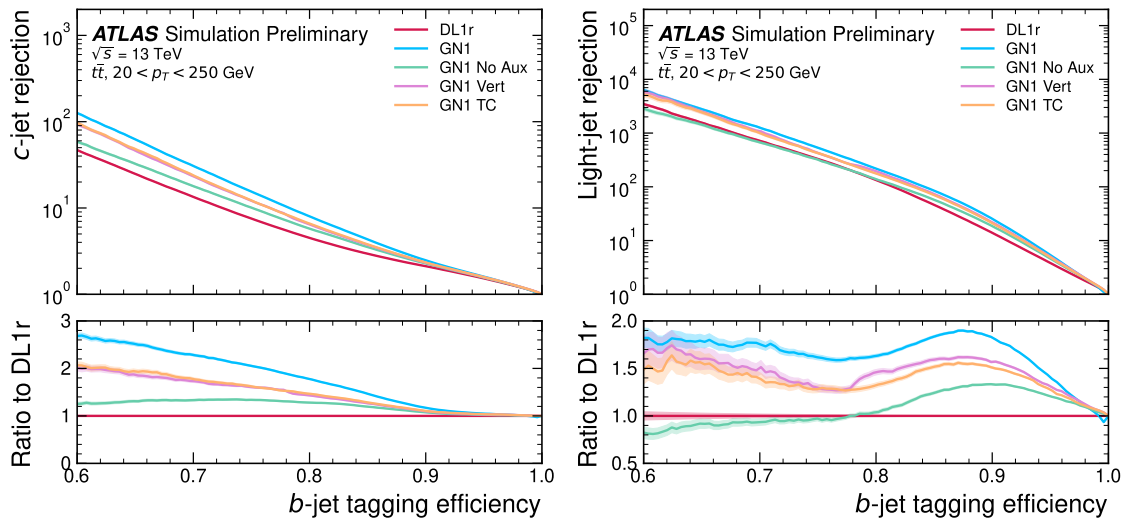


**Figure 6.13:** The  $c$ -jet (left) and light-jet (right) rejections as a function of the  $b$ -jet tagging efficiency for  $t\bar{t}$  jets with  $20 < p_T < 250 \text{ GeV}$ , for the nominal GN1, in addition to configurations where no (GN1 No Aux), only the track classification (GN1 TC) or only the vertexing (GN1 Vert) auxiliary objectives are deployed. The ratio to the performance of the DL1r algorithm is shown in the bottom panels. A value of  $f_c = 0.018$  is used in the calculation of  $D_b$  for DL1r and  $f_c = 0.05$  is used for GN1. Binomial error bands are denoted by the shaded regions. At  $b$ -jet tagging efficiencies less than  $\sim 65\%$ , the light-jet rejection become so large that the effect of the low number of jets are visible. The lower  $x$ -axis range is chosen to display the  $b$ -jet tagging efficiencies usually probed in these regions.

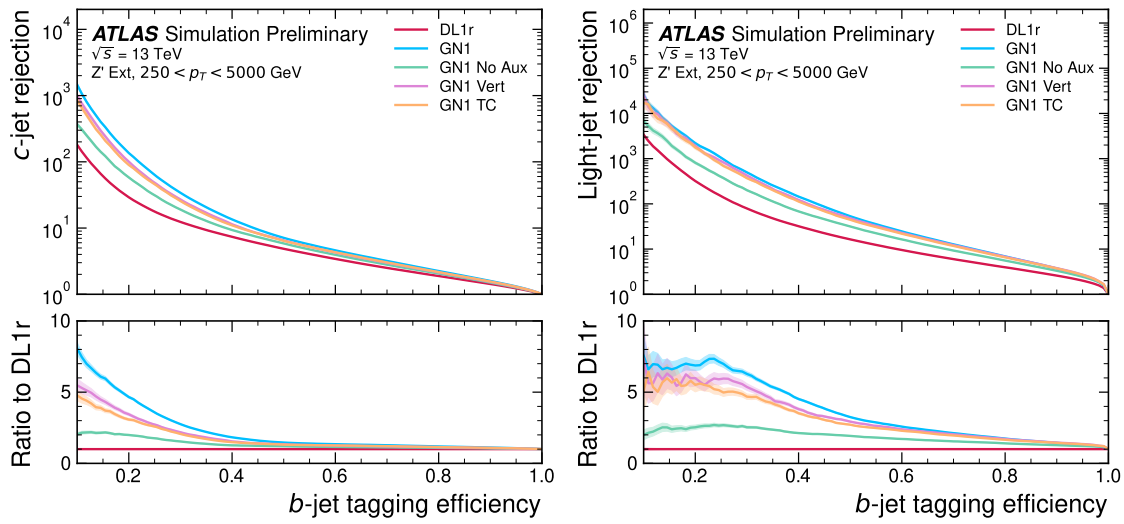


**Figure 6.14:** The  $c$ -jet (left) and light-jet (right) rejections as a function of the  $b$ -jet tagging efficiency for  $Z'$  jets with  $250 < p_T < 5000$  GeV, for the nominal GN1, in addition to configurations where no (GN1 No Aux), only the track classification (GN1 TC) or only the vertexing (GN1 Vert) auxiliary objectives are deployed. The ratio to the performance of the DL1r algorithm is shown in the bottom panels. A value of  $f_c = 0.018$  is used in the calculation of  $D_b$  for DL1r and  $f_c = 0.05$  is used for GN1. Binomial error bands are denoted by the shaded regions. At  $b$ -jet tagging efficiencies less than  $\sim 25\%$ , the light-jet rejection become so large that the effect of the low number of jets are visible. The lower  $x$ -axis range is chosen to display the  $b$ -jet tagging efficiencies usually probed in these regions.

1776 indices were also used to construct an edge feature for the edge classification network,  
1777 which was given a value of one if the track-pair were from a common reconstructed  
1778 V1 or JetFitter vertex, and zero otherwise. The jet classification performance of this  
1779 GN1 model was not significantly different to the baseline model, and in some cases  
1780 the performance was slightly reduced. As GN1 does not benefit from the inclusion  
1781 of information from SV1 and JetFitter it can function as a highly performant  
1782 standalone tagger that does not require (beyond retraining) any manual optimisation  
1783 to achieve good performance in a wide range of phase spaces. A dedicated look at  
1784 the vertexing performance of GN1 with some comparisons to SV1 and JetFitter is  
1785 found in Section 6.5.6

### 1786 6.5.6 Vertexing Performance

1787 From the track-pair vertex prediction described in Section 6.4.2, tracks can be  
1788 partitioned into compatible groups representing vertices (see [111]). As such, GN1  
1789 is able to be used to perform vertex “finding”, but not vertex “fitting”, i.e. the  
1790 reconstruction of a vertex’s properties, which currently still requires the use of a  
1791 dedicated vertex fitter. In order to study the performance of the different vertexing  
1792 tools inside  $b$ -jets, the truth vertex label of the tracks, discussed in Section 6.4.2, are  
1793 used. To estimate the efficiency with which GN1 manages to find vertices inclusively,  
1794 vertices from GN1 containing tracks identified as coming from a  $b$ -hadron are merged  
1795 together and compared to the inclusive truth decay vertices that result from a  
1796  $b$ -hadron decay (where if there are multiple distinct truth vertices from a  $b$ -hadron  
1797 decay they are also merged together). Vertices are compared with the target truth  
1798 vertex and the number of correctly and incorrectly assigned tracks is computed.  
1799 Since secondary vertex information is only recovered for reconstructed tracks, an  
1800 efficiency of 100% here denotes that all possible secondary vertices are recovered  
1801 given the limited track reconstruction efficiency. A vertex is considered matched if  
1802 it contains at least 65% of the tracks in the corresponding truth vertex, and has a  
1803 purity of at least 50%. GN1 manages to achieve an inclusive reconstruction efficiency  
1804 in  $b$ -jets of  $\sim 80\%$ , demonstrating that it effectively manages to identify the displaced  
1805 vertices from  $b$ -hadron decays.

1806 In order to study the performance of the different vertexing tools inside  $b$ -jets, the  
1807 truth vertex label of the tracks, discussed in Section 6.4.2, is used. The reconstructed

1808 vertices from GN1, SV1 and JetFitter are compared to the target truth vertices in  
1809 order to calculate the efficiencies of the different vertexing tools. Since secondary  
1810 vertex information is only recovered for reconstructed tracks, an efficiency of 100%  
1811 here denotes that all possible secondary vertices are recovered given the limited track  
1812 reconstruction efficiency.

1813 There are several caveats to a comparison of the vertexing tools which are a result  
1814 of the different approaches they take to vertexing. SV1 and JetFitter are designed  
1815 to only find secondary vertices in the jet, whereas GN1 is also trained to determine  
1816 which tracks in the jet belong to the primary vertex (the vertex of the hard scatter  
1817  $pp$  interaction). To account for this the GN1 vertex with the largest number of  
1818 predicted primary tracks is excluded from the vertex finding efficiency calculation.  
1819 While JetFitter and GN1 aim to resolve each displaced vertex inside the jet, such  
1820 that secondary vertices from  $b$ -hadron decays are found separately to tertiary vertices  
1821 from  $b \rightarrow c$  decay chains, SV1 by design attempts to find a single inclusive vertex  
1822 per jet. This inclusive vertex groups inclusive  $b$ -hadron decays. These are tracks  
1823 from the  $b$ -hadron decay itself (FromB) and tracks from  $b \rightarrow c$  decays (FromBC).  
1824 In order to fairly compare the performance if the different tools, both the exclusive  
1825 and inclusive vertex finding efficiency is studied. For the exclusive vertex finding  
1826 case JetFitter and GN1 can be directly compared, while a comparison with SV1 is  
1827 not possible due to aforementioned design constraints. The inclusive vertex finding  
1828 performance of all three tools can be compared using the procedure outlined below.

1829 The starting point for the secondary vertex finding efficiency in both the exclusive  
1830 and inclusive cases is to select truth secondary vertices are those containing only  
1831 inclusive  $b$ -hadron decays to be considered as initial targets. For exclusive vertex  
1832 finding, these truth secondary vertices can be used directly as the denominator for the  
1833 efficiency calculation. Meanwhile for the inclusive efficiency all such truth secondary  
1834 vertices in the jet are merged into a single inclusive target vertex. Correspondingly,  
1835 for the inclusive vertex finding case, the vertices found by JetFitter are merged into  
1836 a single vertex, and the vertices found by GN1 with at least one predicted inclusive  
1837  $b$ -hadron decay track are also merged similarly. SV1 does not require any vertex  
1838 merging.

1839 Next, in both cases for each truth secondary vertex, vertices in the jet found by the  
1840 different vertexing tools are compared with the target truth vertex. The number  
1841 of correctly and incorrectly assigned tracks is computed. In order to call a vertex

efficient, it is required to contain at least 65% of the tracks in the corresponding truth vertex, and to have a purity of at least 50%. Single track vertices are required to have a purity of 100%. Additionally, for GN1 only, at least one track in the vertex is required to have a predicted heavy flavour origin.

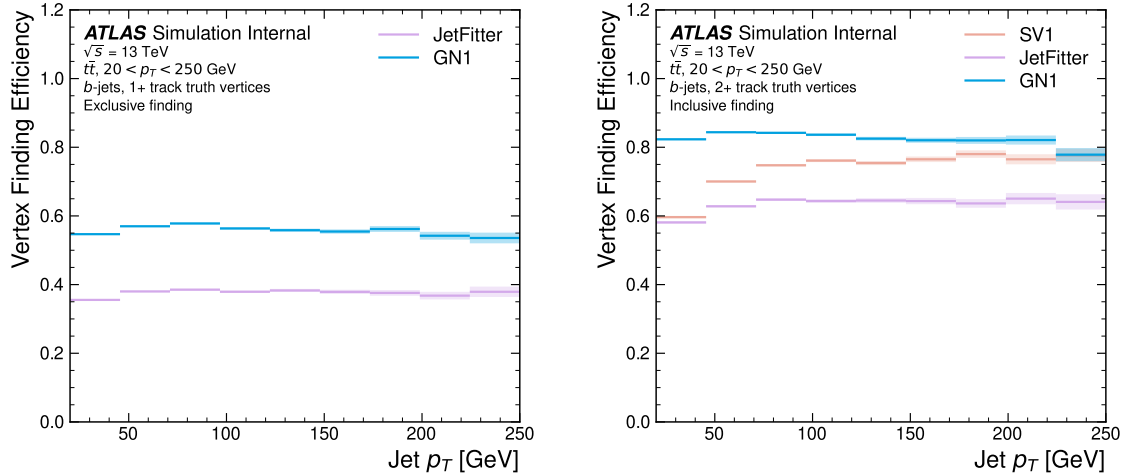


**Figure 6.15:** Vertex finding efficiency as a function of jet  $p_T$  for  $b$ -jets in the  $t\bar{t}$  sample using the exclusive (left) and inclusive (right) vertex finding approaches. Efficient vertex finding requires the recall of at least 65% of the tracks in the truth vertex, and allows no more than 50% of the tracks to be included incorrectly. Binomial error bands are denoted by the shaded regions.

Vertex finding efficiencies for  $b$ -jets in the  $t\bar{t}$  sample are displayed as a function of  $p_T$  separately for the inclusive and exclusive approaches in Fig. 6.15. For  $b$ -jets in the  $t\bar{t}$  sample with  $20 < p_T < 250$  GeV, the exclusive vertex finding efficiency of JetFitter and GN1 is relatively flat as a function of  $p_T$ . Of the truth secondary vertices in this  $p_T$  region, JetFitter efficiently finds approximately 40% and GN1 finds approximately 55%. When finding vertices inclusively the vertex finding efficiency is generally higher. An increased dependence on  $p_T$  is also visible for JetFitter and SV1. As the jet  $p_T$  increases from 20 GeV to 100 GeV, the efficiency of JetFitter increases from 55% to 65%. In the same range, the efficiency of SV1 increases from 55% to 75%. GN1 displays less dependence on  $p_T$  than JetFitter and SV1, efficiently finding upwards of 80% of vertices in  $b$ -jets in this  $p_T$  region. For  $b$ -jets with  $p_T > 100$  GeV, JetFitter finds approximately 65% of vertices, SV1 finds approximately 75% of vertices, and GN1 finds approximately 80% of vertices.

For  $b$ -jets in the  $Z'$  sample, the vertex finding efficiency drops steeply with increasing  $p_T$  up until  $p_T = 3$  TeV. GN1 outperforms SV1 and JetFitter across the  $p_T$  spectrum. In the first bin, the efficiency of GN1 is 75%, while the efficiencies of SV1 and JetFitter are around 60%. The efficiency of SV1 drops rapidly to almost zero above 3 TeV, while JetFitter and GN1 retain approximately 30% efficiency. Fig. 6.16 compares the exclusive vertex finding efficiencies of JetFitter and GN1 for multitrack vertices. JetFitter finds 45-50% of vertices in  $b$ -jets in the  $t\bar{t}$  sample, while GN1 finds 60-65%. For  $b$ -jets in the  $Z'$  sample, JetFitter finds 35% of vertices in the first bin, dropping to 20% of vertices above 2 TeV. GN1 finds 55% of vertices in the first bin, dropping to 30% above 2 TeV.

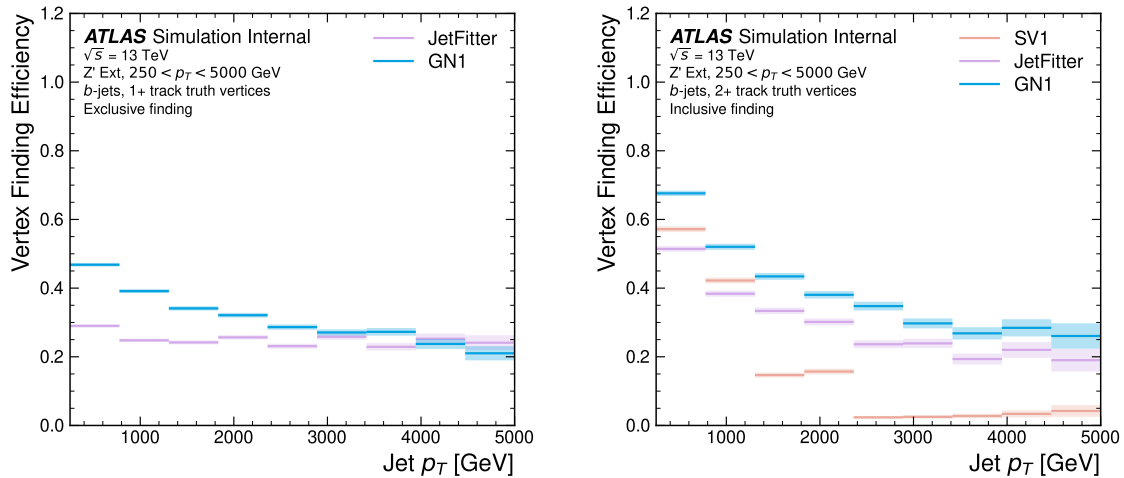


**Figure 6.16:** Inclusive vertex finding efficiency for multitrack truth vertices in  $b$ -jets in the  $t\bar{t}$  sample (left) and jets in the  $Z'$  sample (right) as a function of jet  $p_T$ . Efficient vertex finding requires the recall of at least 65% of the tracks in the truth vertex, and allows no more than 50% of the tracks to be included incorrectly.

### 6.5.7 Track Classification Performance

One of the two auxiliary training objectives used by GN1 is to predict the truth origin of each track associated to the jet, as discussed in Section 6.4.2. Since the equivalent information is not provided by any of the existing flavour tagging tools, a benchmark model based on a standard multi-class feed-forward classification network is trained on the same tracks used for the baseline GN1 training. The model uses precisely the same concatenated track-and-jet inputs as used by GN1 (see Section 6.4.1),

1876 but processes only a single track at a time, meaning it cannot take into account  
1877 the correlations between tracks when determining the track origin. The model is  
1878 made up of five densely connected linear layers with 200 neurons in each layer. The  
1879 performance of the model was found to be unsensitive to changes in the network  
1880 structure.

1881 To measure the track classification performance, the area under the curve (AUC)  
1882 of the receiver operating characteristic (ROC) curve is computed for each origin  
1883 class, using a one-versus-all classification approach. The AUCs for the different  
1884 truth origins are averaged using both an unweighted and a weighted mean. The  
1885 unweighted mean treats the performance of each class equally, while the weighted  
1886 mean uses as a weight the relative abundance of tracks of each class. Table 6.3  
1887 demonstrates clearly that GN1 outperforms the MLP both at  $20 < p_T < 250 \text{ GeV}$   
1888 for jets in the  $t\bar{t}$  sample and at  $250 < p_T < 5000 \text{ GeV}$  for jets in the  $Z'$  sample. For  
1889 example, GN1 can reject 65% of fake tracks in jets in the  $t\bar{t}$  sample, while retaining  
1890 more than 99% of good tracks (i.e. those tracks which are not fake). The GN1 model  
1891 has two advantages over the MLP which can explain the performance improvement.  
1892 Firstly, the graph neural network architecture enables the sharing of information  
1893 between tracks as discussed in Section 6.4.3. This is likely to be beneficial since the  
1894 origins of different tracks within a jet are correlated. Secondly, the jet classification  
1895 and vertexing objectives may be complementary to the track classification objective,  
1896 and so the track classification performance is improved by the combined training of  
1897 complementary objectives.

1898 Fig. 6.17 shows the track origin classification ROC curves for the different track  
1899 origins for jets in both the  $t\bar{t}$  and  $Z'$  samples. In order to improve visual readability  
1900 of the plot, the curves for the heavy flavour truth origins (FromB, FromBC and  
1901 FromC) have been combined (weighted by their relative abundance), as have the  
1902 Primary and OtherSecondary origins. In jets in both the  $t\bar{t}$  and  $Z'$  samples, the AUC  
1903 of all the different origin groups exceeds 0.9, representing strong overall classification  
1904 performance. In both samples fake tracks are the easiest to classify, followed by  
1905 pileup tracks. The FromC tracks which are  $c$ -hadron decay products, are the hardest  
1906 to classify, possibly due to their similarity to both fragmentation tracks and  $b$ -hadron  
1907 decay tracks, depending on the  $c$ -hadron species in question.

		AUC		Precision		Recall		F1	
		Mean	Weighted	Mean	Weighted	Mean	Weighted	Mean	Weighted
$t\bar{t}$	MLP	0.87	0.89	0.39	0.71	0.51	0.56	0.36	0.62
	GN1	<b>0.92</b>	<b>0.95</b>	<b>0.51</b>	<b>0.82</b>	<b>0.64</b>	<b>0.70</b>	<b>0.51</b>	<b>0.74</b>
$Z'$	MLP	0.90	0.94	0.36	0.84	0.47	0.72	0.31	0.76
	GN1	<b>0.94</b>	<b>0.96</b>	<b>0.48</b>	<b>0.88</b>	<b>0.60</b>	<b>0.79</b>	<b>0.48</b>	<b>0.82</b>

**Table 6.3:** The area under the ROC curves (AUC) for the track classification from GN1, compared to a standard multilayer perceptron (MLP) trained on a per-track basis. The unweighted mean AUC over the origin classes and weighted mean AUC (using as a weight the fraction of tracks from the given origin) is provided. GN1, which uses an architecture that allows track origins to be classified in a conditional manner as discussed in Section 6.4.3, outperforms the MLP model for both  $t\bar{t}$  and  $Z'$  jets.

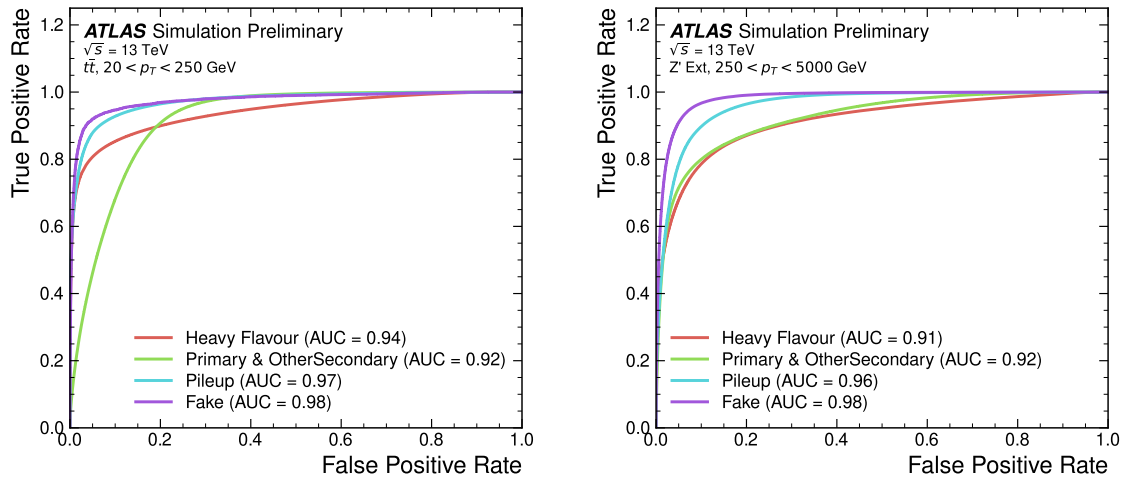


**Figure 6.17:** ROC curves for the different groups of truth origin labels defined in Table 5.1 for jets in the  $t\bar{t}$  sample (left) and jets in the  $Z'$  sample (right). The FromB, FromBC and FromC labels have been combined, weighted by their relative abundance, into the Heavy Flavour category, and the Primary and OtherSecondary labels have similarly been combined into a single category. The mean weighted area under the ROC curves (AUC) is similar for both samples.

### 6.5.8 Looser Track Selection

The track selections used to produce the main results are listed in Table 5.3. This selection includes a cut on the number of shared silicon modules  $N_{\text{shared}}^{\text{Si}}$ . This value is calculated as

$$N_{\text{shared}}^{\text{Si}} = \frac{N_{\text{shared}}^{\text{Pix}} + N_{\text{shared}}^{\text{SCT}}}{2} \quad (6.10)$$

where  $N_{\text{shared}}^{\text{Pix}}$  is the number of shared pixel hits and  $N_{\text{shared}}^{\text{SCT}}$  is the number of shared SCT modules on a track. The nominal cut used elsewhere in this thesis is  $N_{\text{shared}}^{\text{Si}} < 2$ . As the rate of shared hits is significantly higher for  $b$ -hadron decay tracks than for other tracks, this cut rejects a significant proportion of these tracks. Figs. 6.18 and 6.19 show the result of training the GN1 tagger with the full relaxation of this cut, i.e. allowing tracks with any number of shared hits. The shared hit requirements applied by the ambiguity solver as part of track reconstruction (see Section 3.4.1) are still applied. In addition, the maximum allowed value of  $d_0$  is increased from 3.5 mm to 5.5 mm.

## 6.6 Conclusion

In this chapter a novel jet tagger, GN1, is presented. The model has a graph neural network architecture and is trained with auxiliary training objectives, which are shown to improve the performance of the basic model. GN1 significantly improves flavour tagging performance with respect to DL1r, the current default ATLAS flavour tagging algorithm, when compared in simulated collisions. GN1 improves  $c$ - and light-jet rejection for jets in the  $t\bar{t}$  sample with  $20 < p_{\text{T}} < 250$  GeV by factors of  $\sim 2.1$  and  $\sim 1.8$  respectively at a  $b$ -jet tagging efficiency of 70% when compared with DL1r. For jets in the  $Z'$  sample with  $250 < p_{\text{T}} < 5000$  GeV, GN1 improves the  $c$ -rejection by a factor of  $\sim 2.8$  and light-jet rejection by a factor of  $\sim 6$  for a comparative  $b$ -jet efficiency of 30%.

Previous multivariate flavour tagging algorithms relied on inputs from low-level tagging algorithms, whereas GN1 needs no such inputs, making it more flexible. It can be easily fully optimised via a retraining for specific flavour tagging use cases, as demonstrated with  $c$ -tagging and high- $p_{\text{T}}$   $b$ -tagging, without the need for

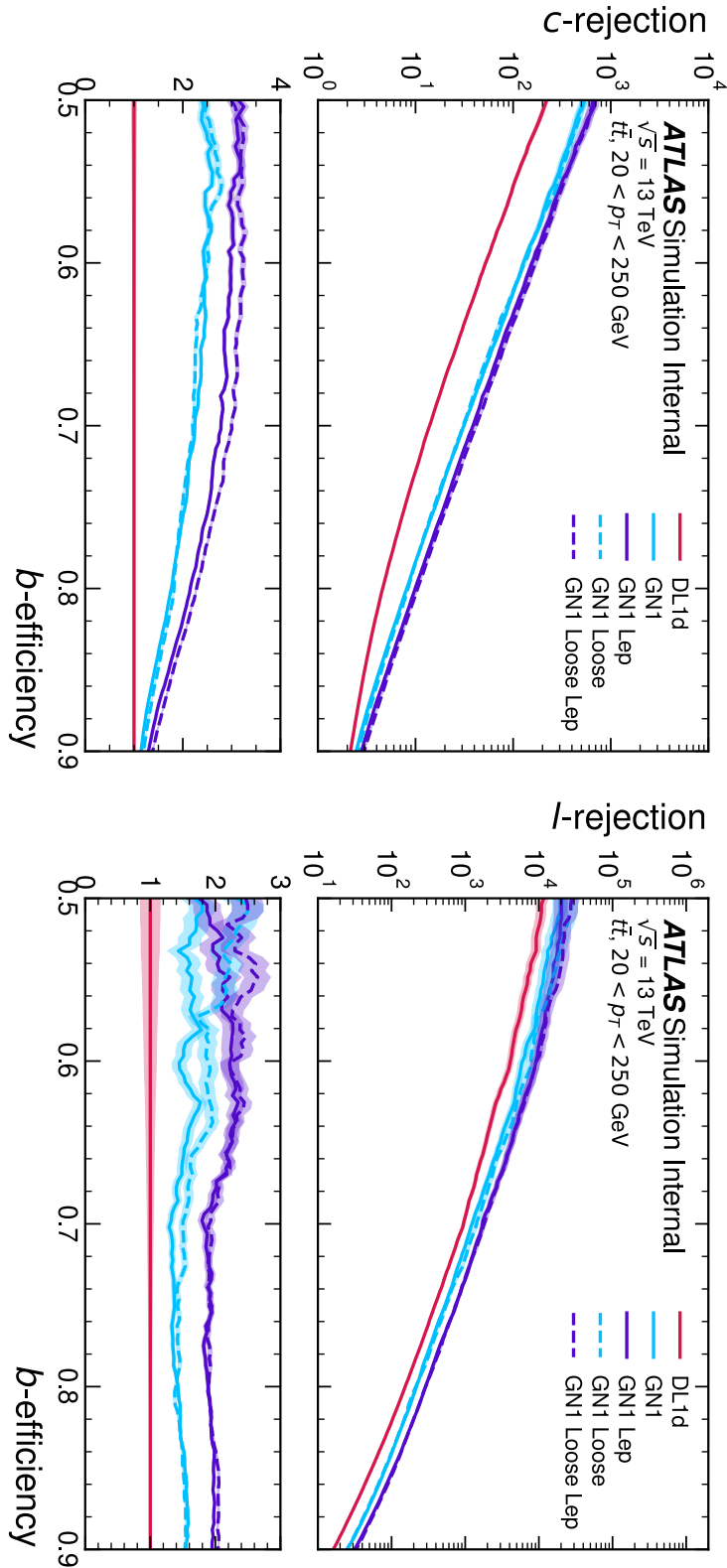


**Figure 6.18:** The  $c$ -jet (left) and light-jet (right) rejections as a function of the  $b$ -jet tagging efficiency for  $t\bar{t}$  jets with  $20 < p_T < 250 \text{ GeV}$ , for the looser track selection trainings of GN1. The ratio to the performance of the DL1d algorithm is shown in the bottom panels. A value of  $f_c = 0.018$  is used in the calculation of  $D_b$  for DL1d and  $f_c = 0.05$  is used for GN1. Binomial error bands are denoted by the shaded regions.

1936 time-consuming retuning of the low-level tagging algorithms. The model is also  
1937 simpler to maintain and study due to the reduction of constituent components.

1938 GN1 demonstrates improved track classification performance when compared with  
1939 a simple per-track MLP and an efficiency of  $\sim 80\%$  for inclusive vertex finding in  
1940  $b$ -jets. The model is also able to perform vertex finding, and preliminary studies  
1941 suggest it outperforms previous manually optimised approaches. The auxiliary track  
1942 classification and vertex finding objectives are shown to significantly contribute to  
1943 the performance in the jet classification objective, and, along with the more advanced  
1944 graph neural network architecture, are directly responsible for the improvement over  
1945 DL1r.

1946 Further improvements in the  $b$ - and  $c$ -tagging performance are likely possible with  
1947 a more thorough optimisation of the model architecture, and the integration of  
1948 additional information from other parts of the ATLAS detector. The addition of  
1949 other auxiliary training objectives, such as the truth  $b$ -hadron decay radius and  
1950 transverse momentum, may also yield additional performance gains.

1951 Additional future work includes the verification of the performance of GN1 on collision  
1952 data, and the full calibration of the model so it can be used by analyses. The flexible  
1953 nature of the model means it can also be readily applied to other related problems  
1954 outside of standard  $b$ - and  $c$ -tagging applications, for example  $X \rightarrow bb$  and  $X \rightarrow cc$   
1955 tagging. The model could also be repurposed as a pileup jet tagger, or general  
1956 primary and secondary vertexing tool.

1957 The model also demonstrates strong performance for the HLLHC ??.

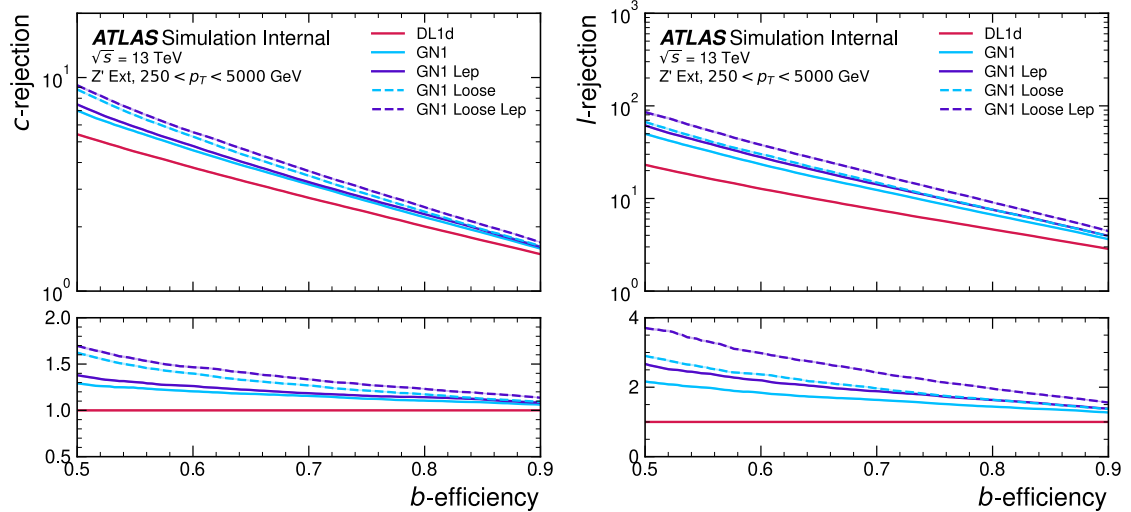


**Figure 6.19:** The *c*-jet (left) and light-jet (right) rejections as a function of the *b*-jet tagging efficiency for  $Z'$  jets with  $250 < p_T < 5000$  GeV, for the looser track selection trainings of GN1. The ratio to the performance of the DL1d algorithm is shown in the bottom panels. A value of  $f_c = 0.018$  is used in the calculation of  $D_b$  for DL1d and  $f_c = 0.05$  is used for GN1. Binomial error bands are denoted by the shaded regions.

<sup>1958</sup> - paper aux mat - paper internal note - bulk it out

<sub>1959</sub> **Chapter 7**

<sub>1960</sub> **Boosted VHbb Analysis**

<sub>1961</sub> The Higgs boson, first observed by ATLAS and CMS at the LHC in 2012 [12, 13],  
<sub>1962</sub> is predicted by the standard model to decay primarily to a pair of  $b$ -quarks, with a  
<sub>1963</sub> branching factor of  $0.582 \pm 0.007$  for  $m_H = 125\text{ GeV}$  [24]. Observation of this decay  
<sub>1964</sub> mode was reported by ATLAS [105] and CMS [26] in 2018, establishing the first  
<sub>1965</sub> direct evidence for the Yukawa coupling of the Higgs boson to down-type quarks  
<sub>1966</sub> (see Section 2.2.2). The  $H \rightarrow b\bar{b}$  process is also important for constraining the total  
<sub>1967</sub> decay width of the Higgs [122].

<sub>1968</sub> Whilst the dominant Higgs production mechanism at the LHC is gluon-gluon fusion  
<sub>1969</sub> as outlined in Section 2.2.3, this mechanism has an overwhelming QCD multijet  
<sub>1970</sub> background and so overall sensitivity to the Higgs is low. The QCD multijet  
<sub>1971</sub> background refers to events containing one or more strongly produced jets which are  
<sub>1972</sub> not the decay product of heavy resonances, for example  $g \rightarrow q\bar{q}$ . The gluon-gluon  
<sub>1973</sub> fusion channel contains to leading order only jets in the final state, and therefore  
<sub>1974</sub> it is extremely difficult to distinguish signal events from the overwhelming multijet  
<sub>1975</sub> background. The  $H \rightarrow b\bar{b}$  observation therefore searched for Higgs bosons produced  
<sub>1976</sub> in association with a vector boson  $V$  (where  $V$  can be a  $W$  or  $Z$  boson) which  
<sub>1977</sub> subsequently decays leptonically. The leptonic final states from the decay of the  
<sub>1978</sub> vector boson allow for leptonic triggering whilst at the same time significantly  
<sub>1979</sub> reducing the multijet background.

<sub>1980</sub> A closely related analysis [123] has more recently measured the associated production  
<sub>1981</sub> of a Higgs boson decaying to  $b$ -quarks in events where the vector and Higgs bosons are  
<sub>1982</sub> highly boosted. The analysis is outlined in Section 7.1. Modelling studies performed  
<sub>1983</sub> by the author are detailed in Section 7.2, and the results of the analysis are presented

1984 in Section 7.4. The author contributed to various signal and background modelling  
1985 studies, fit studies, and to the diboson unblinding effort. This analysis has been  
1986 published in Ref. [123]. Figures and tables from Ref. [123] are reproduced here.

## 1987 7.1 Analysis Overview

1988 The boosted  $VH$ ,  $H \rightarrow b\bar{b}$  analysis is focused on the high transverse momentum  
1989 regime, which has the benefit of being more sensitive to physics beyond the Standard  
1990 Model [124], but the disadvantage of being more challenging due to the increased dif-  
1991 ficulty in the accurate reconstruction of highly energy events (discussed in Chapter 4).  
1992 In order to focus on the high- $p_T$  regime, the reconstructed vector boson is required to  
1993 have  $p_T^V > 250$  GeV (see Section 7.1.2). Events are also split into two  $p_T^V$  bins with the  
1994 first bin covering  $250 \text{ GeV} < p_T^V < 400 \text{ GeV}$  and the second covering  $p_T^V > 400 \text{ GeV}$ ,  
1995 which allows the analysis to account for the improved signal-to-background in the  
1996 high- $p_T$  regime.

1997 The previous ATLAS analysis in Ref. [105] was primarily sensitive to vector bosons  
1998 with a more modest  $p_T^V$  boost in the region of 100–300 GeV. In this regime, the Higgs  
1999 candidate was reconstructed using a pair of jets with radius parameter of  $R = 0.4$ ,  
2000 called small- $R$  jets. However in the high- $p_T$  regime, the decay products of the Higgs  
2001 boson become increasingly collimated and the small- $R$  jets may overlap. In order to  
2002 avoid the associated problems and to aid in the reconstruction of the Higgs boson  
2003 candidate, the present analysis uses instead a large- $R$  jet with radius parameter  
2004  $R = 1.0$  to reconstruct the Higgs boson candidate in all channels (see Section 3.4.3).  
2005 The Higgs candidate is required to have exactly two ghost-associated and  $b$ -tagged  
2006 variable-radius track-jets. The candidate large- $R$  jet is reconstructed using jet  
2007 substructure techniques, for example it is trimmed by removing soft and wide-angle  
2008 components, which helps to remove particles from the underlying event and pileup  
2009 collisions [125]. Refer to Section 3.4.3 for more details on jet reconstruction.

2010 On top of the binning in  $p_T^V$ , selected events are further categorised into 0-, 1- and  
2011 2-lepton channels depending on the number of selected charged leptons (electrons  
2012 and muons) are present in the reconstructed final state (also referred to as 0L, 1L,  
2013 and 2L respectively). The 0-lepton channel targets the  $ZH \rightarrow \nu\nu b\bar{b}$  process, the  
2014 1-lepton channel targets  $WH \rightarrow \ell\nu b\bar{b}$ , and the 2-lepton channel targets  $ZH \rightarrow \ell\ell b\bar{b}$ ,

where  $\ell$  is an electron or muon and  $\nu$  is a neutrino. Each channel has a dedicated set of selections which are listed in more detail in Section 7.1.3. Events in the 0- and 1-lepton channels are further split depending on the number of additional small- $R$  jets not matched to the Higgs-jet candidate. The high-purity signal region (HP SR) has zero such jets, while the low-purity signal region (LP SR) has one or more. The 0- and 1-lepton channels also make use of a dedicated  $t\bar{t}$  control region, described in Section 7.1.4. A complete overview of the different analysis regions is given in Table 7.1.

Channel	Analysis Regions					
	$250 < p_T^V < 400 \text{ GeV}$		$p_T^V \geq 400 \text{ GeV}$			
	0 add. $b$ -track-jets		$\geq 1$ add. $b$ -track-jets	0 add. $b$ -track-jets		$\geq 1$ add. $b$ -track-jets
	0 add. small- $R$ jets	$\geq 1$ add. small- $R$ jets		0 add. small- $R$ jets	$\geq 1$ add. small- $R$ jets	
0-lepton	HP SR	LP SR	CR	HP SR	LP SR	CR
1-lepton	HP SR	LP SR	CR	HP SR	LP SR	CR
2-lepton	SR			SR		

**Table 7.1:** Summary of the definition of the analysis regions. Signal enriched regions are marked with the label SR. There are regions with relatively large signal purity (HP SR) and with low purity (LP SR). Background enriched regions are marked with the label CR. The shorthand ‘‘add’’ stands for additional small- $R$  jets, i.e. number of small- $R$  jets not matched to the Higgs-jet candidate.

### 7.1.1 Data & Simulated Samples

The analysis uses  $pp$  collision data recorded between 2015 and 2018 by the ATLAS detector [31] during Run 2 at the LHC. This dataset corresponds to an integrated luminosity of  $139 \text{ fb}^{-1}$ .

Data from centre-of-mass energy  $\sqrt{s} = 13 \text{ TeV}$  proton-proton collisions at the LHC recorded over the course of Run 2 were used for the analysis. The resulting dataset corresponds to a total integrated luminosity of  $139 \text{ fb}^{-1}$  (see Fig. 3.4).

An overview of the MC simulated samples used in the analysis is given in Table 7.2. These samples are used to model the signal and background processes relevant to the

2032 analysis, with the exception of the multijet background which is modelled using a  
2033 data-driven technique. Data and simulated events are reconstructed using the same  
2034 algorithms, and a reweighting is applied to the simulated events in order to match  
2035 the pile-up distribution observed in the data.

2036 **7.1.2 Object Reconstruction**

2037 The presence of neutrinos in the  $WH \rightarrow \ell\nu b\bar{b}$  and  $ZH \rightarrow \ell\ell b\bar{b}$  signatures can be  
2038 inferred from a momentum imbalance in the transverse plane Section 3.4.5. The  
2039 vector boson transverse momentum  $p_T^V$  is reconstructed as the missing transverse  
2040 energy  $E_T^{\text{miss}}$  in the 0-lepton channel, as the magnitude of the summed  $\mathbf{E}_T^{\text{miss}}$  and  
2041 charged-lepton momentum in the 1-lepton channel, and as the transverse momentum  
2042 of the 2-lepton system in the 2-lepton channel (see Section 3.4.5).

2043 Leptons are used for the channel classification and to select relevant events as outlined  
2044 in Section 7.1.3. Electrons and muons are reconstructed as outlined in Section 3.4.4.  
2045 Electron identification follows the approach outlined in Ref. [105]. In addition to the  
2046 likelihood-based method described in Section 3.4.4, *baseline* electrons are required to  
2047 satisfy  $p_T > 7 \text{ GeV}$ ,  $|\eta| < 2.47$ ,  $s(d_0) < 5$ , and  $|z_0 \sin(\theta)| < 0.5 \text{ mm}$ . *Signal* electron  
2048 additionally are required to satisfy a tighter likelihood identification selection. Muons  
2049 are required to satisfy  $p_T > 7 \text{ GeV}$ ,  $|\eta| < 2.7$ ,  $s(d_0) < 3$ , and  $|z_0 \sin(\theta)| < 0.5 \text{ mm}$ .  
2050 *Baseline* muons are required to pass the ‘loose’ identification described in Ref. [74],  
2051 while *signal* muons are required to pass the ‘medium’ identification working point.  
2052 All signal leptons are required to additionally satisfy a  $p_T > 27 \text{ GeV}$  selection criteria,  
2053 except for muons in the 1-lepton channel where a cut of 25 GeV is used. The number  
2054 of baseline leptons is used to categorise the event into the 0-, 1- or 2-lepton channels.  
2055 The 1- and 2-lepton channels additionally require one signal lepton to be present.

2056 The track-jets matched to the Higgs candidate are  $b$ -tagged using the MV2c10  $b$ -  
2057 tagging algorithm [60, 108, 160]. MV2c10 is a machine learning algorithm using a  
2058 Boosted Decision Tree (BDT) which is tuned to achieve an average  $b$ -jet efficiency of  
2059 70% on simulated  $t\bar{t}$  events. At this efficiency working point, rejection factors for  
2060  $c$ -jets and light-jets are approximately 9 and 304 respectively. The MV2 algorithm  
2061 takes inputs from the outputs of a number of low-level algorithms (IPxD, SV1 and  
2062 JetFitter). The outputs of the low-level algorithms are provided as inputs to the  
2063 boosted decision tree. The efficiency of the tagging algorithm is calibrated to events

Process	ME generator	ME PDF	PS and Hadronisation	UE model tune	Cross-section order
Signal ( $m_H = 125$ GeV and $b\bar{b}$ branching fraction set to 58%)					
$qg \rightarrow W H \rightarrow \ell\nu b\bar{b}$	Powheg-Box v2 [126] + GoSAM [128] + MnLO [129, 130]	NNPDF3.0NLO (*) [94]	Pythia 8.212 [96]	AZNLO	NNLO(QCD) + NLO(EW) [131–137]
$qq \rightarrow ZH \rightarrow \nu\nu b\bar{b}/\ell\ell b\bar{b}$	Powheg-Box v2 + GoSAM + MINLO	NNPDF3.0NLO (*)	Pythia 8.212	AZNLO	NNLO(QCD) (†) + NLO(EW)
$gg \rightarrow ZH \rightarrow \nu\nu b\bar{b}/\ell\ell b\bar{b}$	Powheg-Box v2	NNPDF3.0NLO (*)	Pythia 8.212	AZNLO	NLO + NLL [138–142]
Top quark ( $m_t = 172.5$ GeV)					
$t\bar{t}$	Powheg-Box v2 [126, 143]	NNPDF3.0NLO	Pythia 8.230	A14 [97]	NNLO+NNLL [144]
s-channel	Powheg-Box v2 [126, 145]	NNPDF3.0NLO	Pythia 8.230	A14	NLO [146]
t-channel	Powheg-Box v2 [126, 145]	NNPDF3.0NLO	Pythia 8.230	A14	NLO [147]
$Wt$	Powheg-Box v2 [126, 148]	NNPDF3.0NLO	Pythia 8.230	A14	Approximate NNLO [149]
Vector boson + jets					
$W \rightarrow \ell\nu$	SHERPA 2.2.1 [150–153]	NNPDF3.0NNLO	SHERPA 2.2.1 [154, 155]	Default	NNLO [156]
$Z/\gamma^* \rightarrow \ell\ell$	SHERPA 2.2.1	NNPDF3.0NNLO	SHERPA 2.2.1	Default	NNLO
$Z \rightarrow \nu\nu$	SHERPA 2.2.1	NNPDF3.0NNLO	SHERPA 2.2.1	Default	NNLO
Diboson					
$qq \rightarrow WW$	SHERPA 2.2.1	NNPDF3.0NNLO	SHERPA 2.2.1	Default	NLO
$qq \rightarrow WZ$	SHERPA 2.2.1	NNPDF3.0NNLO	SHERPA 2.2.1	Default	NLO
$qq \rightarrow ZZ$	SHERPA 2.2.1	NNPDF3.0NNLO	SHERPA 2.2.1	Default	NLO
$gg \rightarrow VV$	SHERPA 2.2.2	NNPDF3.0NNLO	SHERPA 2.2.2	Default	NLO

**Table 7.2:** Signal and background processes with the corresponding generators used for the nominal samples. If not specified, the order of the cross-section calculation refers to the expansion in the strong coupling constant ( $\alpha_s$ ). (\*) The events were generated using the first PDF in the NNPDF3.0NLO set and subsequently reweighted to the PDF4LHC15NLO set [157] using the internal algorithm in POWHEG-BOX v2. (†) The NNLO(QCD)+NLO(EW) cross-section calculation for the  $pp \rightarrow ZH$  process already includes the  $gg \rightarrow ZH$  contribution. The  $gg \rightarrow ZH$  process is normalised using the cross-section for the  $pp \rightarrow ZH$  process, after subtracting the  $gg \rightarrow ZH$  contribution. An additional scale factor is applied to the  $gg \rightarrow VH$  processes as a function of the transverse momentum of the vector boson, to account for electroweak (EW) corrections at NLO. This makes use of the  $VH$  differential cross-section computed with HAWK [158, 159].

2064 in data [161–163]. The jet tagging strategy relies on extensive studies into track-jet  
2065  $b$ -tagging in boosted topologies [164, 165].

2066 The jet flavour labelling scheme is described in Section 3.4.3.

### 2067 7.1.3 Selection Criteria

2068 An extensive list of selection cuts are applied to each event in order to reject  
2069 background events whilst retaining as many signal events as possible. A full list of  
2070 selection cuts applied to the different analysis regions is given in Table 7.3, while  
2071 some key selections are listed below.

2072 All channels are require events with at least one large- $R$  jet with  $p_T > 250 \text{ GeV}$   
2073 and  $|\eta| < 2.0$ . The vector boson transverse momentum is also required to satisfy  
2074  $p_T^V > 250 \text{ GeV}$ . The Higgs candidate is chosen as the highest  $p_T$  large- $R$  jet satisfying  
2075 these requirements. As mentioned, the candidate large- $R$  jet is required to have  
2076 two ghost-assciated and  $b$ -tagged variable-radius track-jets. These track-jets are  
2077 required to have at least two constituent tracks with  $p_T > 500 \text{ MeV}$  and  $|\eta| < 2.5$ .  
2078 The track-jets themselves must satisfy  $p_T > 10 \text{ GeV}$  and  $|\eta| < 2.5$ .

2079 In the 0-lepton channel, trigger selections are applied using an  $E_T^{\text{miss}}$  trigger with a  
2080 luminosity-dependent threshold between 70–110 GeV. In the 1-lepton electron sub-  
2081 channel a combination of single electron triggers is used with minimum  $p_T$  thresholds  
2082 between 24–26 GeV. In the muon sub-channel the same  $E_T^{\text{miss}}$  trigger as the 0-lepton  
2083 channel is used. Since muons are not used for the  $E_T^{\text{miss}}$  trigger calculations, this  
2084 is in effect a  $p_T$  requirement on the muon-neutrino system, which in the analysis  
2085 phase space is more efficient than a single-muon trigger. The 2-lepton channel uses  
2086 the same triggering strategy as the 1-lepton channel. In all channels, the trigger  
2087 selections applied are fully efficient for events selected using the full requirements in  
2088 Table 7.3.

2089 The combined selections in Table 7.3 result in a signal efficiency ranging from 6–16%  
2090 for the  $WH$  and  $ZH$  processes depending on the channel and  $p_T^V$  bin.

Selection	0 lepton channel	1 lepton channel	2 leptons channel
Trigger	$E_T^{\text{miss}}$	$e$ sub-channel Single electron	$\mu$ sub-channel $E_T^{\text{miss}}$
Leptons	0 <i>baseline</i> leptons	$p_T > 27 \text{ GeV}$   1 <i>signal</i> lepton no second <i>baseline</i> lepton	2 <i>baseline</i> leptons among which $p_T > 25 \text{ GeV}$ both leptons of the same flavour -   opposite sign muons
$E_T^{\text{miss}}$	$> 250 \text{ GeV}$	$> 50 \text{ GeV}$	-
$p_T^V$			$p_T^V > 250 \text{ GeV}$
Large- $R$ jets		at least one large- $R$ jet, $p_T > 250 \text{ GeV},  \eta  < 2.0$	
Track-jets		at least two track-jets, $p_T > 10 \text{ GeV},  \eta  < 2.5$ , matched to the leading large- $R$ jet	
$b$ -tagged jets		leading two track-jets matched to the leading large- $R$ must be $b$ -tagged (MV2c10, 70%)	
$m_1$			$> 50 \text{ GeV}$
$\min[\Delta\phi(E_T^{\text{miss}}, \text{small-}R \text{ jets})]$	$> 30^\circ$		-
$\Delta\phi(E_T^{\text{miss}}, H_{\text{cand}})$	$> 120^\circ$		-
$\Delta\phi(E_T^{\text{miss}}, E_{T, \text{trk}}^{\text{miss}})$	$< 90^\circ$		-
$\Delta y(V, H_{\text{cand}})$	-		$ \Delta y(V, H_{\text{cand}})  < 1.4$
$m_{\ell\ell}$	-		$66 \text{ GeV} < m_{\ell\ell} < 116 \text{ GeV}$
Lepton $p_T$ imbalance	-		$(p_T^{\ell_1} - p_T^{\ell_2})/p_T^Z < 0.8$

**Table 7.3:** Event selection requirements for the boosted  $VH$ ,  $H \rightarrow b\bar{b}$  analysis channels and sub-channels. Various channel dependent selections are used to maximise the signal efficiency and reduce the number of background events in each analysis region.

### 2091 7.1.4 Control Regions

2092 The  $t\bar{t}$  process presents a major background in the 0- and 1-lepton channels. In these  
 2093 events, the Higgs candidate is often reconstructed from a correctly tagged  $b$ -jet from  
 2094 the top decay  $t \rightarrow Wb$ , and an incorrectly tagged  $c$ - or light-jet from the subsequent  
 2095 decay of the  $W$ , as shown in Fig. 7.1.

not sure  
where the  
0L ttbar  
ETmiss  
comes from

2096 The only known decay mode of the top quark is via the weak force to a  $W$  and  
 2097 a down-type quark. (it is the only quark heavy enough to decay into an on-shell  
 2098  $W$ ). Overwhelmingly (96% of the time) the down-type quark is a  $b$ -quark Hence, the  
 2099 second top quark is also likely to result in a second tagged  $b$ -tagged track-jet outside  
 2100 of the large- $R$  Higgs candidate. To ensure sufficient  $t\bar{t}$  rejections, 0- and 1-lepton  
 2101 channel signal regions are defined using a veto on events with  $b$ -tagged track-jets  
 2102 outside the Higgs-jet candidate. These events are used to construct a control region  
 2103 (CR) which is enriched in  $t\bar{t}$  events. The CR is used to constrain the normalisation  
 2104 of the  $t\bar{t}$  background in the fit.

### 2105 7.1.5 Background Composition

2106 After the selections described in Section 7.1.3 the number of background events  
 2107 mimicking the  $VH$ ,  $H \rightarrow b\bar{b}$  signal is greatly reduced. However, the number of  
 2108 background events still greatly outnumbers that of signal events. The background  
 2109 processes are channel dependent. In the 0-lepton channel the dominant sources of  
 2110 backgrounds are  $Z+jets$  ( $Z \rightarrow \nu\nu$ ) and  $t\bar{t}$ , with  $W+jets$  and diboson events being  
 2111 subdominant. In the event of  $W \rightarrow \tau\nu$ , and subsequent hadronic decay of the  $\tau$  or  
 2112 lack of successful reconstruction/selection of the leptonic decay products,  $W+jets$   
 2113 can also contribute to the 0-lepton channel.  $t\bar{t}$  and  $W+jets$  (with a leptonic decay  
 2114 of the  $W$  as in  $W \rightarrow \ell\nu$ ) are dominant in the 1-lepton channel, while single-top is  
 2115 subdominant. In the 2-lepton channel,  $Z+jets$  ( $Z \rightarrow \ell\ell$ ) is again dominant followed  
 2116 by  $Z Z$  diboson events.

2117 The diboson background  $VV$  consists primarily of  $W Z$  and  $Z Z$  events in which the  
 2118  $Z$  decays to a pair of  $b$ -quarks. This process very closely matches the signal, with  
 2119 a resonant peak occurring at  $m_Z = 91$  GeV and so is considered as an irreducible  
 2120 background ( $V+b$ -jets is also irreducible).

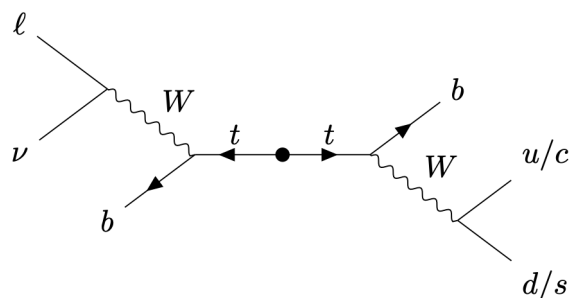
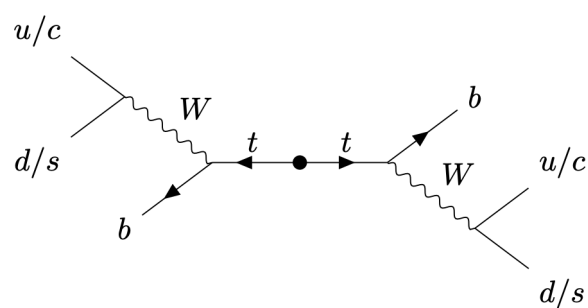
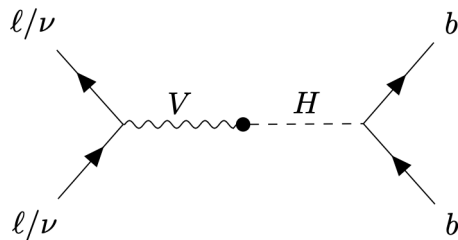


**Figure 7.1:** Diagrams of the signal process (top) and the 0-lepton and 1-lepton  $t\bar{t}$  backgrounds (middle, bottom). Objects to the right of centre are reconstructed within the large- $R$  jet. For the backgrounds, the large- $R$  jet contains a mis-tagged  $c$ - or light-jet.

2121 The  $t\bar{t}V$ ,  $t\bar{t}H$  and multijet backgrounds are negligible in the analysis phase space  
2122 after the selections have been applied, with the exception of the 1-lepton electron  
2123 sub-channel, in which multijet background is not ignored. The multijet background  
2124 is made up of jets with semileptonic heavy-flavour-hadron decays (e.g.  $b \rightarrow c\ell\nu$ ) and  
2125 jets which are mis-tagged by the flavour tagging algorithm MV2c10.

2126 The contributions from the different backgrounds are modelled using Monte Carlo  
2127 event generators and the impacts on the analysis are studied in Section 7.2. The  
2128 multijet background is not modelled but instead estimated using a data-driven  
2129 technique.

## 2130 7.2 Systematic Uncertainties & Background 2131 Modelling

2132 Systemic uncertainties are extensively employed to give the fit model described in  
2133 Section 7.3 enough flexibility to account for inaccuracies in the various inputs to the fit.  
2134 Two main types of systematic uncertainty are considered: experimental and modelling.  
2135 Experimental uncertainties arise due to the limited due to limited detector precision,  
2136 imperfect reconstruction algorithms (in particular the  $b$ -tagging algorithms), and  
2137 due to the imperfect measurement of pile-up and integrated luminosity. Modelling  
2138 is the simulation processes relevant to the analysis using Monte-Carlo (MC) event  
2139 generators, and is used to predict the outcome of the analysis. Modelling uncertainties  
2140 arise due to the imperfections in the simulation of signal and background events, for  
2141 example differences between event generators, or use of different model parameters  
2142 when producing simulated events. In order to observe a certain process, for example  
2143  $VH$ ,  $H \rightarrow b\bar{b}$ , an increase in the number of observed events with respect to the  
2144 background-only hypothesis is looked for. The excess is often relatively small against  
2145 the total number of background events, and hence accurate modelling of the expected  
2146 number of background and signal events is crucial for successfully performing the  
2147 analysis. Particular care is paid to the uncertainties on the modelling predictions as  
2148 discussed in this section.

2149 Modelling uncertainties are described in detail in the following sections. Modelling  
2150 uncertainties: *Nominal* samples are used as a reference to which different vari-

2151    ations can be compared. The nominal samples are chosen as the best possible  
2152    representation of the underlying physical process. *Alternative* samples are used to  
2153    understand inaccuracies that may be present in the nominal samples. Some aspect  
2154    of the nominal model is varied, and the discrepancy with respect to the nominal  
2155    model is quantified. The discrepancy is used to systematic uncertainty associated  
2156    with the model parameter which was changed.

2157    Modelling studies involving  $c$ - and light-jets is hampered by the low available statistics  
2158    of jets pass the analysis selections, due to the high rejection rates of the  $b$ -tagging  
2159    algorithm MV2c10. For modelling studies therefore, truth tagging (TT) is employed  
2160    to ensure sufficient numbers of jets are available to calculate uncertainties. TT works  
2161    by computing a 2-dimensional efficiency map using the jet  $p_T$  and jet  $\eta$ . The two  
2162    leading track-jets associated to the large- $R$  jet automatically passes the  $b$ -tagging  
2163    requirement, and are weighted based on their  $p_T$  and  $\eta$  using the pre-calculated  
2164    efficiency map.

### 2165    7.2.1 Sources of Systematic Uncertainties

2166    This section briefly describes the different sources of uncertainty in the predictive  
2167    model used in the analysis, and how each source of uncertainty is implemented within  
2168    the analysis framework. Considered sources of systematic uncertainty are listed in  
2169    Table 7.4. For each source of uncertainty, acceptance and shape uncertainties are  
2170    derived.

#### 2171    QCD Scales

2172    The  $V+jets$  matrix element calculations contains infrared and ultraviolet divergences.  
2173    These are handled by introducing spurious parameters corresponding to the renormalisation scale ( $\mu_R$ ) and factorisation scale ( $\mu_F$ ). Physical observables are not  
2174    dependent on these parameters when using the infinite perturbation series expansion,  
2175    however at some fixed order in QCD a limited dependence is present. To assess the  
2176    impact of this, both  $\mu_R$  and  $\mu_F$  are independently varied from their nominal values  
2177    by factors of 0.5 and 2 to account for higher order corrections to the calculation of  
2178    the matrix element used to simulate the process.

**2180 PDF Sets**

2181 Parton distribution functions (PDFs) specify the probability of finding a parton  
2182 with a given momentum inside a hadron (in this case, inside colliding protons).  
2183 PDFs have to be derived from data and are a significant source of uncertainty in  
2184 analyses of hadronic collision data. There are three sources of PDF uncertainties:  
2185 the statistical and systematic errors on the underlying data used to derive the PDFs,  
2186 the theory which is used to describe them (which is based on some fixed order  
2187 perturbative QCD expansion), and finally the procedure which is used to extract the  
2188 PDFs from the data. PDF-related uncertainties were derived following Ref. [157].  
2189 This involves considering 100 PDF replicas which, when combined, form a central  
2190 value and associated uncertainty, and also in parallel direct changes to the central  
2191 values of PDFs using the MMHT2014 [166] and CT14NLO [167] PDF sets.

**2192 Event Generator**

2193 The choice of parton shower (PS) and underlying event (UE) generators can affect  
2194 the analysis outcome. Changing these models modifies several aspects of the event  
2195 generation at the same time, such as the accuracy of matrix element predictions and  
2196 different approaches to parton showering. This change tends to lead to the largest  
2197 discrepancy with respect to the nominal samples.

**2198 Resummation and Merging Scales**

2199 Resummation is a technique used in QCD to help cope with calculations involving  
2200 disparate energy scales, and involves the introduction of an associated resummation  
2201 scale, the choice of which introduces some systematic uncertainty into the model.  
2202 Parton showering models are accurate when simulating low- $p_T$  radiation, however  
2203 inaccuracies start to arrive when simulating hard emissions. To combat this, par-  
2204 ton showering models utilise more precise matrix element calculations above some  
2205 momentum threshold. The choice of threshold, or *merging scale* introduces some  
2206 uncertainty into the final result. Resummation (QSF) and merging (CKKW) scale  
2207 variations are available for a subset of the SHERPA samples. The number of available  
2208 events is significantly lower than the number of events in the nominal sample, and no

- 2209 statistically significant discrepancy with respect to the nominal samples is observed.  
2210 The corresponding uncertainties and therefore neglected.

### 2211 7.2.2 Implementation of Variations

- 2212 Modelling variations are implemented in different ways, depending on the associated  
2213 uncertainty. Table 7.4 lists the different sources of uncertainty described in Section 7.2.1  
and for each lists the implementation. As production of high-stastic MC samples

Source of Uncertainty	Implementation
Renormalisation scale ( $\mu_R$ )	Internal weights
Factorisation scale ( $\mu_F$ )	Internal weights
PDF set	Internal weights
Parton Shower (PS) models	Alternative samples
Underlying Event (UE) models	Alternative samples
Resummation scale (QSF)	Parameterisation
Merging scale (CKKW)	Parameterisation

**Table 7.4:** Different sources of uncertainty (i.e. variations in the model) considered for the  $V+jets$  background, and the corresponding implementation. For each uncertainty, acceptance and shape uncertainties are derived.

- 2214
- 2215 is computationally expensive, a technique in state of the art simulation packages  
2216 is to store some sources of variation as internal weights, which can be generated  
2217 alongside the nominal samples, saving computation time. The nominal sample then  
2218 effectively contains information about an ensemble of different samples, corresponding  
2219 to different model parameters, which are accessible via reweightings. When filling  
2220 histograms for the variations, bins are incremented by the internal weight of the  
2221 event associated with the variation in question.

- 2222 While the inclusion of internal weight variation in MC event generators has decreased  
2223 simulation times and increased available statistics, there are in SHERPA 2.2.1 currently  
2224 some sources of systematic uncertainty that are unable to be stored as internal weight  
2225 variations due to technical limitations. Two examples are the choice of resummation  
2226 and merging scales. A method to parameterise the systematic variation using  
2227 one sample, and to then apply this parameterisation to another sample, has been

2228 developed by ATLAS [168]. This method was used to derive resummation and  
2229 merging uncertainties for the nominal SHERPA 2.2.1 sample, using a previous (lower  
2230 statistic) SHERPA 2.1 alternative sample. The resulting uncertainties were studied  
2231 and found to be negligible in comparison with systematics from other sources.

2232 **7.2.3 Vector Boson + Jets Modelling**

2233 After event selection, the  $V+jets$  background is a dominant background in all three  
2234 analysis channels as described in Section 7.1.5. The  $V+jets$  samples are split into  
2235 categories depending on the truth flavour of the track-jets which are ghost-associated  
2236 to the large- $R$  jet Higgs candidate. The categories are  $V+bb$ ,  $V+bc$ ,  $V+bl$ ,  $V+cc$ ,  
2237  $V+cl$ ,  $V+ll$ , and  $V+hf$  refers collectively to the categories containing at least one  
2238  $b$ - or  $c$ -jet.  $V+bb$  is dominant generally accounting for 80% of the jets, while  $V+hf$   
2239 accounts for around 90% of jets. The full flavour composition breakdown for each  
2240 channel and analysis region are given in Tables 7.5, 7.7 and 7.8.

2241 In order to access uncertainties associated with the use of MC generators, varia-  
2242 tions of the data are produced using alternative generators or variation of nominal  
2243 generator parameters as described in Section 7.2.2. As described in Section 7.1.1,  
2244 the nominal MC event generator used for  $V+jets$  events is SHERPA 2.2.1, while  
2245 MADGRAPH5\_AMC@NLO+PYTHIA8 (which uses a different parton showering  
2246 model) is used as an alternative generator.

2247 Modelling systematics can have several impacts, including affecting the overall  
2248 normalisation for different processes, and the relative acceptances between different  
2249 analysis regions (i.e. migrations between HP and LP SRs, between the SR and CR,  
2250 and between  $p_T^V$  bins), and the shapes of the  $m_J$  distributions. Since the fit model  
2251 fits only the large- $R$  jet mass  $m_J$  to data, all shape uncertainties are estimated with  
2252 respect to this observable. Several sources of uncertainty, summarised in Section 7.2.1,  
2253 have been assessed.

Sample	$Mp_T^V$ HP SR	$Hp_T^V$ HP SR	$Mp_T^V$ LP SR	$Hp_T^V$ LP SR	$Mp_T^V$ CR	$Hp_T^V$ CR
<b>Wbb</b>	$79.3\% \pm 4.4\%$	$75.0\% \pm 8.6\%$	$77.4\% \pm 2.5\%$	$71.7\% \pm 4.5\%$	$68.0\% \pm 7.6\%$	$63.5\% \pm 14.0\%$
<b>Wbc</b>	$6.6\% \pm 0.9\%$	$3.4\% \pm 1.7\%$	$6.2\% \pm 0.5\%$	$5.3\% \pm 0.9\%$	$14.5\% \pm 3.2\%$	$3.4\% \pm 3.2\%$
<b>Wbl</b>	$3.9\% \pm 0.9\%$	$11.4\% \pm 3.5\%$	$4.5\% \pm 0.5\%$	$8.7\% \pm 1.4\%$	$9.8\% \pm 2.2\%$	$9.1\% \pm 3.8\%$
<b>Wcc</b>	$5.1\% \pm 1.7\%$	$6.8\% \pm 2.4\%$	$7.1\% \pm 1.0\%$	$6.3\% \pm 1.4\%$	$4.2\% \pm 2.4\%$	$12.3\% \pm 7.0\%$
<b>Wcl</b>	$2.3\% \pm 1.4\%$	$2.4\% \pm 2.1\%$	$3.4\% \pm 0.7\%$	$5.2\% \pm 1.5\%$	$2.6\% \pm 1.5\%$	$3.4\% \pm 2.1\%$
<b>Wl</b>	$2.9\% \pm 1.0\%$	$0.9\% \pm 1.6\%$	$1.3\% \pm 0.7\%$	$2.8\% \pm 0.7\%$	$0.9\% \pm 0.6\%$	$8.4\% \pm 5.1\%$
Events	<b><math>187.5 \pm 7.7</math></b>	<b><math>38.2 \pm 3.1</math></b>	<b><math>429.5 \pm 10.0</math></b>	<b><math>97.8 \pm 4.2</math></b>	<b><math>33.8 \pm 2.5</math></b>	<b><math>8.3 \pm 1.2</math></b>

**Table 7.5:** 0-lepton  $W+jets$  nominal sample flavour composition and total event yield.

Sample	$Mp_T^V$ HP SR	$Hp_T^V$ HP SR	$Mp_T^V$ LP SR	$Hp_T^V$ LP SR	$Mp_T^V$ CR	$Hp_T^V$ CR
<b>Wbb</b>	$77.2\% \pm 2.6\%$	$72.4\% \pm 4.3\%$	$77.8\% \pm 1.8\%$	$69.3\% \pm 2.5\%$	$64.6\% \pm 4.9\%$	$53.5\% \pm 6.3\%$
<b>Wbc</b>	$7.4\% \pm 0.7\%$	$7.3\% \pm 1.1\%$	$6.6\% \pm 0.4\%$	$6.3\% \pm 0.6\%$	$13.7\% \pm 1.9\%$	$16.4\% \pm 3.7\%$
<b>Wbl</b>	$4.0\% \pm 0.5\%$	$6.7\% \pm 1.1\%$	$5.1\% \pm 0.3\%$	$8.7\% \pm 0.8\%$	$10.3\% \pm 1.7\%$	$14.6\% \pm 3.0\%$
<b>Wcc</b>	$6.2\% \pm 1.1\%$	$5.5\% \pm 1.7\%$	$6.6\% \pm 0.6\%$	$6.4\% \pm 0.7\%$	$4.5\% \pm 1.7\%$	$9.5\% \pm 3.0\%$
<b>Wcl</b>	$3.6\% \pm 0.8\%$	$4.2\% \pm 1.8\%$	$2.8\% \pm 0.5\%$	$6.2\% \pm 0.8\%$	$4.6\% \pm 1.2\%$	$4.4\% \pm 1.5\%$
<b>Wl</b>	$1.5\% \pm 0.5\%$	$3.9\% \pm 1.3\%$	$1.1\% \pm 0.2\%$	$3.1\% \pm 0.5\%$	$2.3\% \pm 1.2\%$	$1.6\% \pm 0.6\%$
Events	<b><math>477.1 \pm 11.7</math></b>	<b><math>147.5 \pm 6.4</math></b>	<b><math>784.7 \pm 12.3</math></b>	<b><math>301.8 \pm 7.2</math></b>	<b><math>68.7 \pm 3.5</math></b>	<b><math>26.9 \pm 2.0</math></b>

**Table 7.6:** 1-lepton  $W+jets$  nominal sample flavour composition and total event yield.

Channel	$Mp_T^V$ HP SR	$Hp_T^V$ HP SR	$Mp_T^V$ LP SR	$Hp_T^V$ LP SR	$Mp_T^V$ CR	$Hp_T^V$ CR
<b>Zbb</b>	84.56%	81.84%	82.37%	76.06%	66.12%	63.18%
<b>Zbc</b>	6.03%	6.98%	5.80%	7.46%	15.04%	14.30%
<b>Zbl</b>	4.06%	6.55%	3.83%	6.59%	12.66%	12.81%
<b>Zcc</b>	3.68%	3.40%	5.82%	3.75%	3.36%	3.38%
<b>Zcl</b>	1.23%	0.44%	1.47%	3.97%	1.82%	4.95%
<b>Zl</b>	0.44%	0.78%	0.70%	2.16%	1.00%	1.38%
Events	$259.91 \pm 4.86$	$66.12 \pm 2.04$	$420.45 \pm 5.73$	$141.97 \pm 2.50$	$43.49 \pm 1.73$	$16.07 \pm 0.83$

**Table 7.7:** 0-lepton  $Z+jets$  nominal sample flavour composition and total event yield.

Channel	$Mp_T^V$	$Hp_T^V$	$p_T^V$ inclusive
<b>Zbb</b>	80.80%	76.95%	79.76%
<b>Zbc</b>	8.10%	6.26%	7.60%
<b>Zbl</b>	4.95%	7.06%	5.52%
<b>Zcc</b>	3.97%	4.46%	4.10%
<b>Zcl</b>	1.61%	3.60%	2.14%
<b>Zll</b>	0.57%	1.68%	0.87%
Events	$115.49 \pm 2.42$	$42.42 \pm 1.27$	$157.92 \pm 2.73$

**Table 7.8:** 2-lepton  $Z+jets$  nominal sample flavour composition and total event yield.

---

2254    **Acceptance Uncertainties**

2255    Several different types of acceptance uncertainties have been calculated and imple-  
 2256    mented as nuisance parameters in the fit. These account for uncertainty in the overall  
 2257    number of events in each channel, and for the migration of events between different  
 2258    analysis regions. The acceptance uncertainties relevant to the  $V+jets$  processes are  
 2259    summarised below.

- 2260    • **Overall normalisation:** only relevant where normalisation cannot be left  
       floating (determined as part of the fit). The  $V+hf$  component is left floating in  
       the fit. For other components, independent normalisations used for  $W+hf$  and  
        $Z+hf$ . The contributions are mainly determined by the 1-lepton (for  $W+hf$ )  
       and 2-lepton (for  $Z+hf$ ) SRs respectively and then extrapolated to 0-lepton  
       channel.
- 2266    • **SR-to-CR relative acceptance:** the uncertainty on the normalisation of the  
       signal region due to events migrating between the signal and control regions.
- 2268    • **HP-to-LP relative acceptance:** the uncertainty on the normalisation of the  
       high-purity (HP) signal region due to events migrating between the high- and  
       low-purity signal regions.
- 2271    • **Medium-to-high  $p_T^V$  relative acceptance:** describes any shape effect in  $p_T^V$   
       distribution, given that the analysis only uses two  $p_T^V$  bins (medium and high).
- 2273    • **Flavour relative acceptance:** for each flavour  $V+xx$ , where  $xx \in \{bc, bl, cc\}$   
       the ratio of  $V+xx/V+bb$  events is calculated. This corresponds to the uncer-  
       tainty of  $Vbb$  events due to the miss-tagging of other flavours  $Vxx$ .
- 2276    • **Channel relative acceptance:** corresponding to the uncertainty in the nor-  
       malisation of  $V+jets$  events events due to the migration of events between  
       channels.

2279    The uncertainties arising from the different sources described in Section 7.2.1 are  
 2280    summed in quadrature to give a total uncertainty on each region. A summary of the  
 2281    different acceptance uncertainties that were derived in this way and subsequently  
 2282    applied in the fit are given in Table 7.9. An effort has been made, wherever possible,  
 2283    to harmonise similar uncertainties across different analysis regions and channels.

V+jets Acceptance Uncertainties				
Boson	W		Z	
Channel	0L	1L	0L	2L
Vbb Norm.	30%	-	-	-
SR/CR	90% <sup>†</sup>	40% <sup>†</sup>	40%	-
HP/LP	18%		18%	-
High/Medium $p_T^V$	30%	10%*	10%	
Channel Extrap.	20%	-	16%	-
Vbc/Vbb	30%			
Vbl/Vbb	30%			
Vcc/Vbb	20%			
Vcl Norm.	30%			
VL Norm.	30%			

**Table 7.9:** V+jets acceptance uncertainties. W+jets SR and CR uncertainties marked with a superscript † are correlated. The 1L W+jets H/M uncertainty marked by \* is applied as independent and uncorrelated NPs in both HP and LP signal regions. The 0L W+jets Wbb Norm uncertainty is only applied when a floating normalisation for Wbb cannot be obtained from the 1L channel. A 30% uncertainty for  $Z \rightarrow b\bar{b}$  norm is applied in the 1L channel when a floating normalisation for  $Z \rightarrow b\bar{b}$  cannot be obtained from the 0L or 2L channels.

---

## 2284 Shape Uncertainties

2285 In order to derive shape uncertainties (which as the name suggests affect shapes but  
 2286 not overall normalisations of distributions), the following procedure is carried out.  
 2287 Normalised distributions of the reconstructed large- $R$  Higgs candidate jet mass  $m_J$   
 2288 are compared for the nominal sample and variations. For each variation, the ratio of  
 2289 the variation to nominal is calculated, the up and down variations are symmetrised,  
 2290 and an analytic function is fit to the symmetrised ratio. If different analysis regions  
 2291 or channels show the same pattern of variation, a common uncertainty is assigned.  
 2292 An example of a significant source of uncertainty, arising from choice of factorisation  
 2293 scale  $\mu_R$  is shown in Fig. 7.2. HP SRs split into medium and high  $p_T^V$  bins are shown  
 2294 for the 0-lepton channel for  $W+\text{hf}$  and  $Z+\text{hf}$  jets. The 0- and 1-lepton channels for  
 2295 the  $W+\text{hf}$  contribution and the 0- and 2-lepton channels for the  $Z+\text{jets}$  contribution  
 2296 are merged, since the shapes in  $m_J$  are consistent across channels. An exponential  
 2297 function  $e^{p_0 + p_1 x} + p_2$  has been fitted to the ratio of the normalised distributions.  
 2298 The magnitude of the variation does show  $p_T^V$  dependence, and so two separate  
 2299 uncertainties are added in the fit, and applied individually in each  $p_T^V$  region.  
 2300 The shape uncertainties for  $\mu_R$  were derived on the SRs but are also applied to the  
 2301 CRs, as the low statistics in the CRs make it difficult to derive dedicated shape  
 2302 uncertainties. All the shape uncertainties are fully correlated accross regions.  
 2303 A comparison of the  $m_J$  shapes between SHERPA and MADGRAPH is shown in  
 2304 Fig. 7.3. The plots are split by process and channel, but merged in SR purity and  $p_T^V$   
 2305 bins reflecting similarities between the  $m_J$  shapes across these regions. Due to the low  
 2306 statistics available for the alternate MADGRAPH sample, and the lack of statistically  
 2307 significant variation between the samples, no associated shape uncertainty is added  
 2308 to the fit in this case.  
 2309 The impacts of variations in the factorisation scale  $\mu_F$  and the choice of PDF set on  
 2310  $m_J$  shape were also found to be negligible in comparison with  $\mu_R$  and are hence not  
 2311 associated uncertainty was added to the fit.

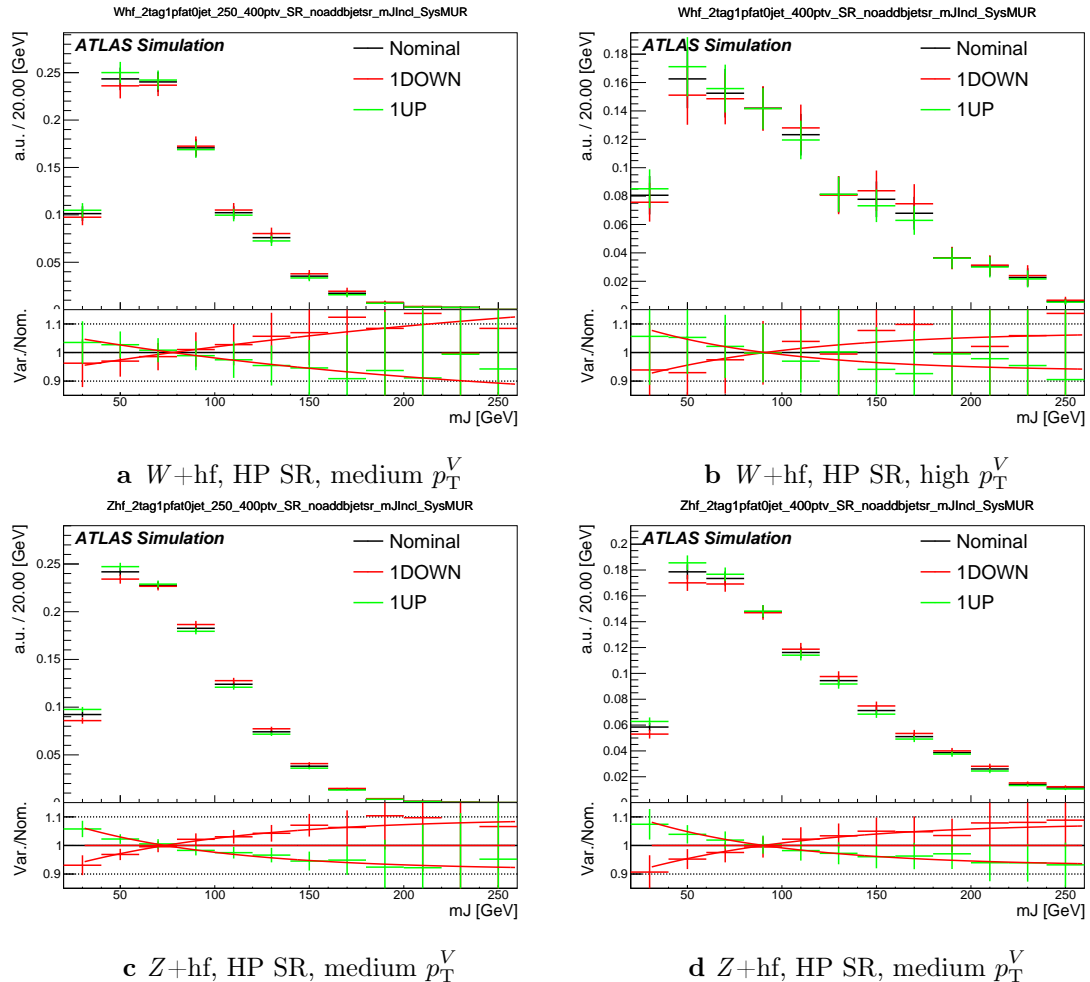


**Figure 7.2:** Normalised leading large- $R$  jet mass distribution from  $Z$  and  $W + hf$  processes in the HP SR of the 0-lepton channel. The renormalisation scale  $\mu_r$  has been varied by a factor of 2 (1up) and 0.5 (1down). An exponential function is fitted to the ratio between the nominal and variation samples.

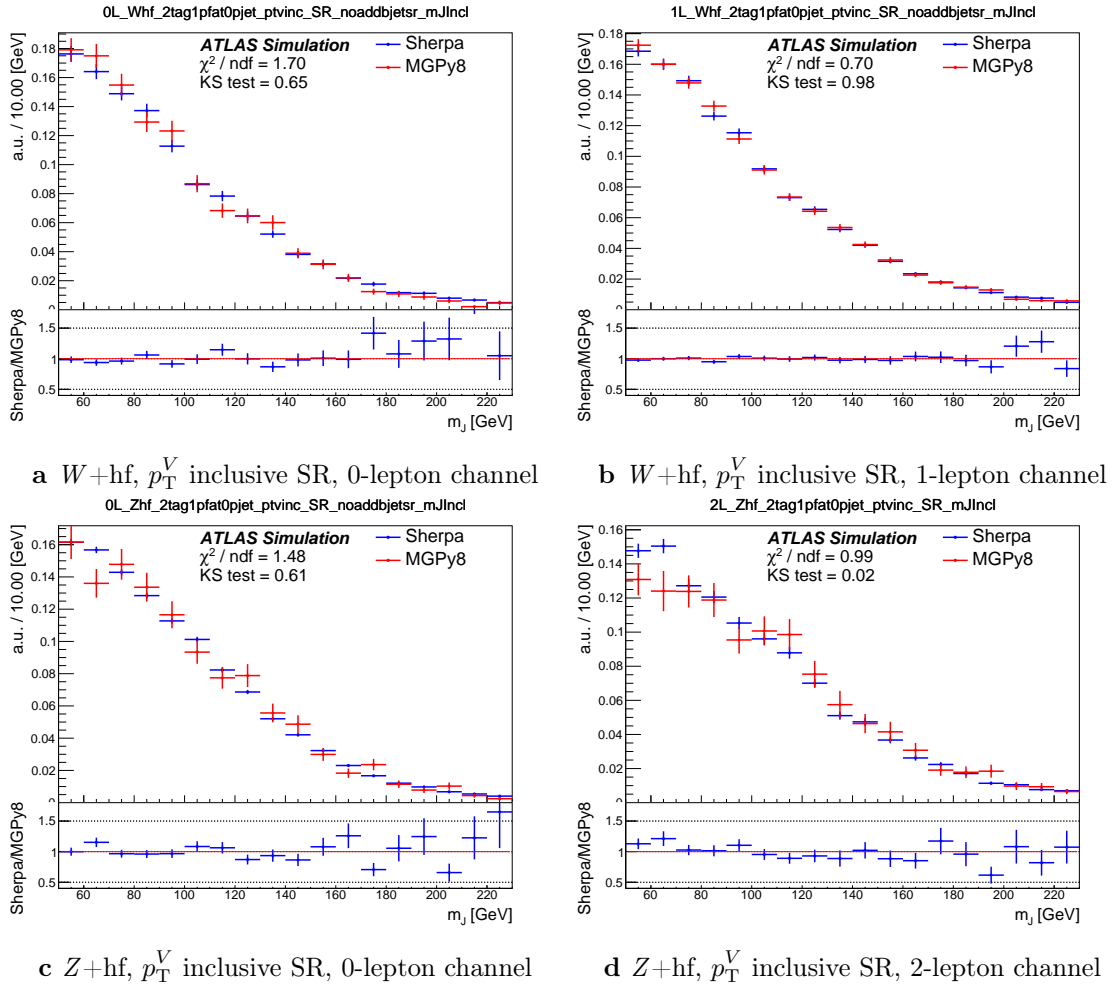


**Figure 7.3:** The comparison on  $m_J$  shapes between SHERPA and MADGRAPH samples from  $V+hf$  process in  $p_T^V$  inclusive signal regions. The Kolmogorov-Smirnov test and  $\chi^2/ndf$  are shown on the plots.

### **2312 7.2.4 Diboson Modelling**

**2313** The uncertainties for the diboson background generally follows that of  $V+jets$ . How-  
**2314** ever an alternative sample was generated using POWHEG interfaced with PYTHIA8,  
**2315** using the AZNLO shower tune with the CTEQ6L1 PDFs [169]. Unlike SHERPA,  
**2316** POWHEG models the off-shell  $Z$  contribution at NLO.

**2317** Acceptance and shape uncertainties are derived in an analogous fashion to  $V+jets$ .

### **2318 Acceptance Uncertainties**

**2319** Diboson acceptance uncertainties are summarised in Table 7.10. Variations from  $\mu_R$ ,  
**2320**  $\mu_F$ , PDF choice and alternative generator are considered and are combined combined  
**2321** through a sum in quadrature as described in Section 7.2.3. The largest modification  
**2322** to the nominal acceptance results from the POWHEG+PYTHIA8 alternate sample,  
**2323** which modifies several parts of the generative model at the same time. Since the  
**2324** diboson contribution to the  $t\bar{t}$  control region is small, no SR-to-CR relative acceptance  
**2325** uncertainty is required.

**2326** For the  $WZ$  contribution, uncertainties are derived using the 1-lepton channel and  
**2327** applied to all three channels. An additional 8% channel migration uncertainty  
**2328** is applied on the 0-lepton channel. For the  $ZZ$  contribution, the normalisation  
**2329** uncertainty is calculated using the 2-lepton channel and applied to all three channels.  
**2330** The 0- and 1-lepton channels have a similar HP-to-LP relative acceptance uncertainty  
**2331** of 18%. The 1-lepton medium-to-high  $p_T^V$  relative acceptance is based off the value  
**2332** obtained from the 2-lepton channel. 30% and 18% channel migration uncertainties  
**2333** are applied in the 0- and 1-lepton channels respectively.

**2334** Since the contribution from  $WW$  is small, dedicated studies are not performed, but  
**2335** a 25% normalisation uncertainty is applied in all the three channels which is based  
**2336** on the modelling studies performed for the previous analysis [105].

### **2337 Shape Uncertainties**

**2338** Diboson shape uncertainties are derived in a similar fashion to  $V+jets$ . Only the  
**2339** uncertainties associated with systematic variation of  $\mu_R$  and the event generator

Diboson Acceptance Uncertainties						
Bosons	WZ			ZZ		
Channel	0L	1L	2L	0L	1L	2L
Normalisation	16%			10%		
HP/LP	18%			18%		
High/Medium	10%			6%	18%	
Channel Extrap.	8%	-	-	30%	18%	-

**Table 7.10:** Diboson acceptance uncertainties. All uncertainties except channel extrapolation uncertainties are fully correlated between  $ZZ$  and  $WZ$  processes and channels.

have a non-negligible impact on the  $m_J$  shape. Variation of  $\mu_R$  produces consistent  $m_J$  shape impacts across all regions and channels, and hence only a single associated uncertainty is derived, shown in Fig. 7.4. A hyperbolic tangent is fitted to the symmetrised ratio.

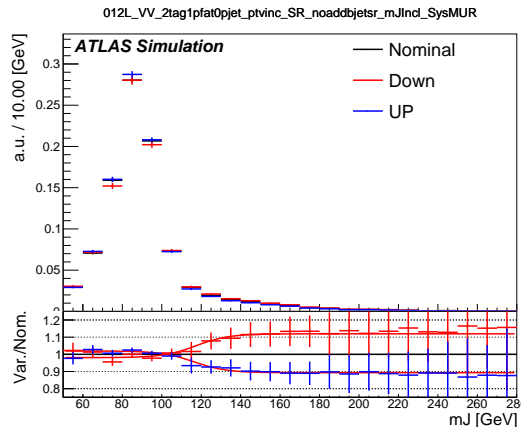


**Figure 7.4:** Normalised leading large- $R$  jet mass distribution from  $WZ$  and  $ZZ$  process, merged among all the signal regions and lepton channels. The renormalisation scale  $\mu_R$  has been varied by a factor of 2 (1up) and 0.5 (1down). The red line shape shows the fitting results of the hyperbolic tangent function.

The comparison between the nominal SHERPA and alternative POWHEG+PYTHIA samples is shown in Fig. 7.5 for the 0- and 1-lepton channels for both  $WZ$  and  $ZZ$  processes. For these channels, the shape of  $m_J$  varies in opposite directions in the LP and HP signal regions. Shapes are similar between  $p_T^V$  bins, the 0- and 1-lepton channels and for  $WZ$  and  $ZZ$ . A third order polynomial is fitted to the ratio, and this function transitions to a constant piecewise function in the high

mass region to accurately represent the shape taking into account large statistical uncertainties. Dependence on event generator was found to be negligible within statistical uncertainty in the 2-lepton channel. All diboson shape uncertainties are fully correlated in the fit.

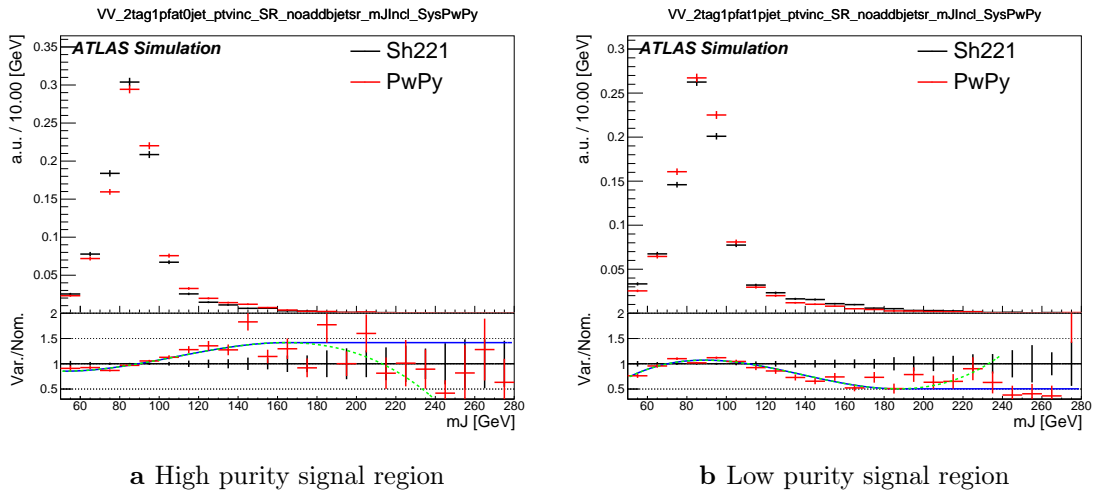


**Figure 7.5:** The comparison on  $m_J$  shapes between SHERPA and POWHEG+PYTHIA 8 samples from  $WZ$  and  $ZZ$  process in high and low purity signal regions.  $p_T^V$  regions and 0- and 1-lepton channels are merged. The dashed green line shows the fitted third order polynomial function and the blue lines show the function after a protection is added in the high mass region.

### 2354 7.3 Statistical Treatment

Selected events are used to perform a statistical test of the background-only hypothesis, i.e. a model which does not include the  $VH$ ,  $H \rightarrow b\bar{b}$  process. The test involves a binned global maximum-profile-likelihood fit from the model to the data using the  $m_J$  distribution, and combines all the analysis regions defined in Table 7.1. The test is based on the profile likelihood ratio test statistic. The signal strength  $\mu = \sigma/\sigma_{SM}$  is defined as the ratio between the observed and predicted cross-sections, where  $\mu = 0$  corresponds to the background-only hypothesis and  $\mu = 1$  corresponds to the SM prediction. It is a parameter of interest (POI) which acts to scale the total number of signal events.

The present analysis makes use of two POIs. The first,  $\mu_{VH}^{bb}$ , is the signal strength for the  $VH$ ,  $H \rightarrow b\bar{b}$  process, the primary process under investigation. The diboson

2366 production strength  $\mu_{VZ}^{bb}$  for the  $VZ$ ,  $Z \rightarrow b\bar{b}$  process is measured simultaneously  
2367 and provides a validation of the analysis apparatus used for the primary  $H \rightarrow b\bar{b}$   
2368 measurement. Alongside the two POIs, the predictive model depends on several  
2369 uninteresting parameters which are not the primary target of measurement. These  
2370 parameters are called nuisance parameters (NPs), collectively referred to as  $\theta$ . Freely  
2371 floating background normalisations are implemented as NPs and are also extracted  
2372 during the fitting processes.

### 2373 7.3.1 Likelihood Function

2374 The statistical setup treats each bin as a Poisson counting experiment and is based on  
2375 the ROOSTATS framework [170]. The combined likelihood over  $N$  bins is constructed  
2376 as the product of Poisson probabilities in each bin. Considering the simplified case  
2377 of a single signal strength parameter  $\mu$ , and neglecting sources of systematic or  
2378 statistical uncertainty, this is given by

$$\mathcal{L}(\mu) = \prod_{i=1}^N \frac{(\mu s_i + b_i)^{n_i}}{n_i!} \exp [-(\mu s_i + b_i)], \quad (7.1)$$

2379 where  $s_i$  ( $b_i$ ) is the expected number of signal (background) events in bin  $i$ , and  $n_i$  is  
2380 the number of observed data events in bin  $i$ .

### 2381 Treatment of Uncertainties

2382 Systematic uncertainties can modify the predicted signal and background yields  $s_i$   
2383 and  $b_i$ . Each source of systematic uncertainty is taken into account by adding an  
2384 additional NP  $\theta_j$  to the likelihood in the form of a Gaussian cost function. The  
2385 combined effect of the NPs is then

$$\mathcal{L}(\theta) = \prod_{j=1}^{N_\theta} \frac{1}{\sqrt{2\pi}\sigma_j} \exp \left[ \frac{-(\bar{\theta}_j - \theta_j)^2}{2\sigma_j^2} \right], \quad (7.2)$$

2386 where  $N_\theta$  is the number of NPs,  $\bar{\theta}_j$  is the nominal value of the  $j$ th NP,  $\theta_j$  is the fitted  
2387 value, and  $\sigma_j$  is the corresponding associated prior uncertainty on  $\theta_j$ . As the fitted  
2388 value of the  $\theta_j$  deviates from its nominal value, a cost is introduced. The presence

2389 of NPs modifies the likelihood as

$$\mathcal{L}(\mu) \rightarrow \mathcal{L}(\mu, \theta) = \mathcal{L}(\mu)\mathcal{L}(\theta). \quad (7.3)$$

2390 The predicted signal and background yields are also modified by the presence of the  
2391 NPs with

$$s_i \rightarrow s_i(\theta), \quad b_i \rightarrow b_i(\theta). \quad (7.4)$$

2392 For NPs which are left freely floating in the fit, no corresponding Gaussian constraint  
2393 is added to the likelihood.

2394 Statistical uncertainty is also present, and implemented using a dedicated NP for  
2395 each bin which can scale the background yield in that bin. Statistical NPs are also  
2396 implemented using a Gaussian constraint.

### 2397 Smoothing and Pruning

2398 Systematic uncertainties are smoothed and pruned in the fit. Smoothing accounts  
2399 for the large statistical uncertainty present in some bins that are subject to large  
2400 fluctuations. The smoothing procedure relies on the assumption that the impact of  
2401 systematics should be approximately monotonic and correlated between neighbouring  
2402 bins.

2403 In addition to smoothing, pruning is the process of removing from the fit those  
2404 systematics which only have a very small effect. This improves the stability of the  
2405 fit by reducing the number of degrees of freedom. Acceptance uncertainties are  
2406 pruned in a given region if they have a variation of less than 0.5%, or if the up and  
2407 down variations have the same sign in that region. Shape uncertainties are pruned  
2408 in a given region if the deviation in each bin is less than 0.5% in that region. In  
2409 addition, acceptance and shape uncertainties are neglected in a given region for any  
2410 background which makes up less than 2% of the total background in a given region.

---

## 2411 Fit Procedure and Statistical Tests

2412 The best-fit value of  $\mu$ , denoted  $\hat{\mu}$ , is obtained via an unconditional maximisation  
 2413 of the likelihood. The likelihood is also used to construct a statistical test which can  
 2414 confirm or reject the background-only hypothesis. The test statistic  $q_\mu$  is constructed  
 2415 from the profile likelihood ratio, as in

$$q_\mu = -2 \ln \frac{\mathcal{L}(\mu, \hat{\theta}_\mu)}{\mathcal{L}(\hat{\mu}, \hat{\theta})} \quad (7.5)$$

2416 where  $\hat{\mu}$  and  $\hat{\theta}$  are chosen to maximise the likelihood  $\mathcal{L}$ , and the profile value  $\hat{\theta}_\mu$  is  
 2417 obtained from a conditional maximisation fo the likelihood for a specific choice of  
 2418  $\mu = 0$  corresponding to the background-only hypothesis.

2419 The test statistic is used to construct a  $p$ -value which is used to confirm or accept  
 2420 the background-only hypothesis. The  $p$ -value is typically reported in terms of the  
 2421 significance  $Z$ , defined as the number of standard deviations for a Gaussian Normal  
 2422 distribution which will produce a one-sided tail integral equal to the  $p$ -value, as in

$$p = \int_Z^\infty \frac{1}{\sqrt{2\pi}} e^{-x^2/2} dx = 1 - \Phi(Z). \quad (7.6)$$

2423 Typically a value of  $Z = 3$  constitutes *evidence* of a processes, while  $Z = 5$  is required  
 2424 for a *discovery*. Alongside the  $p$ -value, the best-fit value of the signal strength  $\hat{\mu}$  and  
 2425 its corresponding uncertainty are typically quoted, and compared to their expected  
 2426 values (see Section 7.3.3).

### 2427 7.3.2 Background Normalisations

2428 The normalisation of the largest backgrounds are left floating and are determined in  
 2429 the fit. The corresponding postfit background normalisations are listed in Table 7.11.  
 2430 A single normalisation factor is used for  $W+\text{hf}$  and  $Z+\text{hf}$ , which constitue more  
 2431 than 90% of the total  $V+\text{jets}$  background, since the use of independent factors in  
 2432 different channels were found to be compatible.

Process	Normalisation factor
$t\bar{t}$ 0-lepton	$0.88 \pm 0.10$
$t\bar{t}$ 1-lepton	$0.83 \pm 0.09$
$W+\text{hf}$	$1.12 \pm 0.14$
$Z+\text{hf}$	$1.32 \pm 0.16$

**Table 7.11:** Factors applied to the nominal normalisations of the  $t\bar{t}$ ,  $W+\text{hf}$ , and  $Z+\text{hf}$  backgrounds, as obtained from the likelihood fit. The errors represent the combined statistical and systematic uncertainties.

2433 The normalisations and shapes of all other backgrounds, with the exception of the  
2434 multijet background which is estimated using a data driven technique, are initialised  
2435 using the simulated samples.

### 2436 7.3.3 Asimov Dataset & Expected Results

2437 The Asimov dataset is constructed by replacing the data with the sum of the signal  
2438 and background predictions  $n_i = s_i + b_i$ . A fit to this dataset using the nominal  
2439 values of the NPs from the simulation will recover the input values and is useful for  
2440 studying constraints on and correlations between the NPs.

2441 Alternatively, a conditional fit to the Asimov dataset can be performed using values  
2442 of the background NPs which are determined from an unconditional fit to data. The  
2443 signal NPs and POIs are fixed at their nominal values from the SM simulation. The  
2444 result of this fit can be used to calculate expected (median) significances, which can  
2445 be compared to their observed values.

## 2446 7.4 Results

2447 In the present analysis, the two signal strength parameters  $\mu_{VH}^{bb}$  and  $\mu_{VZ}^{bb}$  are extracted  
2448 from a simultaneous maximisation of the likelihood described in Section 7.3. The  
2449 results of the analysis are summarised in this section. Post-fit  $m_J$  distributions are  
2450 shown in Section 7.4.1. The observed signal strengths are given in Section 7.4.2,  
2451 along with observed and expected significances. Finally in Section 7.4.3 the impact  
2452 of systematic uncertainties on the results is examined.

### 2453 7.4.1 Post-fit Distributions

2454 In addition to the observed significance and signal strength, it is also useful to study  
 2455 the post-fit  $m_J$  distributions to compare the simulation and data using the best-fit  
 2456 values  $\hat{\mu}$  and  $\hat{\theta}$ . Post-fit  $m_J$  distributions are given for the signal regions in the 0-,  
 2457 1- and 2-lepton channels in Fig. 7.6. The LP and HP regions are merged for the  
 2458 0- and 1-lepton channels. The plots show large falling backgrounds, predominantly  
 2459 made up of  $W$ -jets and  $Z$ -jets events, and a signal distribution corresponding to  
 2460 the Standard Model Higgs boson peaking around  $m_H = 125$  GeV. In general there is  
 2461 a good level of agreement between the simulation and data, indicating the fit model  
 2462 is performing as expected. Fig. 7.7 shows the post-fit plots for the  $t\bar{t}$  control regions.  
 2463 Again, a good level of agreement is observed given the statistical uncertainties on  
 2464 the distributions.

### 2465 7.4.2 Observed Signal Strength & Significance

2466 The measured signal strength is computed as the ratio between the measured signal  
 2467 yield to the prediction from the SM. The combined result for all three lepton channels  
 2468 and all analysis regions is given for  $\mu_{VH}^{bb}$  in Eq. (7.7), and for  $\mu_{VZ}^{bb}$  is given in Eq. (7.8).  
 2469 Both results include a full breakdown of the systematic and statistical uncertainties.

$$\mu_{VH}^{bb} = 0.72^{+0.39}_{-0.36} = 0.72^{+0.29}_{-0.28}(\text{stat.})^{+0.26}_{-0.22}(\text{syst.}) \quad (7.7)$$

2470

$$\mu_{VZ}^{bb} = 0.91^{+0.29}_{-0.23} = 0.91 \pm 0.15(\text{stat.})^{+0.24}_{-0.17}(\text{syst.}) \quad (7.8)$$

2471 The results for  $\mu_{VH}^{bb}$  and  $\mu_{VZ}^{bb}$  agree with the expectation from the SM within their  
 2472 combined uncertainty. The  $\mu_{VH}^{bb}$  measurement is dominated by statistical uncertainty,  
 2473 while the  $\mu_{VZ}^{bb}$  measurement is dominated by systematic sources of uncertainty. These  
 2474 measured signal strength for  $\mu_{VZ}^{bb}$  corresponds to an observed significance of 2.1  
 2475 standard deviations, with an expected (median) significance given the SM prediction  
 2476 of 2.7 standard deviations obtained using the method described in Section 7.3.3. The  
 2477 diboson observed (expected) signal strength significance is 5.4 (5.7). These results  
 2478 are summarised in Fig. 7.8, which shows the background-subtracted  $m_J$  distribution.  
 2479 A clear signal excess is visible around the Higgs mass of  $m_H = 125$  GeV.

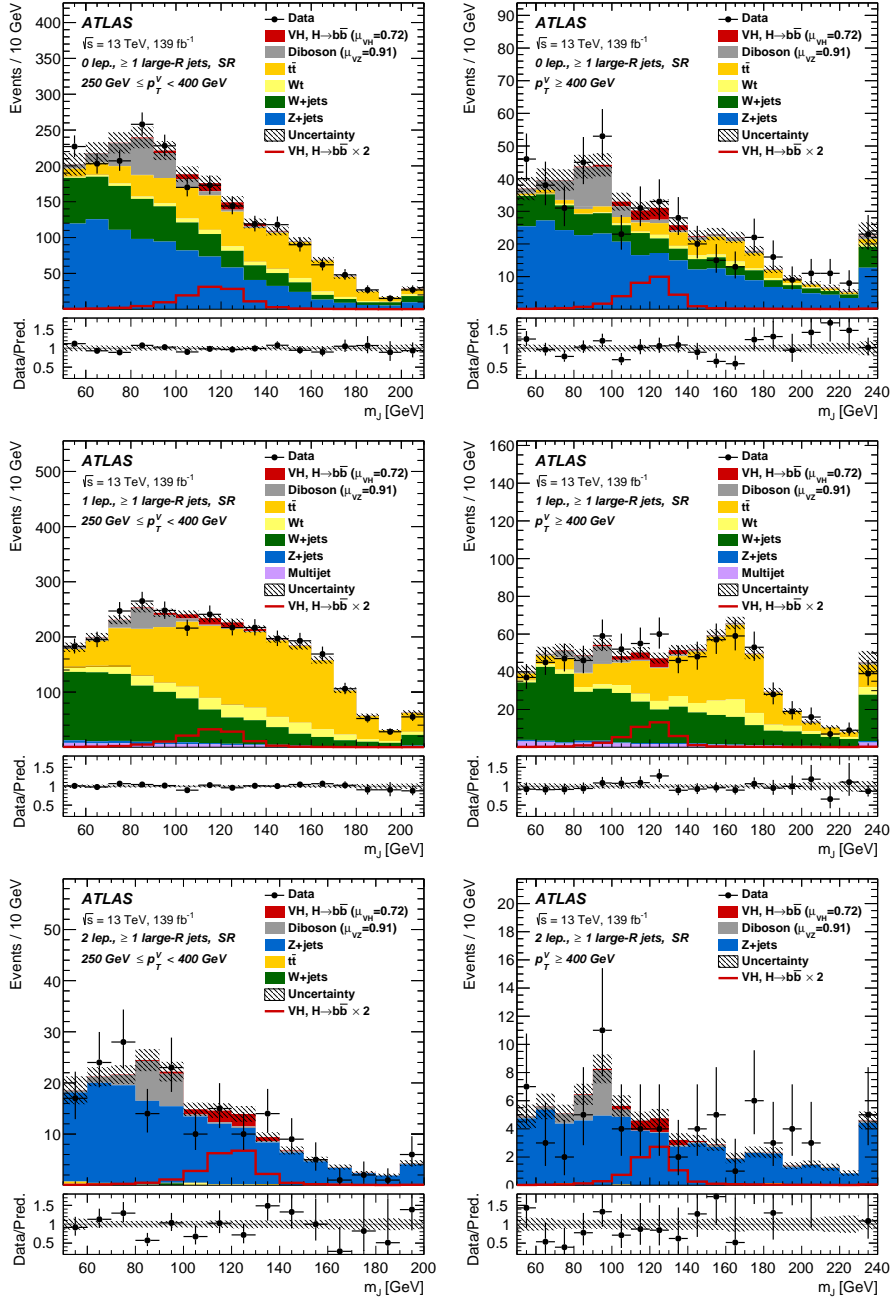


**Figure 7.6:** The  $m_J$  post-fit distributions in (top) the 0-, (middle) 1- and (bottom) 2-lepton SRs for (left)  $250 \text{ GeV} < p_T^V < 400 \text{ GeV}$  and (right)  $p_T^V \geq 400 \text{ GeV}$ . The LP and HP regions are merged for the 0-lepton and 1-lepton channels. The fitted background contributions are shown as filled histograms. The Higgs boson signal ( $m_H = 125 \text{ GeV}$ ) is shown as a filled histogram and is normalised to the signal yield extracted from data ( $\mu_{VH}^{bb} = 0.72$ ), and as an unstacked unfilled histogram, scaled by the SM prediction times a factor of two. The size of the combined on the sum of the fitted signal and background is shown in the hatched band. The highest bin contains the overflow.

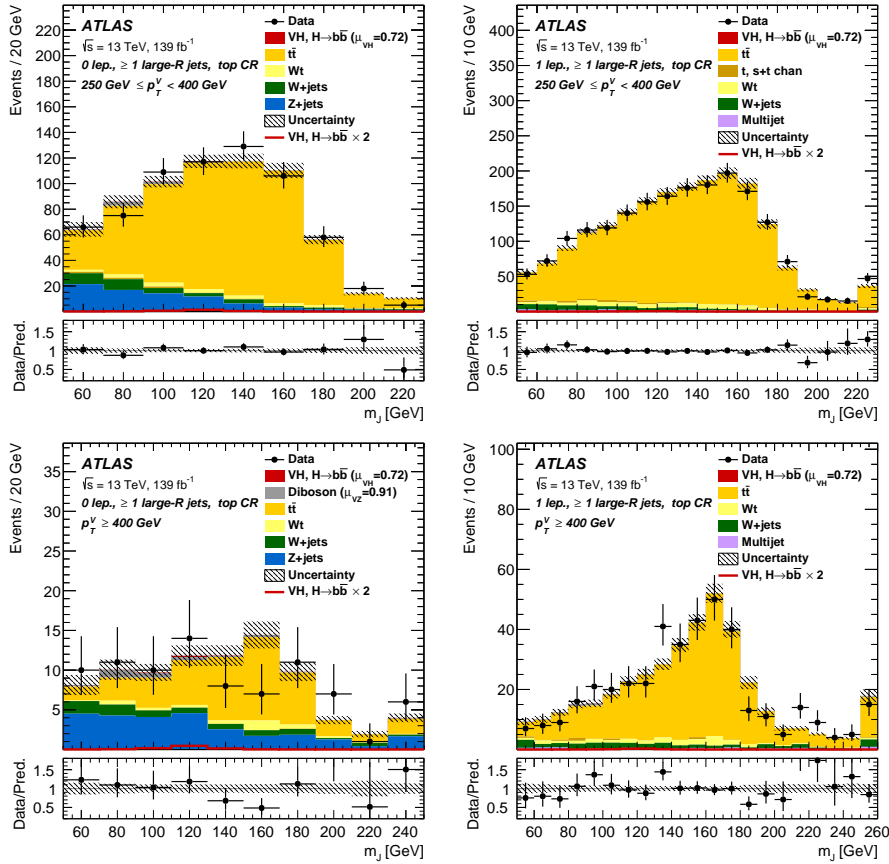


**Figure 7.7:** The  $m_J$  post-fit distributions in the  $t\bar{t}$  control region for (top) the 0-lepton channel and the 1-lepton channel for  $250 \text{ GeV} < p_T^V < 400 \text{ GeV}$  and (bottom) the 0-lepton channel and the 1-lepton channel for  $p_T^V > 400 \text{ GeV}$ . The background contributions after the likelihood fit are shown as filled histograms. The Higgs boson signal ( $m_h = 125 \text{ GeV}$ ) is shown as a filled histogram on top of the fitted backgrounds normalised to the signal yield extracted from data ( $\mu_{VH}^{bb} = 0.72$ ), and unstacked as an unfilled histogram, scaled by the SM prediction times a factor of 2. The size of the combined statistical and systematic uncertainty for the sum of the fitted signal and background is indicated by the hatched band. The highest bin in the distributions contains the overflow.

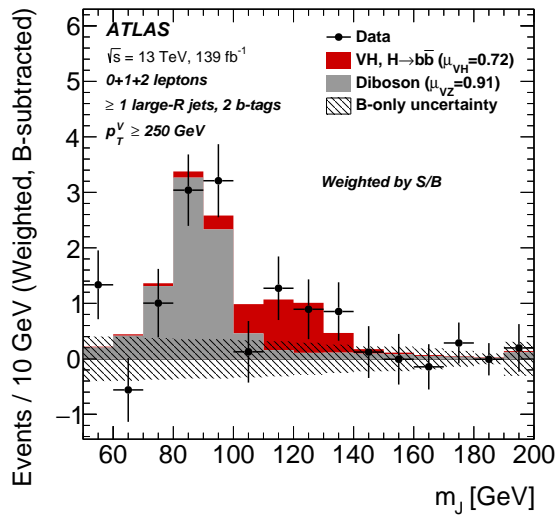


**Figure 7.8:**  $m_J$  distribution in data after subtraction of all backgrounds except for the  $WZ$  and  $ZZ$  diboson processes. The contributions from all lepton channels and signal regions are summed and weighted by their respective values of the ratio of fitted Higgs boson signal and background yields. The expected contribution of the associated  $WH$  and  $ZH$  production of a SM Higgs boson with  $m_H = 125$  GeV is shown scaled by the measured combined signal strength ( $\mu_{VH}^{bb} = 0.72$ ). The diboson contribution is normalised to its best-fit value of  $\mu_{VZ}^{bb} = 0.91$ . The size of the combined statistical and systematic uncertainty is indicated by the hatched band. This error band is computed from a full signal-plus-background fit including all the systematic uncertainties defined in Section 7.2, except for the  $VH/VZ$  experimental and theory uncertainties.

2480 **Compatability Studies**

2481 Alongside the standard 2-POI fit, a (3+1)-POI fit can be performed by splitting  $\mu_{VH}^{bb}$   
2482 into three separate POIs, one for each channel. A simultaneous fit to the channel  
2483 specific signal strengths can then be performned, which allows a comparison of the  
2484 contributions from each channel. Fig. 7.9 compares the best-fit signal strengths.  
2485 The 0- and 1-lepton channels show a signal strength which is consistent with the  
2486 SM prediction, while the 2-lepton channel shows a small deviation within the  $1\sigma$   
2487 uncertainty. Overall, good compatibility is observed via a  $\chi^2$  test with a corresponding  
2488  $p$ -value of 49%.

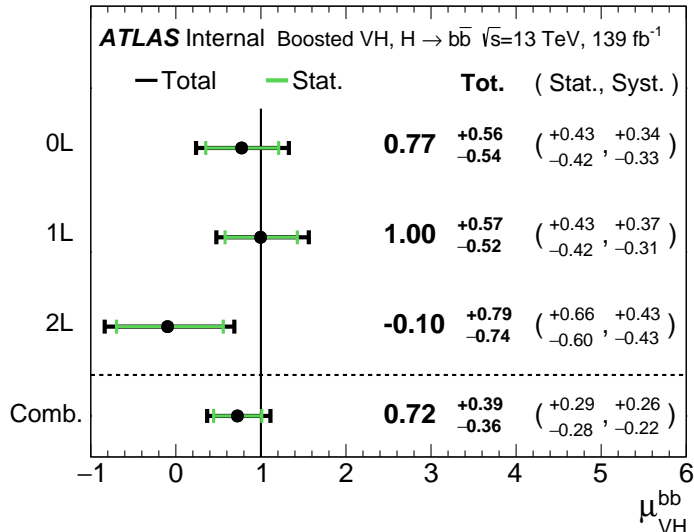


**Figure 7.9:** Signal strength compatibility test between the (3+1)-POI fit (with the three lepton channels splitted) and the default (1+1)-POI fit. The compatibility of the three channels is evaluated via a  $\chi^2$  difference test and results in a  $p$ -value of 49%.

2489 **7.4.3 Impact of Systematics**

2490 The impact of systematic uncertainties on the final fitted value  $\hat{\mu}_{VH}^{bb}$  is studied looking  
2491 at the NP rankings, and the uncertainty breakdown.

2492 Fig. 7.10 shows the NP ranking, which is used to visualise which out of the many  
2493 NPs involved in the fit have the largest impact on the sensitivity to the fitted POI.  
2494 To obtain the ranking, a likelihood scan is performed for each NP  $\theta_j$ . First, an

unconditional fit is used to determine  $\hat{\theta}_j$ . From this best-fit point, the NP is varied in steps and the likelihood is recomputed until the  $\pm 1\sigma_{\hat{\theta}_j}$  values are reached. For each corresponding value of  $\theta_j$ , the change in the best-fit value of the POI,  $\Delta\hat{\mu}_{VH}^{bb}$  is calculated and used to rank the NPs. Also shown in Fig. 7.10 are the pulls and constraints for the highest ranked NPs.

The experimental uncertainty on the signal large- $R$  jet mass resolution (JMR) has the largest impact of any NP. It is a significant contributor to the overall uncertainty on  $\mu_{VH}^{bb}$  in Eq. (7.7). JMR and jet energy scale (JES) uncertainties also have impacts for the  $V+jets$  background and for the diboson background. The freely-floating  $Z+hf$  normalisation is the second highest ranked NP, and is heavily constrained by the fit. The  $VZ$  POI  $\mu_{VZ}^{bb}$  is also a significant NP when considering the primary  $\mu_{VH}^{bb}$  measurement.

The NP ranking highlights individual NPs which have a large impact on the POI measurement sensitivity. Complementary information is provided at a higher level by considering the overall impact of different groups of systematics. The groups are constructed from NPs which have similar physical origin. The impact on each group is calculated by running a fit with all the NPs in the given group fixed to their nominal values. The uncertainty on the POI extracted from this fit is subtracted in quadrature from the the uncertainty on the POI from the nominal fit, and the resulting values are provided as the impact for each group. The full breakdown for the observed impact of uncertainties on the  $\mu_{VH}^{bb}$  signal strength is provided in Table 7.12. The total systematic impact is the difference in quadrature between the nominal uncertainty on  $\mu_{VH}^{bb}$  and the combined statistical impact. The “data stat only” group fixes all NPs at their nominal value, while the total statistical impact fixes all NPs except floating normalisations. The floating normalisations group fixes only the NPs associated with normalisation which are left floating in the fit. The uncertainty on  $\mu_{VH}^{bb}$  is dominated by combined statistcal effects (0.28), although the combined impact of systematics (0.24) is of a comparable size. The signal largest group is the data stat uncertainty (0.25), demonstrating that the analysis would benefit from an increased integrated luminosity or improved efficiency to select signal relevant events (recall from Section 7.1.3 the signal efficiency is in the range of 10%). Of the experimental systematic sources of uncertainty, the dominant impact is the experimental uncertainties associated with the reconstruction of large- $R$  jets (0.13). Other experimental sources of uncertainty are small in comparison. Modelling

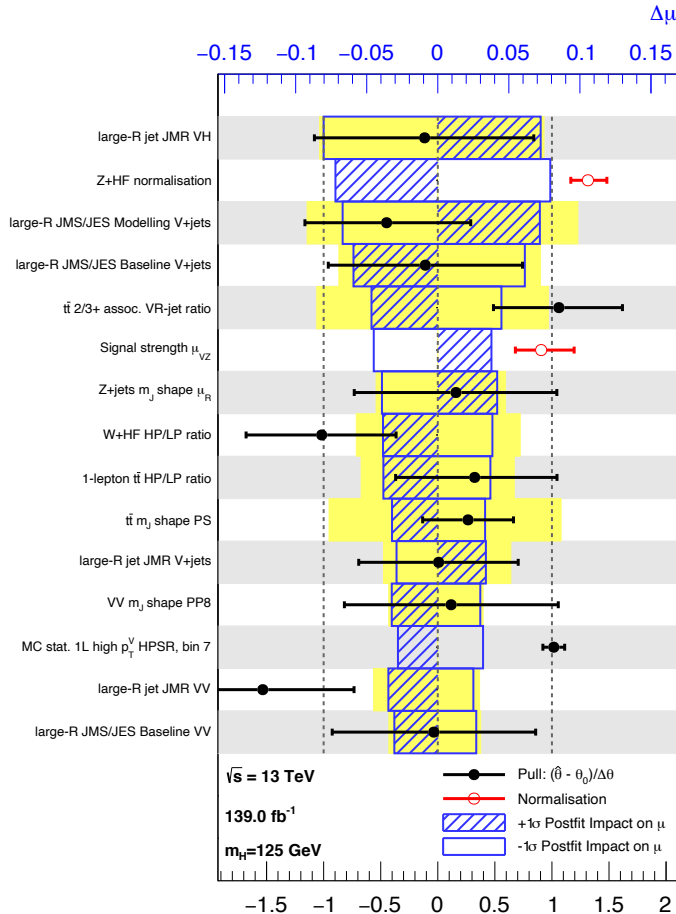


**Figure 7.10:** Impact of systematic uncertainties on the fitted  $VH$  signal-strength parameter  $\hat{\mu}_{VH}^{bb}$  sorted in decreasing order. The boxes show the variations of  $\hat{\mu}$ , referring to the top  $x$ -axis, when fixing the corresponding individual nuisance parameter to its post-fit value modified upwards or downwards by its post-fit uncertainty, i.e.  $\hat{\theta} \pm \sigma_{\hat{\theta}}$ , and repeating the fit. The impact of up- and down-variations can be distinguished via the dashed and plane box fillings. The yellow boxes show the pre-fit impact (top  $x$ -axis) by varying each nuisance parameter by  $\pm 1$ . The filled circles show the deviation of the fitted value for each nuisance parameter,  $\hat{\theta}$ , from their nominal input value  $\theta_0$  expressed in standard deviations with respect to their nominal uncertainties  $\Delta\theta$  (bottom  $x$ -axis). The error bars show the post-fit uncertainties on  $\hat{\theta}$  with respect to their nominal uncertainties. The open circles show the fitted values and uncertainties of the normalization parameters that are freely floating in the fit. Pre-fit, these parameters have a value of one.

2529 uncertainties also have a large contribution to the overall systematic uncertainty. The  
2530 biggest contribution to the overall uncertainty is the combined statistical uncertainty  
2531 on the simulated samples (0.09), which contain only a finite number of events. Out of  
2532 the backgrounds, the  $W+jets$  and  $Z+jets$  have the highest (0.06) and second-highest  
2533 (0.05) impact respectively.

2534 **7.5 Improved  $b$ -tagging using GNNs**

2535 **7.6 Conclusion**

2536 Work has been carried out as part of the boosted VHbb analysis group to understand,  
2537 and implement in the global profile likelihood fit, systematic uncertainties on  $V+jets$   
2538 samples. This background modelling work is an essential part of the success of  
2539 the analysis. So far the fit has proved stable with the inclusion of the  $V+jets$   
2540 uncertainties, and detailed studies are now underway to determine the causes behind  
2541 any observed pulls of the added NPs. Additional work is ongoing to help with the  
2542 derivation of uncertainties on diboson samples, another important background. The  
2543 analysis is already advanced, and is now progressing into its final stages. Publication  
2544 is expected in the new year.

2545 This analysis would benefit greatly from the improved high  $p_T$   $b$ -tagging enabled by  
2546 GN1.

Source of uncertainty	Signed impact	Avg. impact												
Total	+0.388 / -0.356	0.372												
Statistical	+0.286 / -0.280	0.283												
↔ Data stat only	+0.251 / -0.245	0.248												
↔ Floating normalisations	+0.096 / -0.092	0.094												
Systematic	+0.261 / -0.219	0.240												
<hr/>														
Experimental uncertainties														
small-R jets	+0.041 / -0.034	0.038												
large-R jets	+0.161 / -0.105	0.133												
$E_T^{\text{miss}}$	+0.008 / -0.007	0.007												
Leptons	+0.013 / -0.007	0.010												
b-tagging	<table border="0"> <tr> <td><i>b</i>-jets</td> <td>+0.028 / -0.004</td> <td>0.016</td> </tr> <tr> <td><i>c</i>-jets</td> <td>+0.012 / -0.011</td> <td>0.011</td> </tr> <tr> <td>light-flavour jets</td> <td>+0.009 / -0.007</td> <td>0.008</td> </tr> <tr> <td>extrapolation</td> <td>+0.004 / -0.005</td> <td>0.004</td> </tr> </table>	<i>b</i> -jets	+0.028 / -0.004	0.016	<i>c</i> -jets	+0.012 / -0.011	0.011	light-flavour jets	+0.009 / -0.007	0.008	extrapolation	+0.004 / -0.005	0.004	
<i>b</i> -jets	+0.028 / -0.004	0.016												
<i>c</i> -jets	+0.012 / -0.011	0.011												
light-flavour jets	+0.009 / -0.007	0.008												
extrapolation	+0.004 / -0.005	0.004												
Pile-up	+0.001 / -0.002	0.001												
Luminosity	+0.019 / -0.007	0.013												
<hr/>														
Theoretical and modelling uncertainties														
Signal	+0.073 / -0.026	0.050												
Backgrounds	+0.106 / -0.095	0.100												
↔ $Z + \text{jets}$	+0.049 / -0.047	0.048												
↔ $W + \text{jets}$	+0.059 / -0.056	0.058												
↔ $t\bar{t}$	+0.037 / -0.032	0.035												
↔ Single top quark	+0.031 / -0.023	0.027												
↔ Diboson	+0.034 / -0.029	0.032												
↔ Multijet	+0.009 / -0.009	0.009												
↔ MC statistical	+0.091 / -0.092	0.092												

**Table 7.12:** Breakdown of the observed absolute contributions to the uncertainty on the signal strength  $\mu_{VH}^{bb}$  obtained from the (1+1)-POI fit. The average impact represents the average between the positive and negative uncertainties on  $\mu_{VH}^{bb}$ . The sum in quadrature of the systematic uncertainties attached to the categories differs from the total systematic uncertainty due to correlations.

# <sup>2547</sup> Chapter 8

## <sup>2548</sup> Conclusion

<sup>2549</sup> flavour tagging at high pT is important because

<sup>2550</sup> tracking suffers from several problems which might be improved by

<sup>2551</sup> algorithmic gains in flavour tagging can improve things

<sup>2552</sup> ultimately analyses will benefit greatly

<sup>2553</sup> future work:

<sup>2554</sup>     • improve tracking

<sup>2555</sup>     • use more info for flavour tagging

<sup>2556</sup>     • improve jet labelling

<sup>2557</sup>     • boosted xbb tagging

<sup>2558</sup>     • lead to dihiggs

2559    **Bibliography**

- 2560 [1] A. Buckley, *A class for typesetting academic theses*, (2010). [http://ctan.tug.org/  
2561 tex-archive/macros/latex/contrib/heptesis/heptesis.pdf](http://ctan.tug.org/tex-archive/macros/latex/contrib/heptesis/heptesis.pdf).
- 2562 [2] L. Morel, Z. Yao, P. Cladé and S. Guellati-Khélifa, *Determination of the  
2563 fine-structure constant with an accuracy of 81 parts per trillion*, *Nature* **588** (2020)  
2564 pp. 61–65.
- 2565 [3] T. Sailer, V. Debierre, Z. Harman, F. Heiße, C. König, J. Morgner et al.,  
2566 *Measurement of the bound-electron g-factor difference in coupled ions*, *Nature* **606**  
2567 (2022) pp. 479–483.
- 2568 [4] CDF collaboration, *Observation of top quark production in  $\bar{p}p$  collisions*, *Phys. Rev.  
2569 Lett.* **74** (1995) pp. 2626–2631 [[hep-ex/9503002](#)].
- 2570 [5] D0 collaboration, *Observation of the top quark*, *Phys. Rev. Lett.* **74** (1995)  
2571 pp. 2632–2637 [[hep-ex/9503003](#)].
- 2572 [6] S. W. Herb et al., *Observation of a Dimuon Resonance at 9.5-GeV in 400-GeV  
2573 Proton-Nucleus Collisions*, *Phys. Rev. Lett.* **39** (1977) pp. 252–255.
- 2574 [7] UA1 collaboration, *Experimental Observation of Isolated Large Transverse Energy  
2575 Electrons with Associated Missing Energy at  $\sqrt{s} = 540$  GeV*, *Phys. Lett. B* **122**  
2576 (1983) pp. 103–116.
- 2577 [8] DONUT collaboration, *Observation of tau neutrino interactions*, *Phys. Lett. B* **504**  
2578 (2001) pp. 218–224 [[hep-ex/0012035](#)].
- 2579 [9] F. Englert and R. Brout, *Broken Symmetry and the Mass of Gauge Vector Mesons*,  
2580 *Phys. Rev. Lett.* **13** (1964) pp. 321–323.
- 2581 [10] P. W. Higgs, *Broken Symmetries and the Masses of Gauge Bosons*, *Phys. Rev. Lett.*  
2582 **13** (1964) pp. 508–509.
- 2583 [11] G. S. Guralnik, C. R. Hagen and T. W. B. Kibble, *Global Conservation Laws and*

- 2584        *Massless Particles*, *Phys. Rev. Lett.* **13** (1964) pp. 585–587.
- 2585 [12] ATLAS Collaboration, *Observation of a new particle in the search for the Standard  
2586 Model Higgs boson with the ATLAS detector at the LHC*, *Phys. Lett. B* **716** (2012)  
2587 p. 1 [[1207.7214](#)].
- 2588 [13] CMS Collaboration, *Observation of a new boson at a mass of 125 GeV with the CMS  
2589 experiment at the LHC*, *Phys. Lett. B* **716** (2012) p. 30 [[1207.7235](#)].
- 2590 [14] Particle Data Group collaboration, *Review of Particle Physics*, *PTEP* **2022** (2022)  
2591 p. 083C01.
- 2592 [15] C. N. Yang and R. L. Mills, *Conservation of isotopic spin and isotopic gauge  
2593 invariance*, *Phys. Rev.* **96** (1954) pp. 191–195.
- 2594 [16] S. L. Glashow, *Partial Symmetries of Weak Interactions*, *Nucl. Phys.* **22** (1961)  
2595 pp. 579–588.
- 2596 [17] S. Weinberg, *A Model of Leptons*, *Phys. Rev. Lett.* **19** (1967) pp. 1264–1266.
- 2597 [18] A. Salam, *Weak and Electromagnetic Interactions*, *Proceedings of the 8th Nobel  
2598 symposium*, Ed. N. Svartholm, Almqvist & Wiksell, 1968, **Conf. Proc. C680519**  
2599 (1968) pp. 367–377.
- 2600 [19] T. D. Lee and C. N. Yang, *Question of parity conservation in weak interactions*,  
2601 *Phys. Rev.* **104** (1956) pp. 254–258.
- 2602 [20] C. S. Wu, E. Ambler, R. W. Hayward, D. D. Hoppes and R. P. Hudson, *Experimental  
2603 test of parity conservation in beta decay*, *Phys. Rev.* **105** (1957) pp. 1413–1415.
- 2604 [21] R. L. Garwin, L. M. Lederman and M. Weinrich, *Observations of the failure of  
2605 conservation of parity and charge conjugation in meson decays: the magnetic moment  
2606 of the free muon*, *Phys. Rev.* **105** (1957) pp. 1415–1417.
- 2607 [22] Y. Nambu, *Quasi-particles and gauge invariance in the theory of superconductivity*,  
2608 *Phys. Rev.* **117** (1960) pp. 648–663.
- 2609 [23] J. Goldstone, *Field theories with «superconductor» solutions*, *Il Nuovo Cimento  
2610 (1955-1965)* **19** (1961) pp. 154–164.
- 2611 [24] LHC Higgs Cross Section Working Group collaboration, *Handbook of LHC Higgs  
2612 Cross Sections: 4. Deciphering the Nature of the Higgs Sector*, [1610.07922](#).
- 2613 [25] ATLAS Collaboration, *Observation of  $H \rightarrow b\bar{b}$  decays and  $VH$  production with the*

- 2614        *ATLAS detector*, ATLAS-CONF-2018-036 (2018).
- 2615 [26] CMS Collaboration, *Observation of Higgs Boson Decay to Bottom Quarks*, *Phys.*  
2616        *Rev. Lett.* **121** (2018) p. 121801 [[1808.08242](https://arxiv.org/abs/1808.08242)].
- 2617 [27] L. Evans and P. Bryant, *LHC Machine*, *JINST* **3** (2008) p. S08001.
- 2618 [28] The ALICE Collaboration, *The ALICE experiment at the CERN LHC*, *Journal of*  
2619        *Instrumentation* **3** (2008) pp. S08002–S08002.
- 2620 [29] CMS Collaboration, *The CMS experiment at the CERN LHC*, *JINST* **3** (2008)  
2621        p. S08004.
- 2622 [30] The LHCb Collaboration, *The LHCb detector at the LHC*, *Journal of*  
2623        *Instrumentation* **3** (2008) pp. S08005–S08005.
- 2624 [31] ATLAS Collaboration, *The ATLAS Experiment at the CERN Large Hadron Collider*,  
2625        *JINST* **3** (2008) p. S08003.
- 2626 [32] ATLAS Collaboration, *Integrated luminosity summary plots for 2011-2012 data*  
2627        *taking*, (2022). <https://twiki.cern.ch/twiki/bin/view/AtlasPublic/LuminosityPublicResults>.
- 2629 [33] ATLAS Collaboration, *Public ATLAS Luminosity Results for Run-2 of the LHC*,  
2630        (2022). <https://twiki.cern.ch/twiki/bin/view/AtlasPublic/LuminosityPublicResultsRun2>.
- 2632 [34] CERN, “The accelerator complex.” (2012).
- 2633 [35] G. C. Strong, *On the impact of selected modern deep-learning techniques to the*  
2634        *performance and celerity of classification models in an experimental high-energy*  
2635        *physics use case*, [2002.01427](https://arxiv.org/abs/2002.01427).
- 2636 [36] ATLAS Collaboration, *Atlas track reconstruction – general overview*, (2022).  
2637        <https://atlassoftwaredocs.web.cern.ch/trackingTutorial/idoverview/>.
- 2638 [37] ATLAS Collaboration, *Performance of b-jet identification in the ATLAS experiment*,  
2639        *JINST* **11** (2016) p. P04008 [[1512.01094](https://arxiv.org/abs/1512.01094)].
- 2640 [38] ATLAS Collaboration, *Luminosity determination in pp collisions at  $\sqrt{s} = 13$  TeV*  
2641        *using the ATLAS detector at the LHC*, ATLAS-CONF-2019-021 (2019).
- 2642 [39] ATLAS Collaboration, *ATLAS Detector and Physics Performance: Technical Design*  
2643        *Report, Volume 1*, .

- 2644 [40] for the ATLAS Collaboration collaboration, *Status of the ATLAS Experiment*, Tech.  
2645 Rep., Geneva (2010). 10.3204/DESY-PROC-2010-04/1.
- 2646 [41] ATLAS Collaboration, *ATLAS Inner Tracker Pixel Detector: Technical Design  
2647 Report*, ATLAS-TDR-030; CERN-LHCC-2017-021 (2017).
- 2648 [42] ATLAS Collaboration, *ATLAS Inner Tracker Strip Detector: Technical Design  
2649 Report*, ATLAS-TDR-025; CERN-LHCC-2017-005 (2017).
- 2650 [43] ATLAS Collaboration, *The inner detector*, (2022).  
<https://atlas.cern/Discover/Detector/Inner-Detector>.
- 2652 [44] ATLAS Collaboration, *ATLAS Insertable B-Layer: Technical Design Report*,  
2653 ATLAS-TDR-19; CERN-LHCC-2010-013 (2010).
- 2654 [45] B. Abbott et al., *Production and integration of the ATLAS Insertable B-Layer*,  
2655 *JINST* **13** (2018) p. T05008 [[1803.00844](#)].
- 2656 [46] ATLAS Collaboration, *Operation and performance of the ATLAS semiconductor  
2657 tracker*, *JINST* **9** (2014) p. P08009 [[1404.7473](#)].
- 2658 [47] ATLAS Collaboration, *Calorimeter*, (2022).  
<https://atlas.cern/Discover/Detector/Calorimeter>.
- 2660 [48] ATLAS Collaboration, *ATLAS Tile Calorimeter: Technical Design Report*, .
- 2661 [49] G. Artoni, *Muon momentum scale and resolution in pp collisions at  $\sqrt{s} = 8 \text{ TeV}$  in  
2662 ATLAS*, Tech. Rep., Geneva (2016). 10.1016/j.nuclphysbps.2015.09.453.
- 2663 [50] ATLAS Collaboration, *Muon spectrometer*, (2022).  
<https://atlas.cern/Discover/Detector/Muon-Spectrometer>.
- 2665 [51] ATLAS Collaboration, *Performance of the ATLAS trigger system in 2015*, *Eur.  
2666 Phys. J. C* **77** (2017) p. 317 [[1611.09661](#)].
- 2667 [52] ATLAS Collaboration, *The ATLAS Collaboration Software and Firmware*, (2021).
- 2668 [53] T. Cornelissen, M. Elsing, S. Fleischmann, W. Liebig and E. Moyse, *Concepts,  
2669 Design and Implementation of the ATLAS New Tracking (NEWT)*, .
- 2670 [54] ATLAS Collaboration, *The Optimization of ATLAS Track Reconstruction in Dense  
2671 Environments*, ATL-PHYS-PUB-2015-006 (2015).
- 2672 [55] ATLAS Collaboration, *Performance of the ATLAS track reconstruction algorithms in  
2673 dense environments in LHC Run 2*, *Eur. Phys. J. C* **77** (2017) p. 673 [[1704.07983](#)].

- 2674 [56] ATLAS Collaboration, *A neural network clustering algorithm for the ATLAS silicon*  
2675 *pixel detector*, *JINST* **9** (2014) p. P09009 [[1406.7690](#)].
- 2676 [57] R. Jansky, *Truth Seeded Reconstruction for Fast Simulation in the ATLAS*  
2677 *Experiment*, .
- 2678 [58] ATLAS Collaboration, *Reconstruction of primary vertices at the ATLAS experiment*  
2679 *in Run 1 proton–proton collisions at the LHC*, *Eur. Phys. J. C* **77** (2017) p. 332  
2680 [[1611.10235](#)].
- 2681 [59] ATLAS Collaboration, *Development of ATLAS Primary Vertex Reconstruction for*  
2682 *LHC Run 3*, ATL-PHYS-PUB-2019-015 (2019).
- 2683 [60] ATLAS Collaboration, *ATLAS b-jet identification performance and efficiency*  
2684 *measurement with  $t\bar{t}$  events in  $pp$  collisions at  $\sqrt{s} = 13$  TeV*, *Eur. Phys. J. C* **79**  
2685 (2019) p. 970 [[1907.05120](#)].
- 2686 [61] M. Cacciari, G. P. Salam and G. Soyez, *The anti- $k_t$  jet clustering algorithm*, *JHEP*  
2687 **04** (2008) p. 063 [[0802.1189](#)].
- 2688 [62] M. Cacciari, G. P. Salam and G. Soyez, *Fastjet user manual*, *Eur.Phys.J. C***72** (2012)  
2689 p. 1896 [[1111.6097](#)].
- 2690 [63] ATLAS Collaboration, *Topological cell clustering in the ATLAS calorimeters and its*  
2691 *performance in LHC Run 1*, *Eur. Phys. J. C* **77** (2017) p. 490 [[1603.02934](#)].
- 2692 [64] ATLAS Collaboration, *Jet reconstruction and performance using particle flow with*  
2693 *the ATLAS Detector*, *Eur. Phys. J. C* **77** (2017) p. 466 [[1703.10485](#)].
- 2694 [65] ATLAS Collaboration, *Jet energy scale measurements and their systematic*  
2695 *uncertainties in proton–proton collisions at  $\sqrt{s} = 13$  TeV with the ATLAS detector*,  
2696 *Phys. Rev. D* **96** (2017) p. 072002 [[1703.09665](#)].
- 2697 [66] J. M. Butterworth, A. R. Davison, M. Rubin and G. P. Salam, *Jet Substructure as a*  
2698 *New Higgs Search Channel at the Large Hadron Collider*, *Phys. Rev. Lett.* **100** (2008)  
2699 p. 242001 [[0802.2470](#)].
- 2700 [67] ATLAS collaboration, *Measurement of the associated production of a Higgs boson*  
2701 *decaying into  $b$ -quarks with a vector boson at high transverse momentum in  $pp$*   
2702 *collisions at  $\sqrt{s} = 13$  TeV with the ATLAS detector*, *Phys. Lett. B* **816** (2021)  
2703 p. 136204 [[2008.02508](#)].
- 2704 [68] ATLAS collaboration, *Performance of jet substructure techniques for large- $R$  jets in*

- 2705        *proton-proton collisions at  $\sqrt{s} = 7$  TeV using the ATLAS detector*, *JHEP* **09** (2013)  
2706        p. 076 [[1306.4945](#)].
- 2707        [69] ATLAS Collaboration, *In situ calibration of large-radius jet energy and mass in*  
2708        *13 TeV proton–proton collisions with the ATLAS detector*, *Eur. Phys. J. C* **79** (2019)  
2709        p. 135 [[1807.09477](#)].
- 2710        [70] D. Krohn, J. Thaler and L.-T. Wang, *Jets with Variable R*, *JHEP* **06** (2009) p. 059  
2711        [[0903.0392](#)].
- 2712        [71] ATLAS Collaboration, *Variable Radius, Exclusive- $k_T$ , and Center-of-Mass Subjet*  
2713        *Reconstruction for Higgs( $\rightarrow b\bar{b}$ ) Tagging in ATLAS*, ATL-PHYS-PUB-2017-010  
2714        (2017).
- 2715        [72] ATLAS Collaboration, *Improved electron reconstruction in ATLAS using the*  
2716        *Gaussian Sum Filter-based model for bremsstrahlung*, ATLAS-CONF-2012-047 (2012).
- 2717        [73] ATLAS Collaboration, *Electron efficiency measurements with the ATLAS detector*  
2718        *using the 2015 LHC proton–proton collision data*, ATLAS-CONF-2016-024 (2016).
- 2719        [74] ATLAS Collaboration, *Muon reconstruction performance of the ATLAS detector in*  
2720        *proton–proton collision data at  $\sqrt{s} = 13$  TeV*, *Eur. Phys. J. C* **76** (2016) p. 292  
2721        [[1603.05598](#)].
- 2722        [75] ATLAS Collaboration, *Performance of missing transverse momentum reconstruction*  
2723        *with the ATLAS detector using proton–proton collisions at  $\sqrt{s} = 13$  TeV*, *Eur. Phys.*  
2724        *J. C* **78** (2018) p. 903 [[1802.08168](#)].
- 2725        [76] B. R. Webber, *Fragmentation and hadronization*, *Int. J. Mod. Phys. A* **15S1** (2000)  
2726        pp. 577–606 [[hep-ph/9912292](#)].
- 2727        [77] Particle Data Group collaboration, *Review of particle physics*, *Phys. Rev. D* **98**  
2728        (2018) p. 030001.
- 2729        [78] ATLAS Collaboration, *Comparison of Monte Carlo generator predictions for bottom*  
2730        *and charm hadrons in the decays of top quarks and the fragmentation of high  $p_T$  jets*,  
2731        ATL-PHYS-PUB-2014-008 (2014).
- 2732        [79] Nazar Bartosik, *Diagram showing the common principle of identification of jets*  
2733        *initiated by b-hadron decays*, (2022).  
2734        [https://en.m.wikipedia.org/wiki/File:B-tagging\\_diagram.png](https://en.m.wikipedia.org/wiki/File:B-tagging_diagram.png).
- 2735        [80] ATLAS Collaboration, *Tracking efficiency studies in dense environments*, (2022).

- 2736                    <https://atlas.web.cern.ch/Atlas/GROUPS/PHYSICS/PLLOTS/IDTR-2022-03/>.
- 2737 [81] S. Adorni Braccesi Chiassi, *Vector Boson Tagging in the Context of the Search for*  
2738    *New Physics in the Fully Hadronic Final State*, Ph.D. thesis, Geneva U., 2021.  
2739    10.13097/archive-ouverte/unige:158558.
- 2740 [82] E. Boos, M. Dobbs, W. Giele, I. Hinchliffe, J. Huston, V. Ilyin et al., *Generic User*  
2741    *Process Interface for Event Generators*, ArXiv High Energy Physics - Phenomenology  
2742    e-prints (2001) .
- 2743 [83] J. Alwall, A. Ballestrero, P. Bartalini, S. Belov, E. Boos, A. Buckley et al., *A*  
2744    *standard format for Les Houches Event Files*, Computer Physics Communications  
2745    **176** (2007) pp. 300–304.
- 2746 [84] K. Hornik, M. Stinchcombe and H. White, *Multilayer feedforward networks are*  
2747    *universal approximators*, Neural Networks **2** (1989) pp. 359–366.
- 2748 [85] D. E. Rumelhart, G. E. Hinton and R. J. Williams, *Learning representations by*  
2749    *back-propagating errors*, nature **323** (1986) pp. 533–536.
- 2750 [86] W. McCulloch and W. Pitts, *A logical calculus of the ideas immanent in nervous*  
2751    *activity*, The bulletin of mathematical biophysics **5** (1943) pp. 115–133.
- 2752 [87] J. Hopfield, *Neural networks and physical systems with emergent collective*  
2753    *computational abilities*, in *Spin Glass Theory and Beyond: An Introduction to the*  
2754    *Replica Method and Its Applications*, pp. 411–415, World Scientific, (1987).
- 2755 [88] Y. A. LeCun, L. Bottou, G. B. Orr and K.-R. Müller, *Efficient backprop*, in *Neural*  
2756    *networks: Tricks of the trade*, pp. 9–48, Springer, (2012).
- 2757 [89] D. P. Kingma and J. Ba, *Adam: A Method for Stochastic Optimization*, arXiv  
2758    e-prints (2014) p. arXiv:1412.6980 [[1412.6980](https://arxiv.org/abs/1412.6980)].
- 2759 [90] P. Nason, *A new method for combining nlo qcd with shower monte carlo algorithms*,  
2760    Journal of High Energy Physics **2004** (2004) p. 040–040.
- 2761 [91] S. Frixione, G. Ridolfi and P. Nason, *A positive-weight next-to-leading-order monte*  
2762    *carlo for heavy flavour hadroproduction*, Journal of High Energy Physics **2007** (2007)  
2763    p. 126–126.
- 2764 [92] S. Frixione, P. Nason and C. Oleari, *Matching nlo qcd computations with parton*  
2765    *shower simulations: the powheg method*, Journal of High Energy Physics **2007** (2007)  
2766    p. 070–070.

- 2767 [93] S. Alioli, P. Nason, C. Oleari and E. Re, *A general framework for implementing nlo*  
2768       *calculations in shower monte carlo programs: the powheg box*, *Journal of High Energy*  
2769       *Physics* **2010** (2010) .
- 2770 [94] NNPDF collaboration, *Parton distributions for the LHC run II*, *JHEP* **04** (2015)  
2771       p. 040 [[1410.8849](#)].
- 2772 [95] ATLAS Collaboration, *Studies on top-quark Monte Carlo modelling for Top2016*,  
2773       ATL-PHYS-PUB-2016-020 (2016).
- 2774 [96] T. Sjöstrand, S. Ask, J. R. Christiansen, R. Corke, N. Desai, P. Ilten et al., *An*  
2775       *introduction to PYTHIA 8.2*, *Comput. Phys. Commun.* **191** (2015) p. 159  
2776       [[1410.3012](#)].
- 2777 [97] ATLAS Collaboration, *ATLAS Pythia 8 tunes to 7 TeV data*,  
2778       ATL-PHYS-PUB-2014-021 (2014).
- 2779 [98] R. D. Ball et al., *Parton distributions with LHC data*, *Nucl. Phys. B* **867** (2013)  
2780       p. 244 [[1207.1303](#)].
- 2781 [99] D. J. Lange, *The EvtGen particle decay simulation package*, *Nucl. Instrum. Meth. A*  
2782       **462** (2001) p. 152.
- 2783 [100] ATLAS Collaboration, *The ATLAS Simulation Infrastructure*, *Eur. Phys. J. C* **70**  
2784       (2010) p. 823 [[1005.4568](#)].
- 2785 [101] GEANT4 Collaboration, S. Agostinelli et al., *GEANT4 – a simulation toolkit*, *Nucl.*  
2786       *Instrum. Meth. A* **506** (2003) p. 250.
- 2787 [102] ATLAS Collaboration, *Tagging and suppression of pileup jets with the ATLAS*  
2788       *detector*, ATL-CONF-2014-018 (2014).
- 2789 [103] ATLAS Collaboration, *Deep Sets based Neural Networks for Impact Parameter*  
2790       *Flavour Tagging in ATLAS*, ATL-PHYS-PUB-2020-014 (2020).
- 2791 [104] ATLAS Collaboration, *Graph Neural Network Jet Flavour Tagging with the ATLAS*  
2792       *Detector*, ATL-PHYS-PUB-2022-027 (2022).
- 2793 [105] ATLAS Collaboration, *Observation of  $H \rightarrow b\bar{b}$  decays and VH production with the*  
2794       *ATLAS detector*, *Phys. Lett. B* **786** (2018) p. 59 [[1808.08238](#)].
- 2795 [106] ATLAS Collaboration, *Observation of Higgs boson production in association with a*  
2796       *top quark pair at the LHC with the ATLAS detector*, *Phys. Lett. B* **784** (2018) p. 173  
2797       [[1806.00425](#)].

- 2798 [107] ATLAS Collaboration, *Search for new resonances in mass distributions of jet pairs*  
2799        *using  $139\text{ fb}^{-1}$  of  $pp$  collisions at  $\sqrt{s} = 13\text{ TeV}$  with the ATLAS detector*, *JHEP* **03**  
2800        (2020) p. 145 [[1910.08447](#)].
- 2801 [108] ATLAS Collaboration, *Optimisation and performance studies of the ATLAS*  
2802        *b-tagging algorithms for the 2017-18 LHC run*, ATL-PHYS-PUB-2017-013 (2017).
- 2803 [109] ATLAS collaboration, *ATLAS flavour-tagging algorithms for the LHC Run 2 pp*  
2804        *collision dataset*, [2211.16345](#).
- 2805 [110] J. Shlomi, S. Ganguly, E. Gross, K. Cranmer, Y. Lipman, H. Serviansky et al.,  
2806        *Secondary vertex finding in jets with neural networks*, *The European Physical Journal*  
2807        *C* **81** (2021) .
- 2808 [111] H. Serviansky, N. Segol, J. Shlomi, K. Cranmer, E. Gross, H. Maron et al.,  
2809        *Set2Graph: Learning Graphs From Sets*, arXiv e-prints (2020) p. arXiv:2002.08772  
2810        [[2002.08772](#)].
- 2811 [112] ATLAS Collaboration, *Secondary vertex finding for jet flavour identification with the*  
2812        *ATLAS detector*, ATL-PHYS-PUB-2017-011 (2017).
- 2813 [113] ATLAS Collaboration, *Identification of Jets Containing b-Hadrons with Recurrent*  
2814        *Neural Networks at the ATLAS Experiment*, ATL-PHYS-PUB-2017-003 (2017).
- 2815 [114] P. W. Battaglia, J. B. Hamrick, V. Bapst, A. Sanchez-Gonzalez, V. Zambaldi,  
2816        M. Malinowski et al., *Relational inductive biases, deep learning, and graph networks*,  
2817        arXiv e-prints (2018) p. arXiv:1806.01261 [[1806.01261](#)].
- 2818 [115] M. Zaheer, S. Kottur, S. Ravanbakhsh, B. Poczos, R. Salakhutdinov and A. Smola,  
2819        *Deep Sets*, arXiv e-prints (2017) p. arXiv:1703.06114 [[1703.06114](#)].
- 2820 [116] ATLAS Collaboration, *Muon reconstruction performance in early  $\sqrt{s} = 13\text{ TeV}$  data*,  
2821        ATL-PHYS-PUB-2015-037 (2015).
- 2822 [117] ATLAS Collaboration, *Electron reconstruction and identification in the ATLAS*  
2823        *experiment using the 2015 and 2016 LHC proton–proton collision data at*  
2824         *$\sqrt{s} = 13\text{ TeV}$* , *Eur. Phys. J. C* **79** (2019) p. 639 [[1902.04655](#)].
- 2825 [118] D. Hwang, J. Park, S. Kwon, K.-M. Kim, J.-W. Ha and H. J. Kim, *Self-supervised*  
2826        *Auxiliary Learning with Meta-paths for Heterogeneous Graphs*, arXiv e-prints (2020)  
2827        p. arXiv:2007.08294 [[2007.08294](#)].
- 2828 [119] S. Brody, U. Alon and E. Yahav, *How Attentive are Graph Attention Networks?*,

- 2829        *arXiv e-prints* (2021) p. arXiv:2105.14491 [[2105.14491](#)].
- 2830 [120] D. P. Kingma and J. Ba, *Adam: A Method for Stochastic Optimization*, *arXiv e-prints* (2014) p. arXiv:1412.6980 [[1412.6980](#)].
- 2832 [121] J. Bai, F. Lu, K. Zhang et al., *ONNX: Open neural network exchange*, (2019).  
2833        <https://github.com/onnx/onnx>.
- 2834 [122] R. Lafaye, T. Plehn, M. Rauch, D. Zerwas and M. Duhrssen, *Measuring the Higgs Sector*, *JHEP* **08** (2009) p. 009 [[0904.3866](#)].
- 2836 [123] ATLAS Collaboration, *Measurement of the associated production of a Higgs boson decaying into b-quarks with a vector boson at high transverse momentum in pp collisions at  $\sqrt{s} = 13$  TeV with the ATLAS detector*, *Phys. Lett. B* **816** (2021) p. 136204 [[2008.02508](#)].
- 2840 [124] K. Mimasu, V. Sanz and C. Williams, *Higher order QCD predictions for associated Higgs production with anomalous couplings to gauge bosons*, *JHEP* **08** (2016) p. 039 [[1512.02572](#)].
- 2843 [125] ATLAS Collaboration, *Performance of jet substructure techniques for large-R jets in proton–proton collisions at  $\sqrt{s} = 7$  TeV using the ATLAS detector*, *JHEP* **09** (2013) p. 076 [[1306.4945](#)].
- 2846 [126] S. Alioli, P. Nason, C. Oleari and E. Re, *A general framework for implementing NLO calculations in shower Monte Carlo programs: the POWHEG BOX*, *JHEP* **06** (2010) p. 043 [[1002.2581](#)].
- 2849 [127] ATLAS collaboration, *Measurement of the  $Z/\gamma^*$  boson transverse momentum distribution in pp collisions at  $\sqrt{s} = 7$  TeV with the ATLAS detector*, *JHEP* **09** (2014) p. 145 [[1406.3660](#)].
- 2852 [128] G. Cullen, N. Greiner, G. Heinrich, G. Luisoni, P. Mastrolia, G. Ossola et al., *Automated one-loop calculations with GoSam*, *Eur. Phys. J. C* **72** (2012) p. 1889 [[1111.2034](#)].
- 2855 [129] K. Hamilton, P. Nason and G. Zanderighi, *MINLO: multi-scale improved NLO*, *JHEP* **10** (2012) p. 155 [[1206.3572](#)].
- 2857 [130] G. Luisoni, P. Nason, C. Oleari and F. Tramontano,  *$HW^\pm/HZ + 0$  and 1 jet at NLO with the POWHEG BOX interfaced to GoSam and their merging within MiNLO*, *JHEP* **10** (2013) p. 083 [[1306.2542](#)].

- 2860 [131] M. L. Ciccolini, S. Dittmaier and M. Krämer, *Electroweak radiative corrections to*  
2861 *associated WH and ZH production at hadron colliders*, *Phys. Rev. D* **68** (2003)  
2862 p. 073003 [[hep-ph/0306234](#)].
- 2863 [132] O. Brein, A. Djouadi and R. Harlander, *NNLO QCD corrections to the*  
2864 *Higgs-strahlung processes at hadron colliders*, *Phys. Lett. B* **579** (2004) pp. 149–156  
2865 [[hep-ph/0307206](#)].
- 2866 [133] G. Ferrera, M. Grazzini and F. Tramontano, *Associated Higgs-W-Boson Production*  
2867 *at Hadron Colliders: a Fully Exclusive QCD Calculation at NNLO*, *Phys. Rev. Lett.*  
2868 **107** (2011) p. 152003 [[1107.1164](#)].
- 2869 [134] O. Brein, R. V. Harlander, M. Wiesemann and T. Zirke, *Top-quark mediated effects*  
2870 *in hadronic Higgs-Strahlung*, *Eur. Phys. J. C* **72** (2012) p. 1868 [[1111.0761](#)].
- 2871 [135] G. Ferrera, M. Grazzini and F. Tramontano, *Higher-order QCD effects for associated*  
2872 *WH production and decay at the LHC*, *JHEP* **04** (2014) p. 039 [[1312.1669](#)].
- 2873 [136] G. Ferrera, M. Grazzini and F. Tramontano, *Associated ZH production at hadron*  
2874 *colliders: The fully differential NNLO QCD calculation*, *Phys. Lett. B* **740** (2015)  
2875 pp. 51–55 [[1407.4747](#)].
- 2876 [137] J. M. Campbell, R. K. Ellis and C. Williams, *Associated production of a Higgs boson*  
2877 *at NNLO*, *JHEP* **06** (2016) p. 179 [[1601.00658](#)].
- 2878 [138] L. Altenkamp, S. Dittmaier, R. V. Harlander, H. Rzehak and T. J. E. Zirke,  
2879 *Gluon-induced Higgs-strahlung at next-to-leading order QCD*, *JHEP* **02** (2013) p. 078  
2880 [[1211.5015](#)].
- 2881 [139] B. Hespel, F. Maltoni and E. Vryonidou, *Higgs and Z boson associated production via*  
2882 *gluon fusion in the SM and the 2HDM*, *JHEP* **06** (2015) p. 065 [[1503.01656](#)].
- 2883 [140] R. V. Harlander, A. Kulesza, V. Theeuwes and T. Zirke, *Soft gluon resummation for*  
2884 *gluon-induced Higgs Strahlung*, *JHEP* **11** (2014) p. 082 [[1410.0217](#)].
- 2885 [141] R. V. Harlander, S. Liebler and T. Zirke, *Higgs Strahlung at the Large Hadron*  
2886 *Collider in the 2-Higgs-doublet model*, *JHEP* **02** (2014) p. 023 [[1307.8122](#)].
- 2887 [142] O. Brein, R. V. Harlander and T. J. E. Zirke, *vh@nnlo – Higgs Strahlung at hadron*  
2888 *colliders*, *Comput. Phys. Commun.* **184** (2013) pp. 998–1003 [[1210.5347](#)].
- 2889 [143] S. Frixione, G. Ridolfi and P. Nason, *A positive-weight next-to-leading-order Monte*  
2890 *Carlo for heavy flavour hadroproduction*, *JHEP* **09** (2007) p. 126 [[0707.3088](#)].

- 2891 [144] M. Czakon and A. Mitov, *Top++: A program for the calculation of the top-pair*  
2892       *cross-section at hadron colliders*, *Comput. Phys. Commun.* **185** (2014) p. 2930  
2893       [[1112.5675](#)].
- 2894 [145] S. Alioli, P. Nason, C. Oleari and E. Re, *NLO single-top production matched with*  
2895       *shower in POWHEG: s- and t-channel contributions*, *JHEP* **09** (2009) p. 111  
2896       [[0907.4076](#)].
- 2897 [146] N. Kidonakis, *Next-to-next-to-leading logarithm resummation for s-channel single top*  
2898       *quark production*, *Phys. Rev. D* **81** (2010) p. 054028 [[1001.5034](#)].
- 2899 [147] N. Kidonakis, *Next-to-next-to-leading-order collinear and soft gluon corrections for*  
2900       *t-channel single top quark production*, *Phys. Rev. D* **83** (2011) p. 091503 [[1103.2792](#)].
- 2901 [148] E. Re, *Single-top Wt-channel production matched with parton showers using the*  
2902       *POWHEG method*, *Eur. Phys. J. C* **71** (2011) p. 1547 [[1009.2450](#)].
- 2903 [149] N. Kidonakis, *Two-loop soft anomalous dimensions for single top quark associated*  
2904       *production with a  $W^-$  or  $H^-$* , *Phys. Rev. D* **82** (2010) p. 054018 [[1005.4451](#)].
- 2905 [150] T. Gleisberg, S. Höche, F. Krauss, M. Schönherr, S. Schumann, F. Siegert et al.,  
2906       *Event generation with SHERPA 1.1*, *JHEP* **02** (2009) p. 007 [[0811.4622](#)].
- 2907 [151] E. Bothmann et al., *Event generation with Sherpa 2.2*, *SciPost Phys.* **7** (2019) p. 034  
2908       [[1905.09127](#)].
- 2909 [152] F. Cascioli, P. Maierhöfer and S. Pozzorini, *Scattering Amplitudes with Open Loops*,  
2910       *Phys. Rev. Lett.* **108** (2012) p. 111601 [[1111.5206](#)].
- 2911 [153] T. Gleisberg and S. Höche, *Comix, a new matrix element generator*, *JHEP* **12** (2008)  
2912       p. 039 [[0808.3674](#)].
- 2913 [154] S. Schumann and F. Krauss, *A parton shower algorithm based on Catani–Seymour*  
2914       *dipole factorisation*, *JHEP* **03** (2008) p. 038 [[0709.1027](#)].
- 2915 [155] S. Höche, F. Krauss, M. Schönherr and F. Siegert, *QCD matrix elements + parton*  
2916       *showers. The NLO case*, *JHEP* **04** (2013) p. 027 [[1207.5030](#)].
- 2917 [156] S. Catani, L. Cieri, G. Ferrera, D. de Florian and M. Grazzini, *Vector Boson*  
2918       *Production at Hadron Colliders: a Fully Exclusive QCD Calculation at NNLO*, *Phys.*  
2919       *Rev. Lett.* **103** (2009) p. 082001 [[0903.2120](#)].
- 2920 [157] J. Butterworth et al., *PDF4LHC recommendations for LHC Run II*, *J. Phys. G* **43**  
2921       (2016) p. 023001 [[1510.03865](#)].

- 2922 [158] A. Denner, S. Dittmaier, S. Kallweit and A. Mück, *Electroweak corrections to*  
2923 *Higgs-strahlung off W/Z bosons at the Tevatron and the LHC with Hawk*, *JHEP* **03**  
2924 (2012) p. 075 [[1112.5142](#)].
- 2925 [159] A. Denner, S. Dittmaier, S. Kallweit and A. Mück, *HAWK 2.0: A Monte Carlo*  
2926 *program for Higgs production in vector-boson fusion and Higgs strahlung at hadron*  
2927 *colliders*, *Comput. Phys. Commun.* **195** (2015) pp. 161–171 [[1412.5390](#)].
- 2928 [160] ATLAS Collaboration, *Expected performance of the ATLAS b-tagging algorithms in*  
2929 *Run-2*, ATL-PHYS-PUB-2015-022 (2015).
- 2930 [161] ATLAS Collaboration, *Measurements of b-jet tagging efficiency with the ATLAS*  
2931 *detector using  $t\bar{t}$  events at  $\sqrt{s} = 13$  TeV*, *JHEP* **08** (2018) p. 089 [[1805.01845](#)].
- 2932 [162] ATLAS Collaboration, *Calibration of light-flavour b-jet mistagging rates using*  
2933 *ATLAS proton–proton collision data at  $\sqrt{s} = 13$  TeV*, ATLAS-CONF-2018-006  
2934 (2018).
- 2935 [163] ATLAS Collaboration, *Measurement of b-tagging efficiency of c-jets in  $t\bar{t}$  events using*  
2936 *a likelihood approach with the ATLAS detector*, ATLAS-CONF-2018-001 (2018).
- 2937 [164] ATLAS Collaboration, *Flavor Tagging with Track-Jets in Boosted Topologies with the*  
2938 *ATLAS Detector*, ATL-PHYS-PUB-2014-013 (2014).
- 2939 [165] ATLAS Collaboration, *Identification of boosted Higgs bosons decaying into b-quark*  
2940 *pairs with the ATLAS detector at 13 TeV*, *Eur. Phys. J. C* **79** (2019) p. 836  
2941 [[1906.11005](#)].
- 2942 [166] L. A. Harland-Lang, A. D. Martin, P. Motylinski and R. S. Thorne, *Parton*  
2943 *distributions in the LHC era: MMHT 2014 PDFs*, *Eur. Phys. J. C* **75** (2015) p. 204  
2944 [[1412.3989](#)].
- 2945 [167] S. Dulat, T.-J. Hou, J. Gao, M. Guzzi, J. Huston, P. Nadolsky et al., *New parton*  
2946 *distribution functions from a global analysis of quantum chromodynamics*, *Phys. Rev.*  
2947 **D93** (2016) p. 033006 [[1506.07443](#)].
- 2948 [168] J. K. Anders and M. D’Onofrio, *V+Jets theoretical uncertainties estimation via a*  
2949 *parameterisation method*, Tech. Rep. ATL-COM-PHYS-2016-044, Geneva (2016).
- 2950 [169] J. Pumplin et al., *New generation of parton distributions with uncertainties from*  
2951 *global qcd analysis*, *JHEP* **07** (2002) p. 012 [[0201195](#)].
- 2952 [170] L. Moneta, K. Belasco, K. Cranmer, S. Kreiss, A. Lazzaro, D. Piparo et al., *The*

2953        *roostats project, arXiv preprint arXiv:1009.1003* (2010) .

# 2954 List of figures

<small>2955</small>	2.1 The Higgs potential $V(\phi)$ of the complex scalar field singlet $\phi = \phi_1 + i\phi_2$ , with a choice of $\mu^2 < 0$ leading to a continuous degeneracy in the true vacuum states. A false vacuum is present at the origin. The SM Higgs mechanism relies on a complex scalar doublet with a corresponding 5-dimensional potential. . . . .	19
<small>2960</small>	2.2 Diagrams for the four main Higgs boson production modes at the LHC for a Higgs mass $m_H = 125$ GeV at a centre of mass energy $\sqrt{s} = 13$ TeV. . . . .	25
<small>2962</small>	2.3 Higgs boson production cross sections as a function of Higgs mass ( $m_H$ ) at $\sqrt{s} = 13$ TeV [24]. Uncertainties are shown in the shaded bands. At $m_H = 125$ GeV, Higgs boson production is dominated by gluon-gluon fusion, vector boson fusion, associated production with vector bosons, and top quark fusion. . . . .	25
<small>2967</small>	2.4 Higgs boson branching ratios as a function of Higgs mass ( $m_H$ ) at $\sqrt{s} = 13$ TeV [24]. Uncertainties are shown in the shaded bands. At $m_H = 125$ GeV, the Higgs predominantly decays to a pair of $b$ -quarks, around 58% of the time. The leading subdominant decay mode is to a pair of $W$ bosons. . . . .	26
<small>2971</small>	3.1 An overview of the CERN accelerator complex [34]. The LHC is fed by a series of accelerators starting with Linac4. Next are the Proton Synchrotron Booster, the Proton Synchrotron, and finally the Super Proton Synchrotron which injects protons into the LHC. . . . .	29
<small>2975</small>	3.2 The coordinate system used at the ATLAS detector, showing the locations of the four main experiments located at various points around the LHC. The 3-vector momentum $\mathbf{p} = (p_x, p_y, p_z)$ is shown by the red arrow. Reproduced from Ref. [35]. . . . .	30

2979	3.3 The track parameterisation used at the ATLAS detector. Five coordinates $(d_0, z_0, \phi, \theta, q/p)$ are specified, defined at the track's point of closest approach to the nominal interaction point at the origin of the coordinate system. The figure shows the three-momentum $\mathbf{p}$ and the transverse momentum $p_T$ (defined in Eq. (3.2)). The basis vectors $e_x$ , $e_y$ and $e_z$ are also shown. Reproduced from Ref. [36]. . . . .	32
2985	3.4 Delivered, recorded, and usable integrated luminosity as a function of time over the course of Run 2 [33]. A total of $139\text{ fb}^{-1}$ of collision data is labelled as good for physics, meaning all sub-detector systems were operating nominally. . . . .	34
2989	3.5 Average pile-up profiles measured by ATLAS during Run 2 [33]. Higher levels of pile-up are planned for Run 3. . . . .	34
2991	3.6 A 3D model of the entire ATLAS detector [40]. The detector is 46 m long and 25 m in diameter. Cutouts to the centre of the detector reveal the different subdetectors which are arranged in concentric layers around the nominal interaction point. . . . .	35
2995	3.7 A 3D model of the ATLAS ID, made up of the pixel and SCT subdetectors, showing the barrel layers and end-cap disks [43]. . . . .	36
2997	3.8 A cross-sectional view of the ATLAS ID, with the radii of the different barrel layers shown [36]. . . . .	37
2999	3.9 A schematic cross-sectional view of the ATLAS IBL [44]. . . . .	38
3000	3.10 The ATLAS calorimeters [47]. The ECal uses LAr-based detectors, while the HCal uses mainly scintillating tile detectors. In the forward region the HCal also includes the LAr hadronic endcaps. . . . .	40
3003	3.11 The ATLAS muon spectrometer [50]. . . . .	42
3004	3.12 Particles (left) which have enough separation will leave charge depositions which are resolved into separate clusters. Sufficiently close particles (right) can lead to merged clusters. Their combined energy deposits are recon- structed as a single merged cluster [55]. . . . .	46
3008	3.13 A sketch of electron reconstruction using the ATLAS detector [73]. Electron reconstruction makes use of the entire ID and the calorimeters. In particular, discriminating information comes from the TRT and ECal. . . . .	50

3011	4.1 The truth $b$ -hadron decay radius $L_{xy}$ as a function of truth transverse 3012 momentum $p_T$ for reconstructed $b$ -jets in $Z'$ events. Error bars show the 3013 standard deviation. The pixel layers are shown in dashed horizontal lines.	54
3014	4.2 Diagram of a typical $b$ -jet (blue) which has been produced in an event 3015 alongside two light jets (grey) [79]. The $b$ -hadron has travelled a significant 3016 distance (pink dashed line) from the primary interaction point (pink dot) 3017 before its decay. The large transverse impact parameter $d_0$ is a characteristic 3018 property of the trajectories of $b$ -hadron decay products. . . . .	55
3019	4.3 At lower $p_T$ (left) the decay length of the $b$ -hadron is reduced, and the 3020 resulting decay tracks are less collimated. At higher $p_T$ (right) the $b$ -hadron 3021 decay length increases and the resulting decay tracks are more collimated and 3022 have less distance over which to diverge before reaching detector elements. 3023 As a result, the ID may be unable to resolve charged depositions from 3024 different particles, resulting merged clusters. . . . .	56
3025	4.4 $b$ -hadron decay track reconstruction efficiency as a function of truth $b$ -hadron 3026 $p_T$ [80]. Nominal track reconstruction is shown in black, while the track 3027 reconstruction efficiency for track candidates (i.e. the pre-ambiguity solver 3028 efficiency) is shown in green. For high- $p_T$ $b$ -hadrons, the ambiguity solver 3029 is overly aggressive in its removal of $b$ -hadron decay tracks. Suggestions for 3030 the improvement of the track reconstruction efficiency in this regime by the 3031 loosening of cuts in the ambiguity solver are shown in blue and red. . . . .	57
3032	4.5 Hit multiplicities on the IBL (left) and the pixel layers (right) as a function 3033 of the $p_T$ of the reconstructed track. Tracks from the weak decay of 3034 the $b$ -hadron are shown in red, while fragmentation tracks (which are 3035 prompt) are in blue. Baseline tracks are those produced in the standard 3036 reconstruction described in Section 3.4.1, while pseudotracks represent the 3037 ideal performance of the ATLAS detector and are described in Section 3.4.1. 3038 Hit multiplicities on the pseudotracks decrease at high $p_T$ due to the flight 3039 of the $b$ -hadron before its decay. The baseline tracks have more hits than the 3040 pseudotracks, indicating that they are being incorrectly assigned additional 3041 hits on the inner layers of the detector. . . . .	59
3042	4.6 The fraction of hits which are shared on $b$ -hadron decay tracks on the IBL 3043 (left), and the B-layer (right), as a function of the production radius of 3044 the $b$ -hadron decay product. Pseudotracks represent the ideal performance 3045 given the ATLAS detector, see Section 3.4.1. . . . .	60

3046	4.7 The rate to assign good (left) and wrong (right) IBL hits as a function 3047 of $b$ -hadron $p_T$ for tracks using baseline tracking (black) and the modified 3048 version of the outlier removal procedure (red). For each track, the corre- 3049 sponding $p_T$ bin is filled with the number of good or wrong hits and this 3050 value is averaged to show the overall rate. . . . .	62
3051	4.8 (left) $b$ -hadron decay track $d_0$ pulls ( $d_0/s(d_0)$ ) for baseline and modified 3052 GX2F tracks. (right) The absolute value of the $d_0$ pull as a function of 3053 $b$ -hadron transverse momentum. . . . .	63
3054	5.1 A diagram displaying the logical flow of a single neuron with three inputs 3055 $x_i^j$ . Each input is multiplied by a weight $\theta_j$ , and the resulting values are 3056 summed. A bias term $\theta_0$ is added, and the result $z$ is passed to an activation 3057 function. Each neuron can be thought of as a logistic regression model. .	67
3058	5.2 The output of several common choices for the activation function $g(z)$ of 3059 an artificial neuron. The input $z$ is the output of the dot product between 3060 the activation and the weights, plus a bias term. . . . .	68
3061	5.3 Rate of fake tracks as a function of jet transverse momentum (left) and 3062 $\Delta R(\text{track}, \text{jet})$ (right). The rate of fake tracks increases significantly as a 3063 function of $p_T$ , and also increases as the distance to the jet axis decreases.	71
3064	5.4 The light-jet efficiency of the low level tagger SV1 for jets in the $Z'$ sample 3065 with $250 < p_T < 5000 \text{ GeV}$ , as a function of $b$ -jet efficiency. The nominal 3066 tracking setup (black) is shown alongside the case where fake tracks which 3067 are not from the decay of a $b$ -hadron are removed. The light-jet efficiency 3068 is decreased, demonstrating that the presence of fake tracks is detrimental 3069 to the algorithm performance. . . . .	71
3070	5.5 (left) Normalised histogram of the model output separated for signal and 3071 fake tracks, and further separated by those tracks which are from the 3072 decay of a $b$ -hadron. (right) The ROC curve for all tracks (solid line) and 3073 tracks from the decay of a $b$ -hadron (dashed line). The model is able to 3074 successfully discriminate between signal and fake tracks, and shows a very 3075 similar performance when looking specifically at tracks from the decay of a 3076 $b$ -hadron. . . . .	76

3077	5.6 (left) Normalised histogram of the model output separated for tracks from 3078 the decay of a $b$ -hadron and tracks from other sources. The two groups are 3079 further separated into those tracks which are fake. (right) The ROC curve 3080 for all tracks (solid line). . . . .	78
3081	5.7 The effect of applying the fake track identification algorithm together with 3082 the $b$ -hadron decay track identification on the jet tagging performance of 3083 SV1 for jets in the $Z'$ sample with $250 \text{ GeV} < p_T < 400 \text{ GeV}$ (left) and 3084 $400 \text{ GeV} < p_T < 1 \text{ TeV}$ (right). The nominal SV1 light-jet rejection (black) 3085 is compared to two working points of fake track removal, labelled “A” (red) 3086 and “B” (orange), which represent two different 2D working points of the 3087 track classification tools. Removal of fake tracks based on truth information 3088 is shown by the green curves. . . . .	79
3089	6.1 Comparison of the existing flavour tagging scheme (left) and GN1 (right). 3090 The existing approach utilises low-level algorithms (shown in blue), the 3091 outputs of which are fed into a high-level algorithm (DL1r). Instead 3092 of being used to guide the design of the manually optimised algorithms, 3093 additional truth information from the simulation is now being used as 3094 auxiliary training targets for GN1. The solid lines represent reconstructed 3095 information, whereas the dashed lines represent truth information. . . . .	83
3096	6.2 The flow of information through a graph neural network layer for (left) a full 3097 implementation of the layer and (right) a deep sets model [115]. Reproduced 3098 from Ref. [114]. . . . .	86
3099	6.3 The inputs to GN1 are the two jet features ( $n_{\text{jf}} = 2$ ), and an array of 3100 $n_{\text{tracks}}$ , where each track is described by 21 track features ( $n_{\text{tf}} = 21$ ). The 3101 jet features are copied for each of the tracks, and the combined jet-track 3102 vectors of length 23 form the inputs of GN1. . . . .	91
3103	6.4 The network architecture of GN1. Inputs are fed into a per-track initialisation 3104 network, which outputs an initial latent representation of each track. 3105 These representations are then used to populate the node features of a 3106 fully connected graph network. After the graph network, the resulting node 3107 representations are used to predict the jet flavour, the track origins, and 3108 the track-pair vertex compatibility. . . . .	92

---

3109	6.5 Comparison between the DL1r and GN1 $b$ -tagging discriminant $D_b$ for jets in the $t\bar{t}$ sample. The 85% WP and the 60% WP are marked by the solid (dashed) lines for GN1 (DL1r), representing respectively the loosest and tightest WPs used by analyses. A value of $f_c = 0.018$ is used in the calculation of $D_b$ for DL1r and $f_c = 0.05$ is used for GN1. The distributions of the different jet flavours have been normalised to unity area. . . . .	97
3115	6.6 The $c$ -jet (left) and light-jet (right) rejections as a function of the $b$ -jet tagging efficiency for jets in the $t\bar{t}$ sample with $20 < p_T < 250$ GeV. The ratio with respect to the performance of the DL1r algorithm is shown in the bottom panels. A value of $f_c = 0.018$ is used in the calculation of $D_b$ for DL1r and $f_c = 0.05$ is used for GN1 and GN1Lep. Binomial error bands are denoted by the shaded regions. At $b$ -jet tagging efficiencies less than $\sim 75\%$ , the light-jet rejection becomes so large that the effect of the low number of jets is visible. The lower $x$ -axis range is chosen to display the $b$ -jet tagging efficiencies usually probed in these regions of phase space. . . . .	99
3124	6.7 The $c$ -jet (left) and light-jet (right) rejections as a function of the $b$ -jet tagging efficiency for jets in the $Z'$ sample with $250 < p_T < 5000$ GeV. The ratio with respect to the performance of the DL1r algorithm is shown in the bottom panels. A value of $f_c = 0.018$ is used in the calculation of $D_b$ for DL1r and $f_c = 0.05$ is used for GN1 and GN1Lep. Binomial error bands are denoted by the shaded regions. At $b$ -jet tagging efficiencies less than $\sim 20\%$ , the light-jet rejection becomes so large that the effect of the low number of jets is visible. The lower $x$ -axis range is chosen to display the $b$ -jet tagging efficiencies usually probed in these regions of phase space. . . . .	100
3133	6.8 The $b$ -jet tagging efficiency for jets in the $t\bar{t}$ sample (left) and jets in the $Z'$ sample (right) as a function of jet $p_T$ with a fixed light-jet rejection of 100 in each bin. A value of $f_c = 0.018$ is used in the calculation of $D_b$ for DL1r and $f_c = 0.05$ is used for GN1 and GN1Lep. GN1 demonstrates improved performance with respect to DL1r across the $p_T$ range shown. Binomial error bands are denoted by the shaded regions. . . . . . . . . . .	101

3139	6.9 The $b$ -jet (left) and light-jet (right) rejections as a function of the $c$ -jet tagging efficiency for $t\bar{t}$ jets with $20 < p_T < 250$ GeV. The ratio to the performance of the DL1r algorithm is shown in the bottom panels. Binomial error bands are denoted by the shaded regions. At $c$ -jet tagging efficiencies than $\sim 25\%$ , the light-jet rejection becomes so large that the effect of the low number of jets is visible. The lower $x$ -axis range is chosen to display the $c$ -jet tagging efficiencies usually probed in these regions of phase space. . . . .	103
3140		
3141		
3142		
3143		
3144		
3145		
3146	6.10 The $b$ -jet (left) and light-jet (right) rejections as a function of the $c$ -jet tagging efficiency for $Z'$ jets with $250 < p_T < 5000$ GeV. The ratio to the performance of the DL1r algorithm is shown in the bottom panels. Binomial error bands are denoted by the shaded regions. The lower $x$ -axis range is chosen to display the $c$ -jet tagging efficiencies usually probed in these regions of phase space. . . . .	103
3147		
3148		
3149		
3150		
3151		
3152	6.11 A schematic showing the truth track origin and vertex information (left) compared with the predictions from GN1 (right). Vertices reconstructed by SV1 and JetFitter are also marked. Class probabilities $p_b$ , $p_c$ and $p_u$ are rounded to three significant figures. GN1 improves over SV1 and JetFitter by successfully determining the origins and vertex compatibility of all the tracks in the jet with the exception of the truth OtherSecondary track, which is misidentified as pileup. . . . .	105
3153		
3154		
3155		
3156		
3157		
3158		
3159	6.12 A schematic showing the truth track origin and vertex information (left) compared with the predictions from GN1 (right). Vertices reconstructed by SV1 and JetFitter are also marked. Class probabilities $p_b$ , $p_c$ and $p_u$ are rounded to three significant figures. . . . .	105
3160		
3161		
3162		
3163	6.13 The $c$ -jet (left) and light-jet (right) rejections as a function of the $b$ -jet tagging efficiency for $t\bar{t}$ jets with $20 < p_T < 250$ GeV, for the nominal GN1, in addition to configurations where no (GN1 No Aux), only the track classification (GN1 TC) or only the vertexing (GN1 Vert) auxiliary objectives are deployed. The ratio to the performance of the DL1r algorithm is shown in the bottom panels. A value of $f_c = 0.018$ is used in the calculation of $D_b$ for DL1r and $f_c = 0.05$ is used for GN1. Binomial error bands are denoted by the shaded regions. At $b$ -jet tagging efficiencies less than $\sim 65\%$ , the light-jet rejection become so large that the effect of the low number of jets are visible. The lower $x$ -axis range is chosen to display the $b$ -jet tagging efficiencies usually probed in these regions. . . . .	107
3164		
3165		
3166		
3167		
3168		
3169		
3170		
3171		
3172		
3173		

3174	6.14 The $c$ -jet (left) and light-jet (right) rejections as a function of the $b$ -jet 3175 tagging efficiency for $Z'$ jets with $250 < p_T < 5000$ GeV, for the nominal 3176 GN1, in addition to configurations where no (GN1 No Aux), only the track 3177 classification (GN1 TC) or only the vertexing (GN1 Vert) auxiliary objectives 3178 are deployed. The ratio to the performance of the DL1r algorithm is shown 3179 in the bottom panels. A value of $f_c = 0.018$ is used in the calculation of $D_b$ 3180 for DL1r and $f_c = 0.05$ is used for GN1. Binomial error bands are denoted 3181 by the shaded regions. At $b$ -jet tagging efficiencies less than $\sim 25\%$ , the 3182 light-jet rejection become so large that the effect of the low number of jets 3183 are visible. The lower $x$ -axis range is chosen to display the $b$ -jet tagging 3184 efficiencies usually probed in these regions. . . . .	108
3185	6.15 Vertex finding efficiency as a function of jet $p_T$ for $b$ -jets in the $t\bar{t}$ sample 3186 using the exclusive (left) and inclusive (right) vertex finding approaches. 3187 Efficient vertex finding requires the recall of at least 65% of the tracks in 3188 the truth vertex, and allows no more than 50% of the tracks to be included 3189 incorrectly. Binomial error bands are denoted by the shaded regions. . . . .	111
3190	6.16 Inclusive vertex finding efficiency for multitrack truth vertices in $b$ -jets in 3191 the $t\bar{t}$ sample (left) and jets in the $Z'$ sample (right) as a function of jet $p_T$ . 3192 Efficient vertex finding requires the recall of at least 65% of the tracks in 3193 the truth vertex, and allows no more than 50% of the tracks to be included 3194 incorrectly. . . . .	112
3195	6.17 ROC curves for the different groups of truth origin labels defined in Table 5.1 3196 for jets in the $t\bar{t}$ sample (left) and jets in the $Z'$ sample (right). The 3197 FromB, FromBC and FromC labels have been combined, weighted by their 3198 relative abundance, into the Heavy Flavour category, and the Primary and 3199 OtherSecondary labels have similarly been combined into a single category. 3200 The mean weighted area under the ROC curves (AUC) is similar for both 3201 samples. . . . .	114
3202	6.18 The $c$ -jet (left) and light-jet (right) rejections as a function of the $b$ -jet 3203 tagging efficiency for $t\bar{t}$ jets with $20 < p_T < 250$ GeV, for the looser track 3204 selection trainings of GN1. The ratio to the performance of the DL1d 3205 algorithm is shown in the bottom panels. A value of $f_c = 0.018$ is used in 3206 the calculation of $D_b$ for DL1d and $f_c = 0.05$ is used for GN1. Binomial 3207 error bands are denoted by the shaded regions. . . . .	116

---

3208	6.19 The $c$ -jet (left) and light-jet (right) rejections as a function of the $b$ -jet 3209 tagging efficiency for $Z'$ jets with $250 < p_T < 5000$ GeV, for the looser 3210 track selection trainings of GN1. The ratio to the performance of the DL1d 3211 algorithm is shown in the bottom panels. A value of $f_c = 0.018$ is used in 3212 the calculation of $D_b$ for DL1d and $f_c = 0.05$ is used for GN1. Binomial 3213 error bands are denoted by the shaded regions. . . . .	118
3214	7.1 Diagrams of the signal process (top) and the 0-lepton and 1-lepton $t\bar{t}$ back- 3215 grounds (middle, bottom). Object to the right of centre are reconstructed 3216 within the large- $R$ jet. For the backgrounds, the large- $R$ jet contains a 3217 mis-tagged $c$ - or light-jet. . . . .	128
3218	7.2 Normalised leading large- $R$ jet mass distribution from $Z$ and $W+hf$ pro- 3219 cesses in the HP SR of the 0-lepton channel. The renormalisation scale $\mu_r$ 3220 has been varied by a factor of 2 (1up) and 0.5 (1down). An exponential 3221 function is fitted to the ratio between the nominal and variation samples.	138
3222	7.3 The comparison on $m_J$ shapes between SHERPA and MADGRAPH samples 3223 from $V+hf$ process in $p_T^V$ inclusive signal regions. The Kolmogorov-Smirnov 3224 test and $\chi^2/ndf$ are shown on the plots. . . . .	139
3225	7.4 Normalised leading large- $R$ jet mass distribution from $WZ$ and $ZZ$ process, 3226 merged among all the signal regions and lepton channels. The renormalisa- 3227 tion scale $\mu_R$ has been varied by a factor of 2 (1up) and 0.5 (1down). The 3228 red line shape shows the fitting results of the hyperbolic tangent function.	141
3229	7.5 The comparison on $m_J$ shapes between SHERPA and POWHEG+PYTHIA 8 3230 samples from $WZ$ and $ZZ$ process in high and low purity signal regions. 3231 $p_T^V$ regions and 0- and 1-lepton channels are merged. The dashed green line 3232 shows the fitted third order polynomial function and the blue lines show 3233 the function after a protection is added in the high mass region. . . . .	142

---

3234	7.6 The $m_J$ post-fit distributions in (top) the 0-, (middle) 1- and (bottom)	
3235	2-lepton SRs for (left) $250 \text{ GeV} < p_T^V < 400 \text{ GeV}$ and (right) $p_T^V \geq 400 \text{ GeV}$ .	
3236	The LP and HP regions are merged for the 0-lepton and 1-lepton channels.	
3237	The fitted background contributions are shown as filled histograms. The	
3238	Higgs boson signal ( $m_H = 125 \text{ GeV}$ ) is shown as a filled histogram and	
3239	is normalised to the signal yield extracted from data ( $\mu_{VH}^{bb} = 0.72$ ), and	
3240	as an unstacked unfilled histogram, scaled by the SM prediction times a	
3241	factor of two. The size of the combined on the sum of the fitted signal and	
3242	background is shown in the hatched band. The highest bin contains the	
3243	overflow. . . . .	148
3244	7.7 The $m_J$ post-fit distributions in the $t\bar{t}$ control region for (top) the 0-lepton	
3245	channel and the 1-lepton channel for $250 \text{ GeV} < p_T^V < 400 \text{ GeV}$ and (bot-	
3246	tom) the 0-lepton channel and the 1-lepton channel for $p_T^V > 400 \text{ GeV}$ .	
3247	The background contributions after the likelihood fit are shown as filled	
3248	histograms. The Higgs boson signal ( $m_h = 125 \text{ GeV}$ ) is shown as a filled	
3249	histogram on top of the fitted backgrounds normalised to the signal yield	
3250	extracted from data ( $\mu_{VH}^{bb} = 0.72$ ), and unstacked as an unfilled histogram,	
3251	scaled by the SM prediction times a factor of 2. The size of the combined	
3252	statistical and systematic uncertainty for the sum of the fitted signal and	
3253	background is indicated by the hatched band. The highest bin in the	
3254	distributions contains the overflow. . . . .	149
3255	7.8 $m_J$ distribution in data after subtraction of all backgrounds except for the	
3256	$WZ$ and $ZZ$ diboson processes. The contributions from all lepton channels	
3257	and signal regions are summed and weighted by their respective values of	
3258	the ratio of fitted Higgs boson signal and background yields. The expected	
3259	contribution of the associated $WH$ and $ZH$ production of a SM Higgs	
3260	boson with $m_H = 125 \text{ GeV}$ is shown scaled by the measured combined	
3261	signal strength ( $\mu_{VH}^{bb} = 0.72$ ). The diboson contribution is normalised to	
3262	its best-fit value of $\mu_{VZ}^{bb} = 0.91$ . The size of the combined statistical and	
3263	systematic uncertainty is indicated by the hatched band. This error band is	
3264	computed from a full signal-plus-background fit including all the systematic	
3265	uncertainties defined in Section 7.2, except for the $VH/VZ$ experimental	
3266	and theory uncertainties. . . . .	150

3267	7.9 Signal strength compatibility test between the (3+1)-POI fit (with the three	
3268	lepton channels splitted) and the default (1+1)-POI fit. The compatibility	
3269	of the three channels is evaluated via a $\chi^2$ difference test and results in a	
3270	p-value of 49%. . . . .	151
3271	7.10 Impact of systematic uncertainties on the fitted $VH$ signal-strength pa-	
3272	rameter $\mu_{VH}^{bb}$ sorted in decreasing order. The boxes show the variations	
3273	of $\hat{\mu}$ , referring to the top $x$ -axis, when fixing the corresponding individual	
3274	nuisance parameter to its post-fit value modified upwards or downwards by	
3275	its post-fit uncertainty, i.e. $\hat{\theta} \pm \sigma_{\hat{\theta}}$ , and repeating the fit. The impact of	
3276	up- and down-variations can be distinguished via the dashed and plane box	
3277	fillings. The yellow boxes show the pre-fit impact (top $x$ -axis) by varying	
3278	each nuisance parameter by $\pm 1$ . The filled circles show the deviation of the	
3279	fitted value for each nuisance parameter, $\hat{\theta}$ , from their nominal input value	
3280	$\theta_0$ expressed in standard deviations with respect to their nominal uncer-	
3281	tainties $\Delta\theta$ (bottom $x$ -axis). The error bars show the post-fit uncertainties	
3282	on $\hat{\theta}$ with respect to their nominal uncertainties. The open circles show	
3283	the fitted values and uncertainties of the normalization parameters that are	
3284	freely floating in the fit. Pre-fit, these parameters have a value of one. . .	153

# 3285 List of tables

<small>3286</small>	2.1 The fermions of the SM [14]. Three generations of particles are present. Also present (unlisted) are the antiparticles, which are identical to the particles up to a reversed charge sign. . . . .	<small>3287</small>	<small>3288</small>	14				
<small>3289</small>	2.2 The bosons of the SM [14]. The photon, weak bosons and gluons are gauge bosons arising from gauge symmetries, and carry the four fundamental forces of the SM. The recently discovered Higgs boson is the only fundamental scalar particle in the SM. . . . .	<small>3290</small>	<small>3291</small>	<small>3292</small>	15			
<small>3293</small>	3.1 Overview of the different LHC runs [32, 33]. The average number of interac- tions per bunch-crossing is denoted as $\langle \mu \rangle$ (see Section 3.2.3), and is here averaged over the entire run. Numbers for Run 3 are preliminary and are only provided to give an indication of expected performance. . . . .	<small>3294</small>	<small>3295</small>	<small>3296</small>	28			
<small>3297</small>	5.1 Truth origins which are used to categorise the physics process that led to the production of a track. Tracks are matched to charged particles using the truth-matching probability [55]. A truth-matching probability of less than 0.5 indicates that reconstructed track parameters are likely to be mismeasured and may not correspond to the trajectory of a single charged particle. The “OtherSecondary” origin includes tracks from photon conversions, $K_S^0$ and $\Lambda^0$ decays, and hadronic interactions. . . . .	<small>3298</small>	<small>3299</small>	<small>3300</small>	<small>3301</small>	<small>3302</small>	<small>3303</small>	70
<small>3304</small>	5.2 Input features to the fake track classification NN. Basic jet kinematics, along with information about the reconstructed track parameters and constituent hits are used. Shared hits, are hits used on multiple tracks which have not been classified as split by the cluster-splitting neural networks [55], while split hits are hits used by multiple tracks which have been identified as merged, and therefore split. . . . .	<small>3305</small>	<small>3306</small>	<small>3307</small>	<small>3308</small>	<small>3309</small>	74	

3310	5.3 Quality selections applied to tracks, where $d_0$ is the transverse IP of the track, $z_0$ is the longitudinal IP with respect to the PV and $\theta$ is the track polar angle (see Section 3.2.2 for the IP definitions). Shared hits are hits used on multiple tracks which have not been classified as split by the cluster-splitting neural networks [55]. A hole is a missing hit, where one is expected, on a layer between two other hits on a track. . . . .	75
3316	5.4 Hyperparameter for the track classification model . . . . .	75
3317	5.5 Good and fake track selection efficiencies for the combined $t\bar{t}$ and $Z'$ samples. Two working points are defined, cutting on the NN output at 0.06 and 0.12. The continuous output of the model allows for the tuning of good and fake track identification efficiencies. . . . .	77
3321	5.6 Cut values for the fake and $b$ -hadron decay track MVAs for the two defined working points. Working point “B” cuts more aggressively on the MVA outputs than WP “A”, removing more fake tracks but resulting in an increased loss of signal tracks (which here are all $b$ -hadron decay tracks). . . . .	78
3325	6.1 Input features to the GN1 model. Basic jet kinematics, along with information about the reconstructed track parameters and constituent hits are used. Shared hits, are hits used on multiple tracks which have not been classified as split by the cluster-splitting neural networks [55], while split hits are hits used on multiple tracks which have been identified as merged. A hole is a missing hit, where one is expected, on a layer between two other hits on a track. The track leptonID is an additional input to the GN1Lep model. . . . .	89
3332	6.2 A summary of GN1’s different classification networks used for the different training objectives. The hidden layers column contains a list specifying the number of neurons in each layer. . . . .	93
3335	6.3 The area under the ROC curves (AUC) for the track classification from GN1, compared to a standard multilayer perceptron (MLP) trained on a per-track basis. The unweighted mean AUC over the origin classes and weighted mean AUC (using as a weight the fraction of tracks from the given origin) is provided. GN1, which uses an architecture that allows track origins to be classified in a conditional manner as discussed in Section 6.4.3, outperforms the MLP model for both $t\bar{t}$ and $Z'$ jets. . . . .	114

3342	7.1 Summary of the definition of the analysis regions. Signal enriched regions are marked with the label SR. There are regions with relatively large signal purity (HP SR) and with low purity (LP SR). Background enriched regions are marked with the label CR. The shorthand ‘‘add’’ stands for additional small- $R$ jets, i.e. number of small- $R$ jets not matched to the Higgs-jet candidate. . . . .	122
3348	7.2 Signal and background processes with the corresponding generators used for the nominal samples. If not specified, the order of the cross-section calculation refers to the expansion in the strong coupling constant ( $\alpha_s$ ). (★) The events were generated using the first PDF in the NNPDF3.0NLO set and subsequently reweighted to the PDF4LHC15NLO set [157] using the internal algorithm in POWHEG-Box v2. (†) The NNLO(QCD)+NLO(EW) cross-section calculation for the $pp \rightarrow ZH$ process already includes the $gg \rightarrow ZH$ contribution. The $qq \rightarrow ZH$ process is normalised using the cross-section for the $pp \rightarrow ZH$ process, after subtracting the $gg \rightarrow ZH$ contribution. An additional scale factor is applied to the $qq \rightarrow VH$ processes as a function of the transverse momentum of the vector boson, to account for electroweak (EW) corrections at NLO. This makes use of the $VH$ differential cross-section computed with HAWK [158, 159]. . . . .	124
3360	7.3 Event selection requirements for the boosted $VH$ , $H \rightarrow b\bar{b}$ analysis chan- nels and sub-channels. Various channel dependent selections are used to maximise the signal efficiency and reduce the number of background events in each analysis region. . . . .	126
3364	7.4 Different sources of uncertainty (i.e. variations in the model) considered for the $V+jets$ background, and the corresponding implementation. For each uncertainty, acceptance and shape uncertainties are derived. . . . .	132
3367	7.5 0-lepton $W+jets$ nominal sample flavour composition and total event yield. . .	134
3368	7.6 1-lepton $W+jets$ nominal sample flavour composition and total event yield. . .	134
3369	7.7 0-lepton $Z+jets$ nominal sample flavour composition and total event yield. . .	134
3370	7.8 2-lepton $Z+jets$ nominal sample flavour composition and total event yield. . .	134

---

3371	7.9 V+jets acceptance uncertainties. $W+$ jets SR and CR uncertainties marked 3372 with a superscript $\dagger$ are correlated. The 1L $W+$ jets H/M uncertainty 3373 marked by * is applied as independent and uncorrelated NPs in both HP 3374 and LP signal regions. The 0L $W+$ jets Wbb Norm uncertainty is only 3375 applied when a floating normalisation for Wbb cannot be obtained from 3376 the 1L channel. A 30% uncertainty for $Z \rightarrow b\bar{b}$ norm is applied in the 1L 3377 channel when a floating normalisation for $Z \rightarrow b\bar{b}$ cannot be obtained from 3378 the 0L or 2L channels. . . . .	136
3379	7.10 Diboson acceptance uncertainties. All uncertainties except channel extrap- 3380 olation uncertainties are fully correlated between $ZZ$ and $WZ$ processes 3381 and channels. . . . .	141
3382	7.11 Factors applied to the nominal normalisations of the $t\bar{t}$ , $W+hf$ , and $Z+hf$ 3383 backgrounds, as obtained from the likelihood fit. The errors represent the 3384 combined statistical and systematic uncertainties. . . . .	146
3385	7.12 Breakdown of the observed absolute contributions to the uncertainty on the 3386 signal strength $\mu_{VH}^{bb}$ obtained from the (1+1)-POI fit. The average impact 3387 represents the average between the positive and negative uncertainties on 3388 $\mu_{VH}^{bb}$ . The sum in quadrature of the systematic uncertainties attached to the 3389 categories differs from the total systematic uncertainty due to correlations. . . . .	155